Synthesis and Self-Assembly of Metal Carbonyl Building Blocks for Aqueous Colloids with Aggregation-Induced Functions

by

Nimer Murshid

A thesis
presented to the University of Waterloo
in fulfillment of the
thesis requirement for the degree of

Doctor of Philosophy

in

Chemistry (Nanotechnology)

Waterloo, Ontario, Canada, 2017

Examining Committee Membership

The following served on the Examining Committee for this thesis. The decision of the Examining Committee is by majority vote.

External Examiner	JOE B. GILROY Assistant Professor
Supervisor	XIAOSONG WANG Associate Professor
Internal Member	JEAN DUHAMEL Professor
Internal Member	SHIRLEY TANG Associate Professor
Internal-external Member	YUNING LI Associate Professor

Author's Declaration

This thesis consists of material all of which I authored or co-authored: see Statement of Contributions included in the thesis. This is a true copy of the thesis, including any required final revisions, as accepted by my examiners.

I understand that my thesis may be made electronically available to the public.

Statement of Contributions

The research work discussed in Chapter 2 was published in Chemistry - A European Journal. 2015, 21 (52), 19223-19230. Reproduced from Ref. [118] with permission from John Wiley and Sons.

The research work discussed in Chapter 3 was published in the Journal of Organometallic Chemistry, 2016, 819, 109-114. Reproduced from Ref. [215] with permission from Elsevier.

Synthesis of MpC6 and the preparation of the crystal structure were done with cooperation with Mohammad A. Rahman

The research work discussed in Chapter 4 was published in the Journal of Materials Chemistry C 2016, 4 (23), 5231-5240. Reproduced from Ref. [119] with permission from the Royal Society of Chemistry.

Part of this work was performed with collaboration with my co-authors during my research visit to the National Chiao Tung University/Taiwan. Laser trapping experiment was performed by Ken-ichi Yuyama. Gaussian simulation and SAXS experiment were performed by Kuan-Yi Wu and San-Lien Wu, respectively.

I am the first author of all these journal publications and other reported parts in this thesis.

Abstract

Metal carbonyl complexes (MCCs) are potentially useful for a range of biomedical applications, including cell imaging and bioassay. However, the poor solubility and stability of MCCs in water remain obstacles to their use in these applications. This thesis addresses this challenge *via* an investigation of the self-assembly behaviour of hydrophobic Fp (Fp: $CpFe(CO)_2$) or Mp (Mp: $CpMo(CO)_3$) acyl derivatives in water. Hydration of these hydrophobic molecules results in aqueous colloids with aggregation induced functions.

The Fp and Mp acyl derivatives, used in this research, synthesized by the migration insertion reaction (MIR) of Fp and Mp alkyl compounds in the presence of phosphine ligands, e.g. triphenylphosphine (PPh_3), possessed a highly polarized acyl CO group. This group was readily hydrated *via* water-carbonyl interactions (WCIs) during the aggregation of the molecules in water. This aggregation, driven by hydrophobic forces, resulted in highly integrated metal carbonyl vesicles (MCsomes) with liposome-like bilayer membranes. The polarized CO groups associated on the surface of the colloid created a strong local electric field, which induced an aggregation-enhanced IR absorption (AEIRA). When the colloids were exposed to a focused continuous-wave near-IR (NIR) laser beam, a strong gradient (trapping) force was generated, allowing laser-trapping of the MCsome. This strong force resulted from the sharp contrast in the refractive index (RI) between the building blocks (RI = ca. 1.8) and water (RI = 1.33).

Blue-light–emitting MCsomes were created via the synthesis and self-assembly of a bithiophene tethered Fp acyl derivative. The bithiophene groups, associated within the

membrane, generated an aggregation-induced emission (AIE). The separation of the bithiophene group from the metal carbonyl group, by an alkyl spacer, prevented AIE being quenched by the iron elements. The AEIRA, AIE and laser manipulation render the MCsomes potentially useful for vibrational and photoluminescent sensing applications.

In addition, the redox activity of the iron on the surface of the colloids in water was explored. Cyclic voltammetry (CV) results showed two oxidation peaks separated by a redox coupling ($\Delta E_{½}$). The value of $\Delta E_{½}$ is inversely related to the separation distance between the adjacent Fp units located at the surfaces of the colloids, and was used to probe the degree of hydration of the hydrophobic domain. Taking advantage of this redox behaviour, the contribution of hydrophobic hydration to the formation and stabilization of the colloids, assembled from Fp acyl derivatives including hydrophobic and amphiphilic molecules, was systematically investigated. The results indicate that the hydrophobic interaction and hydration are significantly important for colloidal stability.

In conclusion, a novel group of vesicles, MCsome, with multiple functions has been created *via* the aqueous self-assembly of Fp or Mp acyl derivatives. Hydrophobic hydration and interaction are crucial forces for the formation and stabilization of the colloids.

Acknowledgements

First of all, I would like to extend my thanks to my supervisor Prof. Xiaosong Wang for his continuous (24/7) support, guidance and patience throughout the last four years. I would also like to express my appreciation to Prof. Jean Duhamel who gave me the motivation after every frustrating step in my degree. I would like to thank my thesis committee Professors Yuning Li, Shirley Tang, and Jean Duhamel for their invaluable discussion and feedback during both the committee meeting and the comprehensive exam.

I would like to express my great thanks to Prof. Michel Tam, Prof Juewen Liu and their groups' members for providing me the access to their instruments and facilities. Mohammad Rahman is acknowledged for the synthesis of the Mp molecules. I also would like to thank our collaborators from the National Chiao Tung University, Prof. Chien-Lung Wang, Prof. Hiroshi Masuhara, Dr. Ken-ichi Yuyama, San-Lien Wu, and Kuan-Yi Wu for their great scientific discussion and warm hospitality during my research visit to Taiwan. I would like to thank Aklilu Worku and Nathan Nelson-Fitzpatrick for their help in performing the AFM imaging and the ellipsometry experiments, respectively.

I would like to extend my thanks to the Department of Chemistry graduate office team, Prof. Mario Gauthier, Catherine Van Esch, and Kim Rawson for their support and facilitating of earning my PhD degree in all of its process. I also would like to thank all of the Waterloo Institute for Nanotechnology team including Prof. Arthur J Carty, Lisa Pokrajac, Alain Francq, and Caroline Brookes for both their administration and financial support.

Nature Science and Engineering Research Council of Canada (NSERC) is acknowledged for financial support through the NSERC-Post Graduate Doctoral Scholarship.

Next, I would like to thank all of my current and former group mates, Kai Cao, Nicholas Lanigan, Dapeng Liu, Lulu Hu, Mohammad Rahman, Abdelrahman El-Timtami, Shaowei Shi, Diya Geng, Na Zhou, Robert Bennett and Jin Liu for sharing the lab and ideas. A Great thank you for Collin Tittle, Gordon Hall and Nicholas Lanigan for sharing the office with me and the daily fresh coffee that they always prepared in the early morning. I would also like to thank my friends Dr. Ahmad Desoqy, Dr. Kamal Mroue, and Dr. Fathy Hassan for their comments and support.

Finally, I would like to thank my lovely family…my wife Rana Dahouk and my children Razan, Lara and Osama for their support and dealing with a student dad.

Dedication

For my lovely family……

Table of Contents

List of Figures

List of Tables

List of Abbreviations

ACQ	Aggregation-caused quenching
AEH	Aggregation-enhanced hydration
AEIRA	aggregation-enhanced IR absorption
AFM	Atomic force microscopy
AI	Aggregation-induced
AIE	Aggregation-induced emission
AIH	Aggregation-induced hydration
ATR-FTIR	Attenuated total reflection-Fourier transform infrared
CAC	Critical aggregation concentration
CB	Cucurbituril
CCD	Charge-coupled device
CMC	Critical micelle concentration
CO group	Carbonyl group
Cp	Cyclopentadienyl
CV	Cyclic voltammetry
CWC	Critical water content
DCM	Dichloromethane
DLS	Dynamic light scattering
DMF	Dimethylformamide

DMSO	Dimethyl sulfoxide
EDX	Energy-dispersive X-ray spectroscopy
ET	Energy-transfer
Fc	Ferrocene
FL	Fluorescence
Fp	Cyclopentadienyl dicarbonyl iron; $CpFe(CO)_2$
FpC1	$CpFePPh_3(CO)COCH_3$
FpC10	$CpFePPh_3(CO)CO(CH_2)_9CH_3$
FpC12	$CpFePPh_3(CO)CO(CH_2)_{11}CH_3$
FpC14	$CpFePPh_3(CO)CO(CH_2)_{13}CH_3$
FpC18	$CpFePPh_3(CO)CO(CH_2)_{17}CH_3$
FpC3BTh	$CpFePPh_3(CO)CO(CH_2)_3$-bithiophene
FpC5	$CpFePPh_3(CO)CO(CH_2)_4CH_3$
FpC6	$CpFePPh_3(CO)CO(CH_2)_5CH_3$
FpC8	$CpFePPh_3(CO)CO(CH_2)_7CH_3$
FpCn	$CpFePPh_3(CO)COC_nH_{2n+1}$
FpK	Cyclopentadienyl dicarbonyliron potassium
FpP	Cyclopentadienyldicarbonyldiphenylphosphinopropyliron
FT-IR	Fourier transformer-infrared spectroscopy
IR	Infrared
IR s-SNOM	Scattering scanning near-field infrared microscopy

Ls	The separation distance between two adjacent metal at the colloid's surface
MC	Metal carbonyl
MCCs	Metal carbonyl complexes
MCsomes	Aqueous vesicles of MCCs
MD	molecular dynamics
MIP	Migration insertion polymerization
MIR	migration insertion reaction
Mp	cyclopentadienyl tricarbonyl molybdenum; $CpMo(CO)_3$
Mp_2	Cyclopentadienyl tricarbonyl molybdenum dimer
MpC6	$CpMoPPh_3(CO)_2CO(CH_2)_5CH_3$
NIR	Near-IR
NMR	Nuclear magnetic resonance
SAXS	Small-angle X-ray scattering
PDI	Polydispersity index (measure of the broadness of the size distribution in DLS measurements)
PEG	Polyethylene glycol
PFpP	Polycyclopentadienyldicarbonyldiphenylphosphinopropyliron
PFS	Polyferrocenylsilane
PMMA	Polymethylmethacrylate
PPh_3	triphenylphosphine

PS	Polystyrene
R_g	Radius of gyration
R_h	Hydrodynamic radius
RI	Refractive index
RIR	Restriction of intramolecular rotations
SEIRA	Surface enhanced IR absorption
SERS	Surface enhanced-Raman scattering
SLS	Static light scattering
TBAP	Tetrabutylammonium perchlorate
TEM	Transmission electron microscopy
THF	Tetrahydrofuran
WCIs	Water-carbonyl interactions
XPS	X-ray photoelectron spectroscopy
XRD	X-ray diffraction
$\Delta E_{½}$	Redox coupling (separation between two oxidation peaks in a CV wave)
γ	Surface tension
ζ-potential	Zeta potential

Chapter 1

Introduction

This introduction chapter highlights the emergence of a research field focused on metal-containing building blocks for functional nanomaterials, and the need for designing a new group of stable metal carbonyl complexes (MCCs) that can serve as building blocks for aqueous self-assembled structures. The introduction discusses several related topics, with their relevant literature review, including amphiphiles, organometallic amphiphiles, MCCs' structure and applications, Fp-derivatives, and hydrophobic hydration.

1.1. Organometallic Amphiphiles

Protein folding, DNA structures, microtubules, ribosomes, and cell membranes are selective examples of self-assembling that occur in nature and are crucial for living organisms.[1, 2] For example, amphiphilic phospholipids are the main constituents of biological membranes. Phospholipids arrange themselves into bilayers through positioning their polar groups toward the surrounding aqueous medium, with their lipophilic chains forming the inside domain of the bilayer membrane.[1]

Amphiphilic molecules contain both solvophilic (solvent-loving) and solvophobic (solvent-hating) moieties covalently linked to each other, which display lipid-like self-assembly behaviour in solution.[3, 4] When amphiphiles are dispersed in water, the hydrophilic (water-soluble) parts favourably interact with the water, and the hydrophobic segments tend to associate together to reduce the surface area at the water-hydrophobic interface (see section 1.4). As a result, well-defined nanostructures, including micelles, vesicles, lamella

and cylinders, can be generated spontaneously.[5, 6] These assembled nanostructures can be manipulated by selectively using various amphiphilic molecules and adjusting solution conditions (Figure 1.1).[7] These supramolecular organizations have displayed many functions beyond those of their building blocks.[7, 8] These functions open up or enhance a wide range of applications for modern technology, including nanodevices,[9, 10] drug delivery,[11, 12, 13] and cell imaging.[14]

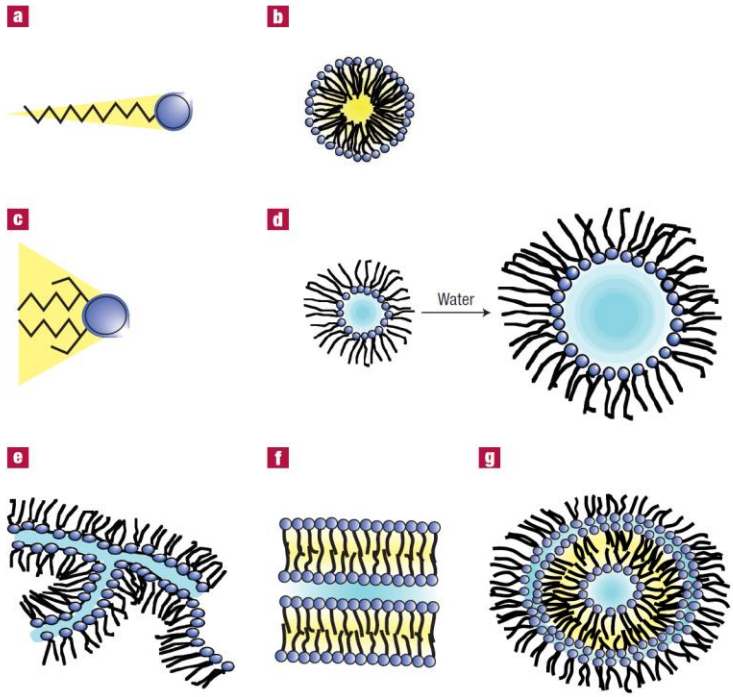

Figure 1.1 Surfactant shapes and various self-assemblies in colloidal solution. Reproduced with permission from Ref [7].[7]

Organometallic amphiphiles,[15, 16] containing transition metal complexes,[17] are interesting due to their diverse functions, such as catalytic, magnetic, optical and electrochemical, arising from their metallic properties.[15] The distinct properties, including

coordination ability, geometry of the transition metal elements, and the crystallinity of metal containing chains, can also be used for controllable engineering of nano-assemblies. For example, coordination-driven self-assembly of organoplatinum (II) molecules results in a tailored structure with metal-containing hydrophobic cores decorated with two polyethylene glycol (PEG) hydrophilic moieties.[18] The shape of the resultant assemblies can be readily tuned from spherical micelles to 1D nanofibers or 2D nanoribbons (Figure 1.2a).[18] On the other hand, the crystallinity of iron-containing polyferrocenylsilane (PFS) block copolymers has been used to form building blocks for living crystallization-driven self-assembly in selective solvents, which generates a range of tailored architectures in one, two, and three dimensions (Figure 1.2b).[19, 20]

Micelles with transition metal elements (metallomicelles),[21, 22] can enhance aqueous catalytic properties, because the metallomicelles provide more metal-containing approachable surface area exposed to water. For example, the hydrolysis of a nitro-activated aryl ester was achieved in the presence of copper-containing micelles in aqueous solution at neutral pH (Figure 1.3a).[23] Another example, ruthenium-containing metallomicelles catalysts were able to catalyze ring-closing metathesis reactions of water-insoluble dienic substrates in pure water at room temperature (Figure 1.3b).[24]

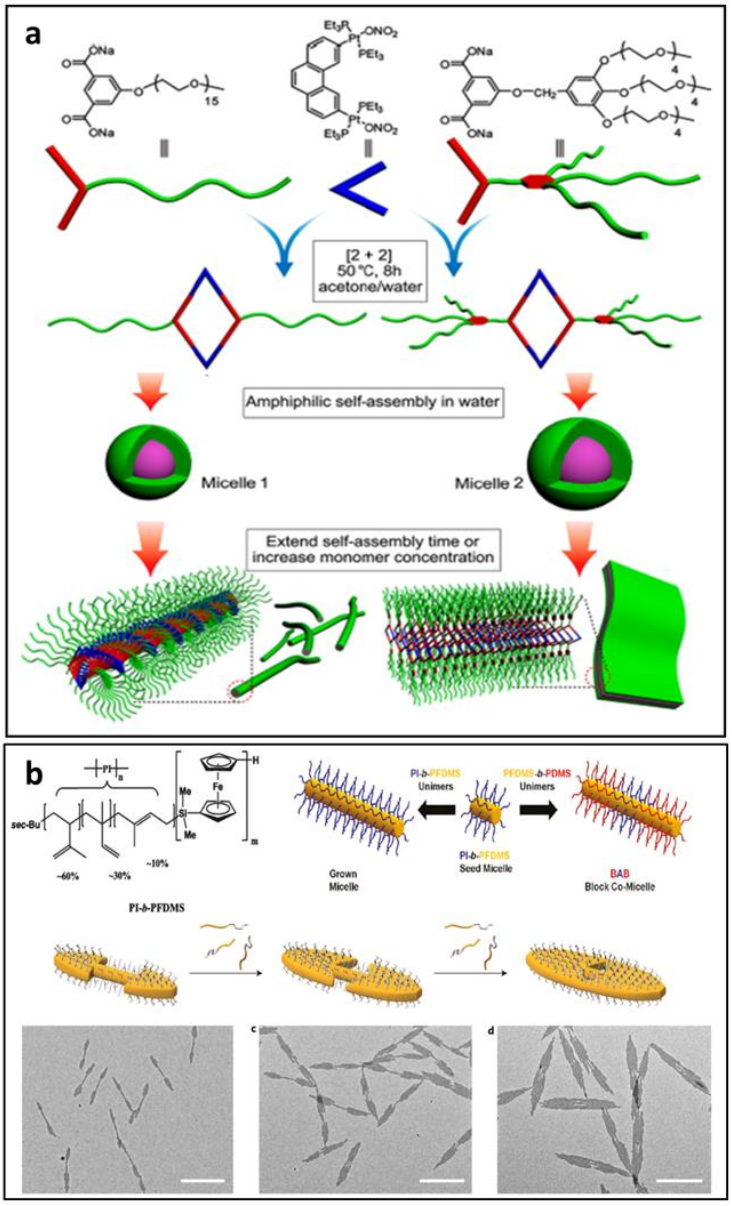

Figure 1.2 (a) Coordination-driven self-assembly of organoplatinum (II) molecules into spherical micelles, 1D nanofibers or 2D nanoribbons. Reproduced with permission from Ref [18].[18] (b) Living crystallization-driven self-assembly of polyferrocenylsilane (PFS) block copolymers. Reproduced with permission from Ref [19].[19, 20]

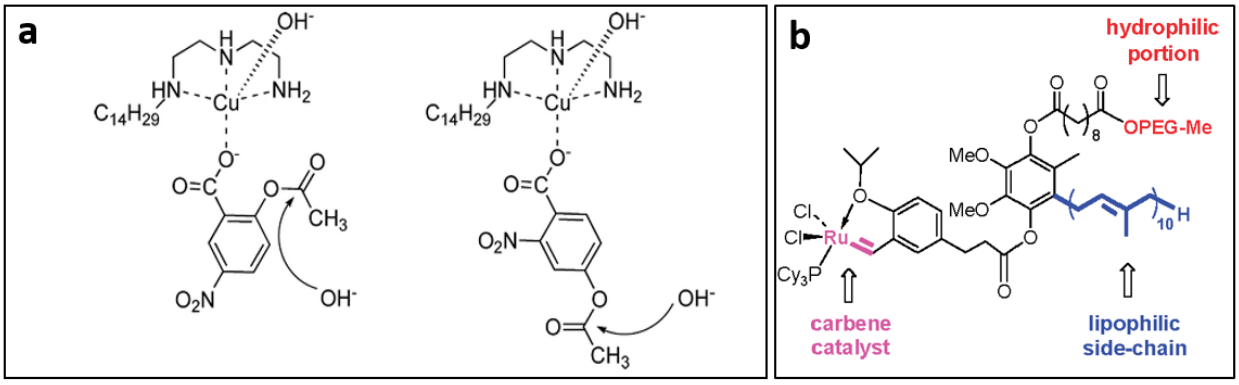

Figure 1.3 (a) Schematic representation of the complexation between the surface of a copper-containing micelle and esters. Reproduced with permission from Ref [23].[23] (b) Ruthenium-containing metallomicelle for catalysis of ring-closing metathesis reactions. Reproduced with permission from Ref [24].[24]

Redox properties of the metal elements have been used as stimuli for the assembly and disassembly of matallovesicles, which is potentially useful for a wide range of biomedical applications including drug delivery and bioassay.[25, 26, 27] For example, metalloamphiphile, consisting of three PEG hydrophilic moieties and a hydrophobic component of ferrocene (Fc)-tethered platinum(II) terpyridyl complex, can assemble in water with the hydrophobic metallic species associating within the bilayer membrane and the PEG-decorated surfaces exposed to water. Upon the oxidation of the Fc units to hydrophilic ferrocenium ions, these assemblies can be disturbed. Furthermore, the Fc groups can be incubated in hydrophilic cucurbituril (CB) host molecules, resulting in water-soluble Fc–CB complexes and consequently, dissociation of the micelles (Figure 1.4a).[26] This host-guest

concept has been used for the synthesis of voltage-stimulated polymer vesicles (polymersome). As shown in Figure 4b, the pseudo-copolymer PS-CD/PEO-Fc is constructed *via* the host-guest interaction between Cyclodextrins (CD) and Fc (Figure 1.4b).[28] The active nature of the host-guest linker can be tuned by changing the oxidation state of the Fc groups. The resulting oxidized Fc is water-soluble and released from the cavity of the CD, which results in the disruption of the polymersome. Meantime, the reversible association has been achieved by using a reductive voltage to reduce the hydrophilic ferrocenium ions back to hydrophobic Fc (Figure 1.4b).[28]

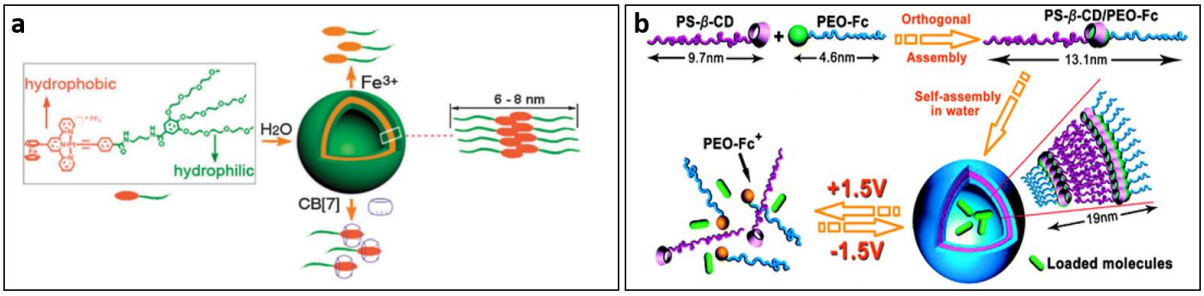

Figure 1.4 (a) Schematic representation of assembly and disassembly of ferrocene (Fc)-tethered platinum(II) amphiphile in water Reproduced with permission from Ref [26].[26] (b) Schematic of the voltage-responsive controlled assembly and disassembly of PS-CD/PEO-Fc vesicles. Reproduced with permission from Ref [28].[28]

By taking advantage of the dynamic nature of metal−ligand coordination, the assembly and disassembly of hexagonal metallodendrimers containing platinum moieties are enabled by the addition or removal of halide ions (Figure 1.5).[29] This stimuli-dynamic phenomenon has been applied for controllable release of encapsulated molecules.

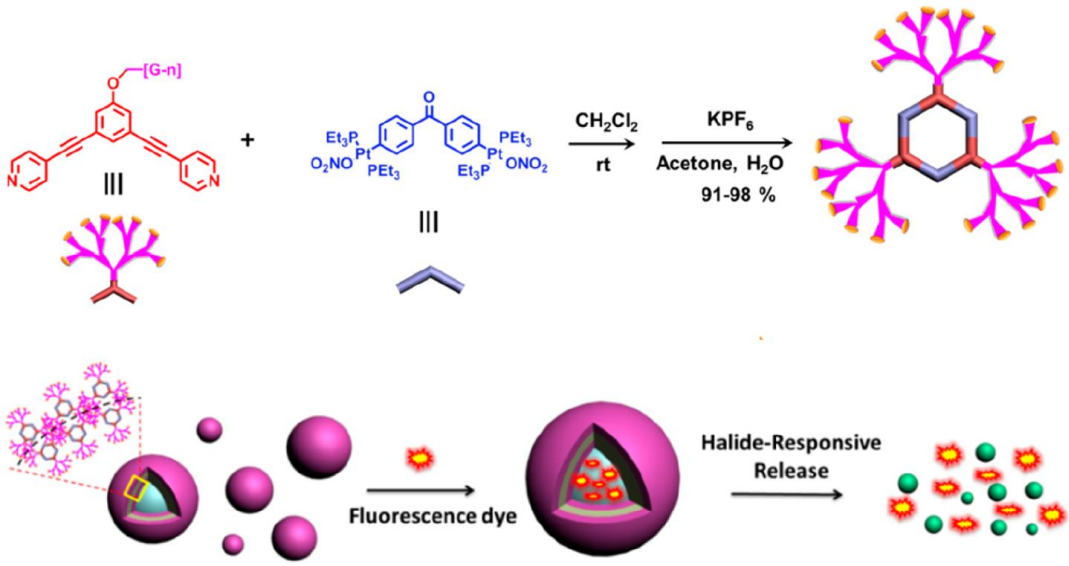

Figure 1.5 Self-assembly of the hexagonal metallodendrimers (upper panel) and the process of halide-responsive release of fluorescent molecules (lower panel). Reproduced with permission from Ref [29].[29]

Transition metal-complexes can be employed as energy donor or acceptor units in energy-transfer (ET) processes. To do so, both energy donors and acceptors need to be next to each other within a certain proximity, which can be achieved *via* the self-assembly of organometallic amphiphiles. For example, micelles assembled from ruthenium (II) metallosurfactants (as energy acceptors) in the presence of iridium (III) analogues (as energy donors) show efficient electronic ET processes. This self-organization endows the assembly with interesting luminescent properties (Figure 1.6).[30]

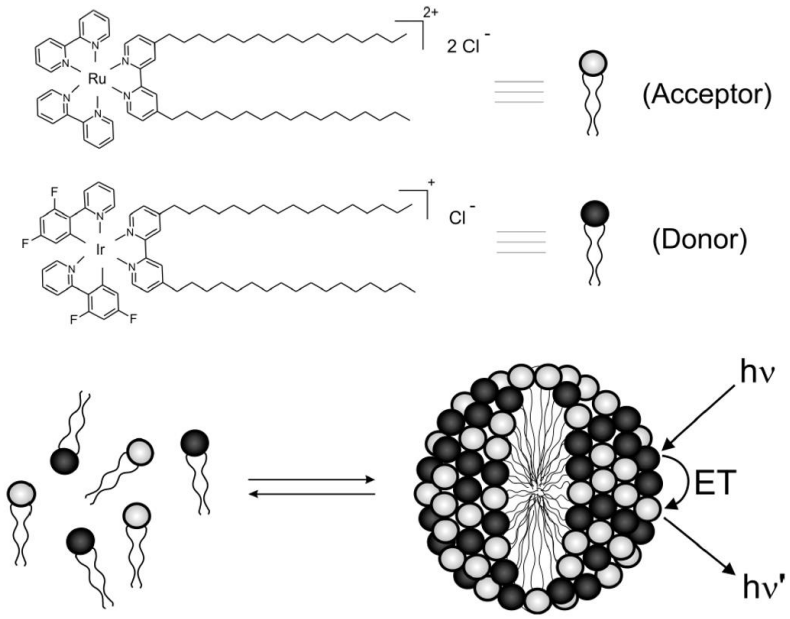

Figure 1.6 Mixed self-assembly of ruthenium (II) and iridium (III) metallosurfactants into an energy transfer metallomicelle. Reproduced with permission from Ref [30].[30]

1.2. Metal carbonyl complexes (MCCs)

Metal carbonyl complexes (MCCs) are organometallic derivatives made from CO-coordinated transition metal elements. Since several decades, a wide range of MC derivatives with various metals and numbers of CO ligands has been synthesized, explored and used for industrial catalysis.[31, 32] Recent explorations suggest that MC complexes are potentially useful for a range of biomedical applications, including CO delivery,[33, 34] antitumor treatment[35, 36] and vibrational bio-sensing.[37, 38] Due to the intense IR absorption of the CO groups within a biologically transparent window, where interference from the absorption of water and most of biological molecules, with wavenumbers between 1800 and 2200 cm^{-1},[37,

[38] MC derivatives have been explored as vibrational IR or Raman probes for cell imaging[39] and bioassay[40] studies. Challenges for practical applications of MC complexes in aqueous medium include low water solubility, stability, and vibrational signal sensitivity. Several studies have shown that their water solubility,[41] cell up-take ratio[13] and IR absorption intensity[42] can be enhanced using colloidal chemistry.

MC compounds serve as CO delivery source for several biological activities including inflammation and redox control.[13, 34] To enhance their solubility and stability in water, MC complexes have been incorporated within inorganic particles,[34] peptide gels and block copolymer micelles.[13] As shown in Figure 1.7, a CO-delivery system has been developed using a polymeric aqueous micelle as CO carrier. The CO-releasing micelles were prepared from triblock copolymer that contained a hydrophilic PEG block and a hydrophobic poly(n-butylacrylamide) block with CO complexes loaded at the middle block.[13] The micelles successfully enhanced the solubility and stability of the MC complex. The CO release was triggered by cellular thiol compounds, which showed the inflammatory response of human monocytes. Moreover, the toxicity of the loaded Ru carbonyl moieties was significantly reduced due to the aggregation of the MC moieties in the core of the micelles and the stealth feature of the hydrophilic PEG corona. These results show that the CO-releasing micelles can provide an effective and non-toxic technique for CO-based therapy.

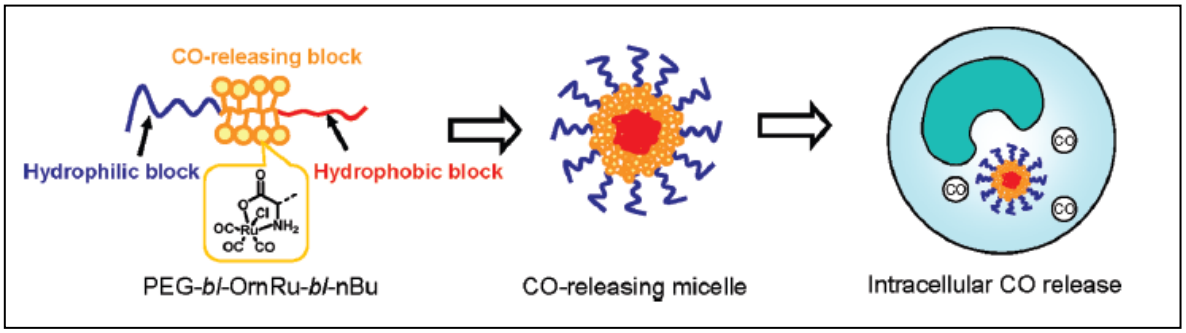

Figure 1.7 Schematic illustration of the PEG-b-OrnRu-b-nBu triblock copolymer and its CO-releasing micelle. Reproduced with permission from Ref [13].[13]

Vibrational spectroscopic techniques for bio-imaging has attracted attention since the 1980s.[42] In contrast to organic fluorophores used in fluorescence microscopy, vibrational spectroscopy involves no photobleaching or quenching limitations.[37, 43] However, the development of vibrational-based probes, in the emerging field of bio-imaging, is a real challenge with a key issue of sensitivity.[37, 42] MC complexes have intense IR absorption in the mid-IR window (1800 – 2200 cm^{-1}) that is transparent for biological environment.[37, 43] Therefore, the MCCs are explored as vibrational probes using both IR and Raman spectroscopy, which has opened up a rewarding research field of bioorganometallic chemistry.[37, 43] Although the sensitivity of MC compounds in FT-IR or Raman analysis is limited to submicromolar concentrations,[43] the MC labels have been integrated with a wide range of biologically active species including steroids, peptides and antibodies for selectively targeting of organisms (Figure 1.8).[36, 43] As shown in Figure 1.8, in an indirect quantitative determination of the amount of an analyte, the analytes are first conjugated with an excess fixed amount of metal carbonyl complexes, as tracers. These conjugates are allowed to bind

with a fixed amount of selective antibodies. The unbound tracers are then extracted and quantified using vibrational based spectroscopy. For example, using this technique, MC complexes have been used as tracers in immunoassays of drugs and pesticides with detection limits in the range of femtomolar concentration.[43] Recently, FT-IR and Raman microscope have been successfully applied for mapping the uptake and distribution of MC based drugs in a single cell.[39, 44]

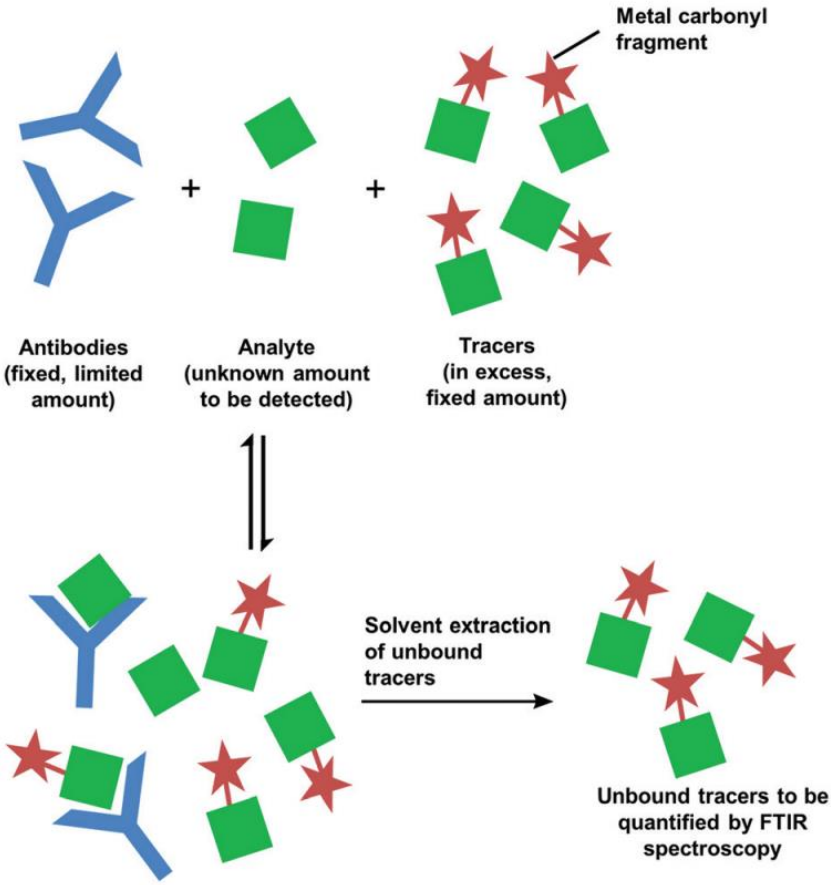

Figure 1.8 Schematic representation of the working principles of metal carbonyl immunoassay. Reproduced with permission from Ref [43].[43]

Surface enhanced-Raman scattering (SERS) or SEIRA using plasmonic (e.g. Au, Ag) or dielectric (e.g. Al_2O_3, CS_2) substrates have been explored to enhance the detection limit of the MC biosensors.[37, 42] Olivo and coworkers have loaded the osmium carbonyl clusters on the surfaces of gold nanoparticles and functionalized the surface with selected antibodies. To enhance the solubility, the conjugates are further coated with water-soluble PEG (Figure 1.9a).[45] The resulting particles were used as bio-tags for the mapping of cancer cells. They reported that the stretching vibration signal of the CO groups can be enhanced by four orders of magnitude (Figure 1.9b-c).

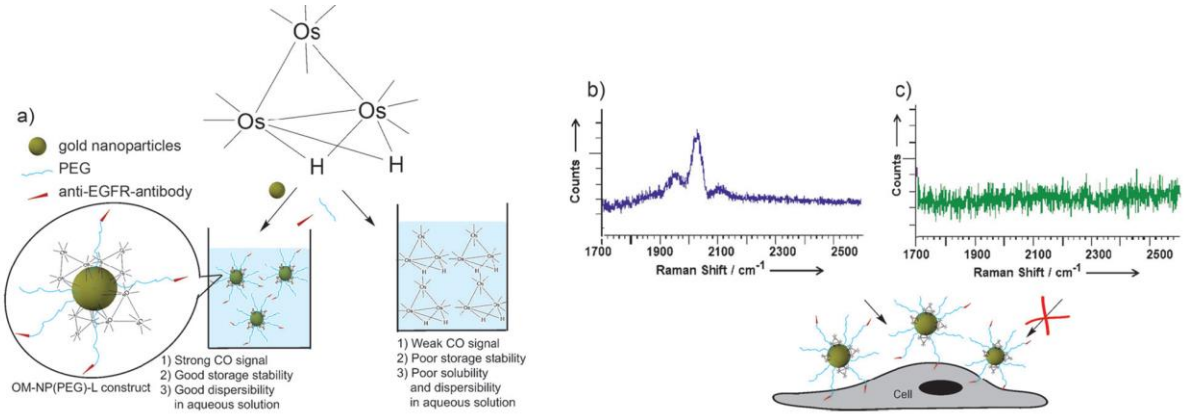

Figure 1.9 (a) Preparation of the antibody-functionalized osmium carbonyl-gold nanoparticles (OC-AuNPs) conjugate. Raman scattering spectra for (b) the functionalized OC-AuNPs conjugate in water and (c) osmium carbonyl complex in ethanol. Reproduced with permission from Ref [45].[45]

IR analysis of MC complexes has also been used for localization and tracking of individual biomolecules.[44] Havenith and coworkers investigated MC complexes as IR-active

labels using scattering scanning near-field infrared microscopy (IR s-SNOM). They demonstrated the selective detection of the $CpMn(CO)_3$ moiety of the cymantrene–peptide conjugate (Figure 1.10).[44] As shown in Figure 1.10 (upper panel), a well-defined self-assembled monolayer was prepared by attaching MC–peptide bioconjugates and octadecanethiol molecules on a gold substrate *via* thiol–gold bonds, in an alternative sequence (upper panel in Figure 1.10). The MC-bioconjugates were mapped successfully using IR s-SNOM with a very good resolution. Imaging can be selectively recorded at specific frequencies. As shown in Figure 1.10 (lower panel), images recorded at MC and amide vibrational frequencies (1944 cm^{-1} and 1658 cm^{-1}, respectively) showed a clear pattern, whereas no distinguished pattern has been observed at off-resonance frequencies.[44] According to these results, using MC-IR active labels in IR s-SNOM provides a new path for biosensing and biomolecular localization studies as an alternative to fluorescence detection techniques.

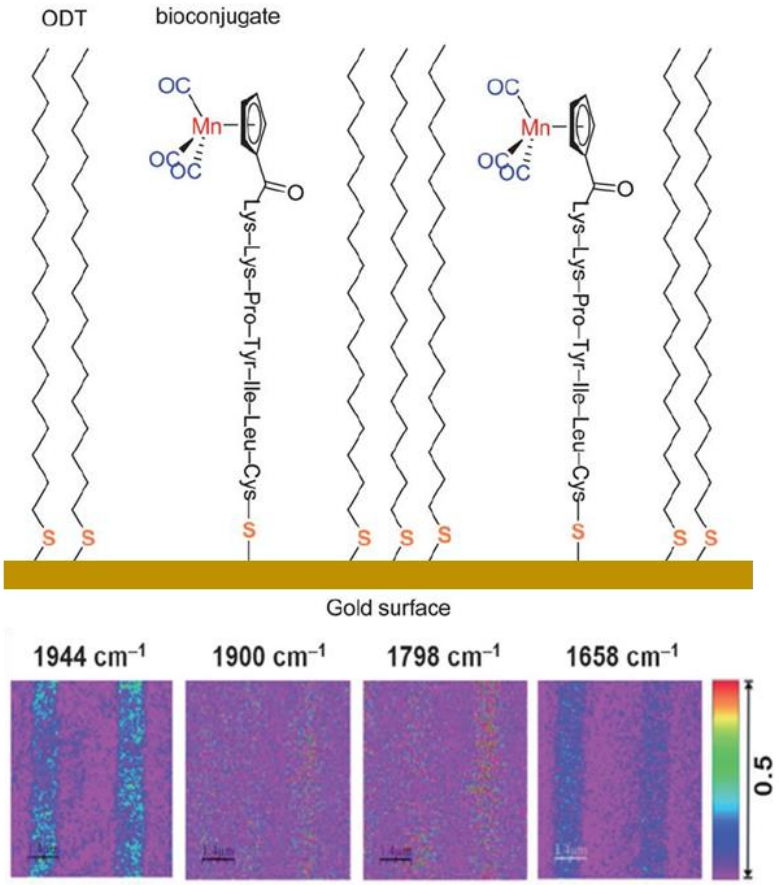

Figure 1.10 Self-assembled monolayer of octadecanethiol and metalcarbonyl–peptide conjugate (upper panel) and near-field contrast images at four distinct frequencies of a laterally structured monolayer (lower panel). Reproduced with permission from Ref [44].[44]

Despite the progress discussed above, the applications of MCCs remain challenging. Many of these challenges stems from the lack of fundamental understanding of the aqueous behaviour of MC compounds in water, which requires substantial studies.

Fp-acyl derivatives (Fp: cyclopentadienyl dicarbonyl iron; $CpFe(CO)_2$), synthesized *via* the well-known migration insertion reaction (MIR),[46, 47, 48] are a group of well-developed

and fairly stable MC compounds.[49, 50, 51] For example, as shown in Figure 1.11, in the presence of a phosphine ligand, one of the terminal CO groups migrates and undergoes an intermolecular 1,1-insertion into the metal-alkyl bond. This MIR of the CO group provides an air stable Fp-acyl complex.[49] The resulting structure possesses a highly polarized acyl group.[52, 53] The stability of the resulting compounds renders them ideal for the study of their aqueous behaviour.

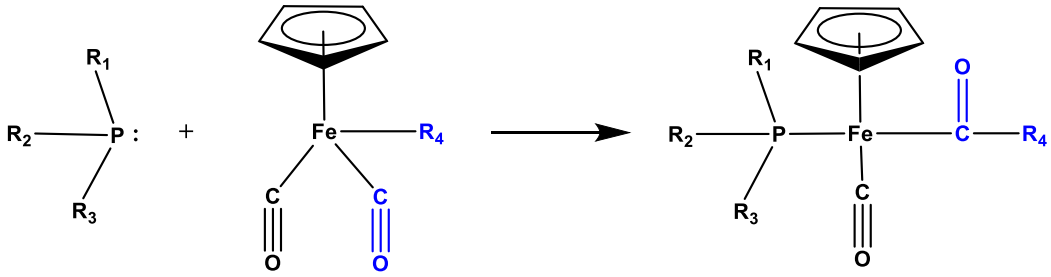

Figure 1.11 Schematic illustration of the MIR of the terminal carbonyl group in the presence of a phosphine ligand.

In our group, we have explored the supramolecular chemistry of Fp-acyl derivatives including small molecules[47] and polymers.[48] We discovered that this group of metal-carbonyl molecules exhibits unique self-assembling behaviour mainly due to the polarity of the CO groups. For example, $CpFePPh_3(CO)CO(CH_2)_5CH_3$ (FpC6) molecules are able to assemble in the solid state into an air stable supramolecular polymer with a truss arrangement of the metal elements (Figure 1.12). The presence of the polarized CO groups, as hydrogen acceptors, is a major contribution to the chain structure (Figure 1.12b).[47]

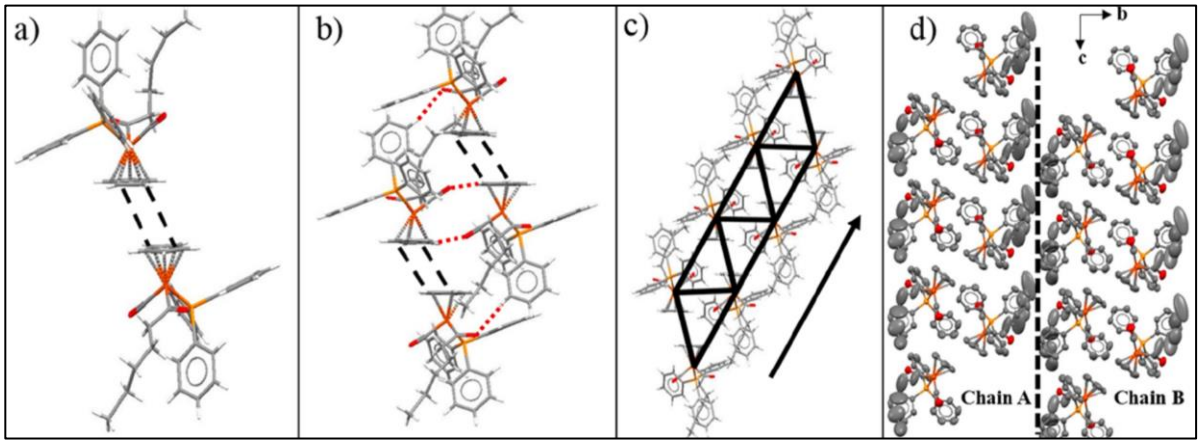

Figure 1.12 Schematic illustration for the formation of FpC6 chain structure. Reproduced with permission from Ref [47].[47]

We have also developed migration insertion polymerization (MIP) and prepared MC macromolecules.[48] As shown in Figure 1.13, di-functional A-B type monomers containing Fp and phosphine groups connected *via* an alkyl spacer (FpP) undergoes intermolecular MIR, which generates an air-stable macromolecule (PFpP). In addition to the MC groups, the polymers also contain phosphorous, which is potentially useful.[54] Taking the advantage of metal-phosphine coordination in the stabilization of MCCs, a group of air-stable phosphine-coordinated MC complexes has been synthesized recently by Joe B. Gilroy group. They reported a series of air-stable and redox-active Group 6 metal pentacarbonyl complexes ($M(CO)_5$; M: Cr, Mo, W) coordinated with primary, secondary and tertiary ferrocenyl ethyl phosphines.[55]

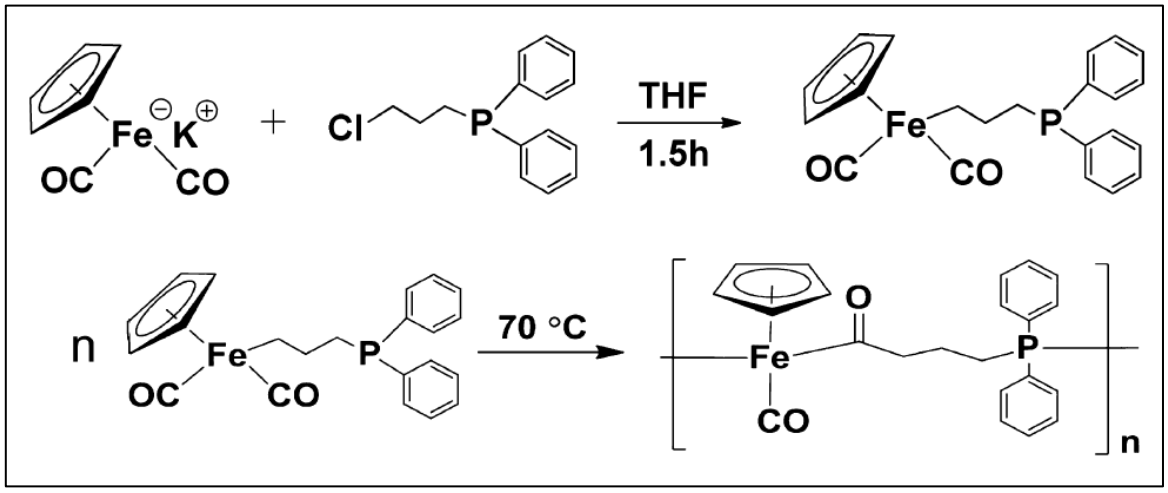

Figure 1.13 Scheme for Synthesis and MIP of FpP. Reproduced with permission from Ref [48].[48]

Although Fp acyl derivatives and PFpP are hydrophobic, the highly polarized CO groups could interact with water *via* water carbonyl interactions (WCI), which would be a starting point to investigate their aqueous behaviour.

1.3. Water Carbonyl Interaction

Hydrophobic hydration plays a crucial role in the organization of living organisms.[56] For example, hydrophobic hydration is essential in driving the self-assembly of the phospholipids to form cell membrane.[57] The stability of protein folding is mainly due to the presence of buried water molecules between the hydrophobic side chains.[58, 59, 60, 61] Buried water molecules are reported to stabilize the protein structure by acting as bridges between amino acids *via* water-carbonyl interaction (WCI).[60] WCI also explains the capability of

lipolytic enzymes to access both hydrophobic triglycerides and water molecules for catalytic fat hydrolysis during metabolism.[62]

WCIs of synthetic molecules containing carbonyl groups, e.g. polymethylmethacrylate (PMMA), have also been studied.[63] The strength of WCIs is related to the degree of polarity of the CO groups.[39, 64, 65] MCCs are usually hydrophobic,[41] but the metal elements are electron-donating centers that can induce negative charges on the oxygen atoms in the CO groups, e.g. the acyl CO in the phosphine-coordinated Fp derivatives (Figure 1.14a-b).[52, 53] Hydration of this group *via* stronger WCIs can then be expected for possible aqueous self-assembly. As a matter of fact, hydrophobic PFpP can assemble into vesicles in water (Figure 1.14c-d).[66] The strong WCI accounts for the colloidal stability in water. However, further research is required to understand the contribution of WCI and other hydrophobic hydration in the aqueous assembly.

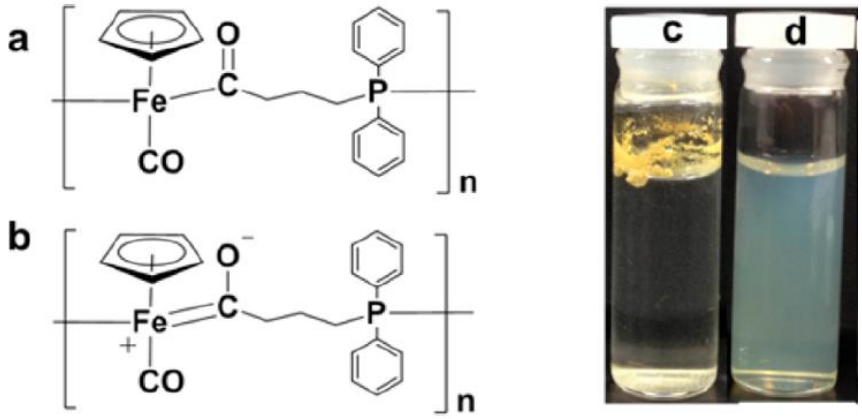

Figure 1.14 (a) Chemical structure of PFpP. (b) PFpP resonance structure. (c) Hydrophobic PFpP floating in water. (d) PFpP colloids in water with polymer concentration of 0.1 mg/mL. Reproduced with permission from Ref [66].[66]

1.4. Hydrophobic Hydration and Self- Assembly

Hydrophobic hydration defines the process of inserting a hydrophobic molecule (solute) into water.[67, 68] This insertion exerts a thermodynamic and structural response of water molecules at the interface of the hydrophobic molecule.[69, 70] However, water molecules tend not to sacrifice their hydrogen bonds; therefore, water molecules around the solute are connected *via* hydrogen bonding forming a water cavity.[71]

The local structure of the interfacial water molecules depends on the size and structure of the hydrophobic molecule. The cavity associated with a small hydrophobic molecule, such as methane, has a cross section less than 0.5 nm (Figure 1.15a).[72] For this small volume, no breaking of hydrogen bonds is required.[67, 72] Therefore, the orientation of the water molecules around the solute allows the hydrogen-bonding patterns similar to that in the bulk liquid water.[72] On the other hand, the surface of a large hydrophobic molecule is extended with a low curvature (Figure 1.15b). Therefore, the hydrogen bond network is disrupted in order to create a relatively larger cavity hosting the large hydrophobic molecule. It is an energetically unfavorable process, because the adjacent water molecules near the surface of the solutes cannot maintain a complete hydrogen-bonding pattern,[72] More water molecules tend to be located closely around the large solute for the formation of a cage, which results in a significant decrease in the entropy and increase in Gibbs energy.[70, 73] To overcome this penalty, hydrophobic molecules tend to assemble together to reduce the ratio of total surface area to volume. In this case, the number of the surrounding water molecules participating in the cage formation decreases, resulting in the increase in entropy.[70, 72]

Moreover, upon the aggregation, the solvation free energy becomes lower than the overall total solvation energy of the individual molecule; therefore, resulting in a favorable driving force for the assembly.[72]

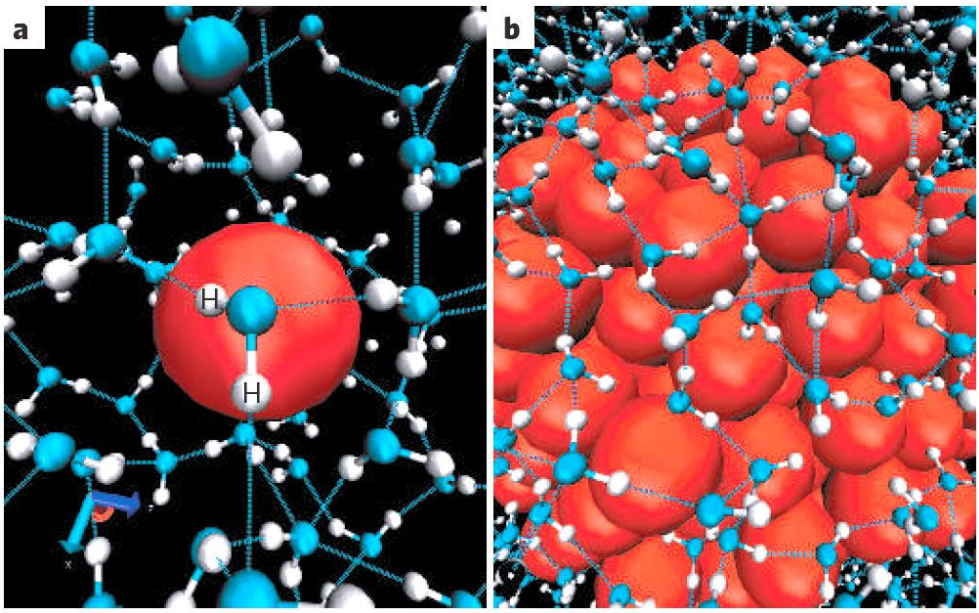

Figure 1.15 Configurations of liquid water molecules near (a) small and (b) large hydrophobic cavities. Reproduced with permission from Ref [72].[72]

In the case of amphiphilic molecules, due to the presence of the hydrophilic segments, the amphiphiles exert strong attractive forces with water molecules. Although the hydrophilic moieties of amphiphiles are not directly responsible for hydrophobic assemblies, they have a crucial role in the arrangement of the molecules for the assemblies.[72] Due to the presence of both weak hydrophobic-water interaction and strong hydrophilic-water interactions, there are two main types of water molecules, bulk and interfacial waters. Bulk water molecules strongly interact with the

hydrophilic moiety; whereas interfacial water molecules, that include dangling or buried water, interact with the hydrophobic part of an amphiphile. Thus, the presence of strong interactions between the hydrophilic parts and water confines and localizes water molecules to a specific location, which minimizes the fluctuation and shaped the self-assembled structures. The different behaviour of these two types of water molecules makes it possible to study the hydration process, micelle structure and biological activities.[74] Several techniques, including calorimetric, spectroscopic and computational methods,[69, 70, 74, 75, 76] have been used to study the hydrophobic hydration process.

However, it is rarely reported how the hydrophobic hydration and hydrophobic interaction contribute to the formation of micelles and the stability of colloids.[77, 78] It is generally accepted that the aqueous self-assembly occurs via the association of the the hydrophobic tails, which results in a central dry hydrophobic core with a smooth spherical surface. A few segments near the hydrophobic core are hydrated.[79, 80] Micelles are stabilized by water-soluble corona chains. However, the Menger model implies that water penetrates deeply into the hydrophobic core.[81, 82] A recent study reported by Ben-Amotz and coworkers supports this model. The micelles are assembled from the surfactants with either cationic or anionic head groups and varied alkyl chain lengths.[74] As shown in Figure 1.16a, the hydrophobic core of the micelle has a corrugated surface containing hydrated cavities penetrating deeply into the core. By probing the dangling water molecules, located at the hydrophobic surface with a

non-H-bonded OH group (Figure 1.16b), using Raman spectroscopy with multivariate curve resolution experiments, they found that the depth of these hydrated cavities were increased with the increase in the length of the surfactant tail (Figure 1.16b).[74] How this hydration cavity contributes to the stability of the micelles is a matter of future work.

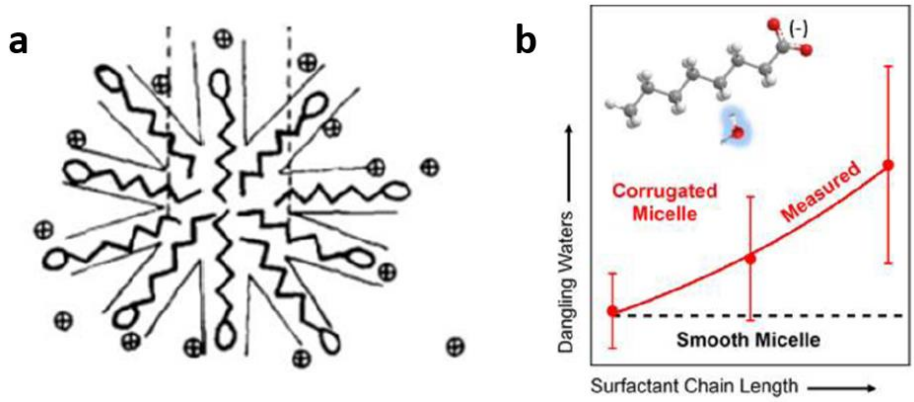

Figure 1.16 (a) Schematic micelle structure showing deep hydrated cavities surrounding a small dry core. (b) The average number of excess dangling water molecules as a function alkyl chain length, compared between corrugated and smooth micelles. Reproduced with permission from Ref [74].[74]

1.5. Thesis outline

This thesis is composed of seven chapters. Chapter 1 (Introduction) provides a general introduction and literature review about thesis related topics including organometallic amphiphiles, metal carbonyl complexes, and hydrophobic hydration. Chapter 2 (Iron-Carbonyl Aqueous Vesicles (MCsomes) *via* Hydration of FpC6: Highly Integrated Colloids

with Aggregation-Enhanced IR Absorption (AEIRA)) reports in detail the aqueous behaviour and hydration driven self-assembly of FpC6 as well as the discovery of AEIRA phenomenon. Chapter 3 (Aggregation-Enhanced IR Absorption (AEIRA) of Molybdenum-Carbonyl Organometallic Aqueous Colloids) discusses the aqueous behaviour and AEIRA of MpC6. This behaviour is compared with that for FpC6. Chapter 4 (Laser Manipulable Aqueous Fp-Bithiophene Vesicles with Aggregation-Induced Emission (AIE) and Aggregation-Enhanced IR Absorption (AEIRA)) describes an Fp derivative with conjugated bithiophene tether (FpC3BTh) and its aqueous solution behaviour. The aqueous vesicles of FpC3BTh show a number of properties including AIE, AEIRA and laser trapping. Chapter 5 (Colloidal Structure-Related Hydrophobic Hydration for the Stability of the Aqueous Assemblies of Hydrophobic Fp Derivatives) discusses the correlation between the colloidal structure-related hydrophobic hydration of Fp derivatives and their stabilities. Chapter 6 (Hydrophobic Effect on the Solution Behaviour of PEG-Fp-Alkyl Amphiphiles) reports the aqueous behaviour of a group of PEG-Fp-R amphiphiles (R = alkyl chain) with varied PEG and alkyl chain lengths. This behaviour is correlated with the colloidal structure and probed by the redox activity of iron elements at the core-shell interphase. Finally, Chapter 7 (Summary and Future Work) provides a general thesis summary and suggestions for potential future work.

Chapter 2

Iron-Carbonyl Aqueous Vesicles (MCsomes) via Hydration of FpC6: Highly Integrated Colloids with Aggregation-Enhanced IR Absorption (AEIRA)

2.1 Introduction

Self-assembly of hydrophobic small molecules into uniform and colloidally stable vesicles in water is beyond the reach of current knowledge,[15, 83, 84] although supramolecular vesicles[85, 86] (e.g. liposomes)[87, 88] associated from amphiphilic molecules (e.g. lipids) are well known and have been widely used for material applications.[15, 83, 84, 89, 90] Amphiphilic molecules are generally surface-active and only assemble above certain concentration (critical micelle concentration (CMC)).[91, 92] As a result, micellar colloids have to be prepared and used at a concentration above the CMC, and the resultant aggregates have low structural integration upon dilution,[91, 93] which imposes challenges for many applications, such as drug delivery,[33, 34, 88, 89] bioassay, and cell imaging.[38, 40, 94] Non-surface-active, hydrophobic assembling building blocks could be used to address this inherent problem, but such a group of building blocks has yet to be developed.

In biology, water-carbonyl interactions (WCIs) explain the capability of lipolytic enzymes to access both hydrophobic triglycerides and water for catalytic fatty hydrolysis during metabolism.[62] Therefore, we envision the possibility of harnessing WCI as a driving force for the creation of aqueous colloids if hydrophobic carbonyl molecules can be properly

designed. Many hydrophobic carbonyl molecules, such as triglycerides and polymethylmethacrylate (PMMA), are not able to self-assemble in water, probably because of their weak WCIs.[63, 95] The strength of WCIs is related to the polarity of the carbonyl groups (CO groups).[64, 65, 96] It is, therefore, tempting to explore the aqueous behaviour of carbonyl molecules with highly polarized CO groups. Metal-carbonyl complexes (MCCs) are usually hydrophobic,[41] but they possess strong electron-donating metal elements and sometimes can induce negative charges on the oxygen in CO, for example, an acyl CO within a phosphine coordinated η^5- cyclopentadienyl dicarbonyl iron (Fp) derivatives.[52, 97] Hydration of this group of molecules through stronger WCIs can then be expected for possible aqueous self-assembly. This exploration of WCI-induced direct self-assembly of MCCs also has high potential for material innovation. Although aqueous colloids directly assembled from MCCs are rarely reported, hybrid nanoparticles with MCC components have been explored for functional materials. For example, by integrating hydrophobic MCCs into block copolymer aqueous micelles, water-soluble CO-delivery agents with a high cell uptake ratio have been developed.[13] In another approach, metal nanoparticles with surface-attached MCCs show enhanced IR and Raman signals for the CO groups, which is desirable for bioassay and cell imaging.[42, 45]

We have recently explored supramolecular chemistry of Fp derivatives, including polymers[48, 98, 99] and small molecules,[47] and discovered that this group of metal-carbonyl molecules exhibits unique self-assembly behaviour mainly due to the polarity of the CO groups. For example, $CpFePPh_3(CO)CO(CH_2)_5CH_3$ (FpC6) is able to assemble in the solid

state into supramolecular polymers with a truss arrangement of iron elements.[47] Hydrogen bonding with polarized CO groups as hydrogen acceptors is a major contribution for the chain structure.

Herein, we report the aqueous behaviour of FpC6. FpC6 is hydrophobic, but its CO groups can be hydrated, which induces the formation of uniform metal-carbonyl vesicles (MCsomes). MCsomes, unlike conventional vesicles that are assembled from amphiphiles, stay integrated and maintain a narrow PDI upon dilution. Moreover, the aggregation of the molecules induces a significant enhancement (more than 100-fold) in the IR absorption for the CO groups. This enhancement is higher than most surface enhanced IR absorption (SEIRA) using external dielectric substances.[42, 100] The highly integrated aqueous colloids of FpC6 with self-enhanced CO signals, therefore, offer a promising approach for addressing current challenges in biomaterial applications of MCCs.[40, 89]

2.2 Results and Discussion

Hydrophobic carbonyl molecules can interact with water through WCIs,[63, 95] but this force is relatively weak and has not been harnessed as a driving force for the preparation of self-assembled aqueous colloids. Hydrophobic FpC6 contains a terminal CO and a highly polarized acyl CO.[47, 52, 97] WCI of the acyl CO initiates the aggregation of the molecules. This aggregation subsequently induces WCI of the terminal CO and enhances WCI of the acyl CO, which results in strong hydration forces that sustain the FpC6 aggregates in water. This aggregation induces a local electric field and consequently significantly enhances the IR absorption of the CO groups. These unprecedented discoveries will be illustrated in the

following sections, starting with the solution behaviour of FpC6, followed by morphology characterization and discussion of the self-assembly mechanism. Aggregation-enhanced IR absorption (AEIRA) is illustrated and discussed as the last part of the paper.

2.2.1 Aqueous solution behaviour of hydrophobic FpC6

By adding water to a solution of FpC6 in THF, followed by N_2 bubbling to remove THF, an aqueous solution of FpC6 with a blue tint was prepared, which suggested that colloids were formed (Figure 2.1). Note that all colloids discussed in the paper are prepared using the same technique.

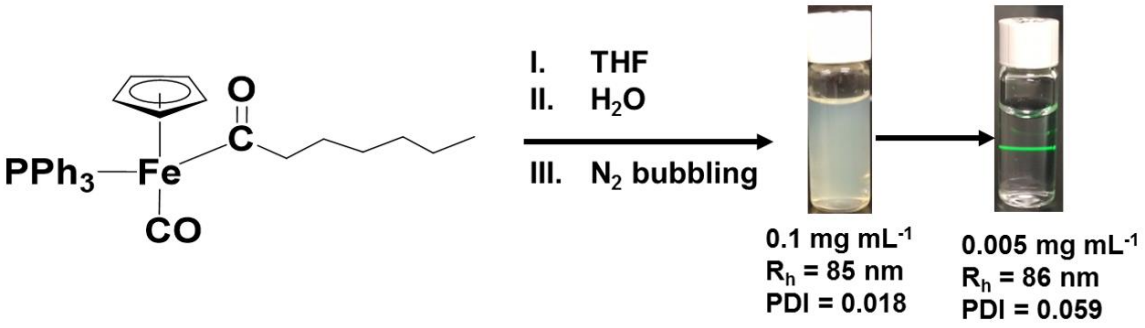

Figure 2.1 Molecular structure of FpC6 and its aqueous colloids.

DLS analysis reveals that the hydrodynamic radius (R_h) of the colloids is ca. 85 nm with an extremely narrow polydispersity (PDI) of 0.018. Where PDI is a dimensionless measure of the broadness of the size distribution calculated from the cumulants analysis. The colloids remain highly integrated even when the solution was extremely diluted (Figure 2.2a). As shown in Figure 2.2a, no change in Rh was observed for any of the measured

concentrations. Even at 0.005 mg/mL (9.54 μM), a concentration much lower than CMC for many amphiphilic surfactants,41, 101 the solution still scatters light (Figure 2.1). DLS of the diluted solution reveals R_h of 86 nm, which suggests that the original colloids are well integrated (Figure 2.1). Moreover, the linear relationship of light scattering intensity as a function of solution concentration suggests that there is no detectable critical aggregation concentration (CAC; Figure 2.2b).

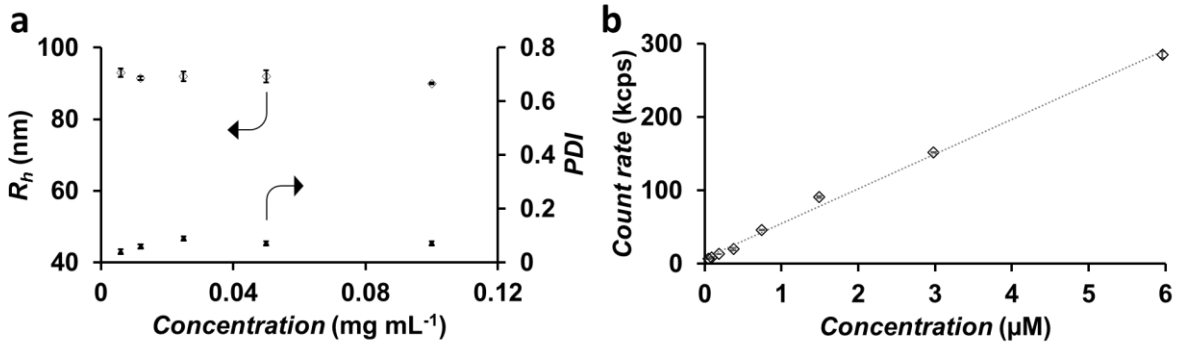

Figure 2.2 (a) Hydrodynamic radius (R_h), polydispersity index (PDI) and (b) Count rates of aqueous colloids as a function of FpC6 concentrations.

^{1}H NMR analysis of the colloids in D_2O shows a single signal due to residual H_2O at 4.67 ppm and no chemical resonance from FpC6 was observed (Figure 2.3a), which verifies that there are no detectable FpC6 molecules in water. Surface tension measurements as a function of solution concentration are illustrated in Figure 2.3b. As shown in the figure, the surface tensions for all solutions remain at the same value of approximately 72.0 mN/m, similar to that for pure water. This set of experiments indicates that FpC6 cannot be classified

as a conventional amphiphile, but can aggregate without CAC (Figure 2.2b). This result explains that the colloids have strong structural integration upon dilution. We also performed ^{1}H and ^{31}P NMR spectroscopy on the molecules recovered from aqueous solution by freeze-drying, which indicated that there is no chemical structure alternation of FpC6. (Figure S2.3). Synthesis of FpC6 is described in details in the Experimental Section and Supporting Information (Figure S2.1 and Figure S2.2).

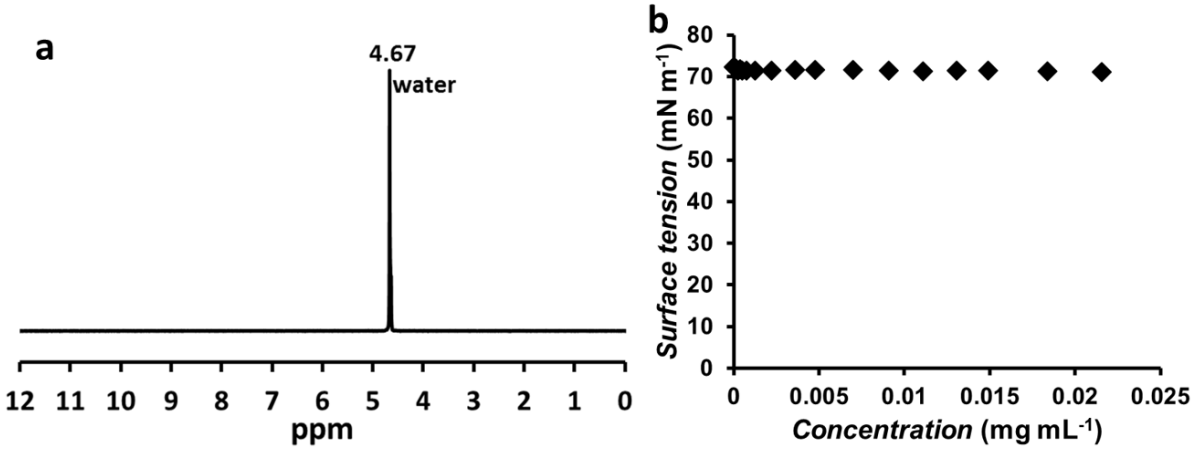

Figure 2.3 (a) ^{1}H NMR of FpC6 colloids in D_2O (0.1 mg/mL), (b) Surface tensions of FpC6 in water as a function of concentration.

2.2.2 Morphology of FpC6 colloids

To investigate the morphology of the prepared aqueous colloids, multi-angle static light scattering (SLS) was performed. As shown in Figure 2.4a, scattered intensities for aqueous solutions of FpC6 (0.006 mg/mL) are plotted as a function of scattering vector q^2. From a Berry plot, the radius of gyration (R_g) is calculated to be 83.6 nm. The hydrodynamic

radius (R_h) obtained from DLS measurements for the same sample is 86.7 nm. By comparing R_g and R_h, the shape factor (R_g/R_h) was found to be 0.96, which suggests that FpC6 is able to self-assemble into vesicles in water. Conventional transmission electron microscope (TEM) was not able to image the sample because the colloids collapsed upon drying (Figure S2.4 in the Supporting information). Therefore, cryo-TEM was performed and a typical image is illustrated in Figure 2.4b. As shown in the figure, the contrast between the periphery and the interior is not sharp but clear, which corroborates the hollow structure and suggests that the wall for the vesicle is thin. The thickness of the wall for the vesicle as measured is ca. 4.0 nm. Although the colloids will not remain integrated upon drying, atomic force microscopy (AFM) analysis of the fragment can verify the thickness of the vesicle membrane. As illustrated in Figure S2.5 in the Supporting Information, the height profiles for the fragments are between 4.0 nm and 4.6 nm, which are comparable with what was revealed from the cryo-TEM images for the wall thickness. Because the total extended length of FpC6, as calculated from its crystal structure, is ca. 1.8 nm,[47] the vesicles may have a bilayer structure with iron-carbonyl units exposed to water and the alkyl chains forming the inner domain of the vesicle wall. This proposition is supported by CV and IR experiments and will be discussed below.

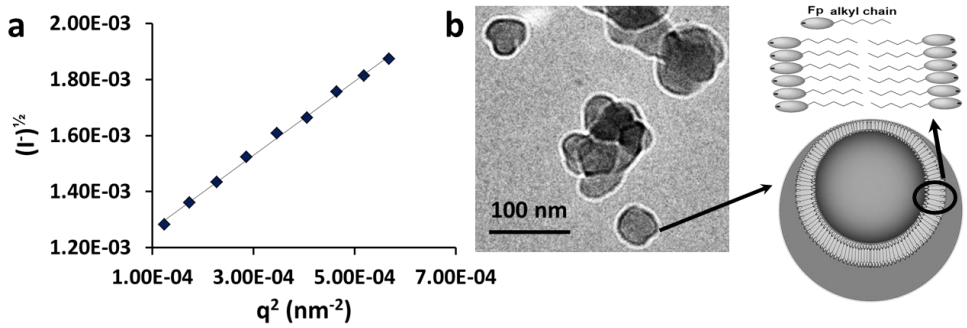

Figure 2.4 (a) Berry plot obtained from multi-angle SLS measurements of FpC6 aqueous colloids (0.006 mg/mL), (b) Cryo-TEM image of FpC6 vesicles. Sample was prepared from FpC6 aqueous colloids (0.1 mg/mL).

2.2.3 FpC6 aqueous aggregation process

To investigate the aggregation process, the critical water content (CWC), the water content at which FpC6 molecules start to aggregate, has been determined in THF. Light scattering count rates from a solution of FpC6 (0.1 mg/mL) in THF with increasing amounts of water were measured and the resultant data are plotted in Figure 2.5a. As shown in the figure, when the water content reaches 60% by volume, an upsurge in count rate is observed, which suggests that aggregation occurs. The CWC is, therefore, determined to be ca. 60 v%. This value is much higher than those for amphiphilic block copolymers.[92, 102] This high CWC can be attributed to the low molar mass of FpC6 and also suggests that the molecules, despite their aqueous insolubility, are able to be hydrated.

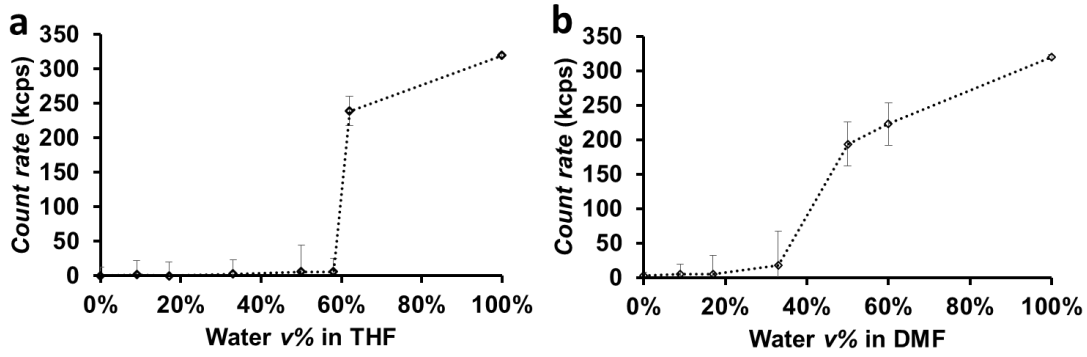

Figure 2.5 DLS count rates for FpC6 solutions (a) in THF/water, (b) in DMF/water as a function of water contents.

We also plan to investigate the aggregation process of FpC6 by using cyclic voltammetry (CV) experiments by taking advantage of the redox properties of FpC6 molecules. Because DMF will be used for the CV experiments instead of THF, the aggregation behaviour of FpC6 in DMF/water was investigated. Figure 2.5b displays the DLS count rates for FpC6 solutions in DMF/water (0.1 mg/mL) as a function of water contents. As shown in Figure 2.5b, the aggregation starts at water content of ca. 30 v% and becomes obvious at water content of ca. 60 v%. The redox activities of the iron complexes following this aggregation process have been examined for the investigation and the results are illustrated in Figure 2.6. As shown in the figure, FpC6 is soluble in pure DMF and shows a reversible redox trace with an oxidation peak at 0.60 V and a reduction peak at 0.46 V (Figure 2.6a). When we added 10 v% water, the FpC6 molecules remained soluble and did not aggregate (Figure 2.5b). As a result, a reversible redox cycle was still observed, though

the redox peaks are weaker (Figure 2.6b). As the water percentage was increased in the DMF/water solution, up to 30 v%, the FpC6 molecules started to aggregate (Figure 2.5b) and became less accessible to the electrode, which resulted in weak cathodic and anodic current (Figure 2.6c). However, when FpC6 aggregation was further enhanced by adding more water (60 v%), the oxidation peaks became visible again (Figure 2.6d), which suggests that FpC6 molecules actually aggregate in a way that makes the metal-carbonyl groups more electrochemically detectable. This is reasonable in light of the proposed bilayer vesicle structure with the metal-carbonyl centres exposed to water. Moreover, unlike the system with lower water content, two oxidation peaks separated by a redox coupling ($\Delta E_{½}$) of ca. 0.26 V became clearly observed (Figure 2.6d). CV experiments of poly(ferrocenylsilane)s also reveal two oxidation peaks, which is explained by the extent interaction between the adjacent ferrocenyl units along the polymer chain.[103, 104, 105] The oxidation of the first iron centre allows the neighboring iron to be oxidized at higher potential with a separation of $\Delta E_{½}$. Therefore, the appearance of the two separated oxidation peaks suggests that the metal carbonyl groups are closely associated as a result of FpC6 aggregation in DMF/Water with 60 v% of water. No reduction peaks are observed in Figure 6d, suggesting that the oxidation of the colloids is not reversible. As the water content further increased to 80 v%, two separated oxidation peaks are still visible but relatively weak (Figure 2.6e), suggesting that the hydrophobic metal-carbonyl heads start to associate tightly and become less accessible to the electrode. The separation in the oxidation peaks ($\Delta E_{½}$) for the system containing 80 v% water is 0.21 V, smaller than that (0.26 V) for the system with a water content of 60 v%.

These two values in different media, however, cannot be compared because oxidation/reduction potential is solvent dependent.[106, 107] In pure water, the redox activity of the metal complex is barely detected (Figure 2.6f), which suggests that the iron-carbonyl heads are highly integrated and have low accessibility to the electrode.

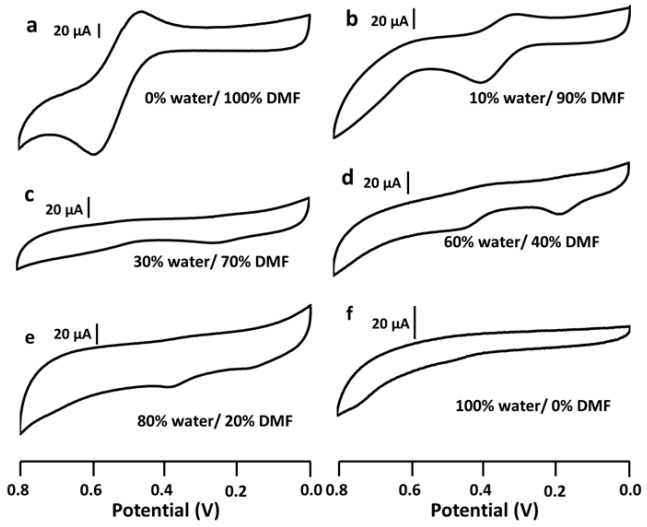

Figure 2.6 Cyclic voltammetry (CV) results, relative to Ag electrode, for solutions of FpC6 in DMF/water with varied water contents.

This set of experiments suggests that FpC6 colloids are formed with metal carbonyls closely packing on the surface. The CV experiments also illustrate that certain groups in FpC6 can be hydrated, which accounts for the solubility of FpC6 in mixed DMF/water solutions with a water content up to 60 v%. In pure water, the hydration force is not strong enough to molecularly dissolve FpC6. We therefore confirmed that FpC6 is water-insoluble

or hydrophobic as indicated by NMR analysis (Figure 2.3a). The colloidal stability of FpC6 vesicles in water can be attributed to solvation interaction of certain groups in FpC6. The motif responsible for the aggregation will be investigated in the following section.

2.2.4 Driven forces for aqueous self-assembly of FpC6

The FT-IR spectrum of FpC6 shows that the absorption for the acyl CO appears at 1610 cm^{-1}.[47] This low frequency absorption has been speculated to be due to the existence of a resonance structure with inductive negative charges on the oxygen of the acyl CO group (Figure 2.7).[52, 97] Therefore, we performed zeta-potential experiments, which indeed revealed that the colloids had a negatively charged surface with a ζ value of ca. -65 mV. This surface charge derived from the metal acyl resonance structure promotes WCIs, which are responsible for the initial hydration and subsequent aggregation of FpC6 molecules. The WCI has been widely explored in biological and geological systems,[64, 65, 96] but this is the first discovery that WCI can function as a driving force for the creation of well-defined aqueous colloids.

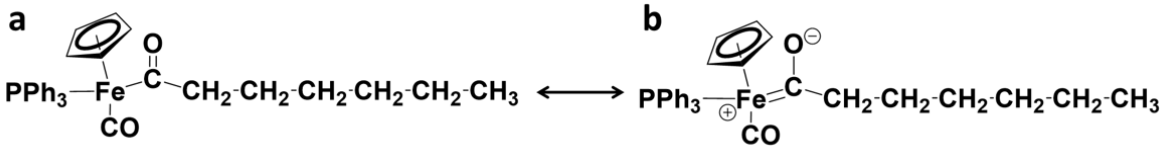

Figure 2.7 Proposed resonance structure for FpC6

The existence of WCI was further demonstrated using NMR spectroscopy. Both ^{1}H and ^{31}P NMR spectra for FpC6 in pure THF-d_8 and THF-d_8/D_2O mixed solvents have been recorded. When the content of D_2O reached CWC (60 v%), the aggregation of the

hydrophobic FpC6 reduced the mobility of the molecules so there was no signal corresponding to FpC6 detectable in ^{1}H NMR spectrum. When the water content was lower than the CWC, FpC6 was mobile and could be detected using ^{1}H NMR spectroscopy (Figure 2.8a). By comparing the spectra of the sample with increasing amounts of D_2O, it was observed that the NMR signals that corresponded to both the Cp ring and methylene protons, α to the acyl carbonyl group, were shifted upfield (Figure 2.8a). The hydration of the carbonyl groups accounted for these observed shifts, which reduceed the deshielding effect on the α-methylene and Cp protons. The shift (Δδ) was ca. 0.12 ppm for the methylene protons when D_2O content increased from 0 to 40 v%. This shift was much larger than that observed for the Cp protons (0.06 ppm). This difference can also be explained by the carbonyl group hydration, which affects its α-proton more effectively than those far away from the carbonyl group. In the ^{31}P NMR spectra, the chemical resonance for the coordinated phosphorus shifted upfield to $\Delta\delta = 2.9$ ppm with increasing amounts of D_2O. This larger shift was attributed to the sensitivity of ^{31}P NMR spectroscopy and wide energy separations between the spin states of ^{31}P (detectable ppm range). Unlike ^{1}H NMR, ^{31}P NMR spectroscopy signals are visible even when D_2O content reaches CWC (Figure 2.8b). Despite the weak signal, the upfield shift at CWC is obvious (Figure 2.8b), suggesting that hydration of carbonyl groups continues even when aggregation occurs. This result is reasonable because the bilayer vesicular aggregation forces the phosphorus coordinated metal carbonyls heads exposed to water. In pure D_2O solution, no ^{31}P NMR signal can be detected, which is similar to ^{1}H NMR spectra. Because the chemical shift could also be related to the variation

of the solvent media, further investigation using solution ATR-FTIR was performed to support the occurrence of CO hydration.

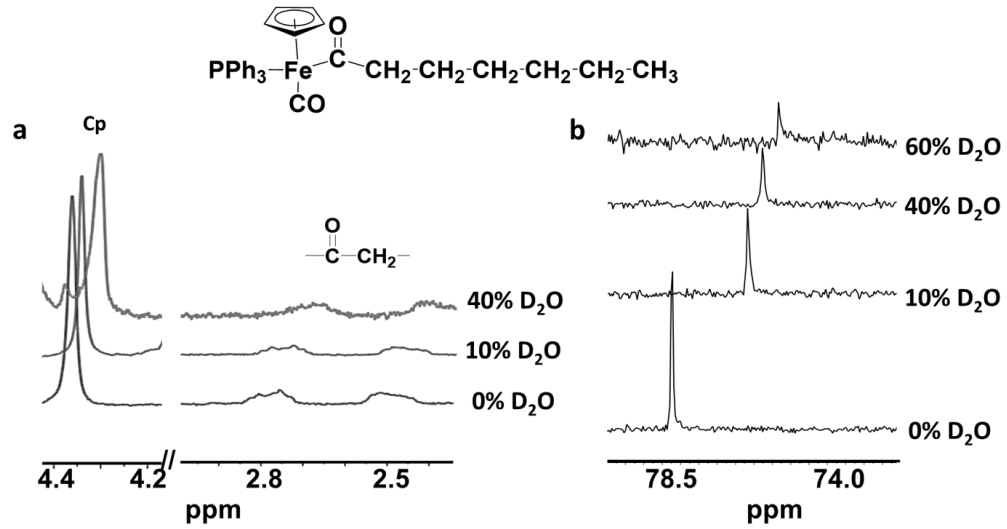

Figure 2.8 (a) Partial ^{1}H and (b) ^{31}P NMR spectra of FpC6 in THF-d_8 (5 mg/mL) and THF-d_8/D_2O mixed solvents.

ATR-FTIR has been used to probe the process of the self-assembly driven by WCI. Upon addition of water, the occurrence of WCI usually shifts the IR absorption of CO groups towards lower wavenumber (Figure 2.9 and Figure S2.6 in the Supporting Information).[63, 95, 108] The degrees of the shifts in wavenumber ($\Delta\nu$), an indicator for the strength of WCI, have been plotted as a function of water content (Figure 2.9) for FpC6 solutions in THF. As shown in Figure 9, when the water content is 10 v%, the shift in wavenumber ($\Delta\nu$) is 7 cm^{-1} and 0 cm^{-1} for the acyl and terminal CO groups, respectively. This difference suggests that the acyl CO groups can be readily hydrated but there is no hydration of the terminal CO groups. No obvious changes in $\Delta\nu$ for both types of CO groups are observed when the water content

increases from 20 v% to 40 v%. The solubility of the hydrophobic molecules at this fairly high water content (40 v%) can be attributed to the hydration of the acyl CO groups ($\Delta\nu$ = 7 cm^{-1}). The terminal CO groups remain unhydrated ($\Delta\nu$ = 0 cm^{-1}) and thus make no contribution to the solubility. With further increase in the water content to the CWC (60 v%), colloids are formed (Figure 2.5). At this point, $\Delta\nu$ for the acyl CO groups further increased, which indicates an enhanced hydration effect. Additionally, the aggregation induces the hydration of the terminal CO groups which become hydrated with a $\Delta\nu$ of 4 cm^{-1} (Figure 2.9). This result suggests that the hydration of the terminal CO groups is aggregation-induced. This aggregation-induced WCI (AI-WCI) may be caused by the creation of a local electric field when polarized acyl CO groups pack together at the surfaces.

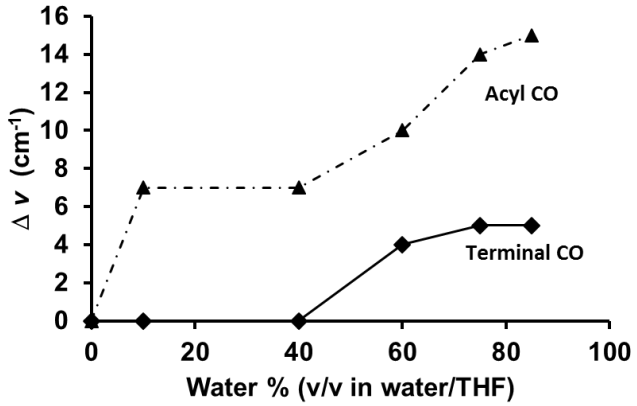

Figure 2.9 The degrees of FT-IR red shifts in frequencies for terminal and acyl carbonyl groups of FpC6 in THF/water solutions as a function of water contents.

2.2.5 Aggregation-enhanced IR absorption (AEIRA)

In addition to the observed shifts in IR absorption for the carbonyl groups, their intensities are also varied and related to the water content (Figure S2.6). At relatively high water contents (> 40 v%), the IR absorption for the acyl CO groups (1601 cm^{-1}) interfere with the signal due to water absorption (scissors bending at 1650 cm^{-1}), but the absorption at 1910 cm^{-1}, due to the terminal CO groups, does not overlap with the signals from most other molecules, including water and biological species. This is actually the advantage of IR-based bioassay stated in previous literature.[38, 40, 94] Therefore, we used this absorption to investigate the observed aggregation-enhanced IR absorption (AEIRA). The absorption due to the terminal CO groups in the IR spectra of an FpC6 solution in THF with increasing amounts of water are listed in Figure 2.10a. As shown in the figure, the intensity of the IR signal initially decreases as the solution is diluted and this decrease in intensity becomes obvious when the water content is 40 v%. Upon further addition of water up to the CWC (60 v%), aggregation occurs and concurrently an abrupt enhancement in IR absorption is observed (Figure 2.10a). Once the colloids are formed, the addition of water (up to 75 v%) causes a slight drop in the intensity probably due to the effect of dilution. One may argue that hydration of the carbonyl groups, rather than aggregation, might be a reason for the enhancement of the IR absorption. This possibility can be excluded when we examine the IR absorption due to the acyl CO groups as a function of water content (Figure S2.6). Although acyl CO groups are hydrated before the occurrence of aggregation at the WC (60 v%) (Figure 2.9), their IR absorption intensity is not enhanced until FpC6 aggregates (Figure S2.6).

IR absorption can be enhanced by the surface of metallic or dielectric materials, for example, films or nanoparticles.[42, 109, 110] This phenomenon is known as surface-enhanced IR absorption (SEIRA). Unlike conventional SEIRA, we observed AEIRA without the assistance of external substrates.[111] As we know that the surface of MCsomes is packed with highly polarized CO groups, which create a local electric field. This field increases the polarization of the CO groups and subsequently induces AI-WCI of terminal CO groups and enhances WCI of the acyl CO groups (Figure 2.9). Upon electromagnetic interaction with the incident light, this local electric field is polarized and their electromagnetic irradiation is consequently strengthened, resulting in the observed AEIRA.[100, 112, 113, 114, 115]

The enhancement in IR signals *via* conventional SEIRA is typically less than 100-fold.[42] For example, the IR absorption signal of 4-nitrobenzoic acid is enhanced by a factor of 20 using thin Ag metal over- and under-layers.[110] If thin films of Pt/Ru alloy are used to enhance the IR absorption of carbonyl ligands, the enhancement factors are between 10.5 to 13.1 folds.[116] SEIRA has also been reported for anthracene on the substrates that consist of polar dielectric nanoparticles of silicon carbide and aluminum oxide with enhancement of approximately 100-fold.[109] To compare our discovery with conventional SEIRA, we have quantified the degree of the enhancement caused by AEIRA. The experiments were designed to compare the detection limit for FpC6 in molecular and assembled forms. ATR-FTIR spectra of FpC6 in pure THF were first recorded at different concentrations (Figure S2.7) and the CO signal became undetectable when the concentration was dropped to 5.0 mM. ATR-FTIR spectra for FpC6 aggregates in THF/water solutions (60 v% of water) were then

recorded and are displayed in Figure 2.10b. As shown in the figure, the CO absorption is still fairly strong at 5.0 mM and remains detectable even when the concentration drops to the micromolar range (50.0 μM). By comparing this value to the detection limit of FpC6 molecules in THF, AEIRA improves the IR sensitivity by at least 100-fold (Figure 2.10c), which is the upper limit of the enhancement using conventional SEIRA assisted with external dielectric substrates.[42, 100]

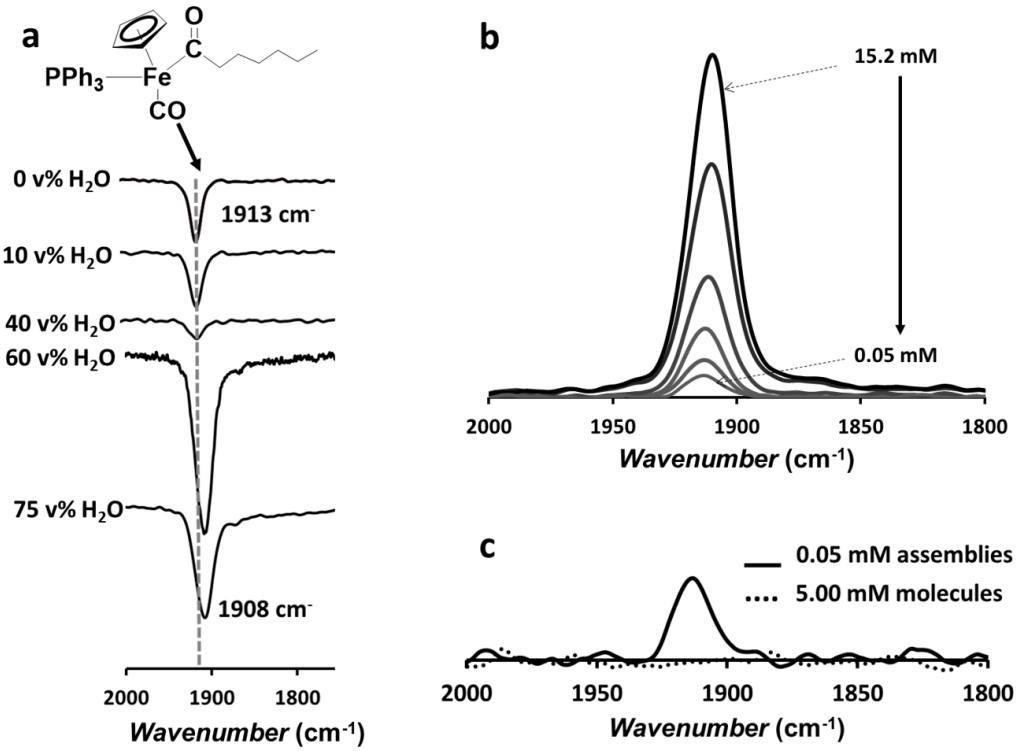

Figure 2.10 Partial ATR-FTIR spectra for FpC6 solutions in (a) THF/water solution with varied water contents, (b) THF/water solution (60 v% of water, CWC) with varied FpC6 concentrations, (c) THF with FpC6 concentration of 5.0 mM and THF/water at CWC with FpC6 concentration of 0.05 mM.

Although conventional SEIRA has been explored for biological sensing and cell imaging,[42, 100] complicated synthesis, less defined nanostructures, and the requirement for substrates impose restrictions in their practical applications. The use of AEIRA without external dielectric substrates is, therefore, promising for future technology advances.

2.3 Conclusions

In summary, we have demonstrated that FpC6 molecules are hydrophobic and non-surface active, but are able to self-assemble in water into monodispersed metal-carbonyl vesicles (MCsomes) with strong structural integration. The WCI has been identified as a driving force responsible for aggregation. Hydration of the highly polarized acyl CO groups initiates the aggregation, which subsequently enhances WCIs of the acyl CO groups and induces WCI of the terminal CO groups. It is reasonable to think that the MCsomes, as suggested by the cryo-TEM and AFM images, contain a bilayer structure with associated metal-CO groups exposed towards water and the inner domain formed from packed alkyl chains. The association of the metal carbonyl groups creates a local electric field, which induces AEIRA for the CO groups. AEIRA has not been reported before and can improve the detection limit by at least 100-fold. Our discoveries open up a new research topic on WCI-driven self-assembly of hydrophobic molecules for highly structural integrated colloids and the observed AEIRA will potentially address the challenge of relatively low sensitivity of IR-based sensing and imaging.[42, 94, 100]

2.4 Experimental Section

2.4.1 Materials and Instrumentation

Materials: Potassium metal (99.5%, rods in mineral oil) and sodium metal (99.9%, cubes in mineral oil), cyclopentadienyl iron (II) dicarbonyl dimer (99%), triphenylphosphine (98%), benzophenone (99%) and 1-bromohexane (>98.0%) were purchased from Sigma-Aldrich and used as received. Tetrahydrofuran (THF) was distilled over sodium/benzophenone before use. All other solvents were obtained from local commercial providers and used as received.

Dynamic light scattering (DLS) and static light scattering (SLS): DLS results were obtained at 25 ^{o}C using Zetasizer Nano Series (Nano-S90, Malvern Instruments) with laser wavelength of 633 nm at fixed angle of 90^{0}. The broadness of the size distribution (Polydispersity index (PDI)) is calculated by the cumulants analysis from the ratio between the normalized variance of rate decay and the square value of the mean decay rate. Multi-angle SLS measurements were carried out using Brookhaven Laser Light Scattering System with a BI-200 SM goniometer. A vertically polarized helium−neon diode laser with wavelength of 636 nm was used as the light source. Measurements were taken at scattering angles (θ) between 50°and 130° with 10° intervals. Toluene was used as the reference for the Rayleigh ratio.

Nuclear magnetic resonance (NMR) spectroscopy: ^{1}H and ^{31}P NMR spectra were recorded on Bruker-300 (300 MHz) spectrometer at room temperature using the appropriate

solvent as mentioned for each experiment. ^{1}H NMR chemical shifts are reported relative to residual solvent signals and ^{31}P NMR resonances are referenced to an external standard sample of 85% H_3PO_4 in D_2O.

Cyclic Voltammetry: Cyclic voltammetry (CV) experiments of FpC6 solutions (0.1 mg/mL) in water/DMF were performed at room temperature using DY2000 Multi-Channel Potentiostat (Digi-Ivy Inc.) workstation with a scan rate of 50 mV/sec and silver wire as a reference electrode. A water solution of KCl (2 mg/mL, 2.68 mM) and a DMF solution of tetrabutylammonium perchlorate (TBAP) (2 mg/mL, 5.8 mM) were prepared. First, FpC6 was dissolved in the DMF solution and the water solution was subsequently added to prepare the mixed solutions of FpC6 in water/DMF.

Surface tension: Surface tension of pure water and FpC6 aqueous colloids with different concentrations were measured at 24 ^{o}C using a tensiometer Data Physics DCAT 21 system.

Zeta potential: ζ-potential measurements were performed at 25 ^{o}C on a Malvern Zetasizer nano ZS instrument using disposable folded capillary cells.

ATR/FTIR: Fourier transform infrared (FT-IR) spectra for FpC6 solid sample was recorded on a Bruker Tensor 27 spectrophotometer with a resolution of 4 cm^{-1}. Pellets were prepared by grinding and compressing of FpC6 (2% by weight) in anhydrous KBr using Nujol mulls. Attenuated total reflection-fourier transform infrared (ATR-FTIR) spectra of FpC6 in THF/water solutions were recorded on the same instrument using a germanium

crystal Pike MIRacleTM ATR Attachment. A drop of the solutions was placed on the germanium crystal. IR frequency of FpC6 solutions in THF were measured first. Afterward, water was successively added to the THF solutions and IR spectra were recorded at different water contents.

TEM and Cryo-TEM: Conventional transmission electron microscopy (TEM) images were recorded on a low voltage (5 kV) LVEM5 electron microscope (Delong Instruments). TEM samples were prepared by dropping the solution onto a carbon-coated copper grid (Cu-300CN, Pacific rid Tech) and the grid was then then left to dry at ambient temperature. Cryo-TEM images were obtained using a high voltage (200 kV) field emission FEI Tecnai G2 F20 Cryo-TEM microscope. The cryo-TEM sample was prepared by placing 5.0 µL of FpC6 (0.1 mg/mL) aqueous solution onto a glow discharged coper grid with holy carbon film (Quantifoil Multi A) and thinned by blotting with a filter paper. The grid was then quickly plunged into a liquid ethane bath and transferred under liquid nitrogen to a Gatan 914 cryo-holder and viewed at -179 ^{o}C.

AFM: Atomic force microscopy (AFM) experiments were conducted on a Nanoscope MultiModeTM AFM microscope using a Conical AFM tip with a spring constant of 40N/m, resonance frequency of 300 KHz and tip radius of 8 nm. The samples were prepared by transferring 3 drops of the FpC6 aqueous colloids on freshly cleaved mica substrate. The sample was then spun for 45 s and left to dry overnight before scanning.

2.4.2 Synthesis of FpC6

$CpFePPh_3(CO)CO(CH_2)_5CH_3$ (FpC6) was prepared as follows.[47] A solution of 1-bromohexane (1.00 mL, 7.12 mmol) in THF (10 mL) was added dropwise to a suspension of FpK (1.69 g, 7.84 mmol) in THF (20 mL) at 0 ºC under vigorous stirring. The mixture was then stirred at 23 ºC for 1 h. Afterwards, THF was removed via rotary evaporation and the residue was dissolved in degased hexane and passed through a celite column. Hexane was subsequently removed using rotary evaporation. The resulting solid was dissolved in THF (20 mL) and mixed with triphenylphosphine (2.05 g, 7.84 mmol) in THF (10 mL). After the solution was refluxed at 70 ºC for 72 hours, it was cooled to 23 ºC and THF was removed under vacuum. The resulting brownish solid was chromatographed using a silica column. The column was first washed using degassed hexane and a yellow band, identified to be ($CpFe(CO)_2(CH_2)_5CH_3$), was removed. Subsequently, the column was flashed using hexane/DCM (3/1 v/v) and an orange band was collected. The solvents were removed using rotary evaporation resulting in a brown oil-like product. The product was then completely dried under vacuum overnight (yield 3.18 g, 85.0 %). ^{1}H NMR (300 MHz, C_6D_6): 7.71 ppm (t, 6 H, *m*–Ph), 6.95-7.09 ppm (b, 9H, *o*- and *p*-Ph), 4.26 ppm (s, 5H Cp), 3.00-3.15 ppm (m, 1H ,(α-H)-$COCH_2$-), 2.84-2.97 ppm (m, 1H, ,(α-H) -$COCH_2$), 1.45-1.63 ppm (b, 1H, ,(β-H)-$COCH_2CH_2$-), 1.30-1.43 ppm (b, 1H, ,(β-H)-$COCH_2CH_2$-), 1.05-1.27 ppm (b, 6H, -$COCH_2CH_2(CH_2)_3$-), 0.86 ppm (t, 3H,(terminal CH_3) -$COCH_2CH_2(CH_2)_3CH_3$). ^{1}H NMR (300 MHz, $CDCl_3$): 7.50 ppm (t, 6 H, *m*–Ph), 7.30-7.40 ppm (b, 9H, *o*- and *p*-Ph), 4.40 ppm (s, 5H, Cp ring), 2.91-2.78 ppm (m, 1H ,(α- H)-$COCH_2$-), 2.60-2.47 ppm (m, 1H, ,(α-H) -

$COCH_2$-), 1.26-0.91 ppm (mb, 8H, -$COCH_2(CH_2)_4$-), 0.83 ppm (t, 3H,(terminal CH_3)$COCH_2CH_2(CH_2)_3CH_3$).^{31}P NMR (300 MHz, C_6D_6): 79.0 ppm, (300 MHz, THF-d_6): 78.2 ppm, (300 MHz, $CDCl_3$): 77.9 ppm. FTIR of amorphous FpC6 (KBr pellet): 1910 cm^{-1} (terminal C≡O), 1610 cm^{-1} (acyl C=O). (see Figure S2.1 and Figure S2.2 in the Supporting Information)

2.4.3 FpC6 Colloid preparation

FpC6 aqueous colloids (0.1 mg/mL) were prepared by adding 10.0 mL distilled deionized water to 1.0 mL THF solution of FpC6 (1.0 mg/mL) under stirring. Subsequently, THF was removed *via* nitrogen bubbling for one and a half hour. We also prepared FpC6 colloids in D_2O and the ^{1}H NMR spectrum of the solution was acquired to determine the bubbling conditions (time and speed of N_2 flow) for the complete removal of THF.

2.4.4 Critical water content (CWC)

Following successive addition of water to a THF solution of FpC6, DLS count rates were recorded. The resultant data were plotted against water contents, which shows an upsurge in the intensity at water content of 60 v%. This point was assigned as a CWC.

2.4.5 FpC6 recovery by freeze-drying of FpC6 colloids

FpC6 molecules were recovered from their aqueous colloids by adding 5 mL of the prepared FpC6 colloid (0.1 mg/mL) in a long-neck 50 mL round bottom flask. The flask was then placed in a liquid nitrogen bath with continuous swirling for two minutes to achieve a thin layer of frozen solution. Subsequently the flask was removed from the liquid nitrogen

bath and connected to a vacuum pump (Edwards RV3, A65201906). After six hours, all FpC6 molecules were recovered and the residue was then dissolved in 1 mL of $CDCl_3$ and characterized by NMR.

Chapter 3

Aggregation-Enhanced IR Absorption (AEIRA) of Molybdenum-Carbonyl Organometallic Aqueous Colloids

3.1 Introduction

Metal-carbonyl (MC) complexes and colloids[13, 41] have been explored for biomedical applications, such as CO delivery,[33, 34] biosensors,[38] and cancer therapy,[35, 36] due to the IR absorption of their CO groups, within the biological transparent window between the wavenumbers of 1800 and 2200 cm^{-1}.[37] It is, therefore, an advantage to use MC derivatives as vibrational IR or Raman probes for cell imaging[39] and bioassay.[40] However, the intensity of the IR absorption is not high enough for possible applications in a diluted solution. Attachment of MC compounds on the surface of plasmonic or dielectric nanoparticles[42, 117] has been reported to enhance the IR signals via surface enhanced Raman scattering (SERS) [117] and surface enhanced IR absorption (SEIRA).[42]

We have discovered that hydrophobic Fp acyl derivatives (Fp: $CpFe(CO)_2$) can be hydrated *via* water carbonyl interactions (WCIs) and self-assemble into aqueous MC vesicles (MCsomes).[66, 118, 119] For example, $CpFe(CO)(PPh_3)CO(CH_2)_5CH_3$ (FpC6) is hydrophobic and able to self-assemble into liposome-like MCsome in water with a highly integrated bilayer membrane.[118] This assembly induces an aggregation-enhanced IR absorption (AEIRA) of the CO groups.[118] This enhanced IR absorption without using external substrates will be an advantage for sensing applications. It is, therefore, tempting to create an array of

this novel group of colloids for potential material exploration. This research is facilitated by well-developed synthetic chemistry for desired FpC6 analogues as building blocks.[120, 121, 122] For example, Pannell *et al*.[123] reported a one-pot reaction of $[CpMo(CO)_3]^-$ (Mp) with epibromohydrin in the presence of an excess amount of triphenylphosphine generating trans-$CpMo(CO)_2(PPh_3)$-2-furan. A phosphine coordinated Mp acyl complex was proposed as a reaction intermediate. The oxygen on the acyl CO group in the intermediate was nucleophilic and attacked the epoxide ring yielding the furan complex.[123, 124]

Herein, we report the synthesis and aqueous behaviour of MpC6 (MpC6: $CpMo(CO)_2(PPh_3)CO(CH_2)_5CH_3$). MpC6 is prepared *via* a reaction of Mp anion with alkyl bromide in the presence of triphenylphosphine. Surface tension and light scattering experiments suggested that MpC6 is non-surface active, but can self-assemble in water *via* WCIs without critical aggregation concentration (CAC). The aggregates of MpC6 exhibit a significant enhancement (ca. 70-fold) in IR absorption of the carbonyl groups. The colloidal stability and AEIRA function render the MpC6 colloids potentially useful as a sensing material.[43]

3.2 Results and discussion

3.2.1 Synthesis of MpC6

To prepare MpC6 (**3.2**), the Mp anion was first reacted with 1-bromohexane in THF at 40 ^oC, producing $[CpMo(CO)_3(CH_2)_5CH_3]$ (**3.1**). Subsequently, the reaction mixture was cooled to room temperature (23 ^oC) and triphenylphosphine was added. After stirring the

solution at room temperature for 7 days, MpC6 was produced. Alternatively, as shown in Figure 3.1, the migratory insertion reaction (MIR) was completed within 24 hours when it was carried out at 60 ^{o}C.

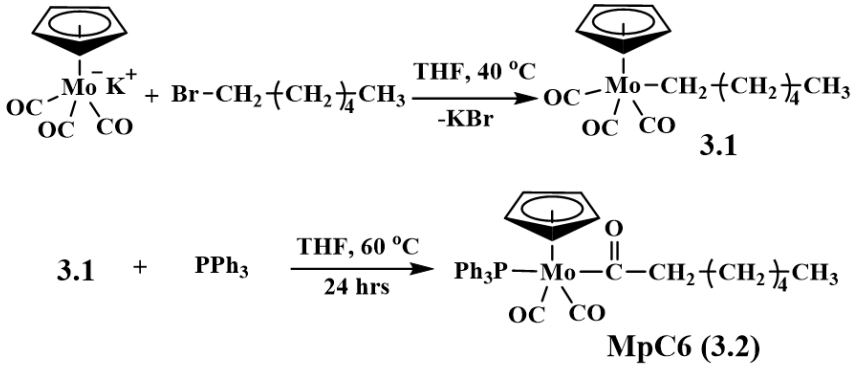

Figure 3.1 Synthesis of MpC6 complex.

FT-IR and NMR spectra for MpC6 are illustrated in Figure 3.2. As shown in Figure 3.2a, two IR absorption bands appear at 1932 and 1850 cm^{-1} for the terminal CO groups and one band appears at 1616 cm^{-1} for the acyl CO group. ^{31}P NMR spectrum (Figure 3.2b) shows a single peak at 71.0 ppm corresponding to the coordinated phosphine group.[48, 118] These analyses suggest that the MIR has occurred.[48] Figure 1c displays the ^{1}H NMR spectrum of MpC6. As shown in Figure 1c, the chemical shifts at 7.36 and 4.92 ppm are attributed to the phenyl and Cp protons, respectively; the proton signals appearing upfield are assigned to the alkyl protons as indicated in Figure 1c. The integration ratio of these signals is consistent with the expected value for MpC6. Compared to the ^{1}H NMR spectrum of **3.1** (Figure S3.1), the upfield shift of the proton resonance due to the Cp ring (Figure 3.2c)

and downfield shift of the signal due to the α-protons (f in Figure 3.2c) confirm the occurrence of MIR.[48]

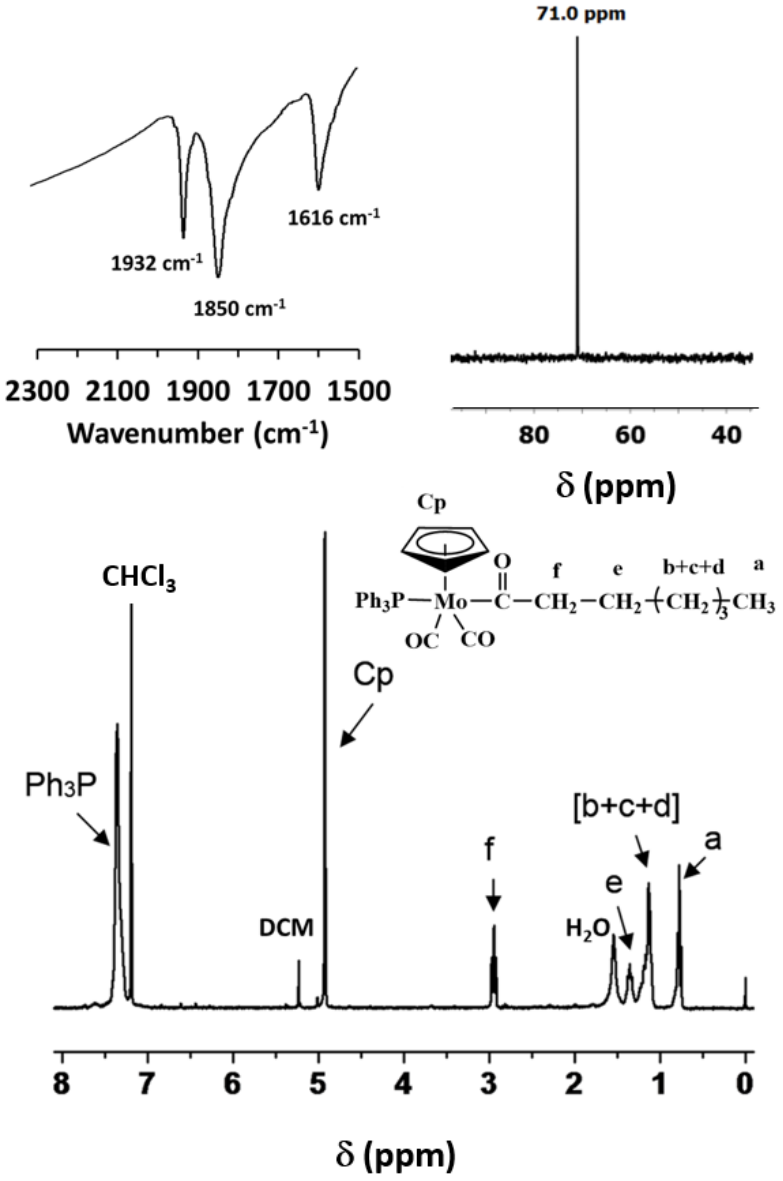

Figure 3.2 (a) Partial IR spectrum (KBr pellet) of MpC6. (b) ^{31}P and (c) ^{1}H NMR spectra ($CDCl_3$, 25 ^{o}C, 300 MHz) of MpC6.

The resultant MpC6 was recrystallized from a hexane solution at - 49 ^{o}C. The X-ray diffraction of the single crystal reveals a triclinic crystal system with a P-1 space group (detailed crystal analysis is summarized in Table S3.1 and Table S3.2, in the Supporting Information). As shown in Figure 3.3, the geometry for MpC6 is a four-legged stool. As shown in Table 3.1, although the metallic elements are different, the CO bond lengths in MpC6 and FpC6[47] are similar. These results suggest that the polarity of the CO groups in these two complexes is comparable and may have a similar strength of WCI-induced hydration.

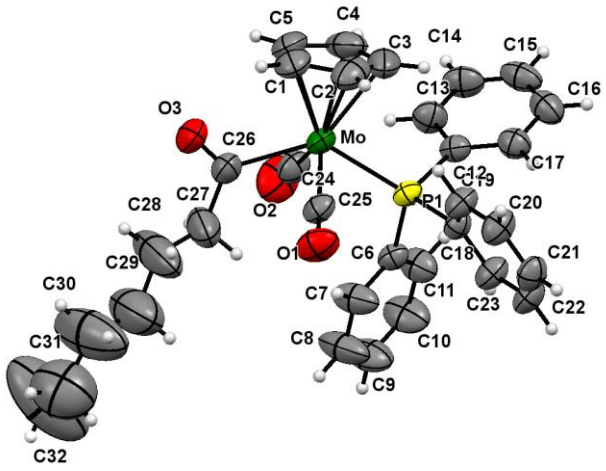

Figure 3.3 Crystal structure for MpC6 complex showing 50% probability of thermal ellipsoids. Labeling of hydrogen atoms is omitted for clarity.

Table 3.1 Bond lengths (Å) of the CO groups in MpC6 and FpC6

Bond	MpC6	FpC6[47]
C-O acyl	1.20	1.20
C-O terminal	1.15 and 1.14	1.15

3.2.2 Aqueous behaviour of MpC6

By adding 10.0 mL of water into a THF (1.0 mL) solution of MpC6 (1.0 mg/mL, 1.78 mM) followed by N_2 bubbling to remove THF, an aqueous MpC6 colloid is obtained (Figure 4.1a). DLS analysis reveals that the average hydrodynamic radius (R_h) for the colloid is ca. 60 nm with a narrow polydispersity index (PDI) of 0.07 (Figure 3.4a). There is no chemical degradation of MpC6 in water as proved by the ^{1}H NMR spectrum of the molecules recovered from an aqueous solution *via* freeze-drying (Figure S3.2). Using dimethyl sulfoxide (DMSO) to replace THF, colloids with R_h of ca. 59 nm was prepared (Figure S3.3), suggesting that the choice of organic solvent did not affect the self-assembly. When basic water (pH = 11) was used, the resulting colloids had a similar size with those prepared using neutral water (pH = 7) (Figure S3.4); whereas, the colloids in acidic solution had a larger particle size (R_h = ca. 150 nm) (Figure S3.4). All colloids, regardless of the pH, exhibited the same stability over time and no precipitation or dissociation were observed after two weeks. Figure 3.4b indicates that the surface tension of the solutions with varied concentrations of MpC6 is similar with that for pure water, suggesting that MpC6 is not surface active. Figure 3.4c shows a linear relationship between the DLS count rates and the solution concentration,[125] suggesting that MpC6 molecules can self-assemble without a detectable critical aggregation concentration (CAC). It can, therefore, be expected that the structural integration of the colloid is high. This is elaborated by the DLS analysis of a set of solutions with varied concentrations. These samples were diluted from an aqueous solution of MpC6 (178 μM). As shown in Figure 3.4d, there is no change in R_h and PDI even at a very low

concentration (5.0 μM). On the other hand, when the colloids were directly prepared using different concentrations of MpC6 in THF, the R_h for the resulting colloids were 68, 60, 53 and 46 nm for the solution with MpC6 concentration of 0.5, 0.1, 0.05 and 0.01 mg/mL, respectively (Figure S3.5). The effect of the concentration on the R_h, therefore, depends on how the solutions were prepared, which suggests that the assembling is kinetically controlled.

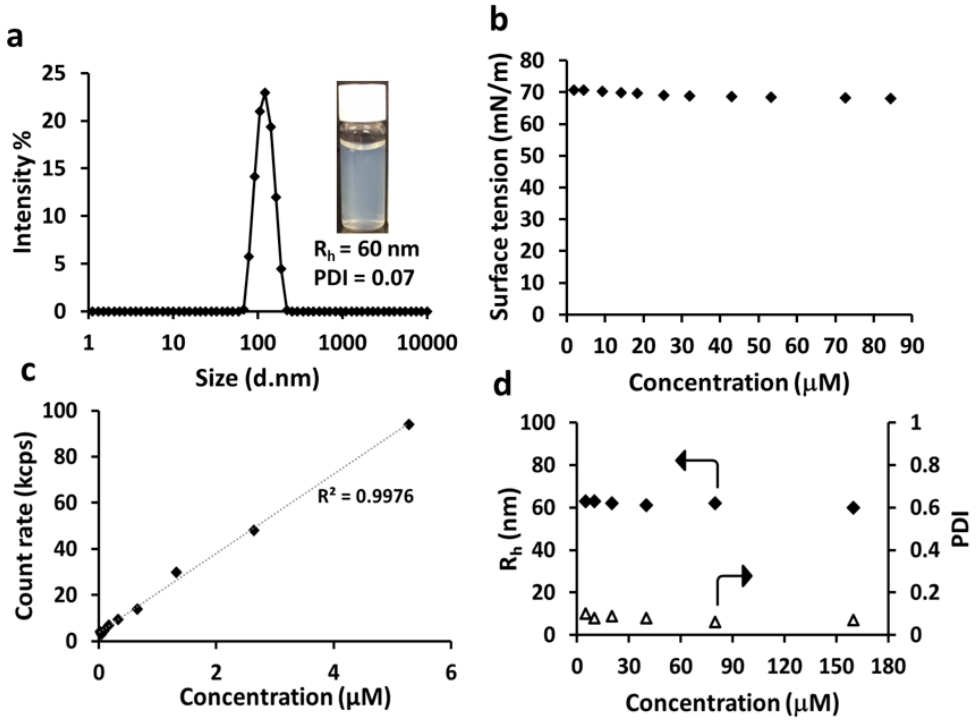

Figure 3.4 (a) DLS analysis and photograph for an aqueous colloid of MpC6 (178 μM). (b) Surface tensions for MpC6 in water as a function of concentration. (c) DLS count rates of the aqueous colloids as a function of MpC6 concentration. (d) Hydrodynamic radii (R_h) and polydispersities (PDI) for MpC6 aqueous colloids prepared *via* a successive dilution of an aqueous MpC6 solution (178 μM).

A multi-angle static light scattering (SLS) measurement reveals that the radius of gyration (R_g) for the colloid is ca. 59.3 nm (Figure S3.6); while a DLS analysis for the same sample reveals an R_h of 55.5 nm. Therefore, the shape factor (R_g/R_h) for the colloids is 1.06, suggesting that MpC6 molecules are able to associate into vesicles in water.[118] This investigation indicates that MpC6 and FpC6[118] have similar solution behaviour and both cannot be classified as traditional amphiphiles.[125, 126, 127]

We have reported that the acyl CO group in FpC6 can be readily hydrated *via* WCI.[118] This hydration induces an aggregation of the FpC6 molecules with a critical water content (CWC) of 60 vol%. The hydration of the terminal CO groups, however, only starts when the amount of water in the system reaches CWC. This aggregation-induced (AI) hydration is caused by the enhancement of the polarity of the terminal CO groups. This enhancement in polarity is explained due to the formation of a local electric field resulting from the aggregation of the MC groups at the surface of the colloid.[118] To test whether this hydration process occurs to MpC6, we measured CWC for MpC6 in THF/water using DLS. As shown in Figure 3.5, only when the water content reaches 60 vol%, a steep increase in DLS count rates is observed, indicating the occurrence of the aggregation. Therefore, MpC6 and FpC6 have the same CWC (60 vol%), implying that the hydration of the acyl CO group is responsible for the assembling. This hypothesis is analyzed using ATR-FTIR spectroscopy. As shown in Figure 3.6, the wavenumber shifts in IR absorption ($\Delta\nu$) for the acyl CO group are observed at water contents lower than 60 vol%. In contrast, the $\Delta\nu$ for the terminal CO groups only occurs after the water content reaches CWC (60 vol%). This behaviour confirms

that the acyl CO group is easier to be hydrated and the hydration of the terminal CO groups is AI.[118] In addition, the Δν is much larger for the acyl CO than for the terminal CO groups (Figure 3.6). For example, Δν is 13 cm^{-1} and 5 cm^{-1} for the acyl and terminal CO groups, respectively, when D_2O content is 80 vol%. This comparison suggests that the degree of the hydration is higher for the more polarized acyl CO group. Based on this IR spectroscopic experiment, it can be proposed that the balance of the acyl CO hydration against the overall hydrophobicity of the molecule determines the CWC. The polarity of the acyl CO groups in both MpC6 and FpC6 are comparable since bond distances are very similar (Table 3.1), which explains why the two building blocks have the same CWC.

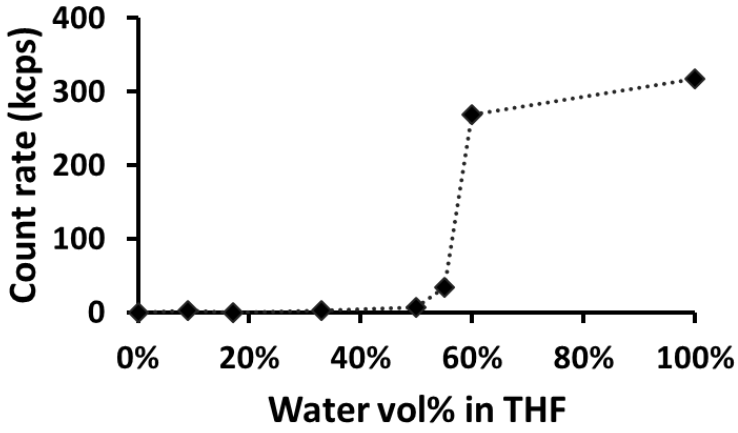

Figure 3.5 DLS count rates of MpC6 in THF/water solutions with varied amount of water.

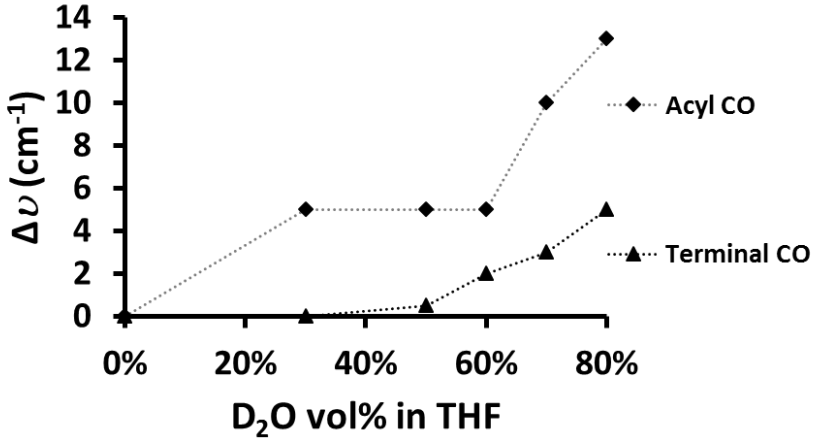

Figure 3.6 Wavenumber shifts in IR absorption for the terminal and acyl CO groups (Δν) for THF/D_2O solutions of MpC6 (5.0 mg/mL) as a function of D_2O content. The average IR shifts for the two terminal CO groups are used for the plot.

As we learned from our previous study on FpC6, the IR absorption of the CO groups can be enhanced upon the formation of the colloids.[118] Unlike conventional surface-enhanced IR absorption (SEIRA),[109, 110, 128] this AEIRA occurs in the absence of external metallic or dielectric substrate.[118] Similar to FpC6, the MpC6 colloids possess a zeta potential (ζ) of ca. -69.60 mV resulted from the polarization of the associated CO groups, which may also induce a local electric field for AEIRA.[118] As shown in Figure 3.6, Figure S3.7 and Figure S3.9, the MpC6 solutions in THF and THF/H_2O with H_2O lower than CWC only show weak IR absorptions for the CO groups. In a sharp contrast, a significant enhancement in the absorption is observed for the same concentration of MpC6 aggregated in THF/water at CWC (60 vol%). The same enhancement in IR absorption was observed for the aggregates in

DMSO/water (Figure S3.10), so the aggregation, rather than the polarity of the solvents, is a major factor inducing the enhancement.

This AEIRA for MpC6 is estimated to be ca. 67-fold by comparing the intensities of the IR absorptions (Figure 3.7b and Figure S3.8), which is smaller than that for the FpC6 colloids (ca. 100-fold) recorded under the same conditions.[118] The size of the colloids may explain this difference, because the polarizability of particles, a parameter determining the strength of the resulting local electric field, depends on the size of the particles.[129, 130] For example, the photocurrent strength of an illuminated light[129] and a surface enhanced Raman scattering (SERS)[131, 132] can be varied by the size of silver nanoparticles.[130] Figure 3.8 shows that the MpC6 colloid is relatively smaller than that for FpC6. Therefore, the smaller MpC6 colloid creates a relatively weaker electric field and correspondingly imparts a lower enhancement in the IR absorption.

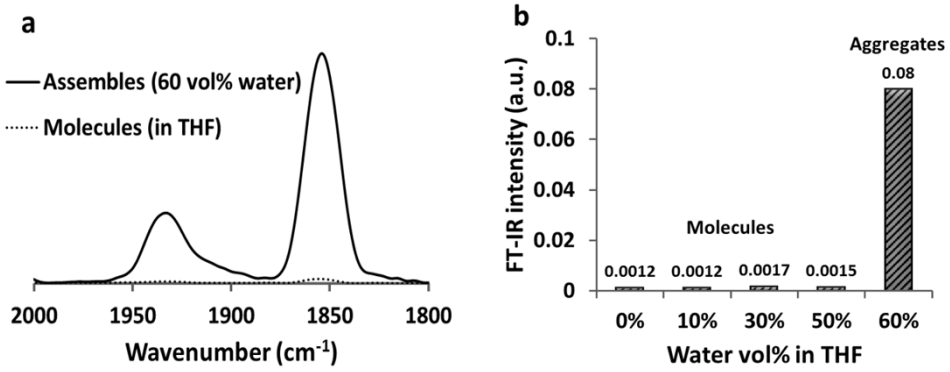

Figure 3.7 (a) IR absorption of the terminal CO groups for the solutions of MpC6 (27 mM) in THF and THF/water (60 vol%). (b) Maximum intensities of IR absorption for the terminal CO groups (at 1855 cm^{-1}) measured from MpC6 solutions in THF/water with varied amount of water.

The colloidal stabilities for FpC6 and MpC6 are also compared in Figure 3.8. As shown in Figure 3.8, the R_h for FpC6 colloid increases gradually from 85 nm to 155 nm and a small amount of insoluble materials was observed after the FpC6 colloid was aged for 7 days. In contrast, R_h for the MpC6 colloid is ca. 60 nm and only enlarged slightly to ca. 80 nm after 14 days (Figure 3.8). In addition, no precipitate was observed even when the solution was aged for two weeks. The MpC6 colloids are therefore more stable than the FpC6 colloids. The number of CO groups in the building blocks can rationalize this difference. Compared to FpC6, MpC6 possesses one more terminal CO group, which may generate a stronger AI-WCI and subsequently improve the stability of the colloids.

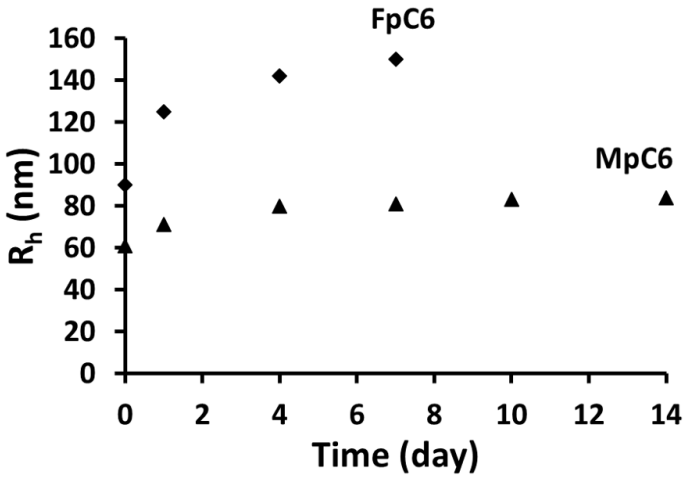

Figure 3.8 Hydrodynamic radii for the aqueous colloids of MpC6 and FpC6 as a function of time.

3.3 Conclusion

In summary, MpC6 is synthesized *via* MIR and its solution behaviour is investigated. This molecule is hydrophobic, non-surface active, but able to self-assemble into highly integrated colloids in water. The balance between the hydration of the acyl CO groups and the hydrophobicity of MpC6 accounts for the formation of the colloids. Upon the aggregation at CWC, the terminal CO groups are polarized by an AI local electric field and subsequently hydrated. The resultant colloids exhibit an AEIRA. This behaviour is similar with its iron analogue (FpC6).[118] MpC6 and FpC6 are, therefore, unlike conventional amphiphiles,[126, 127] represent a new group of self-assembling building blocks. The resultant colloids with the unique AEIRA will be further explored for material applications.

3.4 Experimental section

3.4.1 Materials and instrumentations

All experiments were performed under an atmosphere of dry nitrogen using standard Schlenk techniques unless otherwise indicated. THF was freshly distilled from Na/benzophenone under nitrogen. Hexane and DCM were degassed with dry nitrogen before use. Potassium (K), 1-bromohexane, benzophenone and cyclopentadienyl tricarbonyl molybdenum dimer (Mp_2) were purchased from Sigma-Aldrich Co. Triphenylphosphine was purchased from Tokyo Chemical Industry (TCI). All chemicals were used as received unless otherwise indicated.

^{1}H and ^{31}P NMR spectra were recorded on a Bruker-300 (300 MHZ) spectrometer at ambient temperature using appropriate solvents. FT-IR spectra were recorded using a Perkin Elmer Spectrum RX I FT-IR system. The samples were ground with dry KBr and then pressed into transparent pellets. Attenuated total reflection-Fourier transform infrared (ATR-FTIR) spectra of MpC6 in THF and THF/water solutions were recorded on a Bruker Tensor 27 spectrophotometer with a germanium crystal Pike MIRacleTM ATR Attachment. DLS results were obtained using Zetasizer Nano Series (Nano-S90, Malvern Instruments) with the laser wavelength of 633 nm at a fixed angle of 90^{o}, and the broadness of the size distribution (Polydispersity index (PDI)), in DLS results is calculated by the cumulants analysis from the ratio between the normalized variance of rate decay and the square value of the mean decay rate. SLS measurements were performed using Brookhaven Laser Light Scattering System with a BI-200 SM goniometer. A vertically polarized helium−neon diode laser with wavelength of 636 nm was used as the light source. Measurements were taken at scattering angles (θ) between 50° and 130° with 10° intervals. Zeta (ζ) potential measurements were performed at 25.0 ^{o}C on Malvern Zetasizer nano ZS instrument using disposable folded capillary cells. Surface tensions of pure water and MpC6 aqueous colloids with different concentrations were measured at 24.0 ^{o}C using tensiometer Data Physics DCAT 21 system. Single crystals suitable for X-ray diffraction analysis were mounted onto the tips of glass fibers with thick oil and transferred into the diffractometer cryostat. X-ray data were collected using Mo Kα radiation at 296 K on a Bruker Kappa APEX II System (Madison,

WI, USA). Structures were solved using direct methods and refined by full-matrix least squares on F^2 using the APEX2 package (v2014.11-0).

3.4.2 Synthesis of MpC6

MpC6 was prepared in one pot as illustrated in Figure 3.1. First, potassium benzophenone ketyl was prepared by stirring of benzophenone (0.156 g, 0.86 mmol) and potassium (0.03 g, 0.80 mmol) in dry THF (20 mL) under N_2 at room temperature. The color of the solution turned to dark blue immediately. The solution mixture was stirred for three hours. The dark blue solution was then added dropwise to a THF solution (20 mL) of $[CpMo(CO)_3]_2$ (Mp_2) (0.20 g, 0.40 mmoL) under vigorous stirring. The dark red color of Mp_2 disappeared within several minutes and the solution became yellowish green after stirring for two hours. To this solution, 1-bromohexane (0.11 mL, 0.80 mmoL) was added dropwise and stirred for one hour at 40 ^oC. The color of the solution gradually became brown. Afterward, PPh_3 (0.223 g, 0.85 mmoL) was added to this solution followed by stirring for 24 hours at 60 ^oC. Then, the mixture was cooled to room temperature and the solvent was removed under vacuum. The residue was dissolved in hexane and filtered through a neutral Al_2O_3 column. Hexane was then removed under vacuum and a yellow solid of MpC6 was obtained (0.165 g, Yield: 85%). The resulting yellow solid was recrystallized from a minimum amount of hexane at -49 ^oC. ^1H NMR ($CDCl_3$): 7.36 ppm, (s, 15H), 4.92 ppm (s, 5H), 2.95 ppm (t, 2H), 1.35 ppm (m, 2H), 1.13 ppm (m, 6H) and 0.77 ppm (t, 3H), ^{31}P NMR ($CDCl_3$): 71.0 ppm. IR (KBr): 1932 cm^{-1} and 1850 cm^{-1} (the two terminal CO), 1616 cm^{-1} (acyl CO).

3.4.3 Colloids preparation

MpC6 aqueous colloids (0.1 mg/mL; 178 μM) were prepared by adding 10.0 mL of distilled deionized water to a 1.0 mL THF solution of MpC6 (1.78 mM) under stirring. Subsequently, THF was removed via nitrogen bubbling for one and a half hour.

3.4.4 Critical water content (CWC)

DLS count rates were recorded while water is successively added to a THF solution of MpC6 (178 μM). The resultant data were plotted against water contents. A steep increase in the intensity was observed at the water content of 60 vol%; therefore, this point was assigned as CWC.

Chapter 4

Laser Manipulable Aqueous Fp-Bithiophene Vesicles with Aggregation-Induced Emission (AIE) and Aggregation-Enhanced IR Absorption (AEIRA)

4.1 Introduction

Supramolecular chemistry[133, 134, 135] aims to establish a knowledge system for nanomaterial innovation *via* investigation of the self-assembly behaviour of various building blocks and their aggregation-induced functions.[136, 137, 138, 139, 140] Based on the newly emerged field of metal carbonyl (MC) supramolecular chemistry,[47, 66, 118] we have designed and created highly-integrated, laser manipulable MC vesicles (MCsomes) with aggregation-induced emission (AIE) and aggregation-enhanced IR absorption (AEIRA).

MC complexes are potentially useful for a range of biomedical applications, including CO delivery due to their anti-inflammatory effects,[33, 34] antitumor activity due to their selective cytotoxicity,[35, 36] cell imaging[39] and bioassay[40] by taking advantage of the IR absorption of the CO groups within a biologically transparent window at wavelengths between 1800 and 2200 cm^{-1}.[37, 38] Their water solubility,[41] cell uptake ratio,[13] and IR absorption intensity[42] can be enhanced using colloidal chemistry.[141, 142] For example, a water-soluble CO-delivery system with a high cell uptake ratio has been developed *via* the incorporation of ruthenium carbonyl

complexes into a block copolymer micelle,[13] IR signals of the CO groups can be enhanced *via* surface enhanced IR absorption (SEIRA) by integrating MC compounds on the surface of plasmonic or dielectric nanoparticles.[42]

Aqueous MC colloids with light emission are highly desirable for promoting further study of the materials, because photoluminescent techniques have been well established and widely used for biomedical investigations.[143] However, photoluminescent MC colloids, unlike their organic counterparts,[144, 145, 146, 147, 148] cannot be readily achieved using fluorochromes, because most transition metal elements are fluorescence (FL) quenchers.[149, 150] To address this challenge, it is desirable to develop assembling techniques that enable spatial segregation of fluorochromes and MC complexes within the colloids.

We have initiated a study of MC supramolecular chemistry and discovered that hydrophobic Fp acyl derivatives, including small and macromolecules,[9, 10] are able to self-assemble in water, resulting in MCsomes. These colloids show no critical aggregation concentration (CAC) and exhibit high structural integration upon dilution. Water carbonyl interaction (WCI) is responsible for the colloidal stability.[9, 10] For example, FpC6 ($CpFe(PPh_3)(CO)CO(CH_2)_5CH_3$)[9] is able to assemble into a liposome-like bilayer structure with the alkyl chains aggregated within the membrane and the iron complexes associated on the surface. On the basis of this knowledge, we intend to design MC colloids with a FL readout. A spatial separation of the conjugated group from the MC complex can be expected, if the MCsome is assembled from an Fp

building block tethered to a conjugated system *via* an alkyl spacer. This separation will eliminate the quenching effect of the Fe elements.[149, 150] The crux of the design concerns the selection of an appropriate conjugated system. It is well known that the association of conjugated systems may result in aggregation-caused quenching (ACQ) *via* π-π interactions.[151, 152] In addition, strong π-π interactions, particularly those arising from planar polycyclic aromatic hydrocarbon,[153] may also disturb the balance of the forces responsible for the formation of MCsomes. With this concern in mind, bithiophene, a non-planar small conjugated system,[154, 155, 156] may minimize the possibility of π-π interaction. Although bithiophene groups are non-FL due to the intramolecular rotations of the thiophene units, AIE resulting from the restriction of intramolecular rotations (RIR), can be expected when the conjugated groups are aggregated in an ordered assembled nanostructure.[153]

In addition to the targeted FL readout, highly polarized MC groups with possibly large refractive index (RI) may endow the MCsome with novel properties that liposomes and polymersomes cannot achieve,[85, 86, 157, 158] such as aggregation-enhanced IR absorption (AEIRA) [9, 10] and optical manipulability. Optical trapping of nanosized vesicles (e.g. liposome) using focused near-IR laser beams is challenging.[159, 160, 161] The contribution of the difference in RIs between the lipid membrane (RI ~ 1.46) and water (RI = 1.33) to the gradient (trapping) force is negligible, because the membrane is too thin.[159, 160, 161, 162] Encapsulation of high refractive index additives, such as sucrose,[43] glucose, and NaCl,[162] to enhance the

trapping forces has been reported to address this challenge. The MCsome with polarizable MC groups may offer a high contrast in RI between the membrane and water, which is expected to enhance the trapping force substantially.[163] Manipulation of the MCsome without additives will, therefore, be possible. This expected advance will open up new opportunities to study the stability of the colloids,[93] cell membrane-related biological events[164] and their functions in drug delivery.[165, 166]

Herein, we report our innovation in the creation of functional MCsomes *via* the synthesis and self-assembly of a bithiophene tethered Fp derivative (FpC3BTh **(4.1**)). The building block is hydrophobic, non-surface-active, but is capable of assembly in water *via* WCI, resulting in a MCsome. The MCsome with a bilayer interdigitated membrane, as confirmed by a number of techniques, is highly integrated upon dilution. As designed, the MCsome possesses a number of functions, including AIE, AEIRA of the CO groups and capability of laser trapping without using additives. These novel functions and the unusual solution behaviour of the MCsomes[9, 10] represent a novel group of vesicles and open up a new research topic of MC supramolecular materials.

4.2 Results and discussion

4.2.1 Synthesis and solution behaviour of FpC3BTh.

The building block FpC3BTh, as designed, contains an iron carbonyl and a bithiophene unit connected *via* a butanoyl spacer. Figure 4.1a illustrates the synthetic approach for the targeted molecule. Detailed synthetic scheme and characterization are

described in the Supporting Information for Chapter 4 (Figure S4.1- Figure S4.4). The aqueous colloids of FpC3BTh are prepared through a fast injection of water into a THF solution of **1** followed by N_2 bubbling to remove THF (Figure 4.1b). DLS measurement reveals that the hydrodynamic radius (R_h) for the prepared colloids (154 μM) is ca. 85 nm with a narrow polydispersity index (PDI = 0.05).

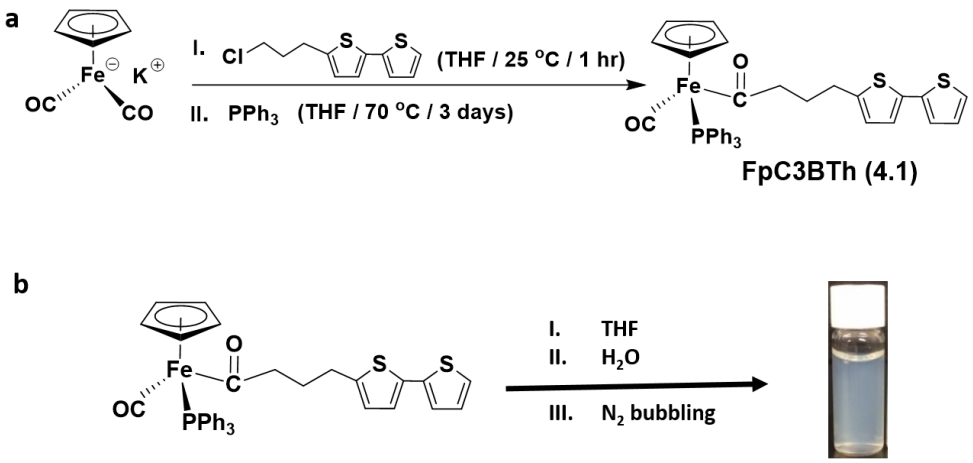

Figure 4.1 (a) Schematic illustration for the synthesis of FpC3BTh. (b) Aqueous solution of FpC3BTh (154 μM) prepared using THF as a co-solvent.

It is necessary to use an organic solvent (e.g. THF) as a co-solvent for the preparation, because FpC3BTh is neither soluble nor dispersible in water. This hydrophobicity of the building block is supported by the ^{1}H NMR spectrum of FpC3BTh in D_2O. As shown in Figure 4.2a, no protons corresponding to FpC3BTh are detectable; the signal at 4.7 ppm is due to the residual H_2O. Figure 4.2b illustrates that there is no obvious change in surface tension for the solutions as the concentration of FpC3BTh decreases, so FpC3BTh is non-surface-active.

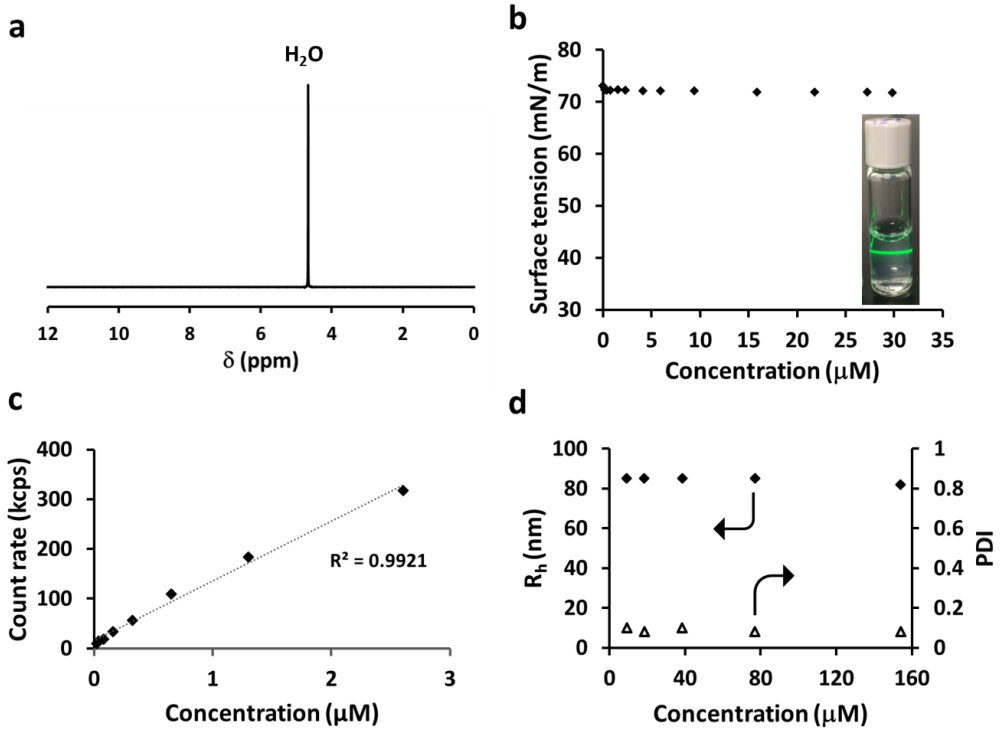

Figure 4.2 (a) ^{1}H NMR spectrum for the colloids of FpC3BTh in D_2O (154 μM). (b) Surface tensions of 1 in water with varied concentrations. (c) DLS count rates of the aqueous colloids of FpC3BTh as a function of concentration. (d) Hydrodynamic radii (R_h) and polydispersities (PDI) for the aqueous colloids of FpC3BTh with varied concentrations prepared by a successive dilution with water. Inset photograph in b is the aqueous solution of FpC3BTh (30 μM).

DLS count rates of the solutions as a function of concentration show a linear relationship (Figure 4.2c), and no CAC can be deduced from the figure. While we dilute an aqueous solution of FpC3BTh, there is no change in both R_h and PDI (Figure 2d). For all measurements, the R_h remains equal to 85 nm with PDIs lower than 0.10

(Figure 4.2d). Similar with FpC6,[118] these analyses suggest that FpC3BTh cannot be classified as a conventional amphiphile.[127] The Fp acyl derivatives therefore represent a new group of building blocks for the aqueous colloids without CAC.[66, 118] This feature renders the MC building blocks highly desirable for some applications, such as drug delivery, where traditional surfactant micelles encounter difficulties due to the disassociation of the micelles at concentrations lower than their CACs.[91, 93, 167, 168]

We have reported that WCI is a motif responsible for the aqueous self-assembly of Fp acyl derivatives that contains acyl and terminal CO groups.[66, 118] Water can readily hydrate the highly polarized acyl CO group, which balances the hydrophobic force for the formation of the colloids in THF/water upon aggregation at the critical water content.[118] The aggregation generates a local electric field, which further polarizes the CO groups. Consequently, the strength of the WCI is enhanced, resulting in an aggregation-induced hydration (AIH) of the terminal CO groups and an aggregation-enhanced hydration (AEH) of the acyl CO groups.[118] This knowledge was deduced from the IR analysis of the CO groups as a function of water content. A similar analysis has been performed for FpC3BTh and the results are illustrated in Figure 4.3. As shown in Figure 4.3, a red shift in wavenumber for the IR absorption ($\Delta\nu$) of the acyl CO group is observed as soon as water is added to the THF solution of FpC3BTh, whereas the IR absorption for the terminal CO group starts to shift only when the water content reaches 60 vol%. This comparison indicates that the acyl CO is more prone to hydration as expected.[118] When the water content reaches 80 vol%,

the Δν values (7.0 cm^{-1}) for the terminal and acyl CO groups are the same (Figure 4.3), suggesting that both CO groups have the same level of hydration. Supporting the previous results for the non-thiophene Fp analogues,[118,66] these results suggest that WCI between the Fp units and water play a crucial role in driving the self-assembly and colloidal stability (Figure S4.5). These findings can serve as a model system to understand the biological functions of WCI.[118, 10, 169, 170]

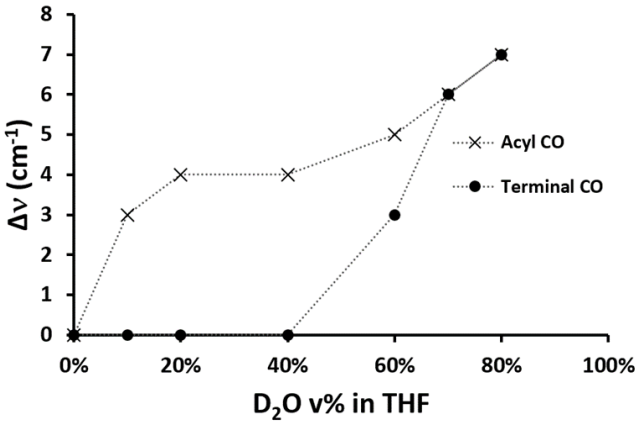

Figure 4.3 The red shifts (Δν) in wavenumber for the IR absorption of the terminal and acyl carbonyl groups from 1 in THF/D_2O solutions as a function of D_2O content.

4.2.2 Nanostructure of the MCsome

The radius of gyration (R_g) for the colloids of FpC3BTh is 83.6 nm, as measured using static light scattering (SLS) technique (Figure S4.6); while R_h, for the same sample obtained from DLS, is 87.1 nm. The shape factor (R_g/R_h) is, therefore, deduced to be ca. 0.96, supporting the conclusion that the molecule FpC3BTh self-assembles into a vesicles in water.[171] Conventional transmission electron microscopy

(TEM) technique has been attempted to image the colloid and a representative TEM image is shown in Figure 4.4a, from which lamellae are observed. The observed morphology may result from the breakage of vesicles. Atomic force microscope (AFM) was subsequently used to verify this conclusion. The AFM specimen was prepared *via* drying a few drops of the solution on a mica substrate. As shown in Figure 4.4b, lamellae were observed, which was consistent with the TEM analysis (Figure 4.4a). The section analysis reveals that the lamellae have an average vertical height of 3.72 ± 0.20 nm (Figure 4.4b and Figure S4.8), which represents the membrane thickness of the broken vesicle. Cryo-TEM confirms that the colloid is spherical (Figure 4.4c). The enlarged image (inset in Figure 4.4c) shows a dark periphery with a width of ca. 3.2 ± 0.7 nm. On the basis of the microscopy experiments, a bilayer membrane structure can be proposed because the fully extended length for FpC3BTh is ca. 1.9 nm (Figure 4.5a). To confirm the bilayer structure and the wall thickness of the MCsome, small-angle X-ray scattering (SAXS) using synchrotron radiation was performed.[172, 173] As shown in Figure 4.4d, although the signal intensity is low due to the low concentration of the sample (15.4 μM), a weak hump at q = 0.26 ($Å^{-1}$) is observed, corresponding to a domain spacing of 2.4 nm between the iron elements on the two sides of the membrane. The distance from the iron centre to the end of the bithiophene is ca. 14.25 Å (Figure 4.5a and Figure S4.9a); therefore, the bilayer with iron-to-iron distance of 2.4 nm suggests that the thiophene units are interdigitated, as illustrated in Figure 4.5b.

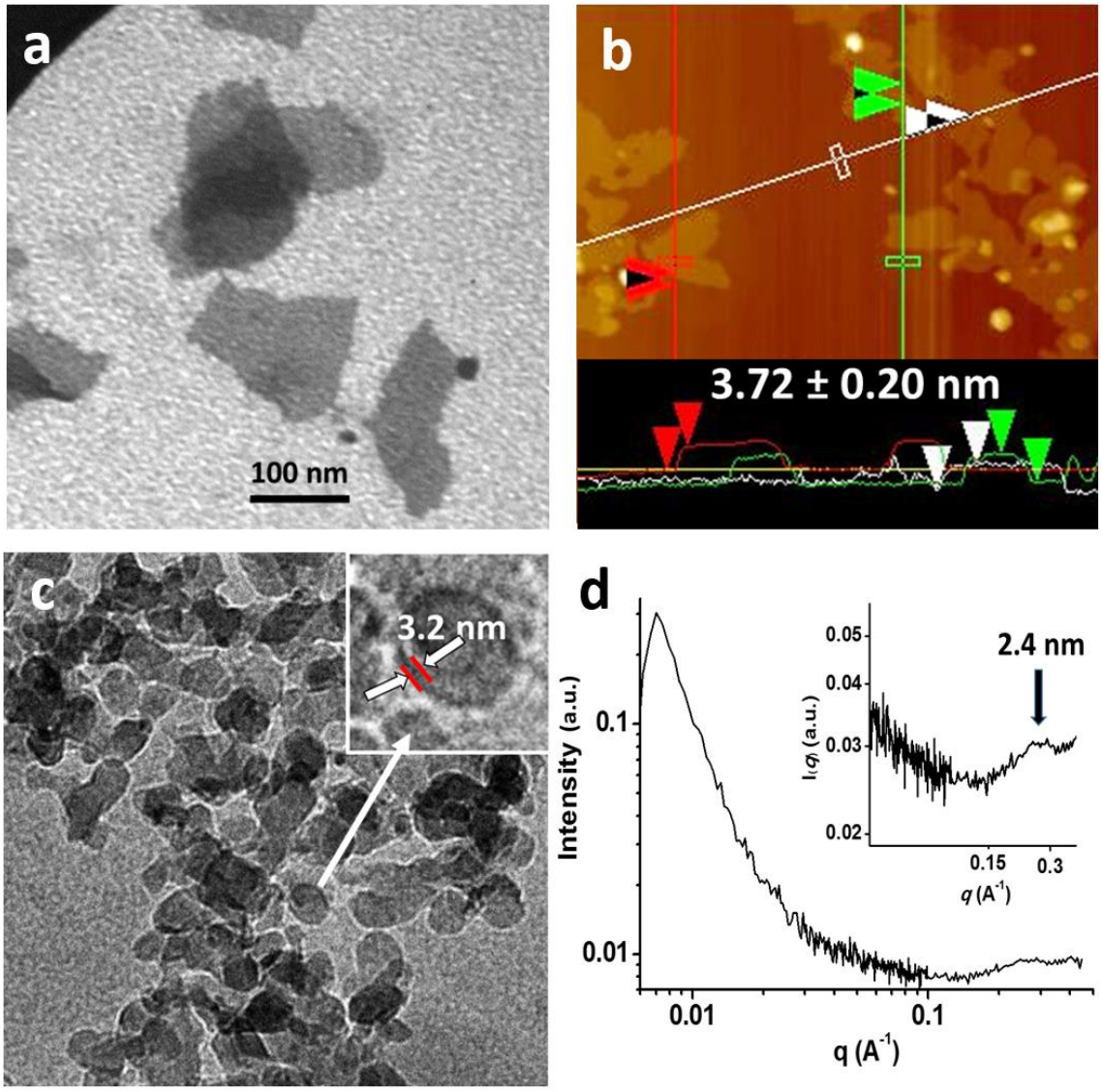

Figure 4.4 (a) TEM image, (b) AFM image with vertical section analysis and (c) cryo-TEM images for the colloids of FpC3BTh. (d) SAXS profile for the aqueous colloids of FpC3BTh (15.4 μM).

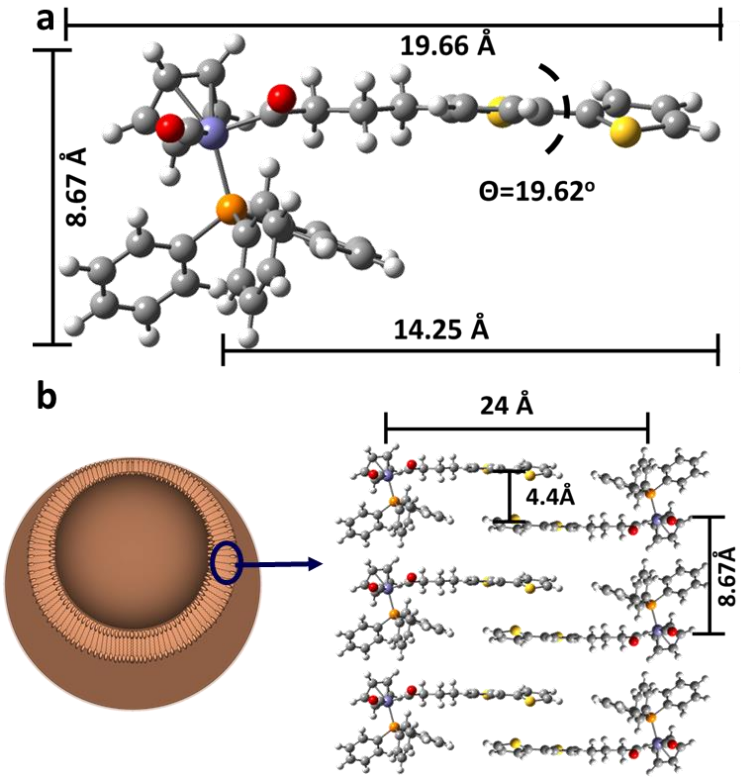

Figure 4.5 (a) Gaussian simulation results for molecular geometry of FpC3BTh. (b) Proposed interdigitated model for the bilayer membrane structure for the MCsome FpC3BTh.

The zeta potential (ζ) for the MCsome as measured is -55.5 mV, suggesting that the highly polarized CO ligands are packed on the surface of the vesicle and interacted with water via WCIs.[9, 10] CV experiments support this membrane structure with a MC surface. Figure 4.6 illustrates the CV curves for the solutions of FpC3BTh in DMF/water with varied water contents. In pure DMF solution, FpC3BTh is soluble and redox active due to the presence of Fe elements. Its CV curve reveals one oxidation peak at 0.61 V and one reduction peak 0.51 V (a in Figure 4.6). After water

is added, two oxidation peaks separated by a redox coupling ($\Delta E_{½}$) appears (b and c in Figure 4.6), suggesting that iron centers are associated closely to each other[103, 104, 105, 118] and accessible to the electrodes. This behaviour is similar to that observed for non-thiophene analogue FpC6.[118]

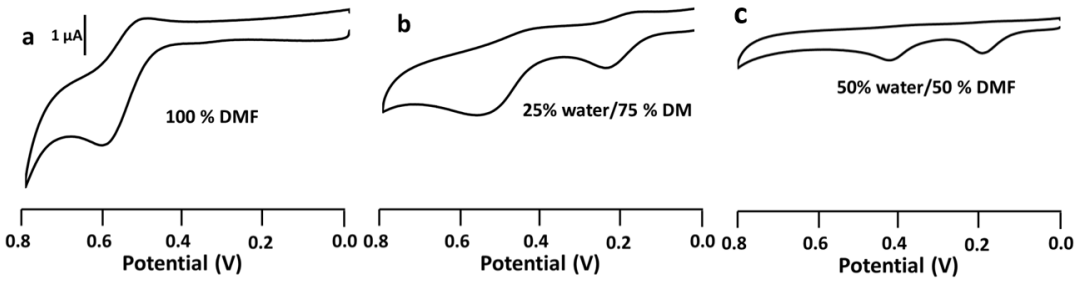

Figure 4.6 Cyclic voltammetry (CV) analyses, relative to Ag electrode, for the solutions of FpC3BTh in DMF/water with different water contents.

4.2.3 Aggregation induced emission (AIE) of the MCsome

The association of the bithiophene moieties within the inner walls of the bilayer vesicles restricts the intramolecular rotation of the thiophene units and, therefore, AIE is expected.[174, 175] As shown in Figure 4.7a, the MCsome in water emits blue FL when exposed to a UV light; whereas the molecule of FpC3BTh in THF does not emit light. The solid sample of FpC3BTh dried from the aqueous solution Figure 4.7b) also has no photoluminescence (Figure 4.7c). This comparison indicates that the bilayer assembly of FpC3BTh is crucial for the observed AIE (Figure 4.5b). The butanoyl spacer separates the conjugated system from the iron elements, which prevents the quenching of the emission.[149, 150] The solution emitted the strongest FL emission when

excited by the light with a wavelength of 360 nm (λ_{ex} = 360 nm). The intensity for the FL emission is decreased when λ_{ex} is lower or higher than 360 nm (Figure S4.10), but there is no obvious shift in the maximum emission wavelength (454 ± 2 nm) with λ_{ex} = 310-360 nm (Figure S4.10a). However, higher excitation wavelength generates multible emission peaks (Figure S4.10b). All the following experiments used an excitation waavelength λ_{ex} = 350 nm.

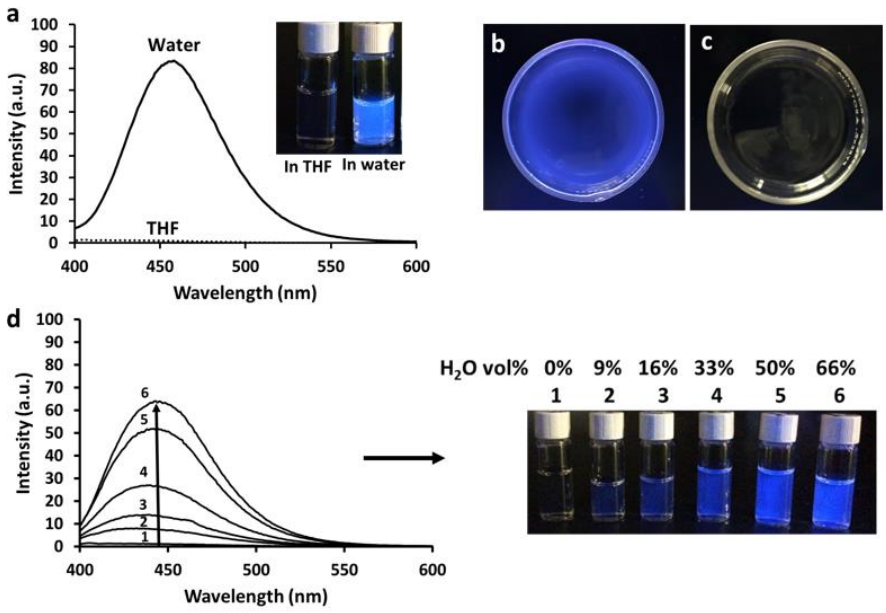

Figure 4.7 (a) Fluorescence emission spectra for the solutions of FpC3BTh (154 μM) in THF and water. Photographs for the water solution of FpC3BTh (b) before and (c) after drying. (d) Fluorescence emission spectra for the solutions diluted from FpC3BTh in THF (154 μM) by the addition of varied amounts of water. The photographs, including insets for (a), (b), (c) and (d), are taken when the samples are irradiated by a UV lamp (λ_{ex} = 350 nm).

FL spectra and photographs of the solutions in THF/water with varied amount of water, are illustrated in Figure 4.7d. As shown in Figure 4.7d, one may notice that the emission appears even for the solution containing a small amount of water (9 vol%). Without aggregation at this low water content (9 vol%), AIE might not be the reason for the emission. We, therefore, performed DLS experiments for a series of THF/water solutions with water contents varying from 0 to 100 vol%.

Figure 4.8a displays the light scattering count rate as a function of water content; the corresponding hydrodynamic radii (R_h) and FL emission intensities of the solutions are plotted in Figure 4.8b. As depicted in Figure 4.8a, a steep enhancement in count rate occurs at a water content of 60 vol%. However, the count rate starts to increase and micron-size aggregates are formed (Figure 4.8b) when the water content is only 9 vol%. Therefore, the emission at the low water content (9 vol%) can be attributed to the aggregation as well (Figure 4.7b). The aggregates gradually shrink from micron-size to 450, 190, and 85 nm, as the water content increases to 30, 60 and 100 vol%, respectively (Figure 4.8b). The RIR of the bithiophene groups is enhanced following this shrinkage, resulting in an enhancement in FL intensity as shown in Figure 4.8b. Meanwhile, there is no strong π-π interactions between the bithiophene groups, because no obvious red shifts in wavelength are observed for both emission and absorption spectra of FpC3BTh in THF/water with water contents less than 80% (Figure 4.7b and Figure S4.11). A slight red shift in the maximum absorption wavelength is observed from the UV-vis spectrum when the water content reaches 80

vol%, suggesting that the π-π interaction starts to form at a higher water content (Figure S4.11). However, this tendency is competed and supressed by the steric hindrance of the bulky MC groups (Figure 4.5),[153, 176, 177, 178] which minimizes the ACQ and RIR remains to be a major factor influencing the emission. Besides, the curvature of the vesicular bilayer may also reduce the possibility of a face-to-face packing of the bithiophene units and consequently prevents a strong ACQ.[151, 152, 179] Therefore, the AIE is obviously observed even in pure water (Figure 7a). The quantum yield (QY) for the aqueous colloid of FpC3BTh, as compared with 1, 4-bis(5-phenyloxazol-2-yl) benzene (POPOP) in cyclohexane,[180] is ca. 7.27 (see section S4.2 in the Supporting Information).

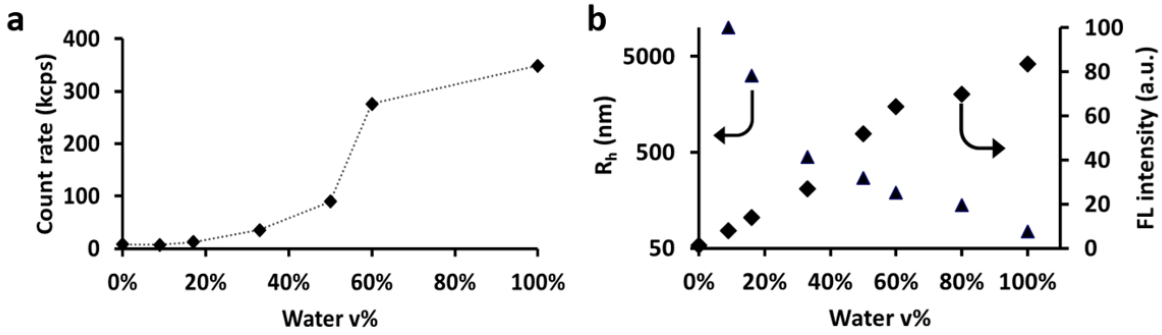

Figure 4.8 (a) DLS count rates, (b) Rh and FL fluorescence intensities for THF/water solutions of FpC3BTh as a function of water content.

The MCsome was able to emit light even when the solution was diluted to 4.8 μM (Figure 4.9a and Figure S4.12). These results agree with the DLS results

(Figure 4.2d) and suggest that the MCsome of FpC3BTh possesses high integrated structure and colloidal stability upon dilution. Furthermore, this AIE is also temperature sensitive. As shown in Figure 4.9b, the FL intensity deceases when the solution is heated. After cooling back to 25 ^{o}C, the original FL intensity is recovered. DLS analysis indicates that the diameter of the aggregates increases by 20 nm upon heating from 25 ^{o}C to 94 ^{o}C. Therefore, the reversible AIE can be explained by the variation of RIR resulted from the temperature-stimulated swellability of the MCsome.[181, 182] The uniform and high integrated MCsomes with temperature-sensitive photoluminescence are therefore potentially useful as drug delivery systems[183, 184] sensors and bioimaging probes.[185, 186]

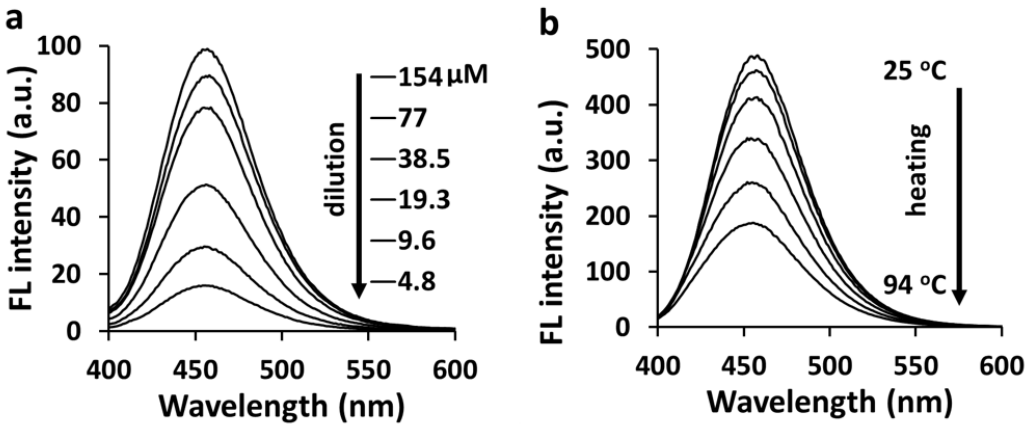

Figure 4.9 (a) FL emission spectra for the aqueous MCsome prepared by successive dilution of an aqueous colloid of FpC3BTh (154 mM). (b) FL emission spectra of the aqueous colloids of FpC3BTh (154 mM) measured at different temperatures (λex = 350 nm).

Similar to the THF/water solutions, the AIE phenomenum is also observed for the solutions of the MCsomes in dimethyl sulfoxide (DMSO)/water and acetonitrile (CH_3CN)/water (Figure S4.13). Meanwhile, by varying the pH of the solution from 3 to 10, there is no obvious change in the emission profile in terms of intensity and emission wavelength (Figure S4.14), so the MCsomes are potentially useful for biological applications.

4.2.4 AEIRA and laser manipulability of the MCsome

The high polarized MC surface of the MCsome endows the colloid with novel properties. It is well studied that the polarized nanoparticles, via interaction with incident light, are able to generate a strong local electromagnetic field applicable for SEIRA.[114, 115] Figure 4.10 displays the IR absorptions of the terminal CO group for the MCsome solutions in THF/water as a function of water content. As shown in Figure 4.10, although the concentration of FpC3BTh (154 μM) for all the solutions are the same, the IR absorption for the solution with 60 vol% of water is ca. 100 times stronger than those for the systems with lower water contents. This AEIRA is also observed for the MCsome assembled from other MC building blocks,[66, 118] supporting that this feature results from the MC groups. 100-fold enhancement in IR absorption has also been reported for the anthracene adsorbed on the surface of silicon carbide particles,[100] and is explained due to the phonon resonance effect caused by the dielectric surface.[100] Phonon resonance is analogous to the plasmon resonance of the coinage metal substrates, a basis for surface-enhanced Raman scattering (SERS)[132]

and SEIRA.[109, 110] It is, therefore, reasonable to think that the surface of the MCsome with tightly associated polarizable MC groups, behaves like dielectric substrates, responsible for the observed AEIRA. MCsomes possess a surface with polarized CO groups, which induce a local electric field with zetal potential of -55.5 mV. Upon irradiation of IR, the local electric field interacts with the electromagnatic field of the illuminated light and become stronger than that for incident light. This stronger electric field enhances the absorption intensity of the CO groups located at the surface of the MCsomes.[100, 114, 118] This enhancement is desirable and potential useful for bioassay and cell imaging.[42]

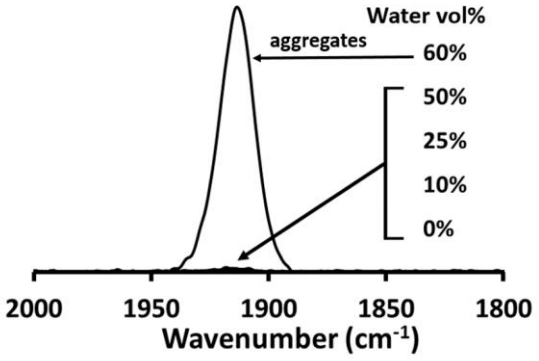

Figure 4.10 Partial ATR-FTIR spectra (terminal CO) for FpC3BTh in THF/water solutions with varied water contents.

The advent of the MCsome offers opportunities to address a challenge in vesicle studies using focused near-infrared (NIR) laser beams. It has been proposed that cell membranes can be studied *via* laser trapping of liposomes as model

systems.[187, 188, 189] However, despite several attempts, [46, 190] laser manipulation of nanosized liposomes with thin membranes remains challenging, due to the weak trapping force (see Section S4.1 in the Supporting Information).[159, 160, 161] Although the RI of the lipids (1.46) is different with that of water (1.33), the contribution of this marginal difference to the trapping forces is found to be negligible.[163, 191] The MCsome assembled from a highly polarizable MC building block may resolve this problem. Although the membrane for the MCsome is only ca. 3.7 nm thick, the RI for the building block (1.71 at λ = 633 nm) (Figure S4.15) is significantly higher than the RI of lipids (1.46) and water (1.33). The high contrast in RI between the membrane and water may result in a trapping force strong enough to trap the MCsome without using additives.[163, 192] Therefore, we performed the laser trapping experiments (Figure 4.11a). As shown in Figure 4.11b, the aggregation of the vesicles appears at the focal point after the solution of MCsome (77 μM) is irradiated with a focused continuous-wave near-IR (NIR) laser beam for 1 second. More MCsomes are attracted to the focal point by prolonging the irradiation time. The images taken at 3 and 6 seconds indicate that the aggregates become larger with improved contrast (Figure 4.11b). After irradiation for 6 seconds, the size of the aggregate remains constant, suggesting that the focal volume is fully occupied by the MCsomes and the laser trapping reaches the equilibrium state.

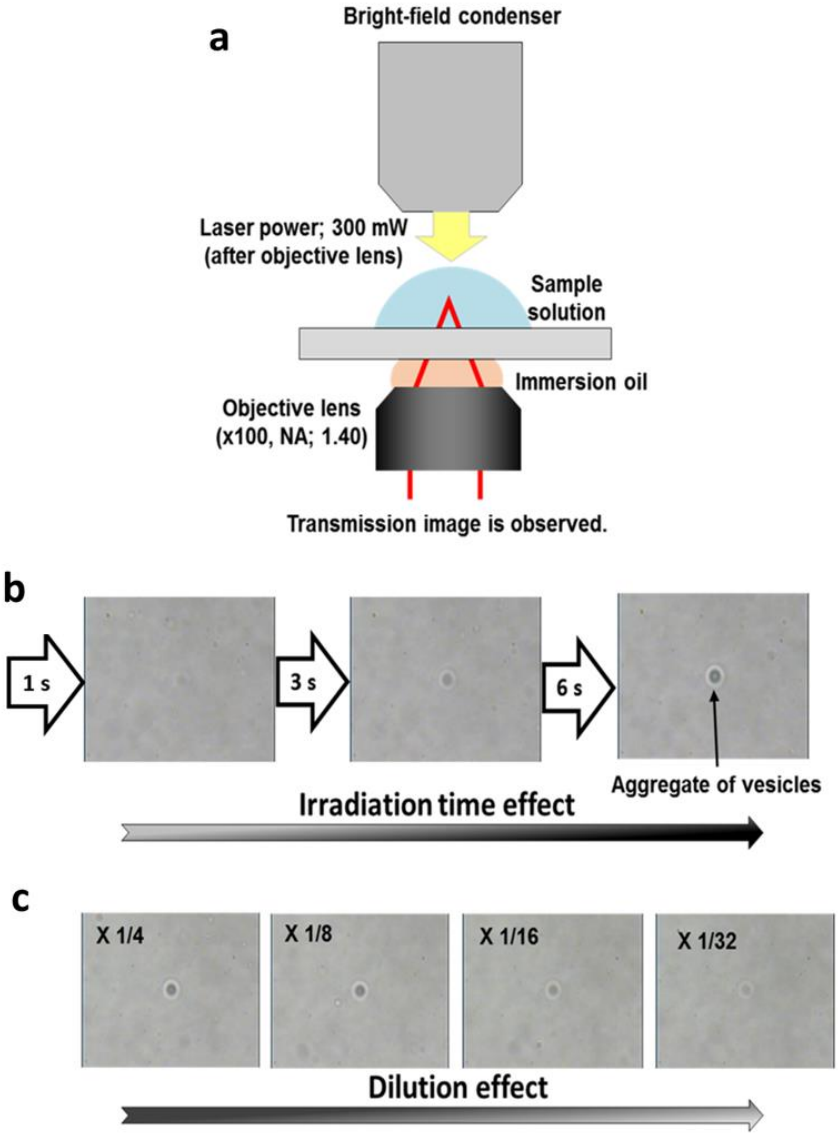

Figure 4.11 (a) Experimental set-up for laser-trapping experiment. (b) The charge-coupled device (CCD) transmission images of the trapped MCsome recorded at 1, 3 and 6 seconds. (c) CCD transmission images, taken at the equilibrium states, for samples diluted from the MCsome solution (77 μM) by 4, 8, 16 and 32 folds. The image size is 48 μm in width and 36 μm in height.

The aqueous solution of the FpC3BTh (77 μM) was subsequently diluted by 4, 8, 16, and 32 times for further experiments. The laser trapping reached equilibrium states after the solutions were irradiated for ca. 20, 35, 60, and 90 seconds, respectively (Figure 4.11c). As shown in Figure 4.11c, the MCsome, due to its high integration upon dilution, are trapped even for the sample with a concentration of 2.3 μM. It is also found that the gathered MCsomes can be moved arbitrarily following the beam and released upon turning off the trapping laser, which verify the success of the trapping experiments. Thus, the MCsome shows a good laser manipulability without additives that is difficult to be achieved for liposomes.[159, 160, 161]

4.3 Conclusions

Bithiophene-tethered Fp acyl derivative (FpC3BTh) is hydrophobic and non-surface-active, but is able to self-assemble in water into a metal carbonyl vesicle (MCsome). The MCsome is colloidally stabilized by WCI and highly integrated upon dilution. The bilayer membrane structure of the MCsome is confirmed by TEM, AFM, CV and SAXS experiments. The bithiophene component are aggregated within the inner wall of the interdigitated membrane and spatially separated from the MC groups associated on the surface of the MCsome, resulting in AIE. The aggregation of the polarizable MC component with a high refractive index endows the particles with novel functions, such as AEIRA and laser manipulability without using additives. The solution behaviour and the properties of the MCsome are unique and desirable as a new group of vesicular materials, complementary to the extensively studied

liposomes[193, 194, 195] and polymersomes[85, 86, 157, 158] for potential applications including nanoreactor,[10, 196, 197, 198] sensors[199, 200] and drug delivery systems.[11, 12, 201, 202]

4.4 Experimental section

4.4.1 Materials and Instrumentation

Potassium (99.5%, rods in mineral oil) and sodium (99.9%, cubes in mineral oil), cyclopentadienyl iron (II) dicarbonyl dimer (99%), 2, 2'-bithiphene (97%), benzophenone (99%) and 1-bromo-3-chloropropane (> 98.0%) were purchased from Sigma-Aldrich and used as received. Triphenylphosphine (98%) was purchased from Tokyo Chemical Industry (TCI) and used as received. Tetrahydrofuran (THF) was distilled over sodium/benzophenone before use. All other solvents were obtained from local commercial providers and used as received.

Dynamic light scattering (DLS) analyses were performed using Zetasizer Nano Series (Nano-S90, Malvern Instruments) with laser wavelength of 633 nm at a fixed angle of 90°. For THF/water solutions with varied water contents, the samples are prepared by successive additions of water to a THF solution of FpC3BTh (154 μM). The broadness of the size distribution (Polydispersity index (PDI)), in DLS results is calculated by the cumulants analysis from the ratio between the normalized variance of rate decay and the square value of the mean decay rate.Multi-angle SLS measurements were carried out using Brookhaven Laser Light Scattering System with a BI-200 SM goniometer. A vertically polarized helium−neon diode laser with

wavelength of 636 nm was used as the light source. Measurements were taken at scattering angles (θ) between 50° and 130° with 10° intervals. Toluene was used as the reference for the Rayleigh ratio. Zeta potential (ζ) measurements were performed at 25 ^{o}C on a Malvern Zetasizer nano ZS instrument using disposable folded capillary cells. Surface tension of pure water and the aqueous colloids of FpC3BTh with different concentrations were measured at 24 ^{o}C using a tensiometer Data Physics DCAT 21 system. Cyclic voltammetry (CV) experiments for solutions of **1** (154 μM) in water/DMF were performed at room temperature using DY2000 Multi-Channel Potentiostat (Digi-Ivy Inc.) workstation with a scan rate of 50 mV/sec and silver wire as a reference electrode. A water solution of KCl (2 mg/mL) and a DMF solution of tetrabutylammonium perchlorate (TBAP) (2 mg/mL) were prepared. FpC3BTh was then dissolved in the DMF solution and the water solution was subsequently added to prepare the solutions of **1** in the water/DMF mixture.

^{1}H and ^{31}P nuclear magnetic resonance (NMR) spectra were recorded on Bruker-300 (300 MHz) spectrometer at room temperature. ^{1}H NMR chemical shifts were reported relative to residual $CDCl_3$ signal and ^{31}P NMR resonances were referenced to an external standard sample of 85% H_3PO_4 (δ = 0.0). Attenuated total reflection-Fourier transform infrared (ATR-FTIR) spectra for the solid sample of FpC3BTh were recorded on a Bruker Tensor 27 spectrophotometer with a resolution of 1 cm^{-1}. Pellets of the solid samples of FpC3BTh were prepared by grinding and compressing of FpC3BTh (2% by weight) in anhydrous KBr using Nujol mulls. ATR-

FTIR spectra of FpC3BTh in THF/water solutions were recorded on the same instrument using a germanium crystal Pike MIRacleTM ATR Attachment using Pike Technologies. A drop of the solution was placed on the germanium crystal. IR absorption of the solutions of FpC3BTh in THF was measured first. Afterward, water was successively added to the THF solution and IR spectra were recorded at different water contents.

Conventional transmission electron microscopy (TEM) images were recorded on a low voltage (5 kV) LVEM5 electron microscope (Delong Instruments). TEM samples were prepared by dropping the solution onto a carbon-coated copper grid (Cu-300CN, Pacific rid Tech) and the grid was then left to dry at ambient temperature. Cryo-TEM images were obtained using a high voltage (200 kV) field emission FEI Tecnai G2 F20 Cryo-TEM microscope. The cryo-TEM samples were prepared by placing 5.0 µL aqueous solution of **1** (154 µM) onto a glow discharged copper grid with holey carbon film (Quantifoil Multi A) and thinned by blotting with a filter paper. The grid was then quickly plunged into a liquid ethane bath and transferred under liquid nitrogen to a Gatan 914 cryo-holder and viewed at -179 ^{o}C. Atomic force microscope (AFM) experiments were conducted on a Nanoscope MultiModeTM AFM microscope using a Conical AFM tip with a spring constant of 40 N/m, resonance frequency of 300 KHz and tip radius of 8 nm. The sample was prepared by transferring 2 drops of the aqueous colloids of FpC3BTh on freshly cleaved mica substrate.

Steady-state fluorescence emission spectra were recorded using a Cary Eclipse Fluorometer. A conventional quartz cell with light path of 1 cm was used for the solution samples. The solutions were excited at 350 nm. UV−vis absorption spectra were recorded on a Varian (Carey 100 Bio) UV−vis spectrophotometer using a quartz cuvette with a path length of 1 cm. Refractive index was executed using a J.A. Woollam Co. VASE® ellipsometer. The data was acquired at angles of incidence of (55°, 60°, 65°, 70°, 75°) with spectral range from 1700 to 400 nm. The measurement was performed for a thin film prepared by spin-coating of 5 w% solution of FpC3BTh in toluene on a silicon waver (Figure S4.15).

The SAXS data was acquired at Beamline 23A1 in the National Synchrotron Radiation Research Center (NSRRC), Taiwan. The energy of the X-ray source and the sample-to-detector distance were 15 keV and 2977.4 mm. The aqueous solution of FpC3BTh (15.4 μM) was introduced into a sample cell consisting of two Kapton windows. To collect the scattering signals, a two-dimensional MarCCD detector with 512 x 512 pixels resolution was used. The SAXS profile was corrected for the empty cell beam scattering, sample transmission, and detector sensitivity. The domain spacing (d) was calculated by $d = 2\pi/q_m$ (q_m: the position of the primary scattering peak). The q range of the small-angle X-ray scattering (SAXS) measurement is between 0.008 to 0.40 $Å^{-1}$ (d = 78.5 - 1.6 nm). Since the R_h of the colloids of FpC3BTh (87.1 nm) is above the detection upper limit, the SAXS data was used to estimate the wall thickness of the MCsome. Quantum-chemical calculations were

performed with the Gaussian09 suite employing the DFT calculations (B3LYP/6-311G). Geometry optimizations were performed with tight SCF and convergence criteria.

For laser trapping experiments, a small amount of the sample solution was put onto a glass substrate (Matsunami, micro cover glass, thickness; 0.12–0.17 mm) placed on the stage of an inverted microscope (Olympus, IX71). A 1064-nm continuous-wave near-infrared laser beam (Spectra Physics, J20I-BL-106C, λ = 1064 nm) was used as the trapping light source and was focused at a position of a few tens of micrometers above the glass through an objective lens (100 magnification, NA = 1.4, oil immersion). The laser power was fixed to 300 mW after the objective lens by adjusting a half-wave plate placed in front of a polarizing beam splitter. The trapping behaviour was observed with a charge-coupled device (CCD) camera (WATEC, WAT-231S2) under halogen-lamp illumination. Laser trapping theory is described in Chapter S4 in Supporting Information.

4.4.2 Synthesis of FpC3BTh (4.1)

5-[3-chloropropyl]-2,2'-bithiophene (**4.3**) was prepared as follow. *n*-butyl lithium (*n*-BuLi) (5.41 mmol) was added dropwise to a solution of 2, 2'-bithiophene (1 g, 6.01 mmol) in THF (100 mL) at -78°C under an atmosphere of dry nitrogen. After stirring for 0.5 hr at -78 °C, 1-bromo-3-chloropropane (595 μL, 6.01 mmol) was slowly added. The reaction mixture was then warmed gradually to room temperature and stirred overnight. The solvent was removed by rotary evaporation and the residue

was subsequently purified using column chromatography on silica gel with hexane as the eluent (yield 0.684 g, 47%). ^{1}H NMR ($CDCl_3$, 25 ^{o}C, 300 MHz) δ (ppm): 2.14 (q, 2H; middle -CH_2-), 2.98 (t, 2H; BTh-CH_2-), 3.59 (t, 2H; -CH_2-Cl), 6.73 (d, 1H; BTh), 7.00 (m, 2H; BTh), 7.11 (d, 1H; BTh), 7.17 (d, 1H; BTh). Detailed synthesis scheme is illustrated in Figure S4.1 and the ^{1}H NMR spectrum of **4.3** is shown in Figure S4.2 in SI.

The purified molecule **4.3** (0.684 g, 2.82 mmol) was then added to a solution of Fp anion (0.67 g, 3.10 mmol) in THF (50 mL) at 0 ºC under vigorous stirring (Figure S4.1). The mixture was stirred at room temperature (23^{o}C) for 1 hour. Triphenylphosphine (0.81 g, 3.10 mmol) was then added to the mixture and subsequently was refluxed at 70 ºC for 72 hours. Afterward, the solution was cooled to room temperature and THF was removed under vacuum. The resulting gold-brownish solid was chromatographed using a silica column with hexane/DCM (2/1 v/v) as the eluent. The solvents were removed using rotary evaporation resulting in a brownish foam-like product of FpC3BTh (yield 1.45 g, 79 %). ^{1}H NMR ($CDCl_3$, 25 ^{o}C, 300 MHz) δ (ppm): 1.35 (m, 2H; middle -CH_2- from the spacer), 2.41 (t, 2H; BTh-CH_2-), 2.67 (m, 1H; -CO-CH_2-), 2.90 (m, 1H; -CO-CH_2-), 4.41 (s, 5H; Cp ring), 6.57 (d, 1H; BTh), 6.9-7.0 (m, 2H; BTh), 7.07 (d, 1H; BTh), 7.14 (d, 1H; BTh) 7.37 (s, 9H; *o*- and *p*-Ph), 7.49 (t, 6H; *m*-Ph). ^{31}P NMR ($CDCl_3$, 25 ^{o}C, 300 MHz) δ (ppm): 77.4. FT-IR (KBr pellet, 25 ^{o}C): 1600 cm^{-1} (acyl C=O), 1905 cm^{-1} (terminal C≡O). The ^{1}H, ^{31}P

NMR and FT-IR spectra of FpC3BTh are shown in Figure S4.3 and Figure S4.4 in Supporting Information.

4.4.3 Self-assembly of FpC3BTh

The aqueous colloids of FpC3BTh (154 μM) were prepared by fast addition of 10.0 mL distilled deionized water to 1.0 mL THF solution of FpC3BTh (1.0 mg/mL, 1.54 mM)) under stirring. THF was then removed through nitrogen bubbling for 90 minutes. A same experiment was performed in D_2O and examined using ^1H NMR, which suggested THF is completely removed.

Chapter 5

Colloidal Structure-Related Hydrophobic Hydration for the Stability of the Aqueous Assemblies of Hydrophobic Fp Derivatives

5.1 Introduction

The hydration of hydrophobic biomolecules is important for biological activity.[2, 203] For example, before reaching the critical level of hydration, proteins lack biological activity.[203] In addition to the hydrophobic interaction between hydrophobic side chains,[59, 204, 205] protein conformation and dynamics are driven and controlled by the surrounding water network.[206, 207] The stability of proteins in water is structurally related to the hydrophobic hydration of the core and surface.[208, 209, 210, 211] For example, water molecules buried in folded three-dimensional proteins play a crucial role in maintaining the protein stability by bridging the folded chains via hydrogen bonding.[210, 211]

Studies have extensively investigated the hydrophobic interaction and hydration of surfactants using calorimetric, spectroscopic and computational techniques.[70, 71, 212] Similar to proteins, the hydrophobic interaction and hydration are responsible for the solubilization and aggregation of surfactant hydrophobic tails.[70,72] Various techniques, including NMR,[213] neutron scattering,[78] and molecular dynamics (MD) simulations,[77, 78] have been used to investigate the aggregation of the hydrophobic tails. The association of hydrophobic tails is generally considered to generate a central dry hydrophobic core with a smooth spherical surface.[79, 80] However, the structure of micellar cores remains a matter for exploration.[74]

Based on the Menger model for the micellar surface, in addition to the hydration water at the micelle surface, a network of water molecules penetrates deeply into the hydrophobic core.[81, 82, 214] This model was recently supported by Ben-Amotz *et al.* using Raman spectroscopy analyses of aqueous solutions of surfactants with various chain lengths.[74] Based on their investigation, water molecules are wedged into hydrated cavities, penetrating deeply into the core.[74] However, systematic studies on the correlation of surface structure with colloidal stability are not well established yet.

As known from our previous studies on FpC6 and other analogues,[66, 118, 119, 215] the acyl CO group is highly polarized and its interaction with water occurs right after the addition of water to the THF solution of FpC6. Although these molecules are hydrophobic and not surface active, the water carbonyl interactions (WCI) provides solubilization of these molecules.[95, 118, 216] The aggregation starts at a critical water content (CWC).[118] For example, FpC6 molecules start to assemble at a CWC of ca. 60 vol% into vesicles driven by the hydrophobic association of the alkyl tails.[72, 118] The aggregation of the polar acyl CO groups, at the colloid surface, generates a local electric field, which is supported by the observation of aggregation-induced enhancement in the IR absorption of the CO groups.[66, 118, 119, 215] The local electric field further polarizes the CO groups, thus initiating hydration of the terminal CO groups and enhancing hydration of the acyl CO groups, as verified by the attenuated total reflectance-Fourier transform infrared (ATR-FTIR) analysis.[66, 118] The association of the CO groups at the colloid surface provided a negative surface charge and strong WCI, which therefore contributed in the colloidal stability. The electrochemical study of the FpC6

molecule in water/DMF solutions, with varied water contents, revealed that the association of the iron metals, upon aggregation, provides cyclic voltammetry (CV) curves with two oxidation peaks separated by a redox coupling ($\Delta E_{1/2}$).[118] It is reported that CV experiments for polyferrocenyls also revealed two oxidation peaks, separated by $\Delta E_{1/2}$, which is inversely proportional to the distance between the adjacent ferrocenyl units along the polymer chain.[104, 105] Taking the advantage of the redox properties of the Fp head at the micelle surface, in this chapter, we systematically studied the surface and core structure of the aqueous assembles of Fp-derivatives and correlated the surface structure with the stability of colloids.[15, 17, 28]

Herein, we report an experimental study of the aggregation process of Fp-derivatives with various alkyl chain lengths and correlate their colloidal stability with the surface and core structures. We monitored colloidal stability over time using dynamic light scattering (DLS) measurements. The results revealed that the colloidal stability increases as the alkyl chain length increases. The trend in the stability was then investigated, based on the contribution of CO groups, alkyl chain length, and the colloidal morphology using CV, ATR-FTIR, and static and dynamic light scattering (SLS/DLD) measurements. The contribution of CO groups was first investigated and showed similar contribution for all the molecules regardless of the of alkyl chain length. The effect of the alkyl chain length was then investigated based on CV and ATR-FTIR experiments. Longer alkyl tails provided more intermolecular hydrophobic interaction, however, remained more hydrated, and exposed to

the water. Colloidal size and morphology were then studied and correlated with the trend in stability.

5.2 Results and Discussions

5.2.1 Synthesis and aqueous self-assembly

FpCn acyl derivatives **5.1**-**5.7** (FpCn; n: number of carbons in the alkyl chain) were synthesized via the migration insertion reaction (MIR) of Fp alkyl derivatives in the presence of triphenyl phosphine (PPh_3) (Figure 5.1).[47, 118] The molecules have been well characterized using ^{31}P NMR, ^{1}H NMR, and FT-IR spectroscopies (see Supporting Information for Chapter 5). Synthesis and characterization were performed similar to that reported for FpC6 in the Experimental Section in Chapter 2.

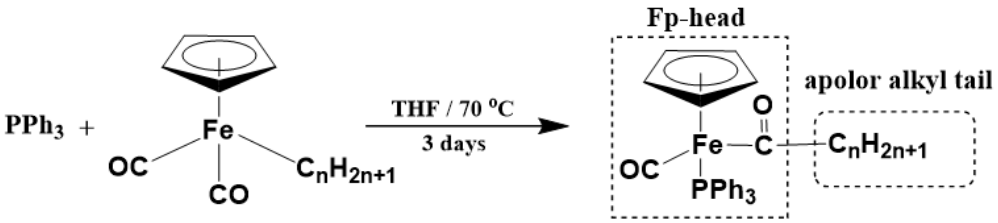

molecule	5.1	5.2	5.3	5.4	5.5	5.6	5.7
n	1	5	6	8	10	14	18
	FpC_1	FpC_5	FpC_6	FpC_8	FpC_{10}	FpC_{14}	FpC_{18}

Figure 5.1 Synthesis and chemical structures of the Fp-derivatives **5.1** – **5.7**

All of the molecules **5.1**-**5.7** are hydrophobic and have no surface activity as proved by surface tension measurements.[26, 27, 28] Based on our previous studies, FpC6 was able to

assemble into vesicles in water and the water-carbonyl interaction (WCI) was identified as one of the forces accounting for the stability of the colloids. To explore the collective forces that drive the assembly and stabilization of the colloids, the aqueous solutions for FpCn with various alky chain lengths were prepared. The resultant solution of **5.1** (FpC1) was cloudy and had a D_h of ca. 270 nm with PDI of 0.80, as characterized by dynamic light scattering (DLS). Precipitates were observed a few hours after the preparation (Figure S5.6); while solutions for other molecules, with longer alkyl tail, scattered light suggesting that the colloids were formed (Figure S5.6). The critical water contents (CWCs) for all FpCn including FpC1 in THF/water mixture were similar (ca. 60 ± 5 vol%) and irrelevant of the length of alkyl chain. The alkyl fragments, as we tested for alkyl chains without Fp head, started to phase separation in THF/water at water content of ca. 20 ± 5 vol%. The Fp acyl head, due to the hydration of the acyl CO group,[95, 118, 216] is therefore responsible for the solubility of FpCn in the system with a higher water content. It was interesting to notice that the aggregates, formed from more hydrophobic FpCn, with longer alkyl tails (n = 5 - 18), form more stable colloids than those assembled from FpC1 (Figure 5.2 and Figure S5.6). This is an opportunity to explore the effect of the hydrophobic hydration on the colloidal stability.

To evaluate the relative stability of the colloids, the hydrodynamic diameter (D_h) of the FpCn colloids as a function of aging time was monitored using DLS. As shown in Figure 5.2, the FpCn (n = 5, 6, 8, 10) colloids grow in size over time and eventually precipitate. The precipitates are observed at the 2^{nd}, 7^{th}, 15^{th} and 30^{th} day, after the

preparation of FpC5, FpC6, FpC8 and FpC10 aqueous solutions, respectively (arrows in Figure 5.2). It is clear that the aggregates assembled from the molecules with longer alkyl tails are actually more stable. This claim is further supported by the solution behaviour of FpC14 and FpC18. These two colloids in water are extremely stable and no precipitation is observed even after 3 months. This stability as a function of the length of the hydrophobic alkyl tail contradicts the commonly accepted concept of the hydrophobic hydration.[71, 72, 73] The longer alkyl chain length is supposed to be more hydrophobic and consume more unfavorable hydration energy, which should promotes the hydrophobic interaction and phase separation and therefore resulting in a lower stability.[17, 74, 217] Our unusual experimental results may result from the assembled structure-correlated hydrophobic hydration as often found in protein systems.[208, 209, 210, 211]

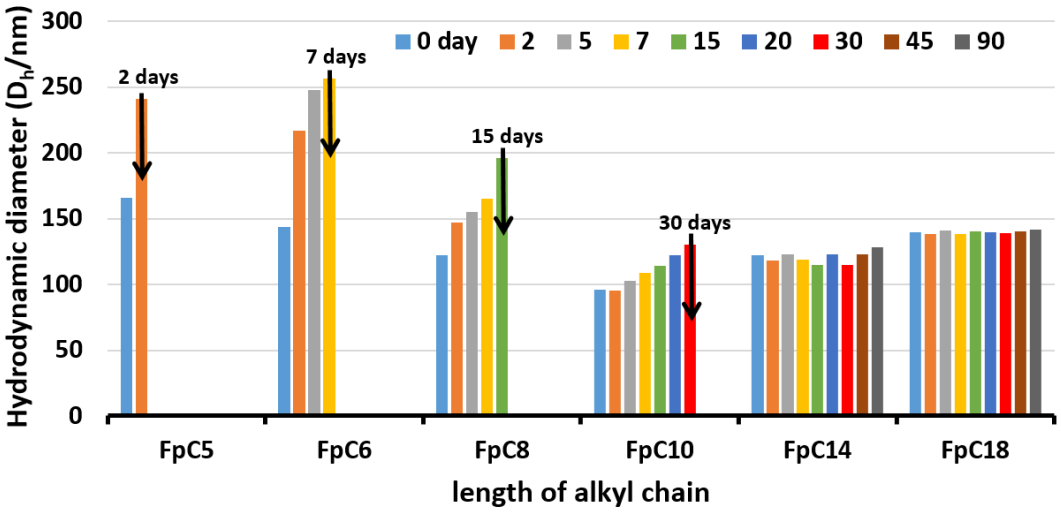

Figure 5.2 DLS results of aqueous solutions (0.1 M) of Fp-derivatives with different alkyl chain length as a function of aging time. The inset arrows and data labels depict the time where colloids starts to precipitate.

The WCIs of the CO groups contribute to the stability, as we have reported before in Chapter 2.[95, 118, 216] The strength of the WCI was evaluated using FTIR analysis for the aggregates in THF/water (66 vol%). FTIR stretching frequencies for both acyl and terminal CO groups are similar for all solutions (Figure S5.7), suggesting that the WCI is similar for all colloids and the contribution of the hydration of CO groups to the stability is similar regardless of the alkyl chain lengths. Therefore, we focus our attention on the effect of the hydrophobic alkyl chains.

5.2.2 Alkyl chain length and stability

Recently, Ben-Amotz studied the micellar core structure of micelles, prepared from surfactants with various alkyl chain lengths, using Raman spectroscopy with multivariate curve resolution experiments,[74] which indicated that the micellar core formed from the hydrophobic alkyl chains in the surfactants, was highly hydrated. Therefore, hydration cavities penetrated deeply into the cores. For the FpCn colloids with the Fp acyl heads exposed to water, the redox activity of the iron elements can be used to probe the hydration cavity in the hydrophobic core. FpCn molecules in DMF show a reversible redox cycle due to the iron element. Upon the aggregation, the redox cycle becomes irreversible probably due to the adsorption of the colloids on the electrode. Nevertheless, two oxidation potentials separated by a redox coupling ($\Delta E_{½}$) are observed (Figure 5.3). Using the knowledge previously reported for polyferrocenyls,[104, 105] this $\Delta E_{½}$ value is inversely proportional to the distance between the adjacent Fp acyl heads (Ls).[104, 105] Thus, this Ls represents the size of the hydrated cavity (Figure 5.3).

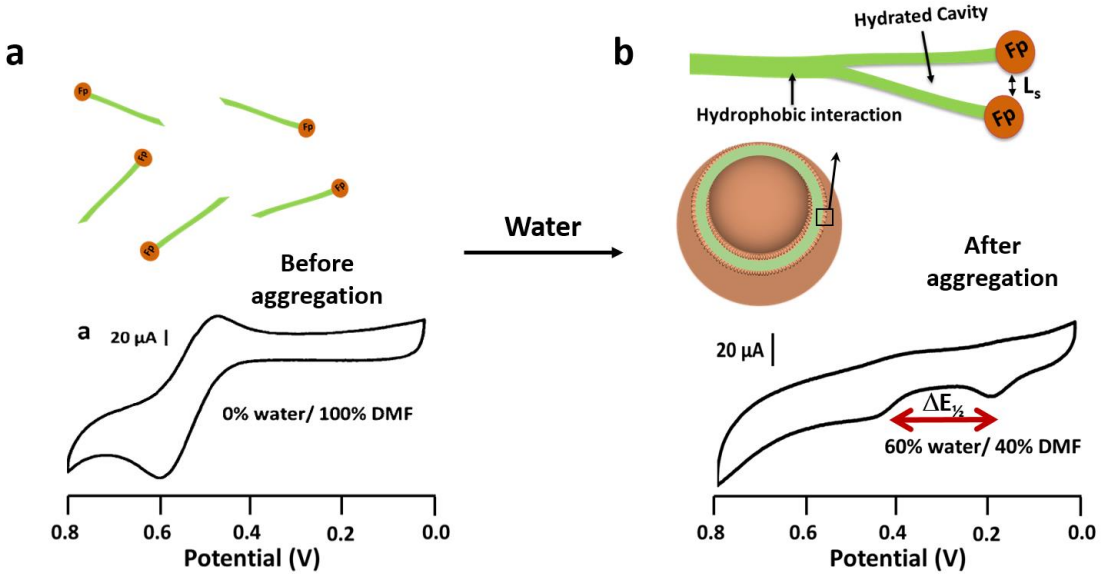

Figure 5.3 Representative cartoon illustration and CV results for Fp-derivatives in DMF solution (before aggregation) and in DMF/water solutions (after aggregation).

Figure 5.4 displays the $\Delta E_{1/2}$ values for the FpCn aggregates with various length of alkyl tails in water/DMF (60 vol% of water). As shown in Figure 5.4, following the increase in the length of the alkyl chain, $\Delta E_{1/2}$ decreases. This result suggest that the FpCn molecules with longer alkyl tails assemble into colloids with larger Ls and thus larger hydration cavities, which is in line with what has been reported by Ben-Amotz.[74] The larger cavity size allows for a deeper penetration of water into the hydrophobic domain, which favours the formation of a water network to suspend the particles and compensate the energy required for the hydrophobic hydration. This could explains why FpCn molecules with longer hydrophobic tails form more stable colloids.

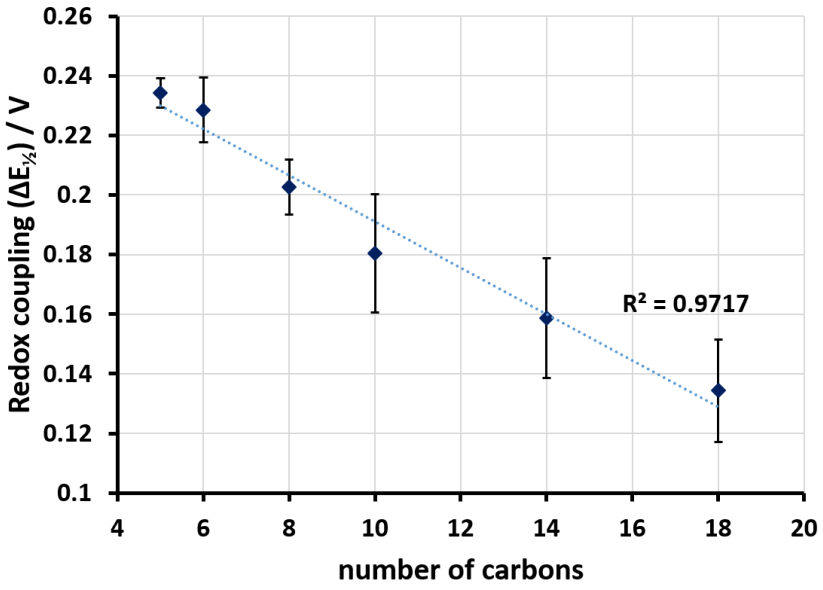

Figure 5.4 Redox coupling ($\Delta E_{½}$), revealed from CV measurements, as a function of alkyl chain length of Fp-derivatives **5.2**-**5.7** in DMF/water solution (60 vol% of water). Error bars represent standard deviation calculated from five repeated experiments.

The formation of the hydration cavity is further supported by FTIR experiments. Figure 5.5 illustrates the IR spectra of FpC18 molecules in THF and their aggregates in THF/D_2O solutions. As shown in Figure 5.5, the absorption at 2978 cm^{-1} is due to asymmetric stretching of the terminal CH_3, while the peak at 2867 cm^{-1} is assigned to the symmetric stretching of CH_2.[217, 218, 219] The asymmetry stretching of the CH_2 shows a weak absorption at 2923 cm^{-1},[217, 220] suggesting that the alkyl chains are conformational disordered.[221] This is reasonable because the molecule is well dissolved in THF. However, upon the aggregation of FpC18 in THF/D_2O solution, an absorption peak at 2923 cm^{-1}

appears resulting from a higher trans/gauche bond ratio in the alkyl chain.[221] This is an indication that the alkyl chains are extended, which contributes to the formation the hydration cavity with a water-accessible "wedge" deep into the central hydrophobic core. Figure 5.5 also shows that the absorption peak at 2867 cm^{-1} is shifted to 2860 cm^{-1} when FpC18 molecules associated in THF/D_2O solution. This shift to lower frequency is caused by the packing of alkyl chains due to hydrophobic interaction.[217, 222, 223, 224] This result suggests that both hydrophobic hydration and hydrophobic interactions occur for the octadecyl chain.

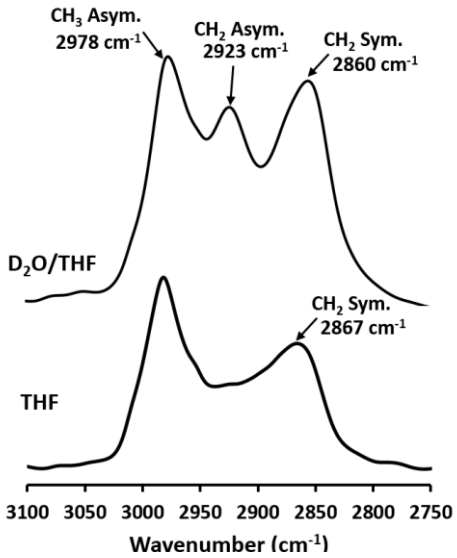

Figure 5.5 ATR-FTIR spectra (C-H stretching region) for FpC18 in THF and THF/D_2O with 60 vol% of D_2O.

The shift toward a lower wavenumber for the symmetric stretching of CH_2 becomes smaller with decreasing alkyl chain length. However, no shift in CH_2 stretching frequency has been observed for FpC5 upon aggregation in D_2O/THF solution (Figure S5.8), suggesting

that the hydrophobic interactions between the pentyl chains are very week. This weak interaction explains the low stability of the FpC5 colloids (Figure 5.2). On the other hand, as shown in Figure S5.8, the red shift of the absorption at 2867 cm^{-1} due to the hydrophobic association occurs to all other FpCn. The shifts are relatively weak for FpC6, FpC8 and FpC10 (less than 3 cm^{-1}) and obvious for FpC14 and FpC18 (larger than 6 cm^{-1}). These results suggest that the balance of the two interactions, hydrophobic hydration and hydrophobic interactions, is related to the nanostructure of the assemblies with their stability.

The relative degree of these two interactions for the aggregates of FpCn in THF/D_2O (60 vol% of D_2O) is compared in Figure 5.6. As shown in Figure 5.6, upon aggregation, the enhancement in the absorption at 2923 cm^{-1} due to the hydration is barely observed for FpC6, but becomes detectable for FpC8 and FpC10 and more obvious for FpC14 and FpC18. Therefore, it is clear that both intra-aggregate hydrophobic interaction and the hydrophobic hydration, in the hydration cavity, are weak for the aggregates assembled from FpCn with shorter alkyl tails. On the other hand, the longer alkyl chains exert a stronger hydrophobic interaction, which integrates the FpCn molecules. Meantime, as revealed from the FTIR and CV analysis, this association creates larger hydration cavities that promote the hydrophobic hydration. The alkyl group in FpC1 is too short to associate into a hydration cavity and thereby tend to precipitate after several hours (Figure S5.6). FpCn (n = 5 – 10) molecules are able to assemble into defined aggregates with hydration cavities that strengthen the hydrophobic hydration. However, the hydrophobic interaction of the alkyl chains within the colloids is not strong enough to maintain the aggregates. As a result, the aggregates tend to

agglomerate driven by the hydrophobic interaction between the colloids to lower the total energy of the system. On the other hand, the stability of the colloids assembled from FpCn molecules with the longer alkyl tails (n = 14, 18) is attributed to the balance between both the strong hydrophobic interaction and hydration within the colloids. This analysis, with the consideration of the structure of the assemblies, explains the effect of the length of the alkyl tails on the stability of the FpCn colloids.

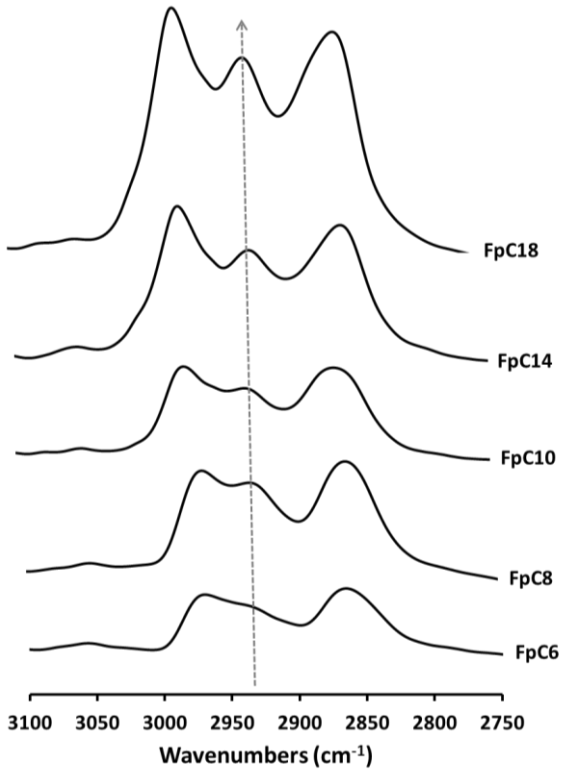

Figure 5.6 ATR-FTIR spectra (C-H stretching region) Fp-derivatives different alkyl chain length in 60 vol% D_2O in THF solutions. The arrow shows the trend in increasing in the absorption intensity for the asymmetric CH_2 stretching with increasing of the alkyl chain lengths.

5.2.3 Morphology and stability

The effect of the structure on the stability is further discussed by taking into account the morphology and size of the aggregates. Several Fp acyl derivatives, including FpC6, are able to self-assemble into vesicles. To investigate the morphology for the aggregates assembled from FpCn, with various length of alkyl tails, static and dynamic light scattering experiments were performed. The R_g/R_h for the colloids is illustrated in Table 5.1. As shown in Table 5.1, the R_g/R_h is ca. 1.0 for the aggregates assembled from FpC6, FpC8 and FpC10, suggesting that vesicles are formed. The vesicular morphology for FpC6 colloids has been reported before (Chapter 2). The cryo-TEM images for FpC10 colloids also reveal the similar vesicular morphology (Figure S5.9). At the same concentration (0.1 M), the D_h for the vesicles decreases with the increase in the length of alkyl tails (Table 5.1). The trend in the size of vesicles is inversely related to their stability trend. Smaller vesicles tend to be more stable, whereas the surface of larger vesicles is extended with a low curvature. The smaller particles with a higher curvature require fewer hydrogen bonds and are therefore more stable.[72, 73]

On the other hand, the colloids assembled from FpC14 and FpC18 are more stable, although their D_h is relatively larger. SLS/DLD analysis indicates that the R_g/R_h for these two assemblies is ca. 1.50, suggesting that Gaussian chains may be formed (Table 5.1). Although it is impossible to reveal the detailed structure of Gaussian chains, we have performed cryo-TEM to image the overall shape of the aggregates. As shown in Figure S5.9, the colloids appear to be particles with deformed spherical shapes, reminiscent of images for globular

proteins. The average size of the particles is ca. 150 ± 20 nm, which is similar with the D_h of the colloids. The conventional TEM image of the colloids dried on a copper grid shows that the particles tend to fuse into one dimensional structures with width of ca 100 ± 15 nm (Figure S5.9). Although the detailed structure of the assemblies cannot be revealed, the SLS/DLS and TEM analyses confirm that the morphology for the colloids assembled from FpCn (n =14 and 18) is different from the vesicles assembled from FpCn (n =6, 8, 10). This difference, in addition to the stronger hydrophobic hydration resulting from longer alkyl groups, may also account for the improved stability of FpCn (n = 14 and 18) colloids. For example, the Gaussian chain, like globular proteins,[210, 211] may involve bridging water buried within the random coils, stabilizing the colloids.

Table 5.1 DLS/SLS results for the assemblies of FpCn in water

FpCn	D_h*	R_g/R_h	Morphology
FpC1	270 ± 15	/	/
FpC5	230 ± 10	/	/
FpC6	144 ± 5	1.06	Vesicles
FpC8	123 ± 5	1.09	Vesicles
FpC10	93 ± 6	1.04	Vesicles
FpC14	109 ± 3	1.54	Gaussian Chain
FpC18	142 ± 3	1.46	Gaussian Chain

*Aqueous solutions with concentration of 0.1 M

5.3 Conclusions

This work provided an experimental investigation about the colloidal structure-related hydrophobic hydration and its correlation with colloidal stability. Spectroscopic, light scattering, and cyclic voltammetry measurements were used to investigate the aqueous

behaviour of Fp-derivatives with various alkyl chain lengths. FpCn (n = 6, 8, 10) molecules assembled into vesicles. The longer the alkyl chains, the smaller vesicles formed. FpC14 and FpC18 aggregated into Gaussian chain structures. Dynamic light scattering (DLS) measurements revealed that the colloidal stability increased with increasing alkyl chain lengths. The hydration of CO groups, as revealed from the ATR-FTIR experiment, shows similar contribution to the stability of the FpCn colloids, regardless of the length of the alkyl chain. CV and IR analyses indicated that longer alkyl tails provided more structural integration and created larger hydration cavities, resulting in more stable colloids. This research illustrates that molecular chemistry can provide simplified systems to effectively elucidate the hydrophobic effect that remains unclear from intensive studies mainly based on complicated protein systems.

Chapter 6

Hydrophobic Effect on the Solution Behaviour of PEG-Fp-Alkyl Amphiphiles

6.1 Introduction

Organometallic surfactants have been explored, by taking advantage of the metal elements, as building blocks for a broad range of materials,[225] including catalysts,[23, 24] sensors[38, 226] and drug delivery systems.[26, 28, 29] The properties of the metal elements, such as redox activity and high electron density, may also facilitate understanding the micellar structure of surfactants and their aggregation behaviour.[227,15] Studies of these structure-related solution behaviours are, however, rarely reported.

Surfactants in water have a well-known ability to assemble into micelles with hydrophobic cores and hydrophilic corona.[92] The structure of the micellar cores, which results from the balance between the hydrophobic interaction and hydrophobic hydration, and its correlation to the solution behaviour of the micelles are still to be explored. A number of techniques, including NMR,[213] neutron scattering,[78] and molecular dynamics (MD) simulations,[77, 78] have been used to acquire knowledge on this aspect, generating diverse, sometimes conflicting, conclusions. It is generally considered that the water-insoluble tails associate into a central dry hydrophobic core with a smooth spherical surface.[79, 80] Only a few segments near the hydrophilic corona

are hydrated, whereas Menger model implies that water penetrates deeply into the hydrophobic core.[81, 82] This model has been supported by small-angle X-ray scattering measurements of aqueous sodium octanoate (C_7COONa) surfactant solutions,[74, 214] and Raman spectroscopy analysis of aqueous solutions of the surfactants with various aliphatic chain lengths.[74] Based on these studies, it is predicated that the surface of the core is not smooth, but corrugated.[74] Water molecules are, therefore, wedged into the furrows, which creates hydrated cavities penetrating deeply into the core.[74] Experimental techniques to probe the relative size of this cavity are highly desirable as they would elaborate the model and promote research, but the ideal technique has yet to be established.

Organometallic surfactants with a metal complex junction are able to assemble into micelles with metal elements arranged at the core-shell interface.[15, 17, 28] The redox potential of the metal elements is sensitive to their microenvironment.[106, 228] Thus, electrochemistry can be used to probe the relative area per surfactant occuping the core-shell interface. This area can be correlated to the size of the hydration cavity, which may shed insight on the solution behaviour of several groups of surfactants.

Although poly(ethylene glycol) alkyl ether (Brij®) surfactants are widely used for household products, biological materials and drug delivery systems,[229, 230, 231] the solution behaviour of some Brij® surfactants is so far not clearly understood. For example, Brij® S10 (poly(ethylene glycol) (10) stearyl ether or PEG(10)-C18) micelles in water,[232] when experimentally monitored, are not stable colloids and

gradually agglomerate into precipitates. It is also reported that Brij® molecules become strongly adsorbed protein molecules via hydrophobic attraction.[233] This hydrophobic interaction characteristics could be the reason for instability of the aqueous Brij® micelles. However, the stability and phase behaviour of Brij® surfactants in different environments remains a matter to be investigated and may be related to the structure of the core.[217, 232, 233, 234] Brij® analogues with a junction of metal element are, therefore, an ideal system for initiating the study. This initiative is expected to create an electrochemical technique to probe the core structure of organometallic micelles, enabling us to understand the micellization in depth.

Herein, we report the synthesis and self-assembly of Brij® analogues with an Fp junction, PEG-PPh_2-Fp-Cn (PEG-PPh_2: polyethylene glycol diphenyl phosphine, M_n = 550 or 2000 g/mol; Fp: $CpFe(CO)_2$; Cn: octadecyl (C18) or hexyl (C6)). This chapter is organized in four sections: The first covers the synthesies and characterization of the organometallic molecules, followed by surface tension measurements indicating that the metal-carbonyl junction has no effect on the surfactant behaviour of the molecules. The third explores the solution behaviour of the micelles with a discussion of the context of micellar structure. Finally, the redox activities of the micelles are correlated to the core-shell interface structure

6.2 Results and discussion

6.2.1 Synthesis of amphiphiles 6.1-6.4

The synthetic scheme for PEG-Fp-Cn (**6.1**-**6.4**) is depicted in Figure 6.1. poly(ethylene glycol) methyl ether chloride (PEG-Cl), converted from poly(ethylene glycol) methyl ether (PEG-OH),[235, 236] was reacted with diphenyl phosphine sodium (PPh_2-Na) generating PEG-PPh_2 **(6.5)**. Fp-alkyl (**6.6**) was prepared via the reaction of cyclopentadienyldicarbonyliron potassium (FpK) with corresponding alkyl halides. Subsequently, migration insertion reaction (MIR) of (**6.6**) in the presence of (**6.5)** was performed in THF at 70 ^oC for three days.

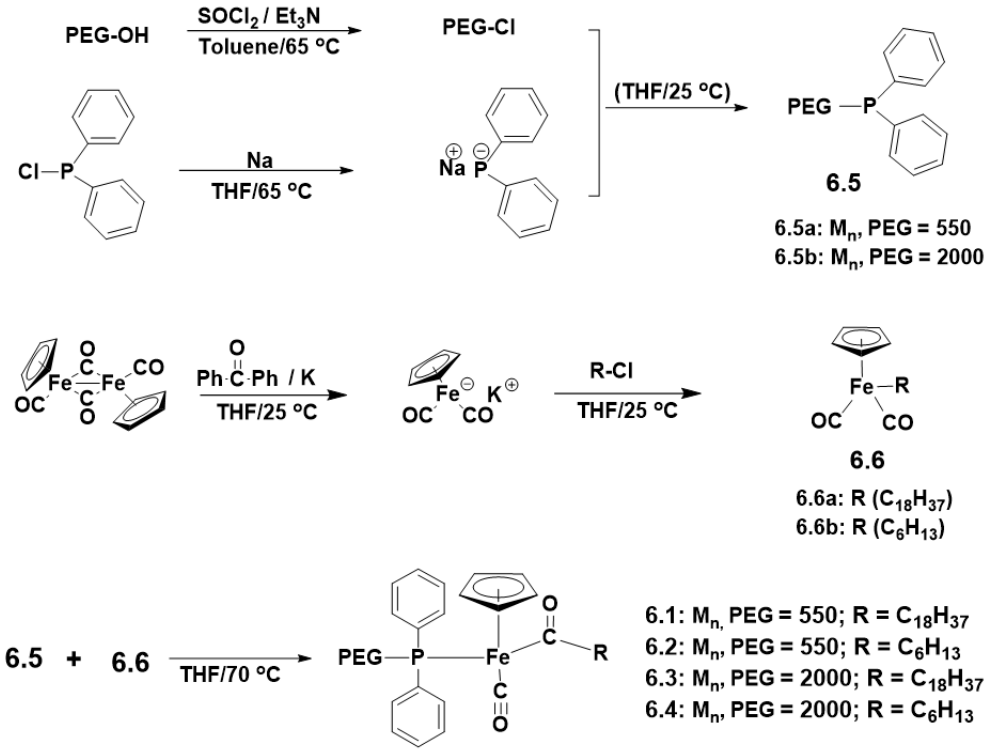

Figure 6.1 Schematic illustration for the synthesis of PEG-Fp-Cn amphiphiles**.**

The resultant amphiphilic molecules (**6.1**-**6.4**) were characterized using ^{1}H and ^{31}P NMR, and IR analyses. Figure 6.3 displays the ^{1}H NMR spectrum for **6.1**. As shown in Figure 6.2 and Figure S6.1, the proton signal due to the Cp ring appears at 4.36 ppm in **6.1** and 4.71 ppm in **6.6** (Figure S6.1). This upfield shift indicates the occurrence of MIR between **6.5** and **6.6** (Figure 6.1 and Figure S6.1).[48] The proton signals due to the PEG chains (3.6 ppm) also appears in the spectrum for **6.1**. In addition, Figure 6.2 shows two multiplet peaks at 2.61 and 2.85 ppm corresponding to the CH_2 α to the acyl CO. The splitting of the signal is due to the chirality of the iron center in **6.1**, which further supports the occurrence of MIR.[48] ^{31}P NMR shows one resonance at 69.5 ppm (Figure 6.3a) suggesting the formation of P-Fe coordination.[48] The FT-IR spectrum (Figure 6.3b) shows two absorptions at 1912 and 1607 cm^{-1}, corresponding to the terminal and acyl CO groups in **6.1**. Before MIR, the IR spectrum for **6.6** shows two absorption signals at 1934 and 1990 cm^{-1} corresponding to the terminal CO groups (Figure S6.1)**.** [48, 237]

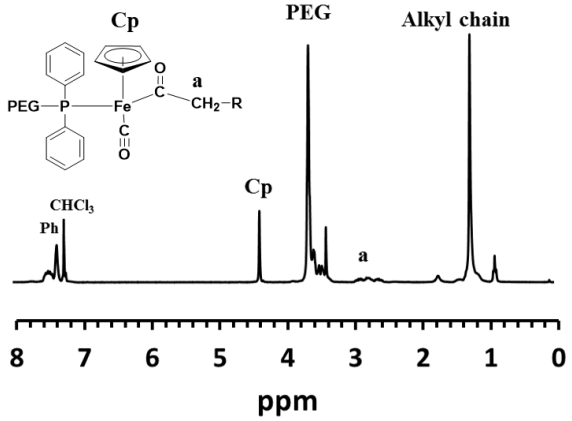

Figure 6.2 ^{1}H NMR spectrum ($CDCl_3$, 25 ^{o}C, 300 MHz) for **6.1**

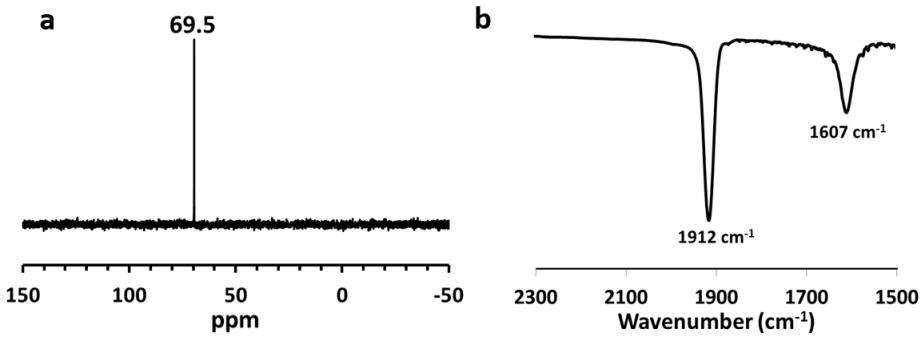

Figure 6.3 (a) ^{31}P NMR spectrum ($CDCl_3$, 25 ^{o}C, 300 MHz) and (b) Partial FT-IR (KBr pellet) spectrum for **6.1**

6.2.2 Amphiphilic properties of 1-4

The surface tension (γ) of the prepared molecules (**6.1**-**6.4)** was evaluated in water. The change in γ as a function of concentration is typical for amphiphilic surfactants (Figure S6.2), from which the critical micelle concentration (CMC) for **6.1**-**6.4** is deduced. The area per molecule (*A*), occupied at the water/air interface,[212, 238] and the maximum surface excess concentration (Γ) are also calculated from the slope of γ as a function of concentration (Figure S6.2 and Table S6.1),[212, 238] and summarized in Table 6.1. As shown in Table 6.1, molecules **6.1** and **6.2** with shorter PEG chains have smaller CMCs and *A* as compared with **6.3** and **6.4**, with longer hydrophilic PEG chains. By comparing **6.1** with **6.2** or **6.3** with **6.4**, it is apparent that the values of the CMC and *A* are smaller for the molecules with longer hydrophobic alkyl chain length. The smaller *A* and larger Γ values is attributed for tight packing of the molecules due to the stronger intermolecular hydrophobic interactions resulting from longer alkyl chain groups at the surface of water. These results are typical for

surfactant molecules[92, 212, 230, 232, 239] and similar with Brij® analogues.[230] Thus, **6.1**-**6.4** molecules are typical surfactants and the metal carbonyl junction has no significant effect on the surfactant behaviour.

Table 6.1 Critical micelle concentration (CMC), maximum surface excess concentration (Γ) and area occupied per molecule (A) adsorbed at the water/air interface for **6.1**-**6.4**.[a]

Molecules	CMC (μM)	Γ x 10^6 (Mole/m^2)	Area/molecule (Å^2)
(**6.1**) PEG_{550}-Fp-C_{18}	29.9 ± 2.3	4.023	41.3
(**6.2**) PEG_{550}-Fp-C_6	40.0 ± 6.2	1.809	91.8
(**6.3**) PEG_{2000}-Fp-C_{18}	82.1 ± 4.5	3.137	52.9
(**6.4**) PEG_{2000}-Fp-C_6	113.3 ± 23	1.25	132

[a] Data are calculated from surface tension measurements.

6.2.3 Aqueous self-assembly of 6.1-6.4

It is well known that Brij® micelles usually undergo agglomeration, which has been used for a variety application.[229, 230, 231] As shown in Figure 3, after aging of Brij® S10 ($C_{18}H_{37}$-PEG(10)) colloids for ca. 15 days, cotton-like agglomerates suspended in the aqueous solution were observed (Figure 6.4a). Similar to Brij® S10, the prepared organometallic surfactants also aggregated into micelles that gradually agglomerate (Figure S6.3) and eventually formed cotton-like suspensions. The suspensions could be re-dispersed upon shaking (Figure 6.4b). The similarity between the two groups of surfactants allowed us

to investigate the agglomeration behaviour of **6.1**-**6.4** (Figure 6.4c) for a better understanding of the solution behaviour of Brij® surfactants.

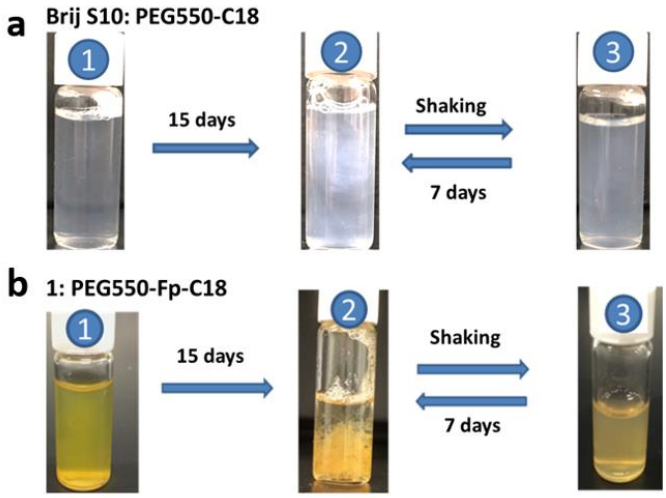

Figure 6.4 Photographs of the aqueous solution of (a) **6.1** and (b) Brij® S10 (5 mg/mL) (1) freshly prepared, (2) after aging for 15 days and (3) after shaking.

Taking advantage of the presence of the iron element at the core-shell interface, TEM analysis was used to explore the possible process for the agglomeration. As shown in Figure 6.5a, the freshly prepared colloids of **6.1** reveal spherical particles with a diameter of ca. 50 ± 6 nm for the core, which have a tendency to agglomerate into necklace chains. This tendency eventually leads to the assembly of all spherical particles into a network. This aggregation is probably due to the hydrophobic inter-micelle interaction.

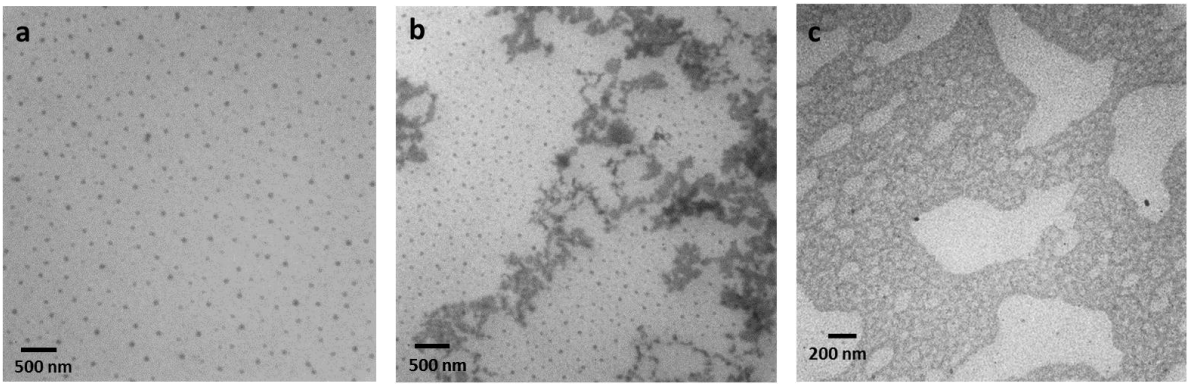

Figure 6.5 TEM images for colloids of **6.1** (**a**) 2 mg/mL aged for 3 days (**b**) 2 mg/mL aged for 5 days and (**c**) 5 mg/mL aged for 5 days.

Figure 6.6 compares the agglomeration time for the aqueous solution of **6.1**-**6.4**. It is clear that the rate for this agglomeration is related to the molecular structure of **6.1**-**6.4**. As shown in Figure 6.6, the longer PEG chains (**6.3** and **6.4**) slow down the agglomeration rate. This is reasonable and can be explained by the shielding effect of the PEO chains. For the micelles with same corona length, the shorter alkyl chain exerts a stronger inter-micelle interaction and promotes the agglomerates. On the other hand, surfactants with longer alkyl chains agglomerate more slowly (Figure 6.6), suggesting that their inter-micelle hydrophobic interaction is weaker. The longer alkyl chains, however, exert stronger hydrophobic interaction within the core, which results in lower CMC values (Table 6.1). However, the balance between the hydrophobic interactions within the micelle core and between the micelles is probably related to the agglomeration rate. Therefore, the redox activity of the iron element at the core-shell interface was explored.

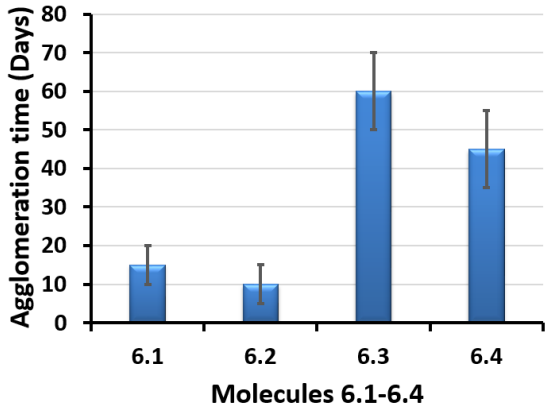

Figure 6.6 The agglomeration time for the aqueous solution of **6.1**-**6.4**.

6.2.4 The effect of the core structure on the agglomeration

In order to understand the effect of the chemical structure, in particular the core-forming alkyl chains on the agglomeration rate, cyclic voltammetry (CV) experiments were performed, because the redox activity of iron is related to its microenvironment.[106, 228] The organometallic surfactant is soluble in DMF and the CV experiment revealed a reversible redox curve. However, upon the micellization in water, the CV curve displayed two oxidation peaks separated by a redox coupling ($\Delta E_{½}$). $\Delta E_{½}$ is caused by the close association of the iron-carbonyl groups at the core-shell interface.[103, 104] The value of $\Delta E_{½}$ is, therefore, inversely related to the separation distance (L_s) between the iron elements (cartoon in Figure 6.7).[118] The L_s represents the area occupied by each molecule at the core-shell interface (cartoon in Figure 6.7). Based on Menger model,[81, 82] this area is proportional to the hydration cavity of the

hydrophobic core. Therefore, $\Delta E_{½}$ values can be used to investigate the micelle structure at the core-shell interface and predict the size of the hydrated cavity.

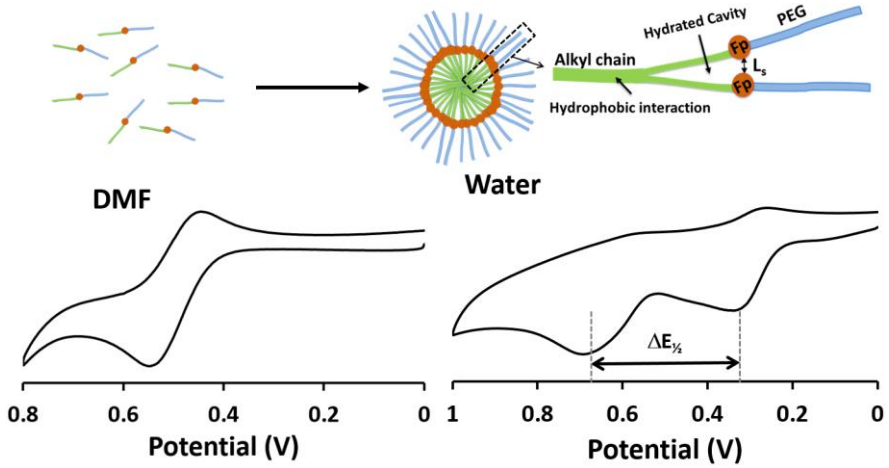

Figure 6.7 Representative CV curves for the surfactants **6.1**-**6.4** in their molecular state (in DMF) and assembles state (in water).

105

Table 6.2 and Figure S6.4 summarize the CV results for the surfactants **6.1**-**6.4** in DMF and their aqueous solutions. As shown in Figure S6.4 and Table 6.2, in DMF, the surfactants with longer PEG (**6.3** and **6.4**) have lower oxidation potentials as compared with those with shorter PEG (**6.1** and **6.2**). However, in water, a higher potential is required to get **6.3** and **6.4** oxidized, probably because the longer PEG shell shields the metal element from getting access to the electrode. Comparison of the $\Delta E_{½}$ values for the aqueous solutions of **6.1**-**6.4** for surfactants with the same alkyl chain length shows that the $\Delta E_{½}$ value decreases with the increase in the length of PEG. This result indicates that the longer water-soluble corona has a larger Ls and

thus larger occupied area per molecule at the core-shell interface. On the other hand, the effect of the length of alkyl chain on $\Delta E_{½}$ values is more obvious. As shown in Table 6.2, $\Delta E_{½}$ values for the micelles with C18 are smaller (0.227 V for **6.1** and 0.201 V for **6.3**) than those with C6 **(**0.346 V for **6.2** and 0.326 V for **6.4**). This comparison suggests that the core assembled from short alkyl chains (**6.2** and **6.4**) has smaller hydrated cavities.[105] The smaller cavity provides weaker intra-micelle hydrophobic interactions and weaker hydration of the core as we have illustrated in Chapter 5. The weaker intra-micelle hydrophobic interactions reduce the force for the integration of the micelles. In the meantime, the small cavity does not provide enough hydration forces to maintain the stability of the core. These two factors promote the inter-micelle hydrophobic interactions for the agglomeration to lower the free energy of the system. Therefore, the core structure contributes significantly to the stability of the micelles. This factor and its correlation to the colloidal stability have not caught sufficient attention in previous studies.[105]

Table 6.2 CV experiment results for **6.1**-**6.4** solutions in both DMF and water

Molecules	In DMF (V)		In water (V)		
	E_{ox}	E_{re}	E_{ox1}	E_{ox2}	$\Delta E_{1/2}$
(6.1) PEG_{550}-Fp-C_{18}	0.607	0.438	0.336	0.553	0.227
(6.2) PEG_{550}-Fp-C_6	0.595	0.431	0.279	0.625	0.346
(6.3) PEG_{2000}-Fp-C_{18}	0.543	0.450	0.353	0.554	0.201
(6.4) PEG_{2000}-Fp-C_6	0.548	0.444	0.287	0.613	0.326

For further investigation of the agglomeration process, CV results were monitored for the surfactant **6.1** over time. Figure 6.8 shows CV curves for freshly prepared and 10 days aged aqueous solutions of **6.1**. After 10 days, where colloids start to agglomerate (Figure S6.3), the CV curve showed a shift in the oxidation peaks toward lower potential.[240] In the meantime, more aggregation resulted in more hydrophobic adsorption at the electrode surface and, therefore, weaker oxidation peaks with smaller current (i_{pa}) values were detected. No change in $\Delta E_{½}$ values over time suggesting that there is no dissociation of the colloids and the agglomeration at room temperature is a particle-particle interaction. The agglomeration could be also attributed to the hydrophobic interactions between the alkyl chains and the hydrophobic hydration within the hydrated cavities.[241]

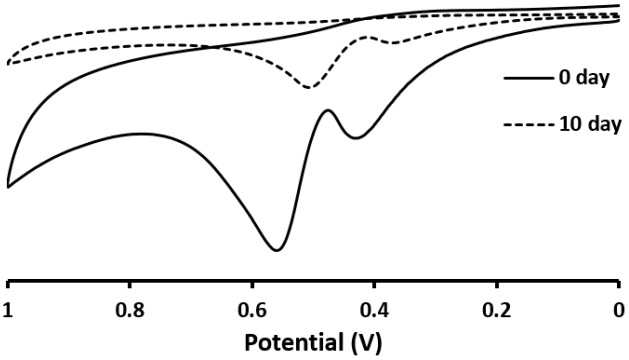

Figure 6.8 CV experiment results for aqueous solution of **6.1** (4 mg/mL) over time. (Scan rate 0.05 V/s)

To further understand the effect of the hydrophobic hydration (within the hydration cavity) and the intra-micelle hydrophobic hydration on the inter-micelle

hydrophobic hydration, the agglomeration of the same micelle at different temperatures was investigated. It is worth noting that the agglomeration rate become faster when solutions were heated at 50 ^{o}C (Figure S6.5). Therefore, the faster agglomeration can be attributed to the increase in the hydrophobic hydration.[242] This increase in the hydrophobic hydration may gradually reduce the hydrophobic interaction between the alkyl chains, which loosen the integration within the core and promotes the inter-micelle aggregations. This agglomeration process is therefore, starts from the dissociation of the micelles, which will separate the surfactants. This rationalization is supported by the CV experiment as a function of temperature. As shown in Figure 6.9a, as temperature increases, the oxidation peaks shift toward lower potential with smaller current value due to the faster electrophoretic mobility of larger aggregates resulting from the agglomeration.[240] Meantime, as shown in Figure 6.9b, as temperature increases from 20 to 60 ^{o}C, $\Delta E_{½}$ value of the aqueous solution of **6.1** decreases from 0.135 to 0.061 V, suggesting that the L_s become larger resulting from the disintegration of the micelles. This disintegration becomes clear at 70 ^{o}C, where only one oxidation peak is observed (Figure S6.6), suggesting that the molecules are not closely associated together. The larger separation between the Fp groups proves that the hydrophobic hydration is enhance whereas the integration of the core is decreased resulting from weaker hydrophobic interaction between the alkyl chains. These results suggest that the stability of the colloids is strongly related to the degree

of the hydrophobic hydration and the strength of the hydrophobic interaction within the micelle core.

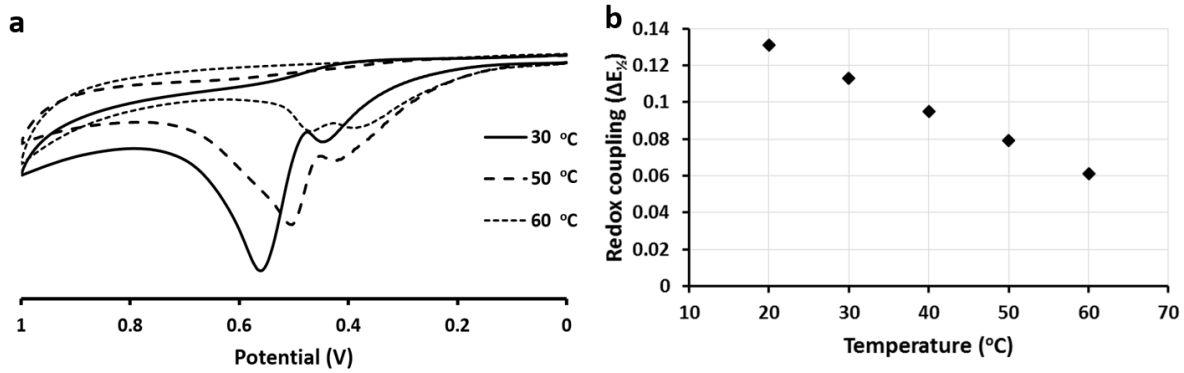

Figure 6.9 CV experiment results for aqueous solution of **6.1** (4 mg/mL) at different temperatures. (Scan rate 0.05 V/s).

6.3 Conclusions

The first example of organometallic amphiphile with an Fp junction, PEG-Fp-R, was prepared via migration insertion reaction of Fp-alkyl derivative with PEO-phosphine. The prepared organometallic surfactants exhibit typical surfactant behaviour, similar to their analogues without Fp junction (Brij® amphiphilic molecules). The Fp junctions offer advantages for the investigation of the agglomeration, commonly observed for Brij® surfactants. The redox activity of the iron elements, located at the core-shell interface, as a function of molecular structure was used to investigate the hydrophobic core structure of the micelle. The CV results

suggest that the longer hydrophobic alkyl tails exert a relatively stronger intra-micelle hydrophobic interaction and larger hydrated cavity within the hydrophobic core, therefore, the agglomeration rate is relatively slower.

6.4 Experimental Section

6.4.1 Materials and instrumentations

1-chlorooctadecan (>98.0%), and thionyl chloride (≥99.0%) were purchased from TCI America and Fluka Analytical, respectively. 1-Bromohexane (>98.0%), cyclopentadienyliron (II) dicarbonyl dimer (99%), triethylamine (≥99%), chlorodiphenylphosphine (98%), benzophenone (99%) and poly(ethylene glycol) methyl ether (PEO, M_n = 550 and 2000) were purchased from Sigma-Aldrich and used as received. Potassium metal (99.5%, rods in mineral oil) and sodium metal (99.9%, cubes in mineral oil) were purchased from Sigma-Aldrich, cut into small pieces and washed in hexane before use. Tetrahydrofuran (THF) was distilled over sodium/benzophenone before use. All other solvents were obtained from local commercial providers and used as received.

^{1}H and ^{31}P nuclear magnetic resonance (NMR) spectra were recorded on Bruker-300 (300 MHz) spectrometer at room temperature using appropriate solvents as reported in each case. Fourier transform infrared (FT-IR) spectra were recorded on a Bruker Tensor 27 spectrophotometer with a resolution of 1 cm^{-1} at room temperature. Samples were prepared using KBr pellets by grinding and compressing of the amphiphile in anhydrous KBr using Nujol mulls. Dynamic light scattering

(DLS) experiments were performed at 25 °C using Zetasizer Nano Series (Nano-S90, Malvern Instruments) with laser wavelength of 633 with a fixed angle of 90º. Transmission electron microscopy (TEM) images was performed using a low voltage (5 kV) LVEM5 electron microscope (Delong Instruments). TEM samples were prepared by dropping the solution onto a carbon-coated copper grid (FCF-200, Electron Microscopy Science) and the grid was then left to dry at the ambient temperature. Cyclic voltammetry (CV) measurements were obtained using DY2000 Multi-Channel Potentiostat (Digi-Ivy Inc.) workstation with a scan rate of 50 mV/sec and silver wire as a *pseudo*-reference electrode. All samples were measured in both DMF and water using tetrabutylammonium perchlorate (TBAP, 2 mg/mL) and KCl (2 mg/mL), respectively. Surface tension of pure water and the aqueous solutions of the prepared metallo-amphiphiles with different concentrations were measured at 22 ºC using tensiometer Data Physics DCAT 21 system.

6.4.2 Synthesis of the amphiphiles 6.1-6.4.

Synthetic procedures of the amphiphile (PEG(550)-Fp-C18) **6.1** that contains PEG (M_n= 550 g/mol) and octadecyl chain, as representative amphiphile, will be discussed in detail in this section. All synthetic steps were conducted under a dry atmosphere of nitrogen gas using Schlenk line techniques.

6.4.3 Synthesis of (6.5)

Synthesis of PEG(550)-Cl.[92, 236] A toluene solution (17 mL) of poly(ethylene glycol) methyl ether, M_n = 550 (2.0 g, 3.6 mmol) and triethylamine (0.40 g, 4.0 mmol) was added dropwise into a 100-mL Schlenk flask containing thionyl chloride $SOCl_2$ (2.60 g, 22 mmol) at 0 ^oC (ice bath). After the addition, the ice bath was replaced with oil bath and the solution was gradually heated up to 65 °C. After stirring at 65 °C overnight, the solution was passed through a celite column to remove the resulted triethylamine hydrochloride salt and the filtrate was subject to rotary evaporation to remove toluene. The crude product was then dissolved in a minimal amount of dry THF and precipitated out in hexane as cloudy oil. The final product was collected and dried under vacuum to yield PEG(M_n = 550)-Cl (1.74 g, 71%). ^{1}H NMR (300 MHz, $CDCl_3$, δ): 3.75 (t, 2H, -CH_2Cl), 3.55-5.65 (s, 44H, CH_2CH_2O), 3.50 (t, 2H, - O - CH_2- CH_2Cl), 3.37 (s, 3H, CH_3O). ^{1}H NMR results for PEO(M_n = 2000)-Cl as follow. ^{1}H NMR (300 MHz, $CDCl_3$, δ): 3.74 (tbr, 2H, -CH_2Cl), 3.58-5.68 (sbr, 176H, CH_2CH_2O), 3.54 (brt, 2H, - O - CH_2- CH_2Cl), 3.37 (s, 3H, CH_3O). (see Figure S6.7)

Synthesis of $NaPPh_2$.[48, 98] Sodium diphenylphosphide ($NaPPh_2$) was prepared as previously reported by our group. ^{31}P NMR (300 MHz, THF, δ): -20 (s,1P, Ar_2PNa) (Figure S6.1).

Synthesis of PEG(550)-PPh_2 (6.5a). PEG-Cl (1.01 g, 1.78 mmol) was added to a 100-mL Schlenk flask and dissolved in dry THF (5 mL). The flask was placed in an ice bath. To the flask, 5.5 mL sodium diphenylphosphide solution (0.55 g, 2.65

mmol; excess) was added dropwise. The resulting mixture was left under stirring for 2 hours. Then, degassed methanol (2 mL) was added dropwise to react with the excess sodium diphenylphosphide. As a result, the color of the solution was changed from deep red to pale yellow. After the solution was passed through a celite column, the mixed solvents of THF/methanol were removed under vacuum, leaving pale yellow oil as crude product. The crude product was dissolved in a minimal volume of dry THF and subsequently precipitated out in degassed hexane. After this step of purification, the final product was collected and dried under vacuum, yield 0.89 g (69.6 %). ^{31}P NMR (300 MHz, $CDCl_3$, δ): -21 ppm; ^{31}P NMR (300 MHz, THF, δ): -19 ppm; ^{1}H NMR (300 MHz, $CDCl_3$, δ): 7.15, 7.55 (sbr, 10H, ArH), 3.48 (sbr, 48H, CH_2CH_2O), 3.20 (s, 3H, CH_3O). (Figure S6.1)

6.4.4 Synthesis of (6.6)

Fp-Cn chain (**6.6**) was synthesized by coupling of cyclopentadienyldicarbonyliron potassium (FpK),[243] with 1-chlorooctadecane (**6.6a**) or 1-chlorohexane (**6.6b**). For **6.6a**, under stirring at 0 °C, a solution of $C_{18}H_{37}Cl$ (2.5 cmL, 7.3 mmol) in THF (5 mL) was added to an orange suspension of FpK (2 g, 9.3 mol) in THF (20 mL). The orange suspension gradually turned to brown and was kept stirred at room temperature for 2 hours. THF was then removed by rotary evaporation and the residue was extracted using degassed hexane. The supernatant was collected and rotary evaporated. The resulting solid was chromatographed using a plug of silica column and a degassed hexane/DCM (4:1 v/v) mixture was used as eluent. The first

yellow band was collected and solvents were removed using rotary evaporation. The bright yellow crystals were collected and dried under vacuum. Yield 2.80 g (89.2 %). ^{1}H NMR (300 MHz, $CDCl_3$, δ): 4.71 (s, 5H, Cp ring), 1.44 (br, 2H, Fe-CH_2-alkyl chain), 1.25 (br, 32H, CH_2-alkyl chain), 0.87 (t, 3H, terminal CH_3); FT-IR (KBr): ν =1990 and 1934 cm^{-1} (two CO groups stretching). (Figure S6.1 and Figure S6.8)

6.4.5 Synthesis of PEG(550)-Fp-C18 (6.1)

A solution in THF (60 mL) containing **6.5a** (1.0 g, 1.39 mmol) and **6.6a** (0.72 g, 1.7 mmol) was prepared in a 100-mL Schlenk flask. The solution was then heated up and refluxed at 70 ºC for three days. THF was subsequently removed *via* rotary evaporation, resulting in a dark-brown crude product. The crude product was then suspended in a minimal volume of degassed hexane and transferred to a silica column. The column was first flushed using degassed hexane to remove the excess Fp-C18 (**6.6a**), and subsequently washed using dry THF. The product appearing as a dark brown band was collected. After removing the solvent, a viscous dark brown oil was collected and dried under vacuum, 1.27 g (79.5 %). ^{31}P NMR (300 MHz, $CDCl_3$, δ): 69.5 (Ph_2-P-C); ^{1}H NMR (300 MHz, $CDCl_3$, δ): 4.36 (s, 5H, Cp ring), 2.61 and 2.85 (m, 2H, acyl-CH_2-alkyl chain), 1.25 (br, 32H, CH_2-alkyl chain), 0.87 (t, 3H, terminal CH_3), 3.6 (br, 42H, CH_2CH_2O), 3.37 (s, 3H, CH_3O), 2.78 (t, 2H, CH_2-P, overlapped); FT-IR (KBr): ν =1912 cm^{-1} (terminal CO stretching), 1607 cm^{-1} (migrated acyl carbonyl). (Figure 6.2 and Figure 6.3)

6.4.6 Preparation of the micelles

Typically a 2.0 mg/mL aqueous solution was prepared by the addition of 10.0 mL of water into a THF solution of each prepared amphiphiles **6.1**-**6.4 (**20 mg in 0.5 mL THF) under stirring. Subsequently, THF was removed *via* either bubbling with N_2 for an hour or dialysis over night against water.

Chapter 7

Summary and Future Work

7.1 Summary

The self-assembly of hydrophobic molecules into aqueous colloids contradicts common chemical intuition, but was achieved in this research *via* hydration of $CpFePPh_3(CO)CO(CH_2)_5CH_3$ (FpC6). The resultant metal carbonyl aggregates were proved to be bilayer vesicles with iron complexes exposed to water and alkyl chains that formed the inner walls (MCsomes). These MCsomes showed high structural integration upon dilution. The highly polarized CO groups on the surface of MCsomes resulted in negative zeta potential (-65 mV) and created a local electric field, thereby significantly enhancing the IR absorption of CO groups more than a 100 fold. This is the first discovery of aggregation-enhanced IR absorption (AEIRA) without the assistance of external dielectric or plasmonic substrates (Chapter 2).

Molybdenum-carbonyl aqueous colloids were prepared from the self-assembly of η^5-$CpMo(CO)_2(PPh_3)CO(CH_2)_5CH_3$ (MpC6) in water. MpC6 was synthesized through a reaction of $CpMo(CO)_3$ anion (Mp^-) with $Br(CH_2)_5CH_3$ in the presence of PPh_3. Similar to its Fe-analogue, FpC6, the aqueous assembly of MpC6 generated vesicles with an aggregation-enhanced IR absorption (AEIRA) phenomenon (Chapter 3).

A highly-integrated, laser manipulable multi-functional metal carbonyl nanovesicle (MCsome) with aggregation-induced emission (AIE) and aggregation-enhanced IR absorption (AEIRA) was created *via* the self-assembly of the bithiophene tethered-Fp acyl

derivative (FpC3BTh). The spatial segregation of the AIE-active bithiophene domain, from the iron-carbonyl units, by the butanoyl spacers prevented the quenching effect of the iron elements and resulted in a photoluminescent MCsome. The polarizable iron-carbonyl groups on the surface of the MCsome provided an enhancement (ca. 100-fold) in IR absorptions for the carbonyl groups. Upon the interaction of MCsomes with a focused continuous-wave near-IR (NIR) laser beam, a strong gradient (trapping) force was generated and allowed the laser trapping of the MCsome without the need for additives. (Chapter 4).

The experiments detailed in Chapter 5 investigated colloidal structure-related hydrophobic hydration and confirmed its correlation with colloidal stability. In addition to spectroscopic and light scattering techniques, cyclic voltammetry measurements were used to investigate the aggregation process of the Fp-derivatives with various alkyl chain lengths (Chapter 5).

PEG-PPh_2-Fp-Cn (PEG-PPh_2: polyethylene glycol diphenyl phosphine, M_n = 550 or 2000 g/mol; Fp: $CpFe(CO)_2$; Cn: octadecyl (C18) or hexyl (C6)) amphiphilic molecules with an iron-carbonyl junction were synthesized. Surface tension measurements indicated that the molecules, despite bearing an iron-carbonyl junction, behaved as typical surfactants. The redox behaviour of organometallic micelles with iron elements, sitting at the core-shell interface, was interrelated to the micellar core structure. This discovery enabled us to explore the effect of the core structure on the solution behaviour of the surfactants (Chapter 6).

7.2 Suggestions for Future Work

The prepared Fp-derivatives showed unique multi-functional properties including SEIRA, AIE, and laser manipulability. These characteristics should serve a wide range of potential biological applications including cell imaging, bioassay and drug delivery. The stability of the prepared molecules and their aqueous colloids was tested over time in neutral, acidic (e.g. ascorbic and hydrochloric acids) and basic (e.g. sodium hydroxide) aqueous solutions. However, in order to introduce these molecules in biological systems, further investigation of their stability, bioviability and biosensing properties in real and biocompatible buffers and cell culture environments is needed.

The hydrophobic hydration of the Fp-derivatives with correlations to their aqueous colloidal stability and their colloids' surface structure was investigated using conventional electrochemical and spectroscopic methods. To validate the method established in this thesis, computational simulation and calorimetric titration experiments are suggested. Morphology of the prepared Fp-derivative colloids with varied alkyl chain lengths can be investigated using cryo-TEM. However, a cryo-TEM imaging protocol needs to be further validated by collaboration with a professional imaging research center. More cryo-TEM and simulation could be used to confirm the vesicular morphology for FpC3Bth colloids.

The work in this thesis has focused on Fp-derivatives with varied hydrophobic alkyl chains. The triphenyl phosphine ligand was used in all reported molecules. Preliminary results showed that colloids prepared from Fp-derivatives with the trimethyl phosphine

ligands exhibited less stability over time compared to those with the triphenyl phosphine ligands. Therefore, the effect of the phosphine ligands (e.g. triphenyl, trimethyl, tricyclohexyl and isopropyl) on the colloidal structure and stability are worth investigating. In addition, synthesis and study of the aqueous behaviour of Fp analogues using other transition metals, such as ruthenium and platinum, should add great value to the aqueous MCCs research area.

Use of the prepared PEO-Fp-R amphiphiles (Chapter 6), as a stabilizer, during emulsion polymerization would provide latex particles with metal-containing surfaces. Having an iron metal at the latex surface will provide new latex nanoparticles that could be fabricated into a functional latex film with conductivity, redox, and magnetic properties. Preliminary results have shown that, through miniemulsion polymerization technique, this group of iron-containing amphiphiles can be used to prepare a polystyrene (PS) latex. Reduction of the gold ions into gold nanoparticles at the surface of the prepared PS latex film was also achieved and confirmed with UV-vis spectroscopy. Furthermore, the presence of the polarized carbonyl groups at the latex surface should provide an active medium for the hydrolysis of silica at the latex surface. However, further investigation of the composition of the PS latex surface, using elemental analysis such as X-ray photoelectron spectroscopy (XPS) or Energy-dispersive X-ray spectroscopy (EDX), is still needed.

Letter of Copyright Permission

License Number	4080051030006
License date	Apr 01, 2017
Licensed Content Publisher	John Wiley and Sons
Licensed Content Publication	Chemistry - A European Journal
Licensed Content Title	Iron–Carbonyl Aqueous Vesicles (MCsomes) by Hydration of [Fe(CO){CO(CH2)5CH3}(Cp)(PPh3)] (FpC6): Highly Integrated Colloids with Aggregation-Induced Self-Enhanced IR Absorption (AI-SEIRA)
Licensed Content Author	Nimer Murshid,Xiaosong Wang
Licensed Content Date	Nov 13, 2015
Licensed Content Pages	8
Type of use	Dissertation/Thesis
Requestor type	Author of this Wiley article
Format	Print and electronic
Portion	Full article
Will you be translating?	No
Title of your thesis / dissertation	Synthesis and Self-Assembly of Metal carbonyl Building Blocks for Aqueous Collides with Aggregation Induced Functions
Expected completion date	Apr 2017
Expected size (number of pages)	240
Requestor Location	Nimer Murshid 759 Laurelwood Dr Waterloo, ON N2V2W2 Canada Attn: Nimer Murshid
Publisher Tax ID	EU826007151
Billing Type	Invoice
Billing address	Nimer Murshid 759 Laurelwood Dr Waterloo, ON N2V2W2 Canada Attn: Nimer Murshid
Total	0.00 CAD

License Number	4080051326955
License date	Apr 01, 2017
Licensed Content Publisher	Elsevier
Licensed Content Publication	Journal of Organometallic Chemistry
Licensed Content Title	Aggregation-enhanced IR absorption (AEIRA) of molybdenum-carbonyl organometallic aqueous colloids
Licensed Content Author	Nimer Murshid,Mohammad A. Rahman,Xiaosong Wang
Licensed Content Date	15 September 2016
Licensed Content Volume	819
Licensed Content Issue	n/a
Licensed Content Pages	6
Type of Use	reuse in a thesis/dissertation
Portion	full article
Format	both print and electronic
Are you the author of this Elsevier article?	Yes
Will you be translating?	No
Order reference number	
Title of your thesis/dissertation	Synthesis and Self-Assembly of Metal carbonyl Building Blocks for Aqueous Collides with Aggregation Induced Functions
Expected completion date	Apr 2017
Estimated size (number of pages)	240
Elsevier VAT number	GB 494 6272 12
Requestor Location	Nimer Murshid 759 Laurelwood Dr Waterloo, ON N2V2W2 Canada Attn: Nimer Murshid
Total	0.00 CAD

Highly-integrated, laser manipulable aqueous metal carbonyl vesicles (MCsomes) with aggregation-induced emission (AIE) and aggregation-enhanced IR absorption (AEIRA)

N. Murshid, K. Yuyama, S. Wu, K. Wu, H. Masuhara, C. Wang and X. Wang, *J. Mater. Chem. C*, 2016, **4**, 5231
DOI: 10.1039/C6TC01222A

References

1. Kumar, A.; Balbach, J. Real-time protein NMR spectroscopy and investigation of assisted protein folding. *Biochim. Biophys. Acta, Gen. Subj.* **2015**, *1850* (10), 1965-1972.
2. Le Bihan, D.; Fukuyama, H. *Water: The forgotten biological molecule*; Pan Stanford Publishing 2010, pp 23-89.
3. Nagarajan, R. *Amphiphiles: Molecular Assembly and Applications*; American Chemical Society 2011.
4. Hirst, L. S. *Fundamentals of soft matter science*; CRC Press 2012, pp 71-82.
5. Hamley, I. W. *Introduction to soft matter: synthetic and biological self-assembling materials*; John Wiley & Sons2013, pp 193-263.
6. Roy, A.; Roy, S. Spontaneous Formation of Vesicles by Self-Assembly of Nicotinyl Amino Acid Amphiphiles: Application as "Turn-On" Fluorescent Sensors for the Selective Detection of Trace-Level Hg (II) in Water. *Ind. Eng. Chem. Res.* **2016,** *55* (38), 10104-10113.
7. Pileni, M.-P. The role of soft colloidal templates in controlling the size and shape of inorganic nanocrystals. *Nat. Mater.* **2003,** *2* (3), 145-150.
8. Pileni, M. Control of the size and shape of inorganic nanocrystals at various scales from nano to macrodomains. *J. Phys. Chem. C* **2007,** *111* (26), 9019-9038.
9. Wang, J.; Gao, W. Nano/microscale motors: biomedical opportunities and challenges. *ACS nano* **2012,** *6* (7), 5745-5751.
10. Elani, Y.; Law, R. V.; Ces, O. Vesicle-based artificial cells as chemical microreactors with spatially segregated reaction pathways. *Nat. Commun.* **2014,** *5*.
11. Egli, S.; Nussbaumer, M. G.; Balasubramanian, V.; Chami, M.; Bruns, N.; Palivan, C.; Meier, W. Biocompatible functionalization of polymersome surfaces: a new approach to surface immobilization and cell targeting using polymersomes. *J. Am. Chem. Soc.* **2011,** *133* (12), 4476-4483.
12. Wang, X.; Hu, J.; Liu, G.; Tian, J.; Wang, H.; Gong, M.; Liu, S. Reversibly Switching Bilayer Permeability and Release Modules of Photochromic Polymersomes

Stabilized by Cooperative Noncovalent Interactions. *J. Am. Chem. Soc.* **2015,** *137* (48), 15262-15275.

13. Hasegawa, U.; Van Der Vlies, A. J.; Simeoni, E.; Wandrey, C.; Hubbell, J. A. Carbon monoxide-releasing micelles for immunotherapy. *J. Am. Chem. Soc.* **2010,** *132* (51), 18273-18280.
14. Huang, Z.; Zhang, X.; Zhang, X.; Wang, S.; Yang, B.; Wang, K.; Yuan, J.; Tao, L.; Wei, Y. Synthesis of amphiphilic fluorescent PEGylated AIE nanoparticles via RAFT polymerization and their cell imaging applications. *Rsc Adv.* **2015,** *5* (109), 89472-89477.
15. Lanigan, N.; Wang, X. Supramolecular chemistry of metal complexes in solution. *Chem. Commun.* **2013,** *49* (74), 8133-8144.
16. Gohy, J.-F. Metallo-supramolecular block copolymer micelles. *Coord. Chem. Rev.* **2009,** *253* (17), 2214-2225.
17. Griffiths, P. C.; Fallis, I. A.; Tatchell, T.; Bushby, L.; Beeby, A. Aqueous solutions of transition metal containing micelles. *Adv. Colloid Interface Sci.* **2008,** *144* (1), 13-23.
18. Yan, X.; Li, S.; Cook, T. R.; Ji, X.; Yao, Y.; Pollock, J. B.; Shi, Y.; Yu, G.; Li, J.; Huang, F. Hierarchical self-assembly: Well-defined supramolecular nanostructures and metallohydrogels via amphiphilic discrete organoplatinum (II) metallacycles. *J. Am. Chem. Soc.* **2013,** *135* (38), 14036-14039.
19. Hudson, Z. M.; Boott, C. E.; Robinson, M. E.; Rupar, P. A.; Winnik, M. A.; Manners, I. Tailored hierarchical micelle architectures using living crystallization-driven self-assembly in two dimensions. *Nat. chem.* **2014,** *6* (10), 893-898.
20. Gädt, T.; Schacher, F. H.; McGrath, N.; Winnik, M. A.; Manners, I. Probing the scope of crystallization-driven living self-assembly: studies of diblock copolymer micelles with a polyisoprene corona and a crystalline poly (ferrocenyldiethylsilane) core-forming metalloblock. *Macromolecules* **2011,** *44* (10), 3777-3786.

21. K Ghosh, K.; Gupta, B.; Bhattacharya, S. Metallosurfactant Aggregates as Catalysts for the Hydrolytic Cleavage of Carboxylate and Phosphate Esters. *Curr. Organocatal.* **2016,** *3* (1), 6-23.
22. Gohy, J.-F.; Lohmeijer, B. G.; Schubert, U. S. Metallo-supramolecular block copolymer micelles. *Macromolecules* **2002,** *35* (12), 4560-4563.
23. Polyzos, A.; Hughes, A. B.; Christie, J. R. Catalysis of aryl ester hydrolysis in the presence of metallomicelles containing a copper (II) diethylenetriamine derivative. *Langmuir* **2007,** *23* (4), 1872-1879.
24. Lipshutz, B. H.; Ghorai, S. PQS: A New Platform for Micellar Catalysis. RCM Reactions in Water, with Catalyst Recycling. *Org. Lett.* **2008,** *11* (3), 705-708.
25. Meng, F.; Hennink, W. E.; Zhong, Z. Reduction-sensitive polymers and bioconjugates for biomedical applications. *Biomaterials* **2009,** *30* (12), 2180-2198.
26. Xing, L.-B.; Yu, S.; Wang, X.-J.; Wang, G.-X.; Chen, B.; Zhang, L.-P.; Tung, C.-H.; Wu, L.-Z. Reversible multistimuli-responsive vesicles formed by an amphiphilic cationic platinum (II) terpyridyl complex with a ferrocene unit in water. *Chem. Commun.* **2012,** *48* (88), 10886-10888.
27. Liu, L.; Rui, L.; Gao, Y.; Zhang, W. Self-assembly and disassembly of a redox-responsive ferrocene-containing amphiphilic block copolymer for controlled release. *Polym. Chem.* **2015,** *6* (10), 1817-1829.
28. Yan, Q.; Yuan, J.; Cai, Z.; Xin, Y.; Kang, Y.; Yin, Y. Voltage-responsive vesicles based on orthogonal assembly of two homopolymers. *J. Am. Chem. Soc.* **2010,** *132* (27), 9268-9270.
29. Chen, L.-J.; Zhao, G.-Z.; Jiang, B.; Sun, B.; Wang, M.; Xu, L.; He, J.; Abliz, Z.; Tan, H.; Li, X. Smart stimuli-responsive spherical nanostructures constructed from supramolecular metallodendrimers via hierarchical self-assembly. *J. Am. Chem. Soc.* **2014,** *136* (16), 5993-6001.

30. Guerrero-Martínez, A. s.; Vida, Y.; Domínguez-Gutiérrez, D.; Albuquerque, R. Q.; De Cola, L. Tuning emission properties of Iridium and Ruthenium metallosurfactants in micellar systems. *Inorg. Chem.* **2008,** *47* (20), 9131-9133.

31. Pandey, I. K.; Natarajan, M.; Kaur-Ghumaan, S. Hydrogen generation: Aromatic dithiolate-bridged metal carbonyl complexes as hydrogenase catalytic site models. *J. Inorg. Biochem.* **2015,** *143*, 88-110.

32. Kochi, J. *Organometallic mechanisms and catalysis: the role of reactive intermediates in organic processes*; Elsevier 2012.

33. Fujita, K.; Tanaka, Y.; Sho, T.; Ozeki, S.; Abe, S.; Hikage, T.; Kuchimaru, T.; Kizaka-Kondoh, S.; Ueno, T. Intracellular CO Release from Composite of Ferritin and Ruthenium Carbonyl Complexes. *J. Am. Chem. Soc.* **2014,** *136* (48), 16902-16908.

34. Tabe, H.; Fujita, K.; Abe, S.; Tsujimoto, M.; Kuchimaru, T.; Kizaka-Kondoh, S.; Takano, M.; Kitagawa, S.; Ueno, T. Preparation of a Cross-Linked Porous Protein Crystal Containing Ru Carbonyl Complexes as a CO-Releasing Extracellular Scaffold. *Inorg. Chem.* **2014,** *54* (1), 215-220.

35. Ott, I.; Kircher, B.; Bagowski, C. P.; Vlecken, D. H.; Ott, E. B.; Will, J.; Bensdorf, K.; Sheldrick, W. S.; Gust, R. Modulation of the biological properties of aspirin by formation of a bioorganometallic derivative. *Angew. Chem., Int. Ed.* **2009,** *48* (6), 1160-1163.

36. Schlawe, D.; Majdalani, A.; Velcicky, J.; Heßler, E.; Wieder, T.; Prokop, A.; Schmalz, H. G. Iron-Containing Nucleoside Analogues with Pronounced Apoptosis-Inducing Activity. *Angew. Chem., Int. Ed.* **2004,** *43* (13), 1731-1734.

37. Clède, S.; Policar, C. Metal–Carbonyl Units for Vibrational and Luminescence Imaging: Towards Multimodality. *Chem. - Eur. J.* **2015,** *21* (3), 942-958.

38. Meister, K.; Niesel, J.; Schatzschneider, U.; Metzler-Nolte, N.; Schmidt, D. A.; Havenith, M. Label-Free Imaging of Metal–Carbonyl Complexes in Live Cells by Raman Microspectroscopy. *Angew. Chem., Int. Ed.* **2010,** *49* (19), 3310-3312.

39. Policar, C.; Waern, J. B.; Plamont, M. A.; Clède, S.; Mayet, C.; Prazeres, R.; Ortega, J. M.; Vessières, A.; Dazzi, A. Subcellular IR imaging of a metal–carbonyl moiety using photothermally induced resonance. *Angew. Chem., Int. Ed.* **2011,** *50* (4), 860-864.

40. Fischer-Durand, N.; Salmain, M.; Rudolf, B.; Dai, L.; Jugé, L.; Guérineau, V.; Laprévote, O.; Vessières, A.; Jaouen, G. Site-specific conjugation of metal carbonyl dendrimer to antibody and its use as detection reagent in immunoassay. *Anal. Biochem.* **2010,** *407* (2), 211-219.

41. Parera, E.; Comelles, F.; Barnadas, R.; Suades, J. Formation of vesicles with an organometallic amphiphile bilayer by supramolecular arrangement of metal carbonyl metallosurfactants. *Chem. Commun.* **2011,** *47* (15), 4460-4462.

42. Aroca, R. F.; Ross, D. J.; Domingo, C. Surface-enhanced infrared spectroscopy. *Appl. Spectrosc.* **2004,** *58*, 324A-338A.

43. Lam, Z.; Kong, K. V.; Olivo, M.; Leong, W. K. Vibrational spectroscopy of metal carbonyls for bio-imaging and-sensing. *Analyst* **2016,** *141* (5), 1569-1586.

44. Kopf, I.; N'Dongo, H. W. P.; Ballout, F.; Schatzschneider, U.; Bründermann, E.; Havenith, M. Introducing cymantrene labels into scattering scanning near-field infrared microscopy. *Analyst* **2012,** *137* (21), 4995-5001.

45. Kong, K. V.; Lam, Z.; Goh, W. D.; Leong, W. K.; Olivo, M. Metal Carbonyl–Gold Nanoparticle Conjugates for Live-Cell SERS Imaging. *Angew. Chem. Int. Ed.* **2012**, *51*, 9796 –9799

46. Spessard, G. O.; Miessler, G. L. *Organometallic Chemistry*; Oxford University Press2010.

47. Lanigan, N.; Assoud, A.; Wang, X. Intermolecular Interactions of CpFePPh3 (CO) CO (CH2) 5CH3: From a Crystalline Solid to a Supramolecular “Iron-Truss” Polymer. *ACS Macro Lett.* **2014,** *3* (12), 1281-1285.

48. Wang, X.; Cao, K.; Liu, Y.; Tsang, B.; Liew, S. Migration insertion polymerization (MIP) of cyclopentadienyldicarbonyldiphenylphosphinopropyliron (FpP): a new

concept for main chain metal-containing polymers (MCPs). *J. Am. Chem. Soc.* **2013,** *135* (9), 3399-3402.

49. Theys, R. D.; Dudley, M. E.; Hossain, M. M. Recent chemistry of the η 5-cyclopentadienyl dicarbonyl iron anion. *Coord. Chem. Rev.* **2009,** *253* (1), 180-234.
50. Kumar, M.; Metta-Magana, A.; Sharma, H. K.; Pannell, K. H. Phosphine induced migratory CO insertion into the Fe–CH 2 bond of the organometallic polymer-[(η 5-C 5 H 4) Fe (CO) 2 CH 2 SiMe 2] n-and characterization of model iron complexes. *Dalton T* **2010,** *39* (30), 7125-7131.
51. Sharma, H. K.; Cervantes-Lee, F.; Pannell, K. H. Isolation and Ring-Opening of New 1-Sila-3-metallacyclobutanes (η5-C5H4Fe)(CO) 2CH2SiR2 Leading to A New Class of Organometallic Polymer. *J. Am. Chem. Soc.* **2004,** *126* (5), 1326-1327.
52. King, R. Reactions of Alkali Metal Derivatives of Metal Carbonyls. II. Reactions between Acid Chloride Derivatives and the Sodium Derivative of Cyclopentadienyliron Dicarbonyl. *J. Am. Chem. Soc.* **1963,** *85* (13), 1918-1922.
53. Green, M.; Hurley, C. Evidence for an iron—carbene complex. *J. Organomet. Chem.* **1967,** *10* (1), 188-190.
54. Monge, S.; David, G. *Phosphorus-based polymers: from synthesis to applications*; Royal Society of Chemistry2014; Vol. 11.
55. Kenaree, A. R.; Sauvé, E. R.; Ragogna, P. J.; Gilroy, J. B. Group 6 metal pentacarbonyl complexes of air-stable primary, secondary, and tertiary ferrocenylethylphosphines. *Dalton T* **2016,** *45* (7), 2859-2867.
56. Tanford, C. The hydrophobic effect and the organization of living matter. *Science* **1978,** *200* (4345), 1012-1018.
57. Koynova, R.; Caffrey, M. Phases and phase transitions of the phosphatidylcholines. *Biochim. Biophys. Acta* **1998,** *1376* (1), 91-145.
58. Kellis, J. T., Jr.; Nyberg, K.; Sali, D.; Fersht, A. R. Contribution of hydrophobic interactions to protein stability. *Nature* **1988,** *333* (6175), 784-6.

59. Pace, C. N.; Fu, H.; Fryar, K. L.; Landua, J.; Trevino, S. R.; Shirley, B. A.; Hendricks, M. M.; Iimura, S.; Gajiwala, K.; Scholtz, J. M. Contribution of hydrophobic interactions to protein stability. *J. Mol. Biol.* **2011,** *408* (3), 514-528.

60. Ernst, J. A.; Clubb, R. T.; Zhou, H.-X.; Gronenborn, A. M.; Clore, G. M. Demonstration of positionally disordered water within a protein hydrophobic cavity by NMR. *Science* **1995,** *267* (5205), 1813-1817.

61. Sirotkin, V. A.; Khadiullina, A. V. Hydration of proteins: excess partial enthalpies of water and proteins. *J. Phys. Chem. B* **2011,** *115* (50), 15110-15118.

62. Hamilton, J. A.; Small, D. M. Solubilization and localization of triolein in phosphatidylcholine bilayers: a 13C NMR study. *Proc. Natl. Acad. Sci. U. S. A.* **1981,** *78* (11), 6878-6882.

63. Horinouchi, A.; Tanaka, K. An effect of stereoregularity on the structure of poly (methyl methacrylate) at air and water interfaces. *Rsc Adv.* **2013,** *3* (24), 9446-9452.

64. Brewer, S. H.; Tang, Y.; Vu, D. M.; Gnanakaran, S.; Raleigh, D. P.; Dyer, R. B. Temperature Dependence of Water Interactions with the Amide Carbonyls of α-Helices. *Biochemistry* **2012,** *51* (26), 5293-5299.

65. Chandra, A. K.; Zeegers-Huyskens, T. A theoretical investigation of the interaction between substituted carbonyl derivatives and water: open or cyclic complexes? *J. Comput. Chem.***2012,** *33* (11), 1131-1141.

66. Cao, K.; Murshid, N.; Li, L.; Lopez, A.; Tam, K. C.; Wang, X. Hydration of Hydrophobic Iron–Carbonyl Homopolymers via Water–Carbonyl Interaction (WCI): Creation of Uniform Organometallic Aqueous Vesicles with Exceptionally High Encapsulation Capacity. *Macromolecules* **2015,** *48* (21), 7968-7977.

67. Southall, N. T.; Dill, K. A. The mechanism of hydrophobic solvation depends on solute radius. *J. Phys. Chem. B* **2000,** *104* (6), 1326-1331.

68. Costas, M.; Kronberg, B. Thermodynamics of aliphatic and aromatic hydrocarbons in water. *Biophys. Chem.* **1998,** *74* (1), 83-87.

69. Mizuno, K.; Ochi, T.; Shindo, Y. Hydrophobic hydration of acetone probed by nuclear magnetic resonance and infrared: Evidence for the interaction C–H⋯ OH2. *J. Chem. Phys.* **1998,** *109* (21), 9502-9507.
70. Bhattacharyya, A.; Sengupta, S.; Bhattacharya, S. K. Hydrophobic hydration from solubilities of aliphatic hydrocarbons in water. *J. Mol. Liq.* **2015,** *204*, 176-183.
71. Blokzijl, W.; Engberts, J. B. Hydrophobic effects. Opinions and facts. *Angew. Chem., Int. Ed. Engl.* **1993,** *32* (11), 1545-1579.
72. Chandler, D. Interfaces and the driving force of hydrophobic assembly. *Nature* **2005,** *437* (7059), 640-647.
73. Lum, K.; Chandler, D.; Weeks, J. D. Hydrophobicity at small and large length scales. *J. Phys. Chem. B* **1999,** *103* (22), 4570-4577.
74. Long, J. A.; Rankin, B. M.; Ben-Amotz, D. Micelle Structure and Hydrophobic Hydration. *J. Am. Chem. Soc.* **2015,** *137* (33), 10809-10815.
75. Lukšič, M.; Urbic, T.; Hribar-Lee, B.; Dill, K. A. Simple model of hydrophobic hydration. *J. Phys. Chem. B* **2012,** *116* (21), 6177-6186.
76. Singh, T.; Kumar, A. Aggregation behavior of ionic liquids in aqueous solutions: effect of alkyl chain length, cations, and anions. *J. Phys. Chem. B* **2007,** *111* (27), 7843-7851.
77. Mizuguchi, T.; Ishizuka, R.; Matubayasi, N. Effect of diffuseness of micelle boundary on the solute distribution upon solubilization. *Chem. Phys. Lett.* **2015,** *624*, 19-23.
78. Hargreaves, R.; Bowron, D. T.; Edler, K. Atomistic structure of a Micelle in solution determined by wide Q-range neutron diffraction. *J. Am. Chem. Soc.* **2011,** *133* (41), 16524-16536.
79. Dill, K. A.; Flory, P. J. Molecular organization in micelles and vesicles. *Proc. Natl. Acad. Sci. U. S. A.***1981,** *78* (2), 676-680.
80. Gruen, D. The packing of amphiphile chains in a small spherical micelle. *J. Colloid Interface Sci.* **1981,** *84* (1), 281-283.

81. Menger, F.; Jerkunica, J.; Johnston, J. The water content of a micelle interior. The Fjord vs. Reef models. *J. Am. Chem. Soc.* **1978,** *100* (15), 4676-4678.

82. Menger, F.; Doll, D. W. On the structure of micelles. *J. Am. Chem. Soc.* **1984,** *106* (4), 1109-1113.

83. Parera, E.; Comelles, F.; Barnadas, R.; Suades, J. New surfactant phosphine ligands and platinum (II) metallosurfactants. influence of metal coordination on the critical micelle concentration and aggregation properties. *Langmuir* **2009,** *26* (2), 743-751.

84. Xing, P.; Sun, T.; Hao, A. Vesicles from supramolecular amphiphiles. *Rsc Adv.***2013,** *3* (47), 24776-24793.

85. Discher, D. E.; Eisenberg, A. Polymer vesicles. *Science* **2002,** *297* (5583), 967-973.

86. Antonietti, M.; Förster, S. Vesicles and liposomes: a self-assembly principle beyond lipids. *Adv Mater* **2003,** *15* (16), 1323-1333.

87. Janiak, M. J.; Small, D. M.; Shipley, G. G. Temperature and compositional dependence of the structure of hydrated dimyristoyl lecithin. *J Biol Chem* **1979,** *254* (13), 6068-6078.

88. Madni, A.; Sarfraz, M.; Rehman, M.; Ahmad, M.; Akhtar, N.; Ahmad, S.; Tahir, N.; Ijaz, S.; Al-Kassas, R.; Löbenberg, R. Liposomal drug delivery: a versatile platform for challenging clinical applications. *J. Pharm. Pharm. Sci.* **2014,** *17* (3), 401-426.

89. Cao, Y.; Hu, X.-Y.; Li, Y.; Zou, X.; Xiong, S.; Lin, C.; Shen, Y.-Z.; Wang, L. Multistimuli-responsive supramolecular vesicles based on water-soluble pillar [6] arene and SAINT complexation for controllable drug release. *J. Am. Chem. Soc.* **2014,** *136* (30), 10762-10769.

90. Wang, Y.-X.; Zhang, Y.-M.; Wang, Y.-L.; Liu, Y. Multifunctional Vehicle of Amphiphilic Calix [4] arene Mediated by Liposome. *Chem. Mater.* **2015,** *27* (8), 2848-2854.

91. Letchford, K.; Burt, H. A review of the formation and classification of amphiphilic block copolymer nanoparticulate structures: micelles, nanospheres, nanocapsules and polymersomes. *Eur. J. Pharm. Biopharm.* **2007,** *65* (3), 259-269.

92. Mai, Y.; Eisenberg, A. Self-assembly of block copolymers. *Chem. Soc. Rev.* **2012,** *41* (18), 5969-5985.

93. Owen, S. C.; Chan, D. P.; Shoichet, M. S. Polymeric micelle stability. *Nano Today* **2012,** *7* (1), 53-65.

94. Policar, C.; Waern, J. B.; Plamont, M. A.; Clède, S.; Mayet, C.; Prazeres, R.; Ortega, J. M.; Vessières, A.; Dazzi, A. Subcellular IR imaging of a metal–carbonyl moiety using photothermally induced resonance. *Angew. Chem. Int. Ed.* 2011, 50 (4), 860 – 864.

95. Oda, Y.; Horinouchi, A.; Kawaguchi, D.; Matsuno, H.; Kanaoka, S.; Aoshima, S.; Tanaka, K. Effect of Side-Chain Carbonyl Groups on the Interface of Vinyl Polymers with Water. *Langmuir* **2014,** *30* (5), 1215-1219.

96. Makhatadze, G. I.; Privalov, P. L. Contribution of hydration to protein folding thermodynamics: I. The enthalpy of hydration. *J Mol Biol* **1993,** *232* (2), 639-659.

97. Green, M. L. H.; Hurley, C. R. *J. Organornet. Chem* **1967,** *10*.

98. Liu, J.; Cao, K.; Nayyar, B.; Tian, X.; Wang, X. Synthesis and migration insertion polymerization (MIP) of CpFe (CO) 2 (CH 2) 6 PPh 2 (FpC6P) for PFpC6P: macromolecule stability, degradability and redox activity. *Polym. Chem.* **2014,** *5* (23), 6702-6709.

99. Cao, K.; Ward, J.; Amos, R. C.; Jeong, M. G.; Kim, K. T.; Gauthier, M.; Foucher, D.; Wang, X. Organometallic macromolecules with piano stool coordination repeating units: chain configuration and stimulated solution behaviour. *Chem. Commun.* **2014,** *50* (70), 10062-10065.

100. Anderson, M. S. Enhanced infrared absorption with dielectric nanoparticles. *Appl. Phys. Lett.* **2003,** *83* (14), 2964-2966.

101. Domínguez, A.; Fernández, A.; González, N.; Iglesias, E.; Montenegro, L. Determination of critical micelle concentration of some surfactants by three techniques. *J. Chem. Educ* **1997,** *74* (10), 1227.

102. Kita-Tokarczyk, K.; Grumelard, J.; Haefele, T.; Meier, W. Block copolymer vesicles—using concepts from polymer chemistry to mimic biomembranes. *Polymer* **2005,** *46* (11), 3540-3563.

103. Dement'ev, V. V.; Cervantes-Lee, F.; Parkanyi, L.; Sharma, H.; Pannell, K. H.; Nguyen, M. T.; Diaz, A. Structure and electrochemistry of ferrocenyloligosilanes:. alpha.,. omega.-bis (ferrocenyl)-and. alpha.,. omega.-(1, 1'-ferrocenediyl) oligosilanes. *Organometallics* **1993,** *12* (5), 1983-1987.

104. Rulkens, R.; Lough, A. J.; Manners, I.; Lovelace, S. R.; Grant, C.; Geiger, W. E. Linear oligo (ferrocenyldimethylsilanes) with between two and nine ferrocene units: Electrochemical and structural models for poly (ferrocenylsilane) high polymers. *J. Am. Chem. Soc.* **1996,** *118* (50), 12683-12695.

105. Foucher, D. A.; Honeyman, C. H.; Nelson, J. M.; Tang, B. Z.; Manners, I. Organometallic ferrocenyl polymers displaying tunable cooperative interactions between transition metal centers. *Angew. Chem., Int. Ed. Engl.* **1993,** *32* (12), 1709-1711.

106. Tsierkezos, N. G. Cyclic voltammetric studies of ferrocene in nonaqueous solvents in the temperature range from 248.15 to 298.15 K. *J. Solution Chem.* **2007,** *36* (3), 289-302.

107. Spataru, T.; Birke, R. L. The effect of solvent on the electrode process of methylcobalamine as studied by cyclic voltammetry. *J. Electroanal. Chem.* **2006,** *593* (1), 74-86.

108. Tu, C.-W.; Kuo, S.-W. Using FTIR spectroscopy to study the phase transitions of poly (N-isopropylacrylamide) in tetrahydrofuran-d 8/D2O. *J. Polym. Res.* **2014,** *21* (6), 1-8.

109. Hahn, F.; Melendres, C. Anodic oxidation of methane at noble metal electrodes: an ‘in situ’surface enhanced infrared spectroelectrochemical study. *Electrochim. Acta* **2001,** *46* (23), 3525-3534.

110. Hartstein, A.; Kirtley, J.; Tsang, J. Enhancement of the infrared absorption from molecular monolayers with thin metal overlayers. *Phys. Rev. Lett.* **1980,** *45* (3), 201.
111. Ebbesen, S. D.; Mojet, B. L.; Lefferts, L. CO adsorption and oxidation at the catalyst-water interface: An investigation by attenuated total reflection infrared spectroscopy. *Langmuir* **2006,** *22* (3), 1079-1085.
112. Greeneltch, N. G.; Blaber, M. G.; Schatz, G. C.; Van Duyne, R. P. Plasmon-sampled surface-enhanced Raman excitation spectroscopy on silver immobilized nanorod assemblies and optimization for near infrared (λex= 1064 nm) studies. *J. Phys. Chem. C* **2012,** *117* (6), 2554-2558.
113. Rong, Z.; Xiao, R.; Wang, C.; Wang, D.; Wang, S. Plasmonic Ag Core–Satellite Nanostructures with a Tunable Silica-Spaced Nanogap for Surface-Enhanced Raman Scattering. *Langmuir* **2015,** *31* (29), 8129-8137.
114. Osawa, M. Surface-enhanced infrared absorption. In *Near-Field Optics and Surface Plasmon Polaritons*; Springer, 2001, pp 163-187.
115. Chen, X.; Ciracì, C.; Smith, D. R.; Oh, S.-H. Nanogap-enhanced infrared spectroscopy with template-stripped wafer-scale arrays of buried plasmonic cavities. *Nano letters* **2014,** *15* (1), 107-113.
116. Zheng, M.; Sun, S.; Chen, S. Abnormal infrared effects and electrocatalytic properties of nanometer scale thin film of PtRu alloys for CO adsorption and oxidation. *J. Appl. Electrochem.* **2001,** *31* (7), 749-757.
117. Kong, K. V.; Lam, Z.; Goh, W. D.; Leong, W. K.; Olivo, M. Metal Carbonyl–Gold Nanoparticle Conjugates for Live-Cell SERS Imaging. *Angew. Chem., Int. Ed.* **2012,** *51* (39), 9796-9799.
118. Murshid, N.; Wang, X. Iron–Carbonyl Aqueous Vesicles (MCsomes) by Hydration of [Fe (CO){CO (CH2) 5CH3}(Cp)(PPh3)](FpC6): Highly Integrated Colloids with Aggregation-Induced Self-Enhanced IR Absorption (AI-SEIRA). *Chem. - Eur. J.* **2015,** *21* (52), 19223-19230.

119. Murshid, N.; Yuyama, K.-i.; Wu, S.-L.; Wu, K.-Y.; Masuhara, H.; Wang, C.-L.; Wang, X. Highly-integrated, laser manipulable aqueous metal carbonyl vesicles (MCsomes) with aggregation-induced emission (AIE) and aggregation-enhanced IR absorption (AEIRA). *J. Mater. Chem. C* **2016,** *4* (23), 5231-5240.

120. Yin, X.; Moss, J. R. Synthesis and characterization of long chain acyl and alkyl complexes of the types [(η 5-C 5 R′ 5) Fe (CO) 2 {C (O) R}](R′= H, CH 3),[CpW (CO) 3 {C (O) R}] and [CpW (CO) 3 R](R= n-alkyl). *Inorg. Chim. Acta* **1999,** *286* (2), 221-228.

121. Howell, J. A.; Rowan, A. J. Carbon–oxygen and carbon–hydrogen bond cleavage in the reaction of [{Ru (CO) 2 (η 5-C 5 H) 5} 2]+ with phosphite and phosphine ligands. *J. Chem. Soc., Dalton Trans* **1980,** (10), 1845-1851.

122. Amenta, D. S.; Morton, A. D.; Gilje, J. W.; Edelmann, F. T.; Fischer, A.; Blaurock, S. The preparation and crystal structure of (η 5-C 5 H 5)(OC) 3 Mo (CH 2) 3 C 6 H 5. *J. Organomet. Chem.* **2006,** *691* (23), 5065-5068.

123. Pannell, K. H.; Cea-Olivares, R.; Toscano, R. A.; Kapoor, R. N. Synthesis of a molybdenum-substituted furan from [(. eta. 5-C5H5) Mo (CO) 3]-Na+ and epibromohydrin in the presence of triphenylphosphine; trans-[(. eta. 5-C5H5) Mo (CO) 2 (PPh3)(2-furan)]. *Organometallics* **1987,** *6* (8), 1821-1822.

124. Coxon, J. M.; Hartshorn, M.; Swallow, W. Acetate participation in acyclic epoxide systems. Acid-catalyzed rearrangements of trans-and cis-1-acetoxy-3, 4-epoxypentanes,-4, 5-epoxyhexanes, and-5, 6-epoxyheptanes. *J. Org. Chem.* **1974,** *39* (8), 1142-1148.

125. Topel, Ö.; Çakır, B. A.; Budama, L.; Hoda, N. Determination of critical micelle concentration of polybutadiene-block-poly (ethyleneoxide) diblock copolymer by fluorescence spectroscopy and dynamic light scattering. *J. Mol. Liq.* **2013,** *177*, 40-43.

126. Jain, N.; Trabelsi, S.; Guillot, S.; McLoughlin, D.; Langevin, D.; Letellier, P.; Turmine, M. Critical aggregation concentration in mixed solutions of anionic polyelectrolytes and cationic surfactants. *Langmuir* **2004,** *20* (20), 8496-8503.

127. Dominguez, A.; Fernandez, A.; Gonzalez, N.; Iglesias, E.; Montenegro, L. Determination of critical micelle concentration of some surfactants by three techniques. *J. Chem. Educ.* **1997,** *74* (10), 1227.

128. Quirk, A.; Unni, B.; Burgess, I. J. Surface Enhanced Infrared Studies of 4-Methoxypyridine Adsorption on Gold Film Electrodes. *Langmuir* **2016,** *32* (9), 2184-2191.

129. Stuart, H. R.; Hall, D. G. Island size effects in nanoparticle-enhanced photodetectors. *Appl. Phys. Lett.* **1998,** *73* (26), 3815-3817.

130. Cassar, R. N.; Graham, D.; Larmour, I.; Wark, A. W.; Faulds, K. Synthesis of size tunable monodispersed silver nanoparticles and the effect of size on SERS enhancement. *Vib. Spectrosc.* **2014,** *71*, 41-46.

131. Gruenke, N. L.; Cardinal, M. F.; McAnally, M. O.; Frontiera, R. R.; Schatz, G. C.; Van Duyne, R. P. Ultrafast and nonlinear surface-enhanced Raman spectroscopy. *Chem. Soc. Rev.* **2016,** *45* (8), 2263-90.

132. Cathcart, N.; Kitaev, V. Multifaceted prismatic silver nanoparticles: synthesis by chloride-directed selective growth from thiolate-protected clusters and SERS properties. *Nanoscale* **2012,** *4* (22), 6981-6989.

133. Lehn, J. M. Perspectives in Supramolecular Chemistry—From Molecular Recognition towards Molecular Information Processing and Self-Organization. *Angew. Chem., Int. Ed. Engl.* **1990,** *29* (11), 1304-1319.

134. Aida, T.; Meijer, E.; Stupp, S. Functional supramolecular polymers. *Science* **2012,** *335* (6070), 813-817.

135. De Greef, T. F.; Smulders, M. M.; Wolffs, M.; Schenning, A. P.; Sijbesma, R. P.; Meijer, E. Supramolecular polymerization. *Chem. Rev.* **2009,** *109* (11), 5687-5754.

136. Elacqua, E.; Lye, D. S.; Weck, M. Engineering orthogonality in supramolecular polymers: from simple scaffolds to complex materials. *Acc. Chem. Res.* **2014,** *47* (8), 2405-2416.

137. Cook, T. R.; Zheng, Y.-R.; Stang, P. J. Metal–organic frameworks and self-assembled supramolecular coordination complexes: comparing and contrasting the design, synthesis, and functionality of metal–organic materials. *Chem. Rev.* **2012,** *113* (1), 734-777.

138. Würthner, F.; Saha-Möller, C. R.; Fimmel, B.; Ogi, S.; Leowanawat, P.; Schmidt, D. Perylene Bisimide Dye Assemblies as Archetype Functional Supramolecular Materials. *Chem. Rev.* **2015**.

139. Harada, A.; Takashima, Y.; Nakahata, M. Supramolecular polymeric materials via cyclodextrin–guest interactions. *Acc. Chem. Res.* **2014,** *47* (7), 2128-2140.

140. Qiu, H.; Hudson, Z. M.; Winnik, M. A.; Manners, I. Multidimensional hierarchical self-assembly of amphiphilic cylindrical block comicelles. *Science* **2015,** *347* (6228), 1329-1332.

141. Wong, W.-Y.; Dong, Q.; Cheung, S.-H.; Lau, P.-L.; Zhu, N.-Y.; Lo, Y. H.; Li, H. Synthesis, Characterization and Electrochemistry of Some Metal Carbonyl Clusters Derived from Ferrocenylethynylpyridine. *J. Cluster Sci.* **2015,** *26* (2), 461-471.

142. Zukerman-Schpector, J.; Haiduc, I.; Tiekink, E. R. The metal–carbonylπ (aryl) interaction as a supramolecular synthon for the stabilisation of transition metal carbonyl crystal structures. *Chem. Commun.* **2011,** *47* (47), 12682-12684.

143. Amoroso, A. J.; Coogan, M. P.; Dunne, J. E.; Fernández-Moreira, V.; Hess, J. B.; Hayes, A. J.; Lloyd, D.; Millet, C.; Pope, S. J.; Williams, C. Rhenium fac tricarbonyl bisimine complexes: biologically useful fluorochromes for cell imaging applications. *Chem. Commun.* **2007,** (29), 3066-3068.

144. Das, A.; Ghosh, S. Luminescent invertible polymersome by remarkably stable supramolecular assembly of naphthalene diimide (NDI) π-system. *Macromolecules* **2013,** *46* (10), 3939-3949.

145. Deng, S.-L.; Chen, T.-L.; Chien, W.-L.; Hong, J.-L. Aggregation-enhanced emission in fluorophores containing pyridine and triphenylamine terminals: restricted molecular rotation and hydrogen-bond interaction. *J. Mater. Chem. C* **2014,** *2* (4), 651-659.

146. Ravindran, E.; Ananthakrishnan, S. J.; Varathan, E.; Subramanian, V.; Somanathan, N. White light emitting single polymer from aggregation enhanced emission: a strategy through supramolecular assembly. *J. Mater. Chem. C* **2015,** *3* (17), 4359-4371.

147. Shao, A.; Xie, Y.; Zhu, S.; Guo, Z.; Zhu, S.; Guo, J.; Shi, P.; James, T. D.; Tian, H.; Zhu, W. H. Far-Red and Near-IR AIE-Active Fluorescent Organic Nanoprobes with Enhanced Tumor-Targeting Efficacy: Shape-Specific Effects. *Angew. Chem., Int. Ed.* **2015,** *54* (25), 7275-7280.

148. Guo, Z.; Shao, A.; Zhu, W.-H. Long wavelength AIEgen of quinoline-malononitrile. *J. Mater. Chem. C* **2016**.

149. Prodi, L.; Bolletta, F.; Montalti, M.; Zaccheroni, N. Luminescent chemosensors for transition metal ions. *Coord. Chem. Rev.* **2000,** *205* (1), 59-83.

150. Varnes, A. W.; Dodson, R. B.; Wehry, E. Interactions of transition-metal ions with photoexcited states of flavines. Fluorescence quenching studies. *J. Am. Chem. Soc.* **1972,** *94* (3), 946-950.

151. Hong, Y.; Lam, J. W.; Tang, B. Z. Aggregation-induced emission: phenomenon, mechanism and applications. *Chem. Commun.* **2009,** (29), 4332-4353.

152. Chen, G.; Li, W.; Zhou, T.; Peng, Q.; Zhai, D.; Li, H.; Yuan, W. Z.; Zhang, Y.; Tang, B. Z. Conjugation-Induced Rigidity in Twisting Molecules: Filling the Gap Between Aggregation-Caused Quenching and Aggregation-Induced Emission. *Adv Mater* **2015,** *27* (30), 4496-4501.

153. Hong, Y.; Lam, J. W.; Tang, B. Z. Aggregation-induced emission. *Chem. Soc. Rev.* **2011,** *40* (11), 5361-5388.

154. Fedor, A. M.; Allis, D. G.; Korter, T. M. The terahertz spectrum and quantum chemical assignment of 2, 2′-bithiophene in cyclohexane. *Vib. Spectrosc.* **2009,** *49* (2), 124-132.

155. Speck, J. M. u.; Schaarschmidt, D.; Lang, H. Atropisomeric 3, 3′, 4, 4′, 5, 5′-Hexaferrocenyl-2, 2′-bithiophene: Synthesis, Solid-State Structure, and Electrochemistry. *Organometallics* **2012,** *31* (5), 1975-1982.

156. Einkauf, J. D.; Mathivathanan, L.; de Lill, D. T. Structural, spectroscopic, and computational studies of [2, 2′-bithiophene]-5-carboxylic acid. *J. Mol. Struct.* **2016,** *1104*, 33-39.

157. Tanner, P.; Baumann, P.; Enea, R.; Onaca, O.; Palivan, C.; Meier, W. Polymeric vesicles: from drug carriers to nanoreactors and artificial organelles. *Acc. Chem. Res.* **2011,** *44* (10), 1039-1049.

158. Marguet, M.; Bonduelle, C.; Lecommandoux, S. Multicompartmentalized polymeric systems: towards biomimetic cellular structure and function. *Chem. Soc. Rev.* **2013,** *42* (2), 512-529.

159. Bendix, P. M.; Oddershede, L. B. Expanding the optical trapping range of lipid vesicles to the nanoscale. *Nano letters* **2011,** *11* (12), 5431-5437.

160. Cherney, D. P.; Conboy, J. C.; Harris, J. M. Optical-trapping Raman microscopy detection of single unilamellar lipid vesicles. *Anal. chem.* **2003,** *75* (23), 6621-6628.

161. Park, S.; Choi, S. Q.; Song, C.; Kim, M. W.; Choi, M. C. Surface charge effects on optical trapping of nanometer-sized lipid vesicles. *Soft matter* **2014,** *10* (42), 8406-8412.

162. Ichikawa, M.; Yoshikawa, K. Optical transport of a single cell-sized liposome. *Appl. Phys. Lett.* **2001,** *79* (27), 4598-4600.

163. Sugiyama, T.; Yuyama, K.-i.; Masuhara, H. Laser trapping chemistry: From polymer assembly to amino acid crystallization. *Acc. Chem. Res.* **2012,** *45* (11), 1946-1954.

164. Lee, T.-H.; Hirst, D. J.; Aguilar, M.-I. New insights into the molecular mechanisms of biomembrane structural changes and interactions by optical biosensor technology. *Biochim. Biophys. Acta* **2015,** *1848* (9), 1868-1885.

165. Allen, T. M.; Cullis, P. R. Liposomal drug delivery systems: from concept to clinical applications. *Adv. Drug Delivery Rev.* **2013,** *65* (1), 36-48.

166. Suwanpayak, N.; Jalil, M. A.; Teeka, C.; Ali, J.; Yupapin, P. P. Optical vortices generated by a PANDA ring resonator for drug trapping and delivery applications. *Biomed. Opt. Express* **2011,** *2* (1), 159-168.

167. Discher, B. M.; Bermudez, H.; Hammer, D. A.; Discher, D. E.; Won, Y.-Y.; Bates, F. S. Cross-linked polymersome membranes: vesicles with broadly adjustable properties. *J. Phys. Chem. B* **2002,** *106* (11), 2848-2854.

168. Li, F.; Ketelaar, T.; Marcelis, A. T.; Leermakers, F. A.; Cohen Stuart, M. A.; Sudhölter, E. J. Stabilization of polymersome vesicles by an interpenetrating polymer network. *Macromolecules* **2007,** *40* (2), 329-333.

169. Nguyen, Q. N. N.; Lodewyk, M. W.; Bezer, S.; Gagné, M. R.; Waters, M. L.; Tantillo, D. J. Effects of helix macrodipole and local interactions on catalysis of acyl transfer by α-helical peptides. *ACS Catalysis* **2015,** *5* (3), 1617-1622.

170. Wolfenden, R. Interaction of the peptide bond with solvent water: a vapor phase analysis. *Biochemistry* **1978,** *17* (1), 201-204.

171. Mahato, P.; Saha, S.; Choudhury, S.; Das, A. Solvent-dependent aggregation behavior of a new Ru (II)-polypyridyl based metallosurfactant. *Chem. Commun.* **2011,** *47* (39), 11074-11076.

172. Battaglia, G.; Ryan, A. J. Bilayers and interdigitation in block copolymer vesicles. *J. Am. Chem. Soc.* **2005,** *127* (24), 8757-8764.

173. Bouwstra, J.; Gooris, G.; Bras, W.; Talsma, H. Small angle X-ray scattering: possibilities and limitations in characterization of vesicles. *Chem. Phys. Lipids* **1993,** *64* (1), 83-98.

174. Chang, Z.; Jiang, Y.; He, B.; Chen, J.; Yang, Z.; Lu, P.; Kwok, H. S.; Zhao, Z.; Qiu, H.; Tang, B. Z. Aggregation-enhanced emission and efficient electroluminescence of tetraphenylethene-cored luminogens. *Chem. Commun.* **2013,** *49* (6), 594-596.

175. Luo, J.; Xie, Z.; Lam, J. W.; Cheng, L.; Chen, H.; Qiu, C.; Kwok, H. S.; Zhan, X.; Liu, Y.; Zhu, D. Aggregation-induced emission of 1-methyl-1, 2, 3, 4, 5-pentaphenylsilole. *Chem. Commun.* **2001,** (18), 1740-1741.

176. Tang, W.; Xiang, Y.; Tong, A. Salicylaldehyde azines as fluorophores of aggregation-induced emission enhancement characteristics. *J. Org. Chem.* **2009,** *74* (5), 2163-2166.

177. YeuláRyu, S.; YoungáPark, S. Strong fluorescence emission induced by supramolecular assembly and gelation: luminescent organogel from nonemissive oxadiazole-based benzene-1, 3, 5-tricarboxamide gelator. *Chem. Commun.* **2004,** (1), 70-71.

178. Bhongale, C. J.; Chang, C.-W.; Lee, C.-S.; Diau, E. W.-G.; Hsu, C.-S. Relaxation dynamics and structural characterization of organic nanoparticles with enhanced emission. *J. Phys. Chem. B* **2005,** *109* (28), 13472-13482.

179. Zhao, K.; Gong, Q.; Zhang, R. X.; Yang, J.; Huang, Z. Y.; Li, N.; Tang, B. Z. Materials Chemistry C. *J. Mater. Chem* **2015,** *100* (3), 7802-7812.

180. Brouwer, A. M. Standards for photoluminescence quantum yield measurements in solution (IUPAC Technical Report). *Pure Appl. Chem.* **2011,** *83* (12), 2213-2228.

181. Chen, J.; Law, C. C.; Lam, J. W.; Dong, Y.; Lo, S. M.; Williams, I. D.; Zhu, D.; Tang, B. Z. Synthesis, light emission, nanoaggregation, and restricted intramolecular rotation of 1, 1-substituted 2, 3, 4, 5-tetraphenylsiloles. *Chem. Mater.* **2003,** *15* (7), 1535-1546.

182. Mukundam, V.; Dhanunjayarao, K.; Mamidala, R.; Venkatasubbaiah, K. Synthesis, characterization and aggregation induced enhanced emission properties of tetraaryl pyrazole decorated cyclophosphazenes. *J. Mater. Chem. C* **2016**.

183. Qiu, Y.; Park, K. Environment-sensitive hydrogels for drug delivery. *Adv. Drug Delivery Rev.* **2012,** *64*, 49-60.

184. Samad, A.; Sultana, Y.; Aqil, M. Liposomal drug delivery systems: an update review. *Curr. Drug Delivery* **2007,** *4* (4), 297-305.

185. Ryu, S.; Yoo, I.; Song, S.; Yoon, B.; Kim, J.-M. A thermoresponsive fluorogenic conjugated polymer for a temperature sensor in microfluidic devices. *J. Am. Chem. Soc.* **2009,** *131* (11), 3800-3801.

186. Kim, Y.-R.; Jung, S.; Ryu, H.; Yoo, Y.-E.; Kim, S. M.; Jeon, T.-J. Synthetic biomimetic membranes and their sensor applications. *Sensors* **2012,** *12* (7), 9530-9550.

187. Ashkin, A.; Dziedzic, J.; Yamane, T. Optical trapping and manipulation of single cells using infrared laser beams. *Nature* **1987,** *330* (6150), 769-771.

188. Hutchison, J. B.; Rodesney, C. A.; Kaushik, K. S.; Le, H. H.; Hurwitz, D. A.; Irie, Y.; Gordon, V. D. Single-cell control of initial spatial structure in biofilm development using laser trapping. *Langmuir* **2014,** *30* (15), 4522-4530.

189. Pang, Y.; Song, H.; Kim, J. H.; Hou, X.; Cheng, W. Optical trapping of individual human immunodeficiency viruses in culture fluid reveals heterogeneity with single-molecule resolution. *Nat. Nanotechnol.* **2014,** *9* (8), 624-630.

190. Kitamura, N.; Sekiguchi, N.; Kim, H.-B. Optical transformation and fission of single giant vesicles in water by radiation pressure. *J. Am. Chem. Soc.* **1998,** *120* (8), 1942-1943.

191. Hotta, J.-i.; Sasaki, K.; Masuhara, H. A single droplet formation from swelled micelles by radiation pressure of a focused infrared laser beam. *J. Am. Chem. Soc.* **1996,** *118* (47), 11968-11969.

192. Harada, Y.; Asakura, T. Radiation forces on a dielectric sphere in the Rayleigh scattering regime. *Opt. Commun.* **1996,** *124* (5), 529-541.

193. Deshpande, S.; Caspi, Y.; Meijering, A. E.; Dekker, C. Octanol-assisted liposome assembly on chip. *Nat. Commun.* **2016,** *7*.

194. Spring, B. Q.; Sears, R. B.; Zheng, L. Z.; Mai, Z.; Watanabe, R.; Sherwood, M. E.; Schoenfeld, D. A.; Pogue, B. W.; Pereira, S. P.; Villa, E. A photoactivable multi-inhibitor nanoliposome for tumour control and simultaneous inhibition of treatment escape pathways. *Nat. Nanotechnol.* **2016**.

195. Karlsson, M.; Davidson, M.; Karlsson, R.; Karlsson, A.; Bergenholtz, J.; Konkoli, Z.; Jesorka, A.; Lobovkina, T.; Hurtig, J.; Voinova, M. Biomimetic nanoscale reactors and networks. *Annu. Rev. Phys. Chem.* **2004,** *55*, 613-649.

196. Wilson, D. A.; Nolte, R. J.; van Hest, J. C. Autonomous movement of platinum-loaded stomatocytes. *Nat. chem.* **2012,** *4* (4), 268-274.

197. Gaitzsch, J.; Appelhans, D.; Wang, L.; Battaglia, G.; Voit, B. Synthetic Bio-nanoreactor: Mechanical and Chemical Control of Polymersome Membrane Permeability. *Angew. Chem., Int. Ed.* **2012,** *51* (18), 4448-4451.

198. Kim, K. T.; Cornelissen, J. J.; Nolte, R. J.; van Hest, J. A Polymersome Nanoreactor with Controllable Permeability Induced by Stimuli-Responsive Block Copolymers. *Adv. Mater.* **2009,** *21* (27), 2787-2791.

199. Lomora, M.; Itel, F.; Dinu, I. A.; Palivan, C. G. Selective ion-permeable membranes by insertion of biopores into polymersomes. *Phys. Chem. Chem. Phys.* **2015,** *17* (24), 15538-15546.

200. Haas, S.; Hain, N.; Raoufi, M.; Handschuh-Wang, S.; Wang, T.; Jiang, X.; Schönherr, H. Enzyme degradable polymersomes from hyaluronic acid-block-poly (ε-caprolactone) copolymers for the detection of enzymes of pathogenic bacteria. *Biomacromolecules* **2015,** *16* (3), 832-841.

201. Lomas, H.; Canton, I.; MacNeil, S.; Du, J.; Armes, S. P.; Ryan, A. J.; Lewis, A. L.; Battaglia, G. Biomimetic pH sensitive polymersomes for efficient DNA encapsulation and delivery. *Adv Mater* **2007,** *19* (23), 4238-4243.

202. Kim, H.; Kang, Y. J.; Kang, S.; Kim, K. T. Monosaccharide-responsive release of insulin from polymersomes of polyboroxole block copolymers at neutral pH. *J. Am. Chem. Soc.* **2012,** *134* (9), 4030-4033.

203. Rupley, J. A.; Careri, G. Protein hydration and function. *Adv. Protein Chem.* **1991,** *41*, 37-172.

204. Kellis, J. T.; Nyberg, K.; Fersht, A. R. Contribution of hydrophobic interactions to protein stability. **1988**.

205. Wiggins, P. M. Hydrophobic hydration, hydrophobic forces and protein folding. *Phys. A* **1997,** *238* (1), 113-128.

206. Qin, Y.; Wang, L.; Zhong, D. Dynamics and mechanism of ultrafast water–protein interactions. *Proc. Natl. Acad. Sci. U. S. A.***2016,** *113* (30), 8424-8429.

207. Kuffel, A.; Zielkiewicz, J. Why the solvation water around proteins is more dense than bulk water. *J. Phys. Chem. B* **2012,** *116* (40), 12113-12124.

208. Cheng, Y.-K.; Rossky, P. J. Surface topography dependence of biomolecular hydrophobic hydration. *Nature* **1998,** *392* (6677), 696-699.

209. Zhang, L.; Hermans, J. Hydrophilicity of cavities in proteins. *Proteins: Struct., Funct., Bioinf.* **1996,** *24* (4), 433-438.

210. Ernst, J. A.; Clubb, R. T.; Zhou, H.-X.; Gronenborn, A. M.; Clore, G. M. Demostration of positionally disordered water within a protein hydrophobic cavity by NMR. *Science* **1995,** *267* (5205), 1813.

211. Roche, J.; Louis, J. M.; Bax, A.; Best, R. B. Pressure-induced structural transition of mature HIV-1 protease from a combined NMR/MD simulation approach. *Proteins: Struct., Funct., Bioinf.* **2015,** *83* (12), 2117-2123.

212. Sastry, N. V.; Vaghela, N. M.; Aswal, V. K. Effect of alkyl chain length and head group on surface active and aggregation behavior of ionic liquids in water. *Fluid Phase Equilib.* **2012,** *327*, 22-29.

213. Menger, F. M.; Shi, L. Exposure of self-assembly interiors to external elements. A kinetic approach. *J. Am. Chem. Soc.* **2006,** *128* (29), 9338-9339.

214. Svens, B.; Rosenholm, B. An investigation of the size and structure of the micelles in sodium octanoate solutions by small-angle X-ray scattering. *J. Colloid Interface Sci.* **1973,** *44* (3), 495-504.

215. Murshid, N.; Rahman, M. A.; Wang, X. Aggregation-enhanced IR absorption (AEIRA) of molybdenum-carbonyl organometallic aqueous colloids. *J. Organomet. Chem.* **2016,** *819*, 109-114.

216. Symons, M. C.; Eaton, G. Solvation of acetone in protic and aprotic solvents and binary solvent mixtures. *J. Chem. Soc., Faraday Trans. 1* **1985,** *81* (8), 1963-1977.

217. Meng, J.-y.; Tang, X.-f.; Li, W.; Shi, H.-f.; Zhang, X.-x. Crystal structure and thermal property of polyethylene glycol octadecyl ether. *Thermochim. Acta* **2013,** *558*, 83-86.

218. Hill, I. R.; Levin, I. W. Vibrational spectra and carbon–hydrogen stretching mode assignments for a series of n-alkyl carboxylic acids. *The J. Chem. Phys.* **1979,** *70* (2), 842-851.

219. Marchessault, R.; Liang, C. The infrared spectra of crystalline polysaccharides. VIII. Xylans. *J. Polym. Sci.* **1962,** *59* (168), 357-378.

220. Snyder, R.; Hsu, S.; Krimm, S. Vibrational spectra in the C□ H stretching region and the structure of the polymethylene chain. *Spectrochim. Acta, Part A* **1978,** *34* (4), 395-406.

221. Snyder, R.; Strauss, H.; Elliger, C. Carbon-hydrogen stretching modes and the structure of n-alkyl chains. 1. Long, disordered chains. *J. Phys. Chem.* **1982,** *86* (26), 5145-5150.

222. Nebot, V. J.; Armengol, J.; Smets, J.; Prieto, S. F.; Escuder, B.; Miravet, J. F. Molecular Hydrogels from Bolaform Amino Acid Derivatives: A Structure–Properties Study Based on the Thermodynamics of Gel Solubilization. *Chem. - Eur. J.* **2012,** *18* (13), 4063-4072.

223. Liu, Y.; Wolf, L. K.; Messmer, M. C. A study of alkyl chain conformational changes in self-assembled n-octadecyltrichlorosilane monolayers on fused silica surfaces. *Langmuir* **2001,** *17* (14), 4329-4335.

224. Stein, M. J.; Weidner, T.; McCrea, K.; Castner, D. G.; Ratner, B. D. Hydration of sulphobetaine and tetra (ethylene glycol)-terminated self-assembled monolayers

studied by sum frequency generation vibrational spectroscopy. *J. Phys. Chem. B* **2009,** *113* (33), 11550-11556.

225. Polarz, S.; Landsmann, S.; Klaiber, A. Hybrid Surfactant Systems with Inorganic Constituents. *Angew. Chem., Int. Ed.* **2014,** *53* (4), 946-954.

226. Roldán-Carmona, C.; González-Delgado, A. M.; Guerrero-Martínez, A.; De Cola, L.; Giner-Casares, J. J.; Pérez-Morales, M.; Martín-Romero, M. T.; Camacho, L. Molecular organization and effective energy transfer in iridium metallosurfactant–porphyrin assemblies embedded in Langmuir–Schaefer films. *Phys. Chem. Chem. Phys.* **2011,** *13* (7), 2834-2841.

227. Gohy, J. F.; Lohmeijer, B. G.; Schubert, U. S. From Supramolecular Block Copolymers to Advanced Nano-Objects. *Chem. - Eur. J.* **2003,** *9* (15), 3472-3479.

228. Torriero, A. A.; Howlett, P. C. Ionic liquid effects on the redox potential of ferrocene. *Electrochemistry communications* **2012,** *16* (1), 84-87.

229. Harris, J. M.; Struck, E. C.; Case, M. G.; Paley, M. S.; Yalpani, M.; Van Alstine, J. M.; Brooks, D. E. Synthesis and characterization of poly (ethylene glycol) derivatives. *J. Polym. Sci. : Polymer Chemistry Edition* **1984,** *22* (2), 341-352.

230. Ribeiro, M. E.; de Moura, C. L.; Vieira, M. G.; Gramosa, N. V.; Chaibundit, C.; de Mattos, M. C.; Attwood, D.; Yeates, S. G.; Nixon, S. K.; Ricardo, N. M. Solubilisation capacity of Brij surfactants. *Int. J. Pharm.* **2012,** *436* (1), 631-635.

231. Holme, M. N.; Fedotenko, I. A.; Abegg, D.; Althaus, J.; Babel, L.; Favarger, F.; Reiter, R.; Tanasescu, R.; Zaffalon, P.-L.; Ziegler, A. Shear-stress sensitive lenticular vesicles for targeted drug delivery. *Nat. Nanotechnol.* **2012,** *7* (8), 536-543.

232. Nandy, D.; Mitra, R. K.; Paul, B. K. Phase behavior of mixtures of polyoxyethylene (10) stearyl ether (Brij-76), 1-butanol, isooctane, and mixed polar solvents: I. Water and formamide (or N, N-dimethyl formamide). *J. Colloid Interface Sci.* **2006,** *300* (1), 361-367.

233. Liu, G.; Chen, Y.; Zhang, G.; Yang, S. Protein resistance of (ethylene oxide) n monolayers at the air/water interface: effects of packing density and chain length. *Phys. Chem. Chem. Phys.* **2007,** *9* (46), 6073-6082.

234. Ghosh, S. Comparative studies on brij reverse micelles prepared in benzene/surfactant/ethylammonium nitrate systems: Effect of head group size and polarity of the hydrocarbon chain. *J. Colloid Interface Sci.* **2011,** *360* (2), 672-680.

235. Sugimoto, M.; Yamaguchi, K.; Kouzai, H.; Honma, H. Synthesis and practicability of novel additives for copper electroplating with semiconductor packaging. *J. Appl. Polym. Sci.* **2005,** *96* (3), 837-840.

236. d'Acunz, F.; Kohn, J. Alternating multiblock amphiphilic copolymers of PEG and tyrosine-derived diphenols. 1. Synthesis and characterization. *Macromolecules* **2002,** *35* (25), 9360-9365.

237. Bibler, J. P.; Wojcicki, A. Reactions of Cyclopentadienyl (methyl) iron Dicarbonyl with Various Ligands. Cyclopentadienyl (acetyl) iron Carbonyl Phosphine and Phosphite Complexes. *Inorg. Chem.* **1966,** *5* (5), 889-892.

238. Parera, E.; Comelles, F.; Barnadas, R.; Suades, J. Formation of vesicles with an organometallic amphiphile bilayer by supramolecular arrangement of metal carbonyl metallosurfactants. *Chem. Commun.* **2011,** *47* (15), 4460-2.

239. Prazeres, T. J.; Beija, M.; Fernandes, F. V.; Marcelino, P. G.; Farinha, J. P. S.; Martinho, J. Determination of the critical micelle concentration of surfactants and amphiphilic block copolymers using coumarin 153. *Inorg. Chim. Acta* **2012,** *381*, 181-187.

240. Vorwerg, L.; Antonietti, M.; Tauer, K. Electrophoretic mobility of latex particles: effect of particle size and surface structure. *Colloids Surf., A* **1999,** *150* (1), 129-135.

241. Daidone, I.; Ulmschneider, M. B.; Di Nola, A.; Amadei, A.; Smith, J. C. Dehydration-driven solvent exposure of hydrophobic surfaces as a driving force in peptide folding. *Proc. Natl. Acad. Sci. U. S. A.***2007,** *104* (39), 15230-15235.

242. Murphy, K. P.; Xie, D.; Thompson, K. S.; Amzel, L. M.; Freire, E. Entropy in biological binding processes: estimation of translational entropy loss. *Proteins: Structure, Function, and Bioinformatics* **1994,** *18* (1), 63-67.

243. George, T. A.; Kovar, R. A. Reactions of coordinated dinitrogen. 7. Preparation and characterization of molybdenum bis (dinitrogen) complexes containing mixed tertiary phosphine ligands. *Inorg. Chem.* **1981,** *20* (1), 285-287.

Appendices

Supporting Information for Chapter 2

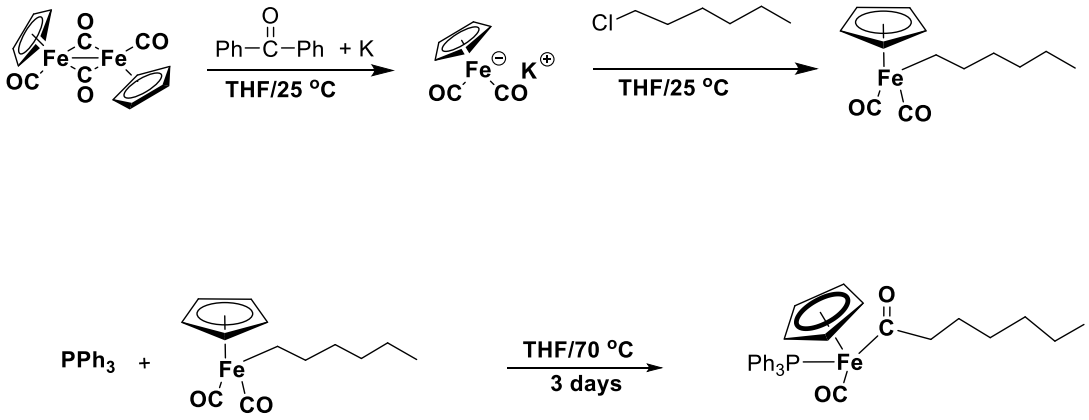

Figure S2.1 Schematic illustration for the synthesis of FpC6 *via* MIR

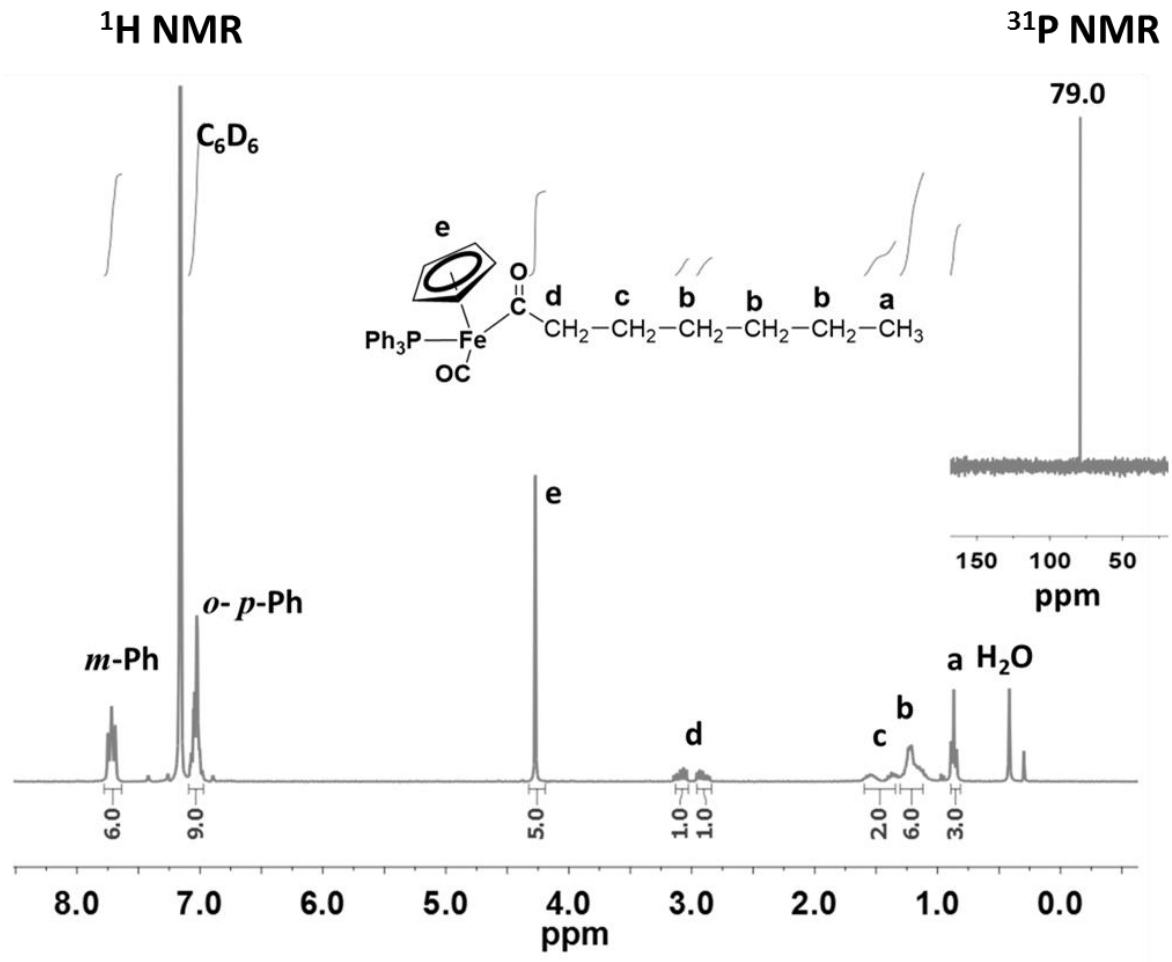

Figure S2.2 ^{1}H NMR and ^{31}P NMR spectra of FpC6 in C_6D_6.

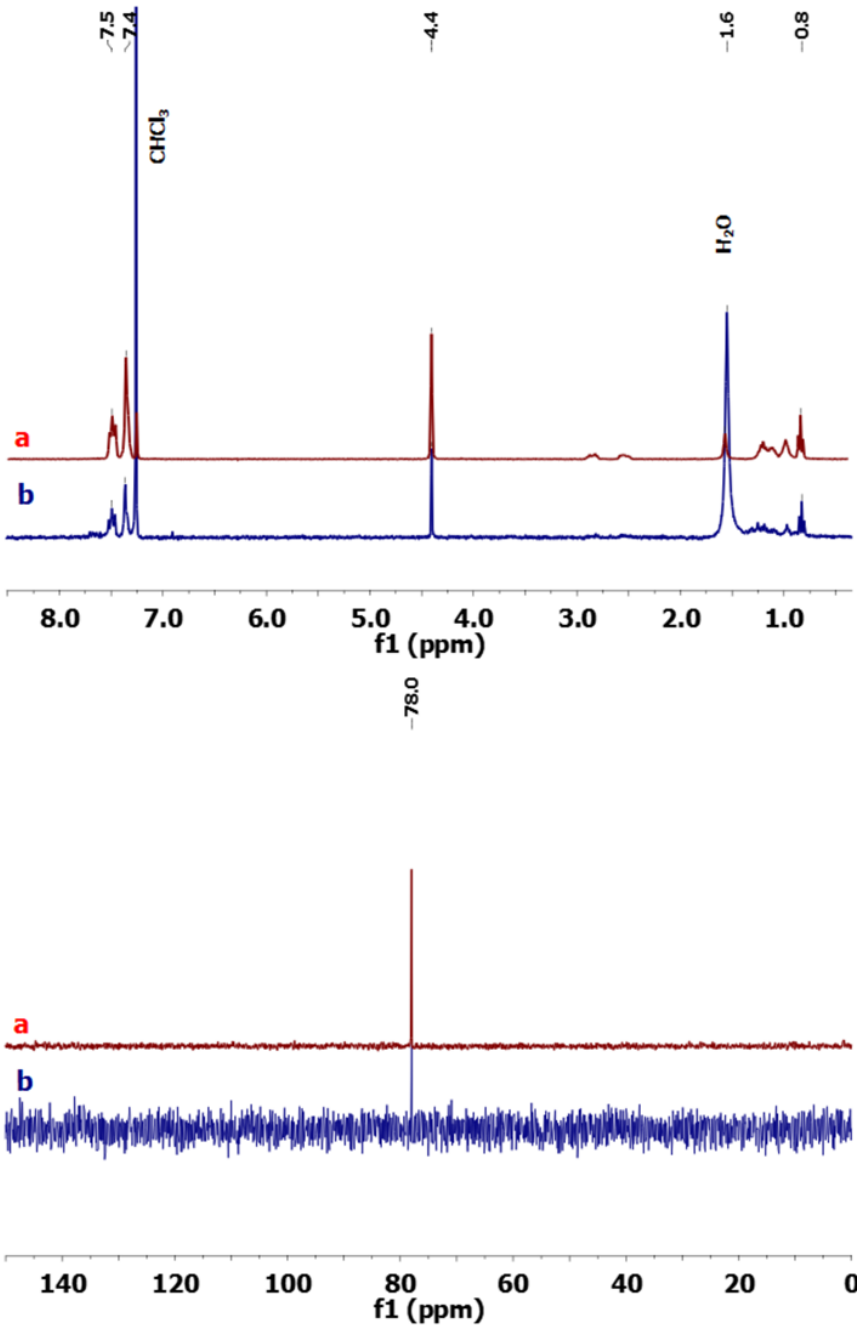

Figure S2.3 ^{1}H NMR (up) and ^{31}P NMR (down) spectra of FpC6 in $CDCl_3$ (a) before and (b) after aqueous self-assemble. FpC6 is recovered from the aqueous colloids via freeze-drying

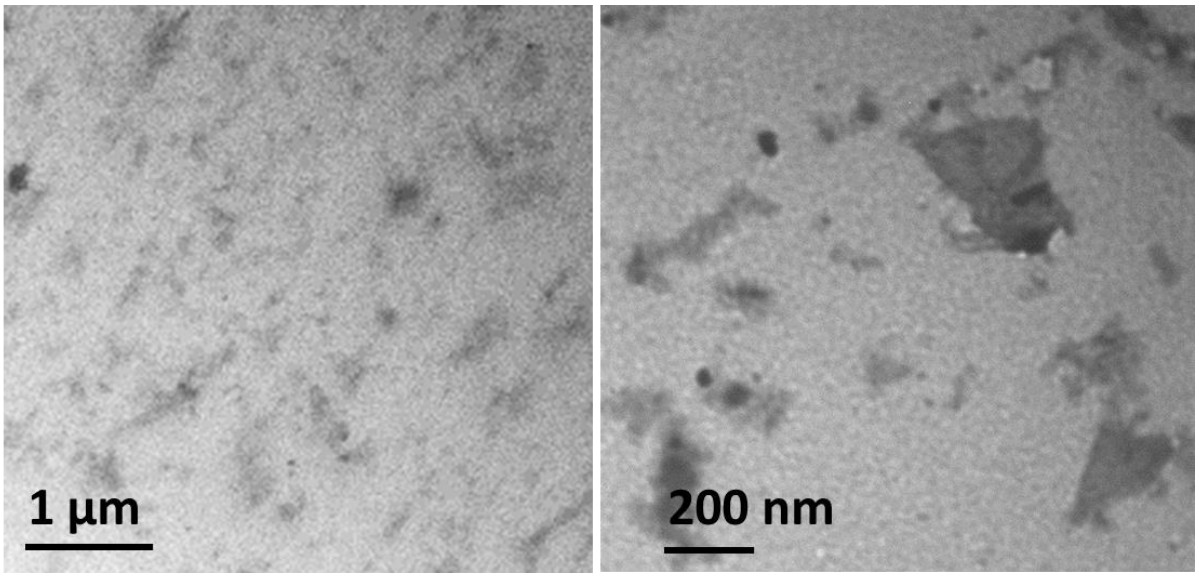

Figure S2.4 TEM images of FpC6 colloids dried from water solution (0.1 mg/mL)

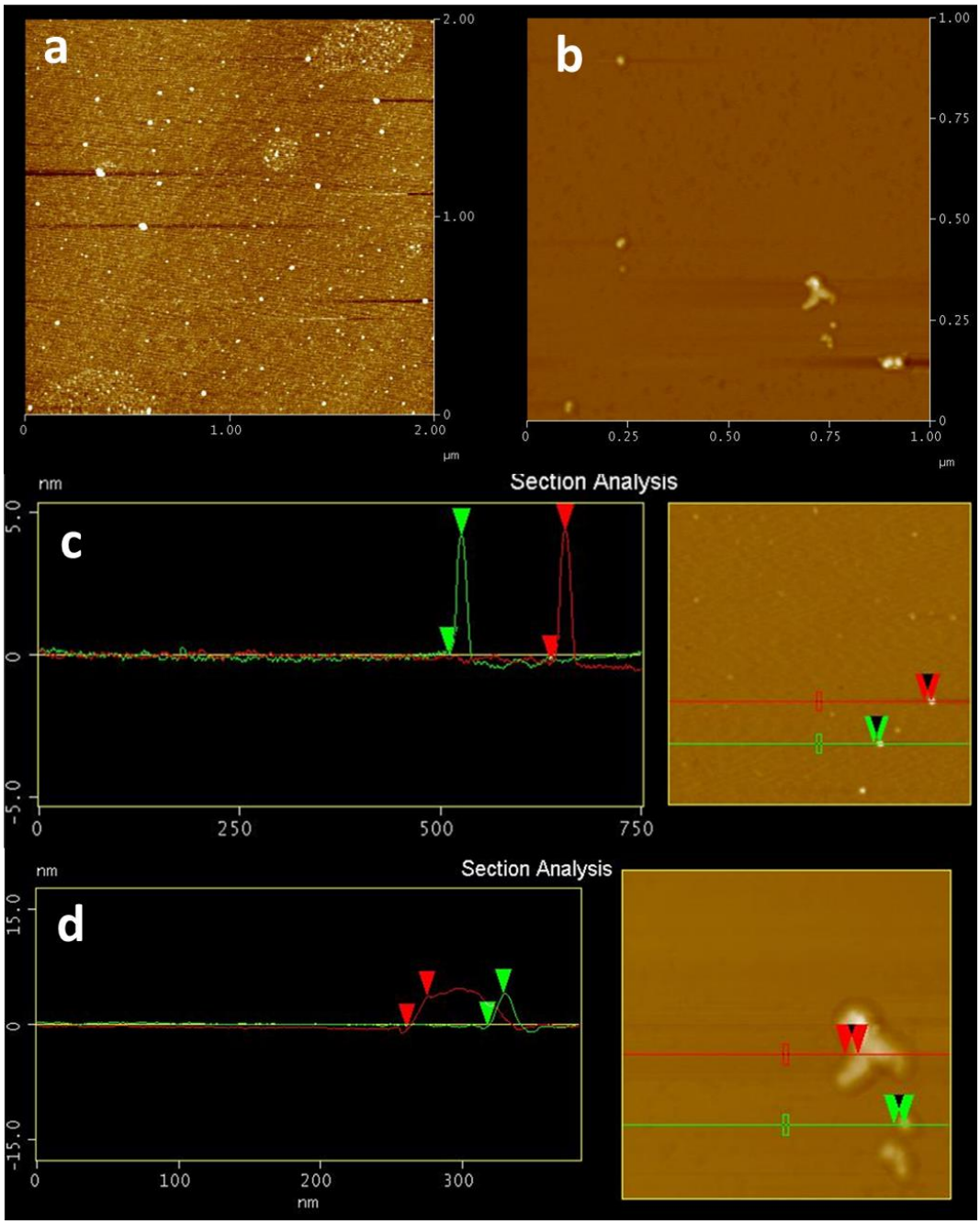

Figure S2.5 Representative AFM images (a-b) and height profile section analysis (c-d) for the fragments of FpC6 colloids dried from water solution (0.1 mg/mL).

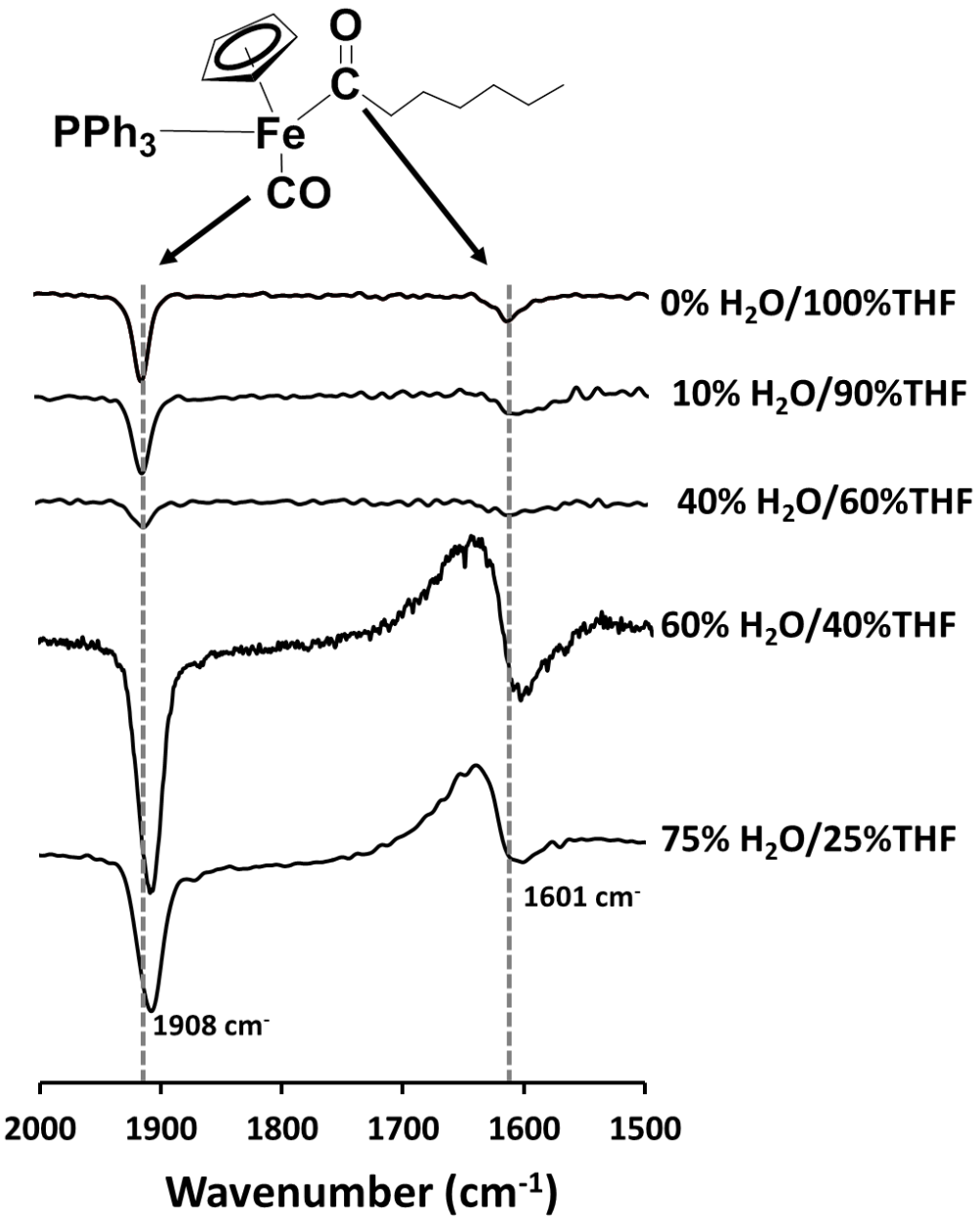

Figure S2.6 Partial ATR-FTIR spectra for FpC6 in THF/water solutions with varied water contents.

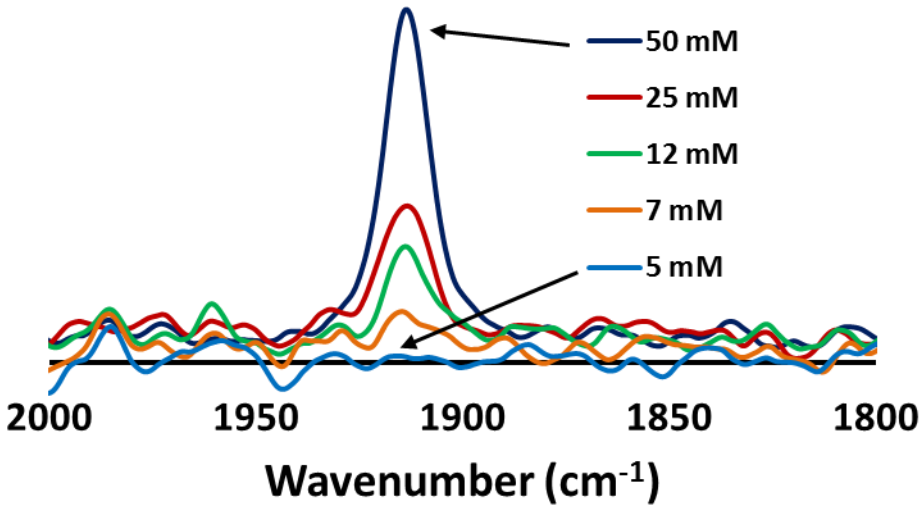

Figure S2.7 Partial ATR-FTIR spectra (terminal CO) for solutions of FpC6 in THF with different concentrations.

Supporting Information for Chapter 3

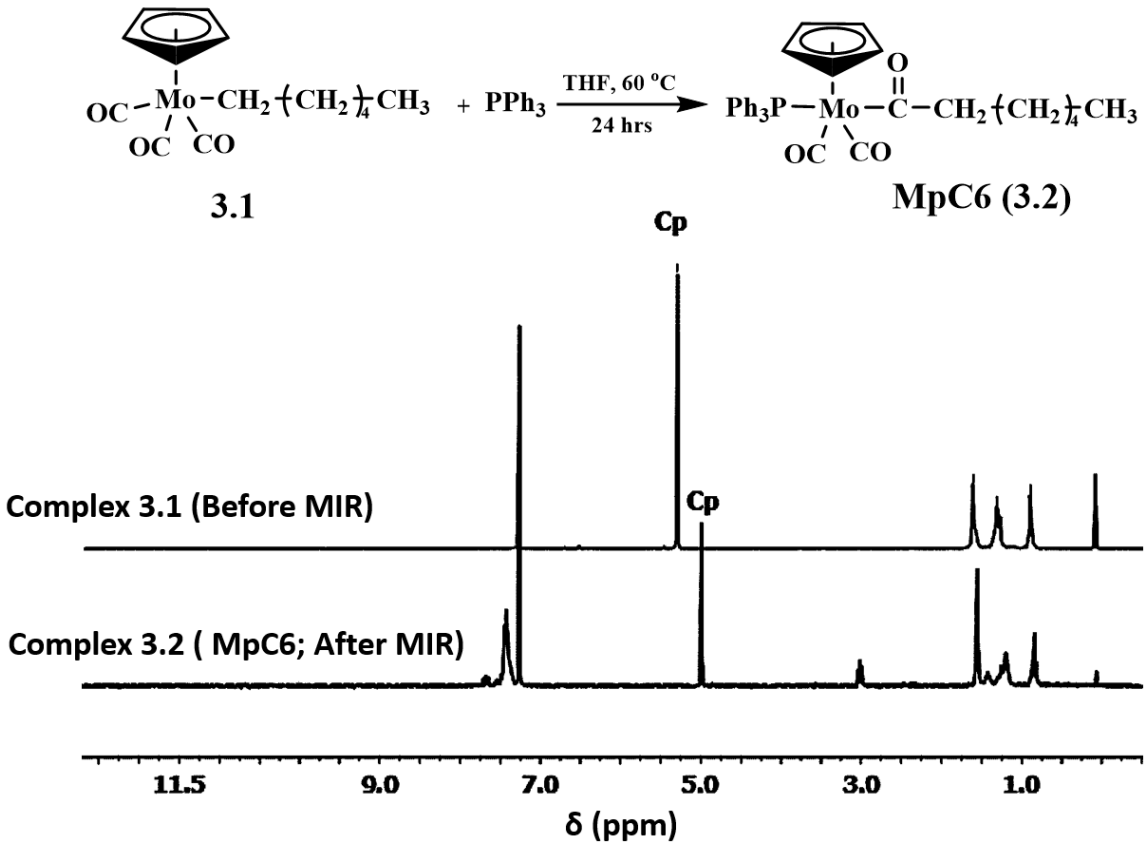

Figure S3.1 ^{1}H NMR spectra ($CDCl_3$) for complex **3.1** before MIR and complex **3.2** after MIR (MpC6).

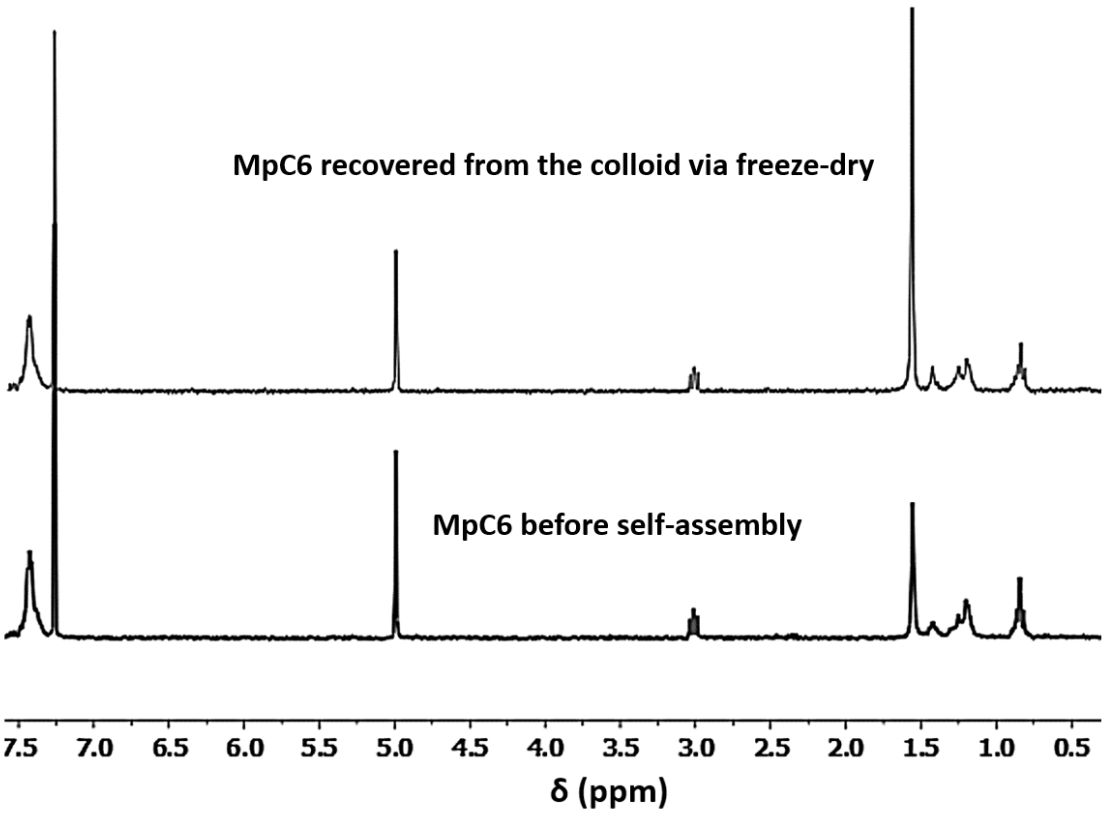

Figure S3.2 ^{1}H NMR spectra ($CDCl_3$) for MpC6 before and after self-assembly in water. MpC6 recovered from water via freeze-dry of the aqueous colloid.

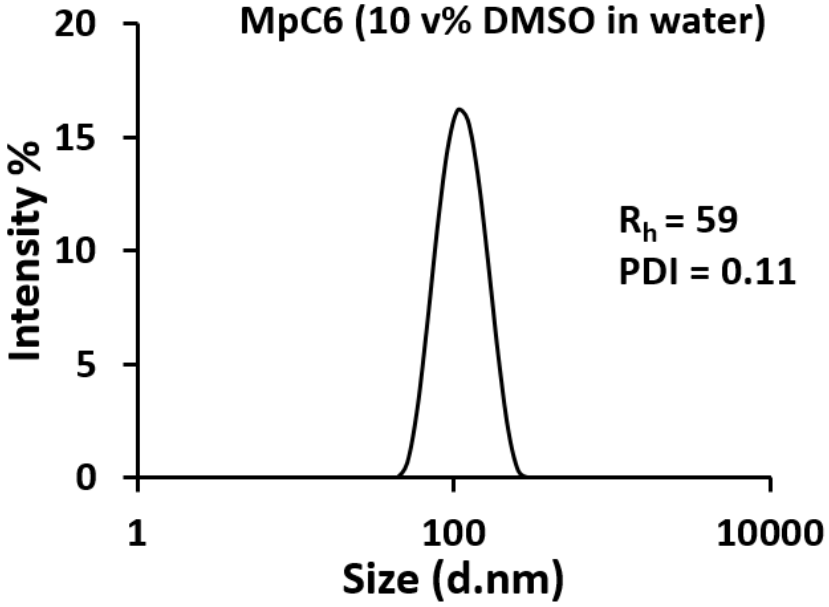

Figure S3.3 DLS analysis for the aqueous colloid of MpC6 (0.1 mg/mL; 178 μM) in DMSO/water solution.

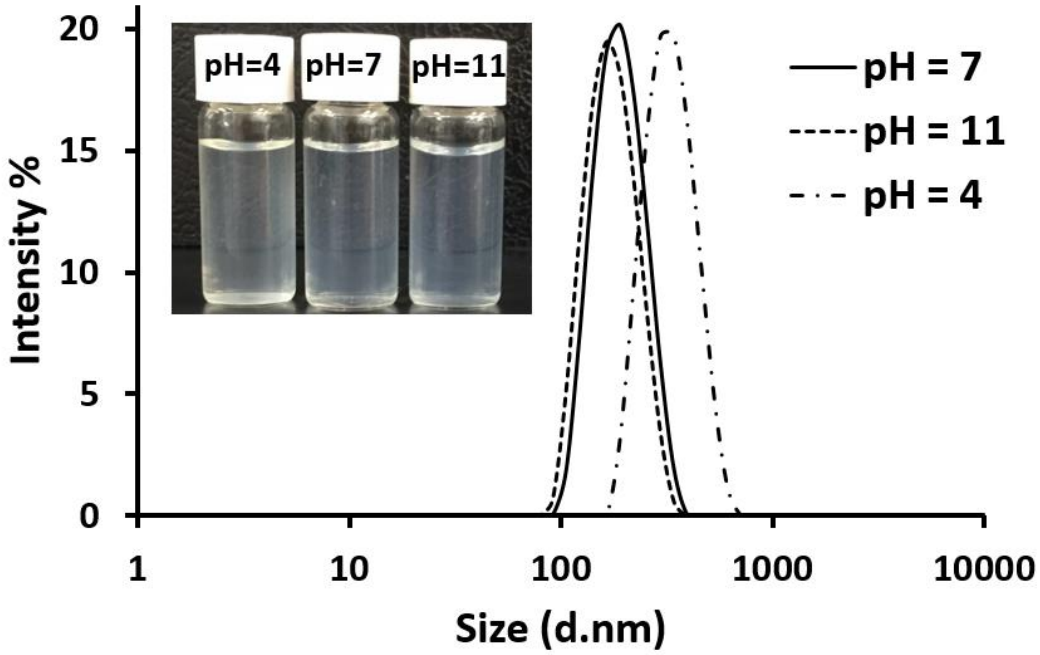

Figure S3.4 DLS analysis for the aqueous colloid of MpC6 (0.1 mg/mL; 178 µM) prepared using pure water (pH = 7), ascorbic acid/water solution (pH = 4) and NaOH/water solution (pH = 11).

Conc. (mg/ mL)	0.01	0.05	0.1	0.5
R_h (nm)	46	53	60	68
PDI	0.29	0.15	0.07	0.17

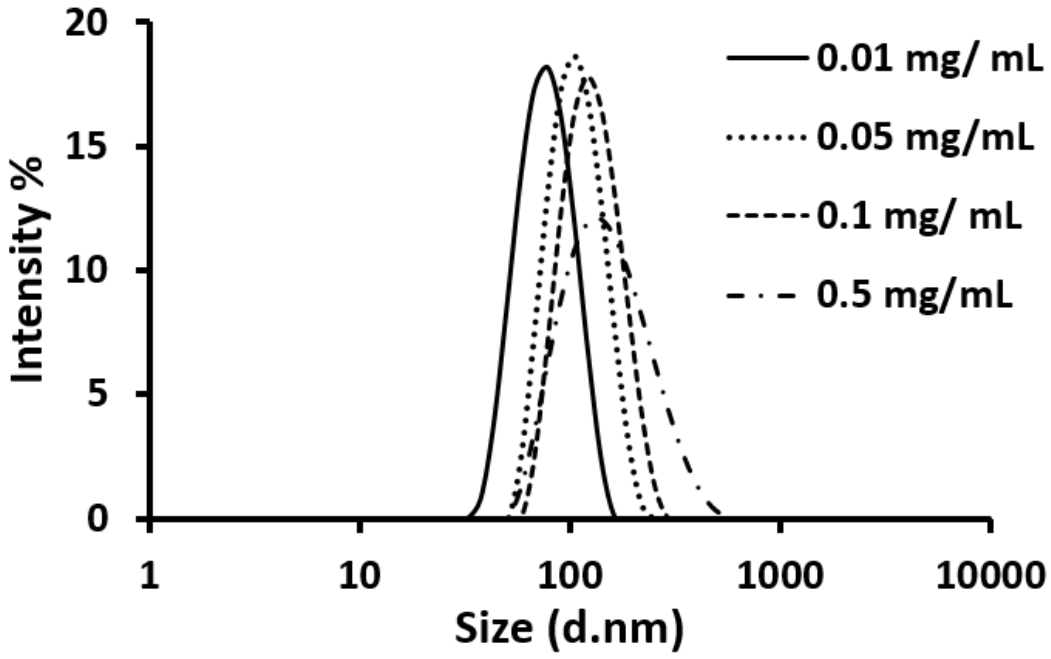

Figure S3.5 DLS analysis for the aqueous colloids prepared with different MpC6 concentrations**.**

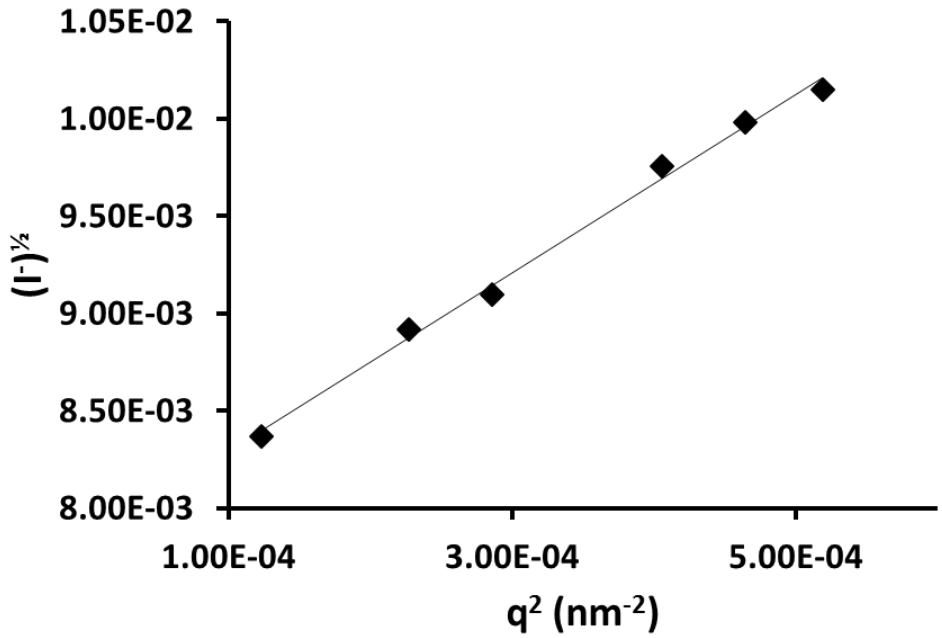

Figure S3.6 Berry plot obtained from the multi-angle SLS measurements of MpC6 aqueous colloids (8.9 μM).

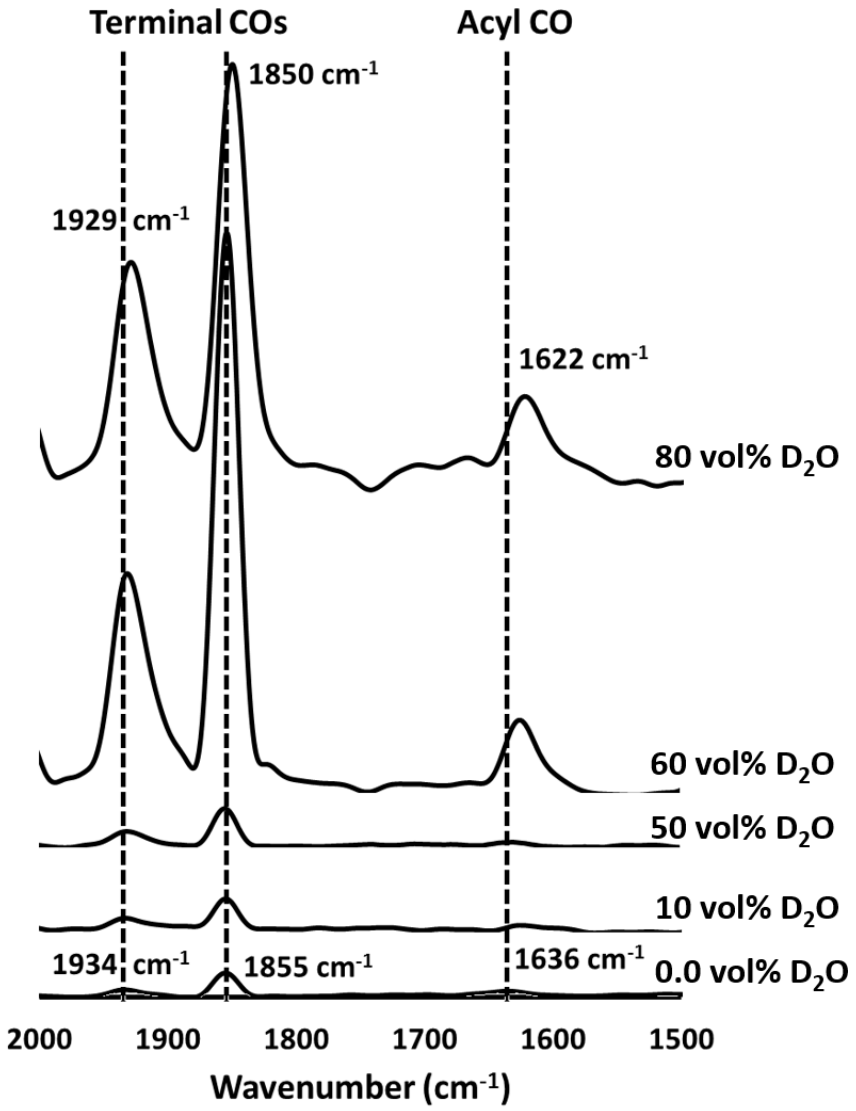

Figure S3.7 IR absorption spectra of MpC6 solution (5 mg/mL) in THF and THF/D_2O with varied amounts of D_2O. (D_2O was used to reduce the interfering of the acyl CO signal with water scissoring peak)

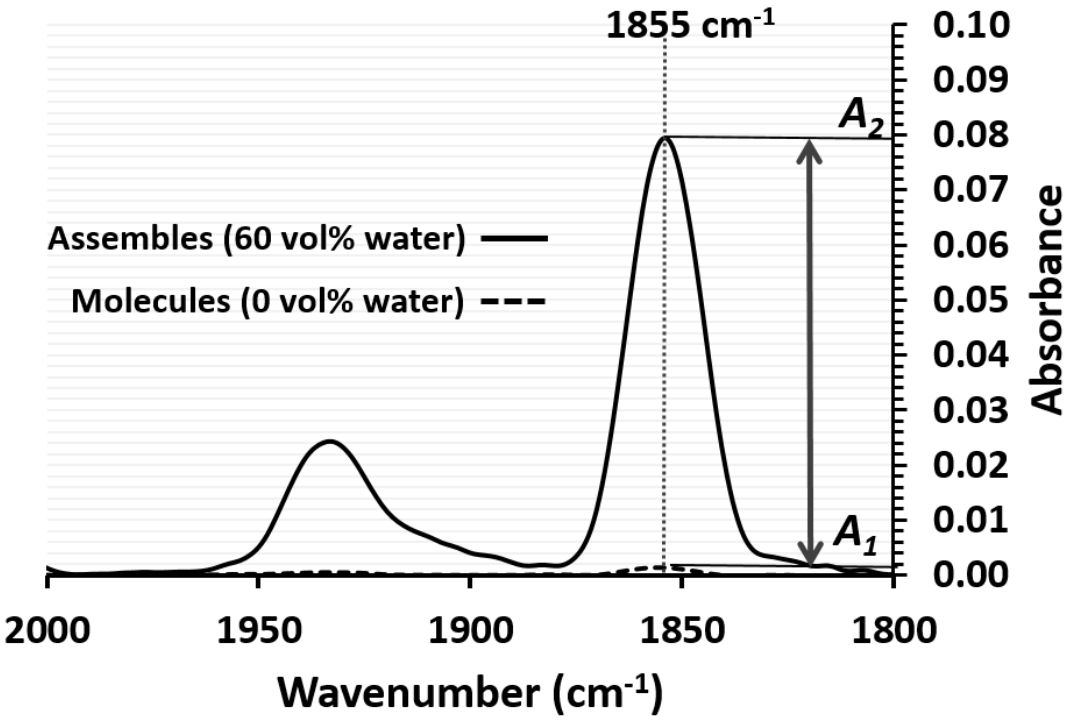

Figure S3.8 IR absorption spectra, normalized to the same concentration, of MpC6 solutions in THF (molecules) and in THF/water with 60 vol% of water (assembles). The enhancement in IR absorption is calculated by comparing the maximum absorption intensities at 1855 cm^{-1}.

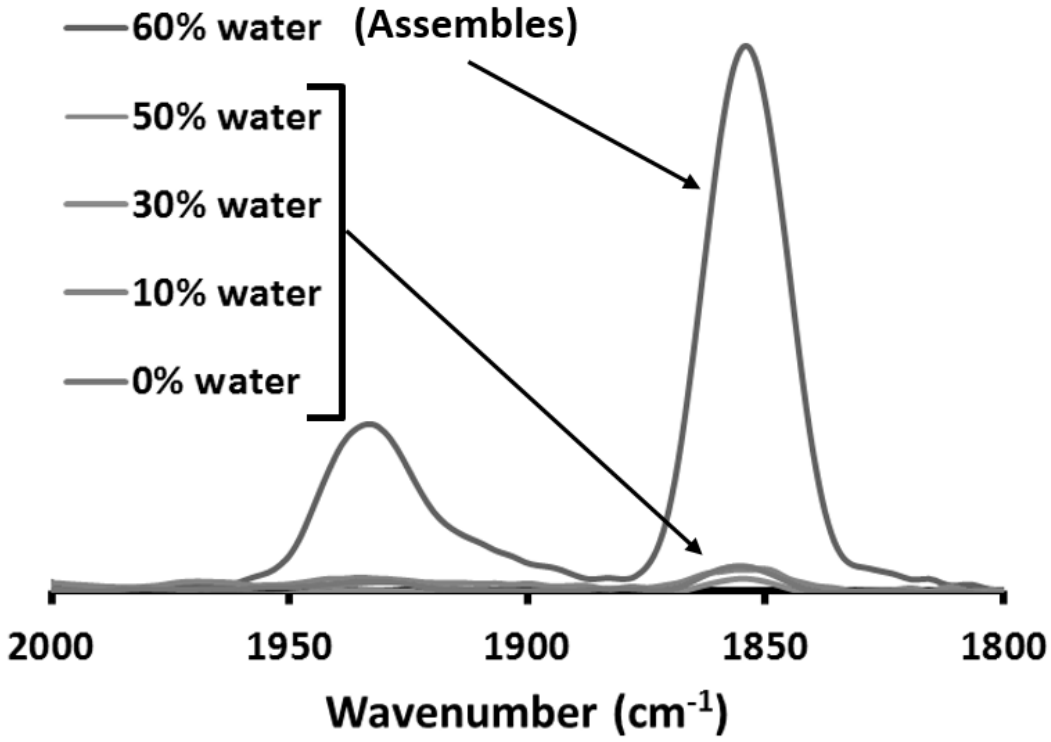

Figure S3.9 IR absorption spectra for the terminal CO groups of MpC6 solution (15 mg/mL) in THF and THF/water with varied amounts of water.

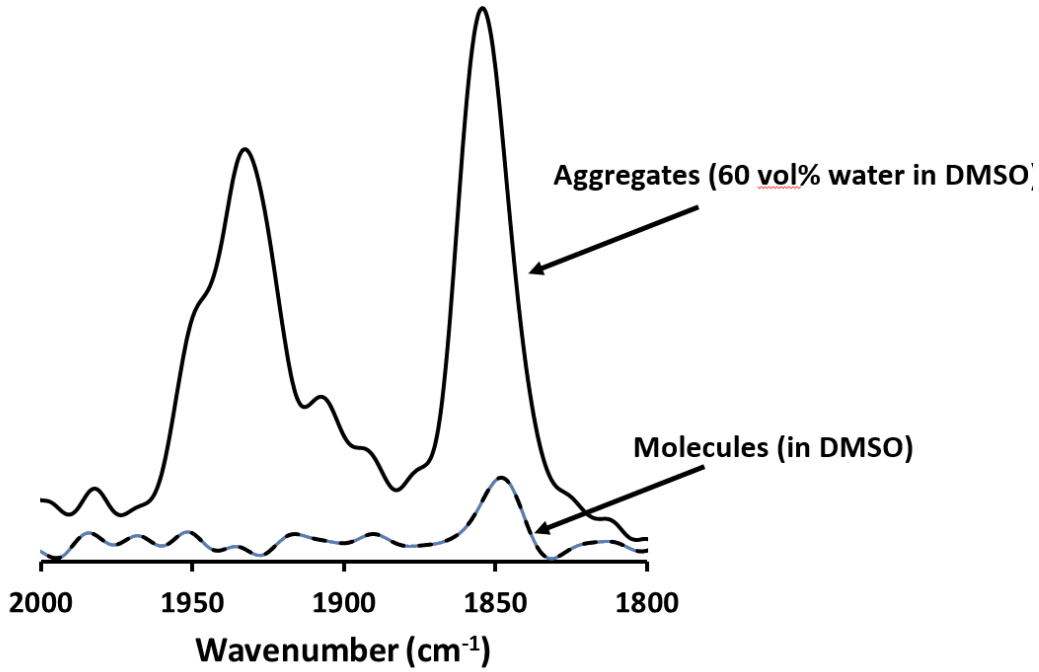

Figure S3.10 IR absorption of the terminal CO groups for the solutions of MpC6 (3.7 mM) in DMSO and in DMSO/water with 60 vol% of water (1.5 mM).

Table S3.1 Crystal data and structure refinement for MpC6

Empirical formula	$C_{32}H_{33}MoO_3P$
Formula weight	592.49
Crystal system	Triclinic
Space group	P-1
a Å	9.43830(10)
b Å	11.3542(2)
c Å	13.9690(2)
α deg	91.8471(6)
β deg	94.5175(6)
γ deg	104.4341(7)
Volume, $Å^3$	1443.14(4)
Z	2
D_{calc}, Mg/m^3	1.363
Absorption coefficient	0.540 mm^{-1}
F(000)	612
Crystal size, mm^3	0.220 x 0.150 x 0.100
θ range, deg	1.464 to 27.994°
Index ranges	-12<=h<=12
	-14<=k<=14
	-18<=l<=18
Reflections collected	27521
Independent reflections	6966 [R(int) = 0.0171]
Max. and min. transmn	0.7460 and 0.7160
Weighting parameters a, b	0.0315, 1.8788
Data/restraints/parameters	6966 / 0 / 335
Goodness-of-fit on F^2	1.406
Final *R* indices [$I>2\sigma(I)$]	R_1 = 0.0351
	wR_2 = 0.0757
R indices (all data)	R_1 = 0.0464
	wR_2 = 0.0919
Largest diff peak and hole, $e.Å^{-3}$	0.522 and -0.353

[a] Details in common: Temperature 296(2) K, refinement method: full-matrix least-squares on F^2.

Table S3.2. Selected bond distances (Å) and angles (θ) for MpC6

Bond lengths			
Mo-C(24)	1.961(3)	C(1)-C(2)	1.402(5)
Mo-C(25)	1.970(3)	C(1)-C(5)	1.406(5)
Mo-C(26)	2.273(3)	C(1)-H(1A)	0.9300
Mo-C(5)	2.315(3)	C(2)-C(3)	1.388(5)
Mo-C(4)	2.328(3)	C(2)-H(2A)	0.9300
Mo-C(3)	2.364(3)	C(3)-C(4)	1.395(5)
Mo-C(2)	2.360(3)	C(3)-H(3A)	0.9300
Mo-C(1)	2.342(3)	C(4)-C(5)	1.401(5)
Mo-P(1)	2.4733(7)	C(4)-H(4A)	0.9300
Bond angles			
C(24)-Mo-C(25)	107.93(12)	C(27)-C(26)-Mo	122.6(2)
C(24)-Mo-C(26)	72.35(11)	C(28)-C(27)-C(26)	117.8(4)
C(25)-Mo-C(26)	73.37(12)	C(29)-C(28)-C(27)	123.8(6)
C(24)-Mo-C(5)	138.28(12)	C(28)-C(29)-C(30)	118.5(7)
C(25)-Mo-C(5)	100.48(13)	C(31)-C(30)-C(29)	120.2(7)
C(26)-Mo-C(5)	87.79(12)	C(32)-C(31)-C(30)	118.7(11)

Supporting Information for Chapter 4

S4.1. Principle of laser trapping

Laser trapping phenomenon for particles with the size much smaller than the wavelength of the trapping laser is conventionally interpreted by Maxwell Boltzmann electromagnetic theory. The gradient force exerted on nanometer-sized objects is given as follows.[163,88]

$$\mathbf{F}_{\text{grad}} = \frac{1}{2}\varepsilon_m \alpha \nabla \mathbf{E}^2 \qquad (1).$$

Here ***E*** denotes the electric field, and ∇ represents a gradient with respect to the spatial coordinates. The parameter of ε_m represents the permittivity of the surrounding medium. The polarizability of the nanoparticle, α, under the dipole approximation, is given by

$$\alpha = 4\pi r^3 \frac{\left(\frac{n_p}{n_m}\right)^2 - 1}{\left(\frac{n_p}{n_m}\right)^2 + 2} \qquad (2).$$

Notations of *r*, is the radius of the nanoparticle. n_p and n_m represent the refractive index of the nanoparticle and the surrounding medium, respectively. As calculated from above equations, no gradient force is given to a target nanometer-sized object in the case that

its refractive index is the same as that of the surrounding medium. When the target object has the refractive index higher than that of the surrounding medium, the gradient force toward the focal spot is exerted on the object, and its magnitude becomes larger with the increase in the refractive index of the target object.

S4.2. Quantum yield measurement

Quantum yield for the aqueous solution of FpC3BTh (**4.1)** was compared with 1,4-bis(5-phenyloxazol-2-yl) benzene (POPOP) in cyclohexane as a reference. UV-vis spectra were measured for diluted solutions of POPOP in cyclohexane and colloid of FpC3BTh in water. Fluorescence spectra were then recorded for the same samples with excitation wavelength of 350 nm. The collected data was used to calculate the quantum yield of FpC3BTh using the following equation.[180]

$$Q = Q_R \times \frac{FL\ integration}{FL_R\ integration} \times \frac{1 - 10^{-A_R}}{1 - 10^{-A}} \times \frac{n^2}{{n_R}^2}$$

Q = Quantum yield for the sample
A = absorbance at excitation wavelength for the sample
n = refractive index of the solvent for the sample
FL integration = area under the emission spectra of the sample

Q_R = Quantum yield for the standard
A_R = absorbance at excitation wavelength for the standard
n_R = refractive index of the solvent for the standard
FL_R integration = area under the emission spectra of the standard
All samples were measured at the same time under same conditions. The florescence emission spectra were measured with excitation wavelength of 350 nm.

S4.3. Synthesis and characterization of FpC3BTh As illustrated in Figure S4.1, the building block (FpC3BTh) is prepared via a migration insertion reaction (MIR) of a bithiophene tethered Fp derivative (**4.2**) in the presence of triphenylphosphine. **4.2** is obtained from the reaction of **4.3** with FpK. Molecule **4.3** is prepared via the reaction of 5-lithio-2,2'-bithiophene with 1-bromo-3-chloropropane. ^{1}H NMR for **4.3** is illustrated in Figure S4.2. Figure S4.3 display the ^{31}P NMR and IR spectra for FpC3BTh. As shown in Figure S4.3, only one signal in the ^{31}P NMR spectrum appears at 77.4 ppm due to the coordinated phosphorus element (Figure S4.3a) and both terminal CO and acyl CO groups appear in the IR spectrum for FpC3BTh (Figure S4.3b) at 1905 and 1600 cm^{-1}, respectively, suggesting that the migration insertion reaction has occurred.[48, 237] In ^{1}H NMR spectrum (Figure S4.4), the down field signals appear at 7.37 – 7.49 ppm are due to the phenyl protons, while those between 6.55 and 7.15 ppm represent the protons from the bithiophene units. The downfield shift for signal due to the protons of Cp ring to 4.41 ppm and upfield shift of the two diastereotopic α-protons with splitting chemical shifts at 2.67 and 2.90 ppm (a in Figure S4.4) suggest that the migration insertion reaction has occurred.[48] The detailed chemical shifts are summarized in the Experimental Section.

S4.4. Supporting Figures and analysis

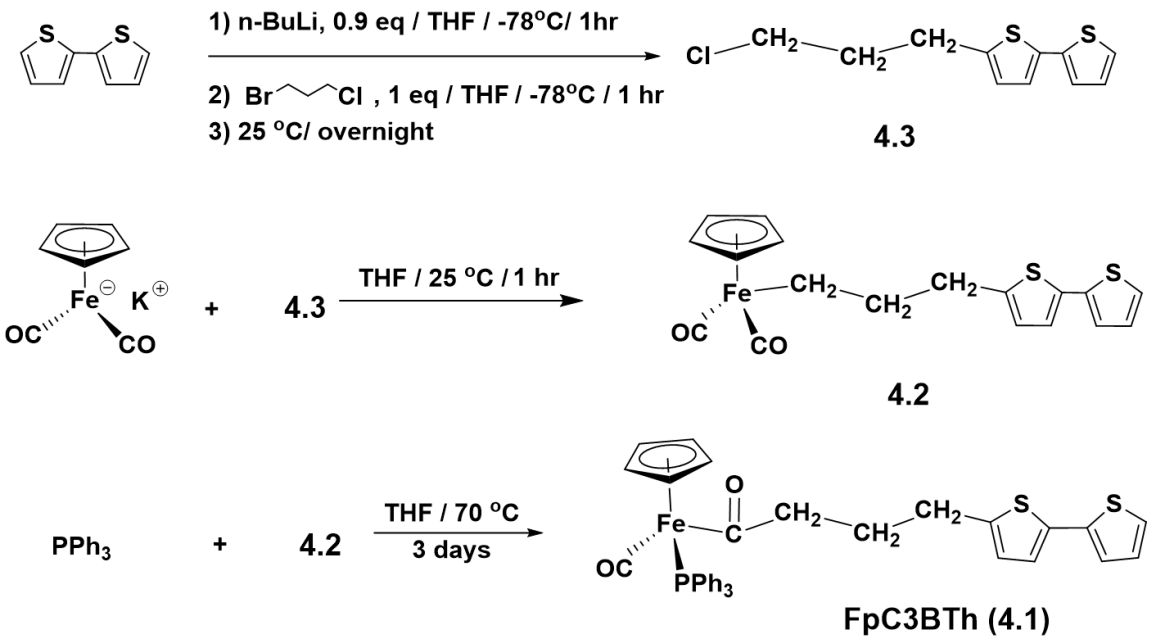

Figure S4.1 Synthesis of FpC3BTh (**4.1**)

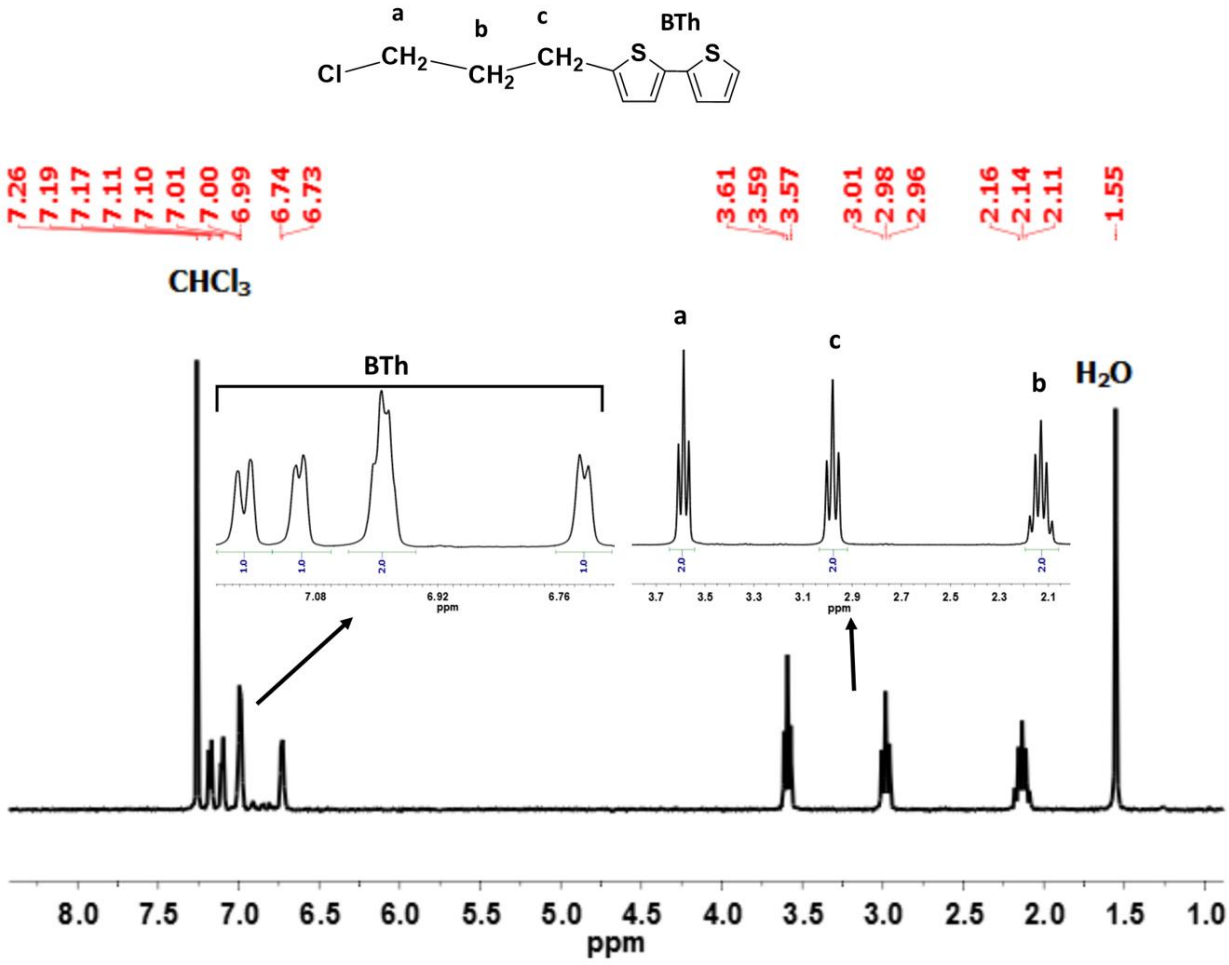

Figure S4.2 ^{1}H NMR spectrum ($CDCl_3$, 25 ^{o}C, 300 MHz) of **4.3**

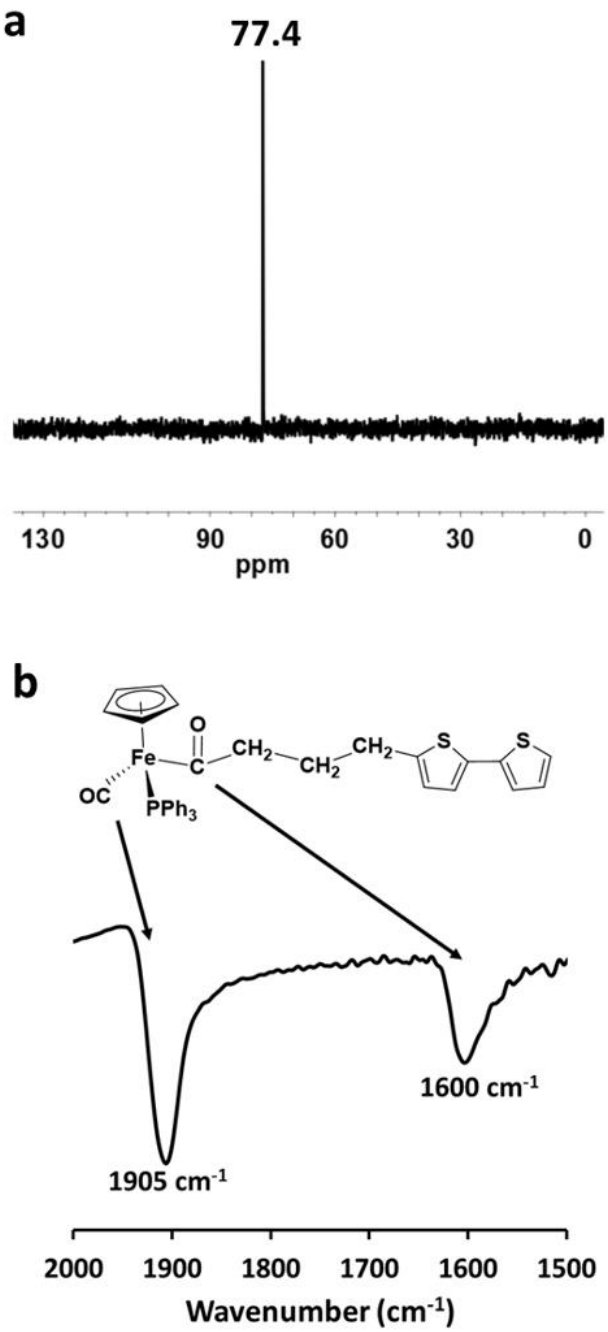

Figure S4.3 (a) ^{31}P NMR spectrum ($CDCl_3$, 25 ^{o}C, 300 MHz) of FpC3BTh; (b) partial FT-IR absorption spectrum (KBr pellet) for terminal and acyl CO groups from FpC3BTh.

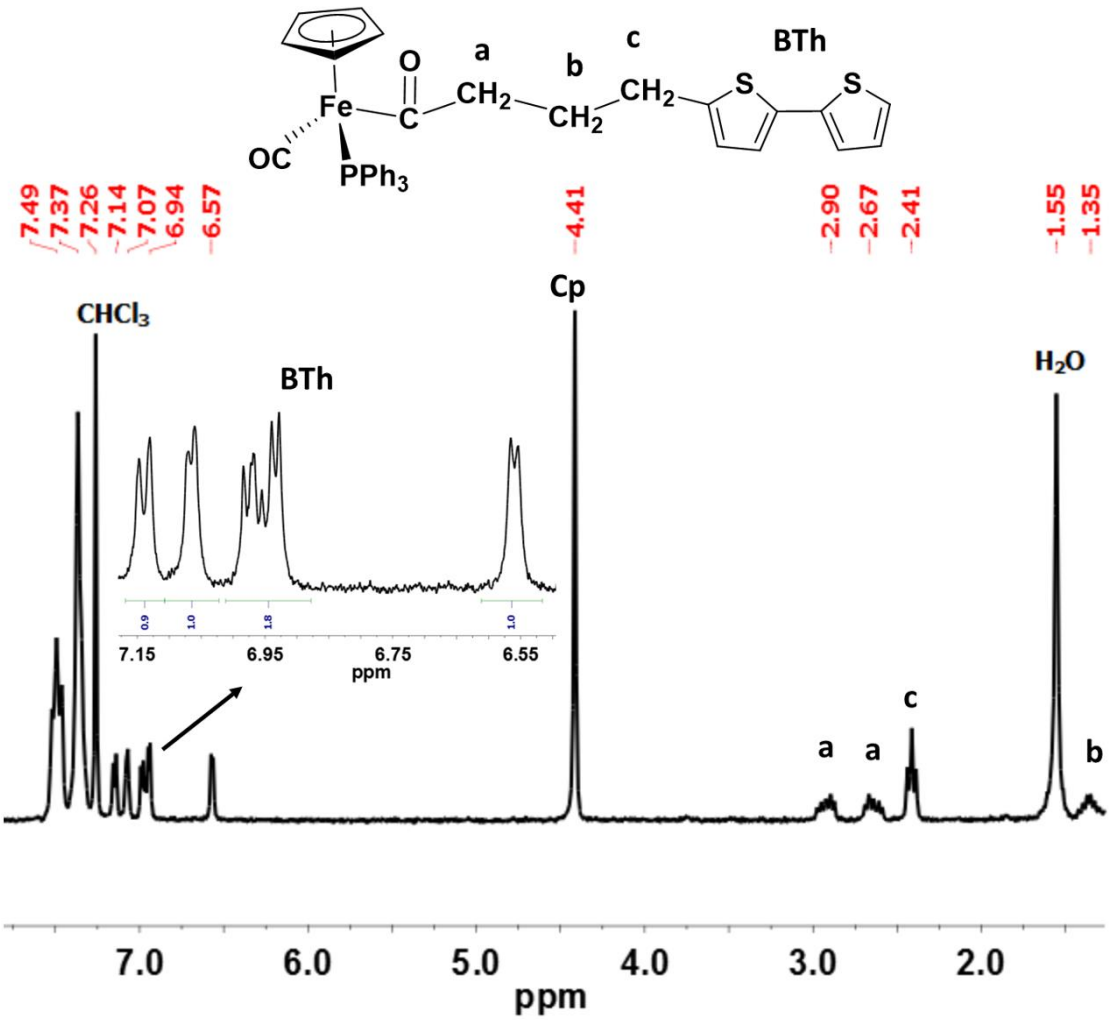

Figure S4.4 ^{1}H NMR spectrum ($CDCl_3$, 25 ^{o}C, 300 MHz) of FpC3BTh

The red shift in wavenumber ($\Delta\nu$) for the IR absorption for both acyl and terminal CO groups of **1** in water/THF solution with water content of 80 vol% is = 7.0 cm^{-1} (Figure 3 in main text)). In contrast, the terminal CO group in the non-thiophene Fp-analogue FpC6 ($\Delta\nu$ = 4.0 cm^{-1}) is less hydrated under the same condition as we reported before.[118] This difference in the degree of hydration may influence the stability of the MC colloids. As shown in Figure S4, DLS analysis indicated that the R_h for the colloids of FpC3BTh maintained unchanged over 60 days, whereas the R_h for the FpC6 colloids gradually increased and a small amount of precipitates was observed after the sample was aged for 7 days.[118] This comparison suggests that, despite the same MC unit in the building blocks, the polarizable CO groups have varied strength of WCI.

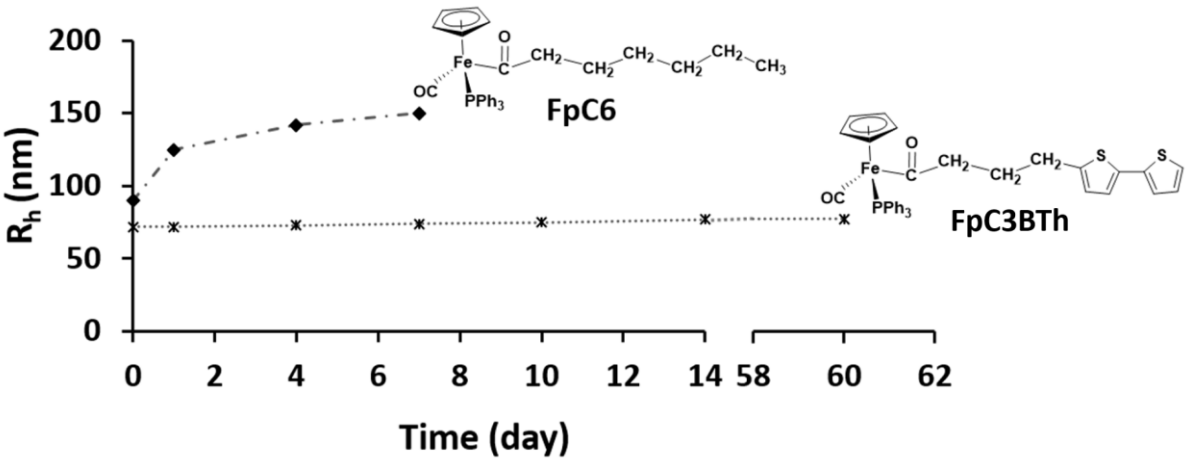

Figure S4.5 Hydrodynamic radii for the aqueous colloids of FpC3BTh and FpC6 as a function of time.

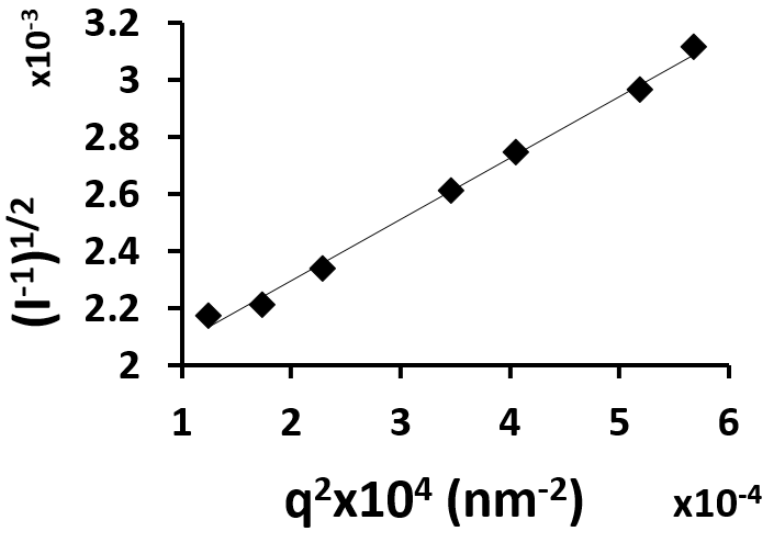

Figure S4.6 Berry plot obtained from multi-angle SLS measurements of the aqueous colloids of FpC3BTh (0.77 μM).

Sample preparation methods for AFM experiments are crucial for the imaging. When the sample was prepared *via* spin coating of the colloidal solution on a freshly cleaved mica substrate, the colloids dissociated and only small fragments with vertical heights of ca. 1.0 nm were observed (Figure S4.7). The observed fragments are therefore the single molecules lying on the substrates, because their heights closely match the dimension of the Fp acyl units (Figure 4.5a). However, when the AFM sample prepared via drying a few drops of the solution, lamella with vertical heights of ca. 3.72 ± 0.20 nm nm were observed (Figure S4.8 and Figure 4.4), which represents the membrane thickness of the broken vesicle.

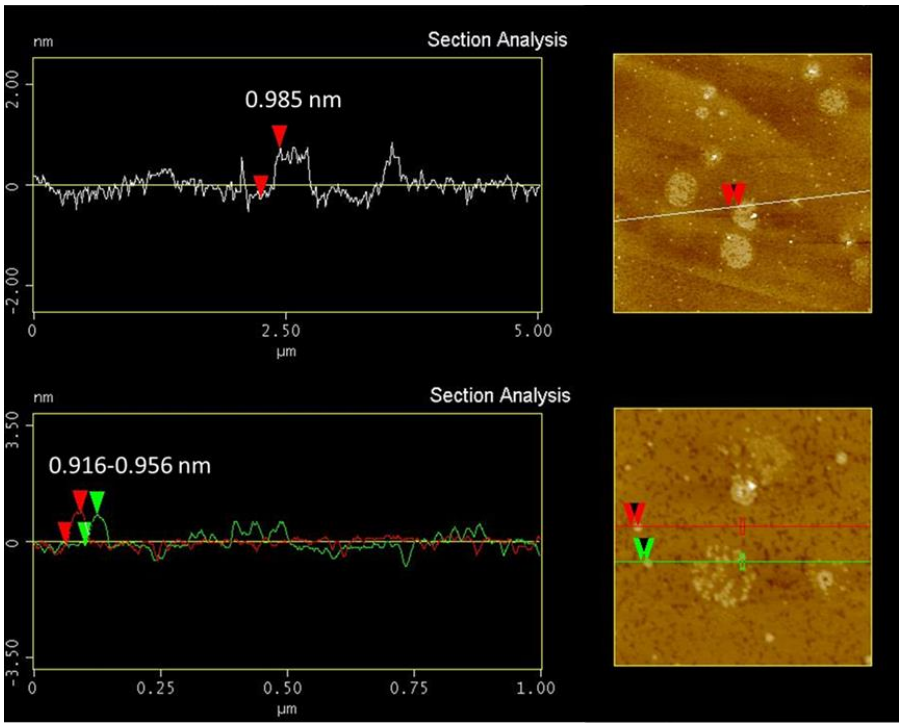

Figure S4.7 Vertical section analyses of the AFM images for the sample of FpC3BTh (77 µM) prepared on mica substrates *via* spin coating.

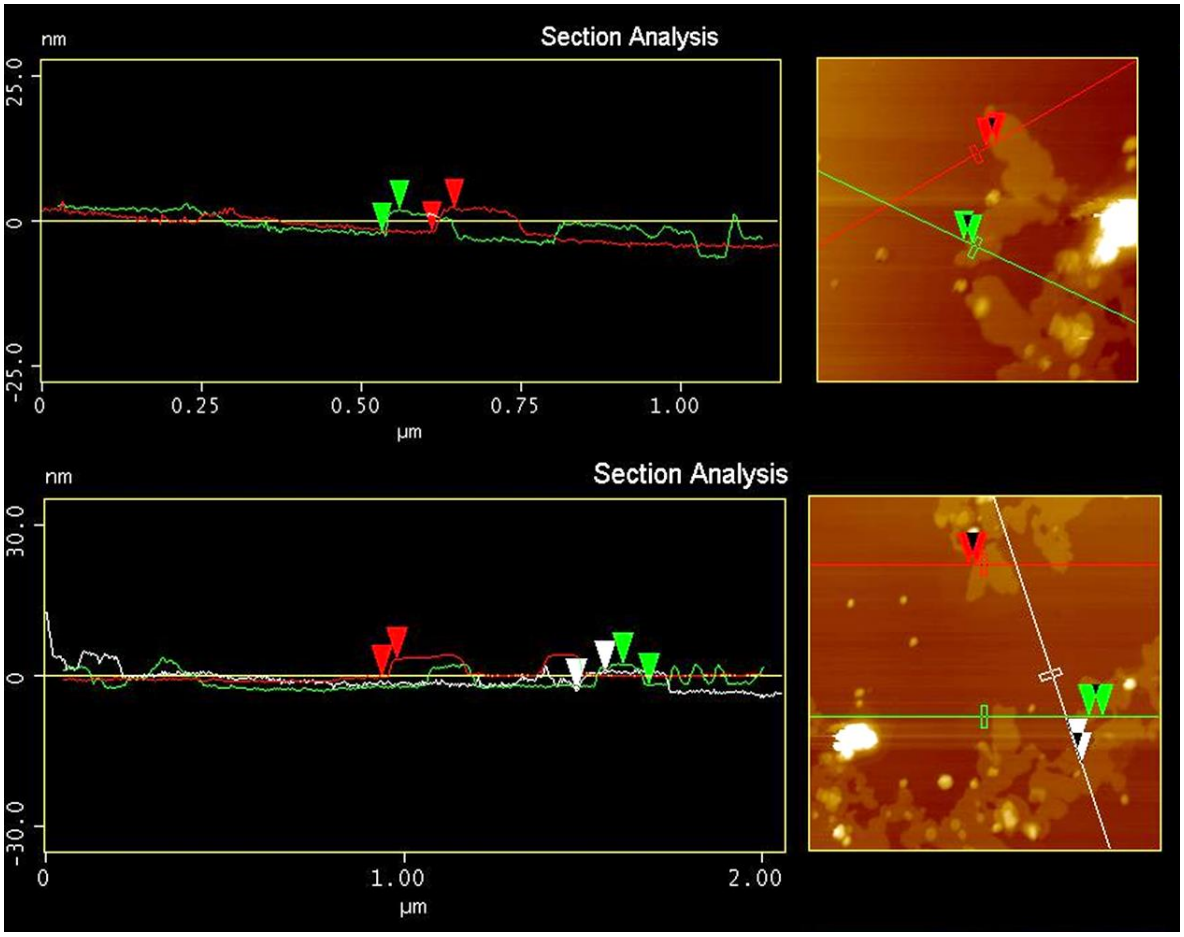

Figure S4.8 Vertical section analyses of AFM images for the colloid sample of FpC3BTh (77 µM) prepared on mica substrates *via* drying a few drops of the solution.

According to the SAXS experimental results, the domain spaces 2.4 nm between the two iron centers. Cryo TEM images reveals that the thickness of the MCsome layer is ca. 3.2 nm. Accordingly, the interdigitated structure (Model 1), as shown in Figure S8a, is more possible than the non-interdigitated bilayer structure (Model 2)

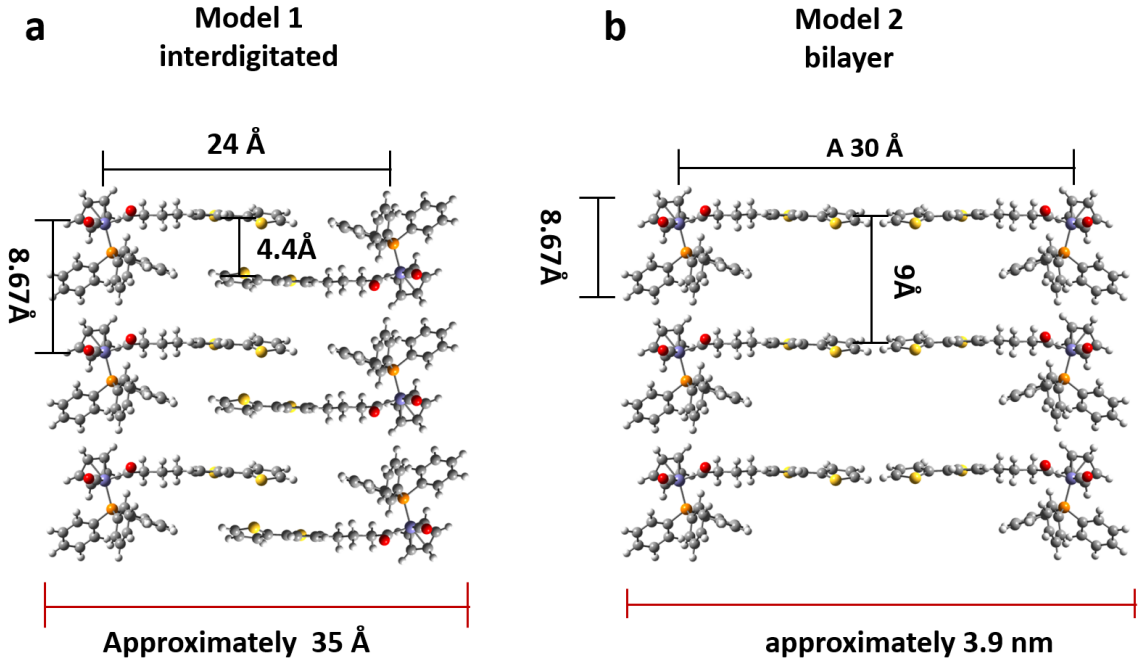

Figure S4.9 (a) interdigitated and (b) non-interdigitated models for the bilayer membrane structure for the MCsome FpC3BTh.

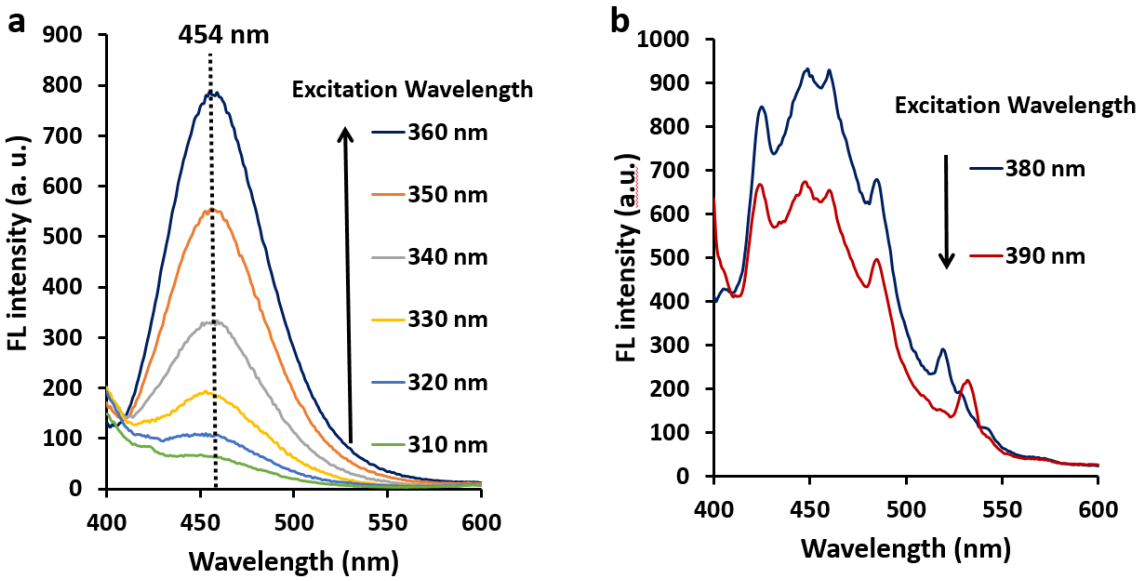

Figure S4.10 FL emission spectra for the solutions of MCsome FpC3BTh in water at different excitation wavelength (λ_{ex}). The arrows represent the trend in the emission intensity with increasing λ_{ex}.

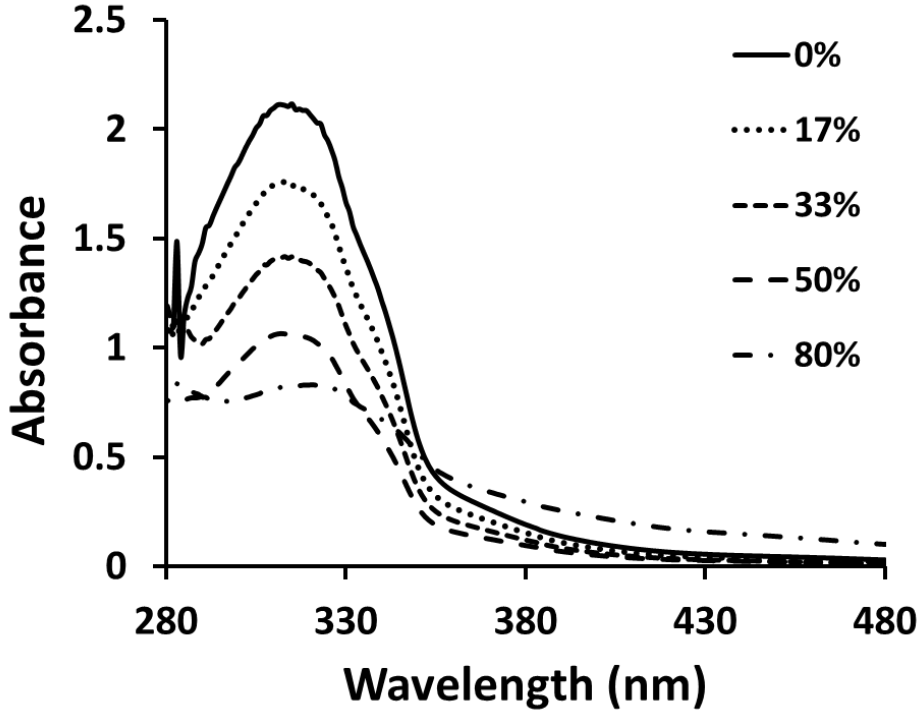

Figure S4.11 UV-vis spectra for the solutions diluted from FpC3BTh in THF (154 μM) by addition of varied amounts of water.

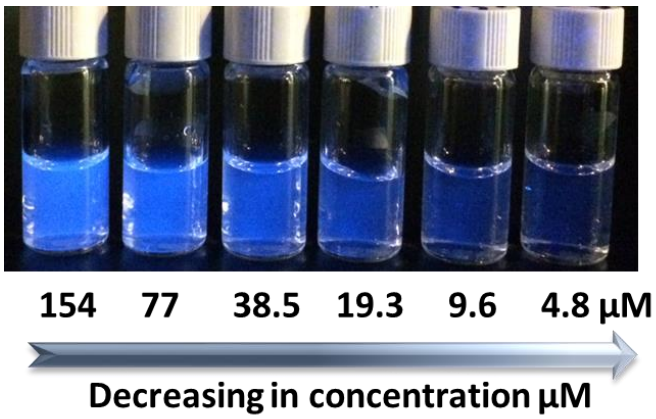

Figure S4.12 Photographs for the aqueous colloids, prepared by successive dilution of the solution of FpC3BTh (154 µM), under irradiation of a UV lamb.

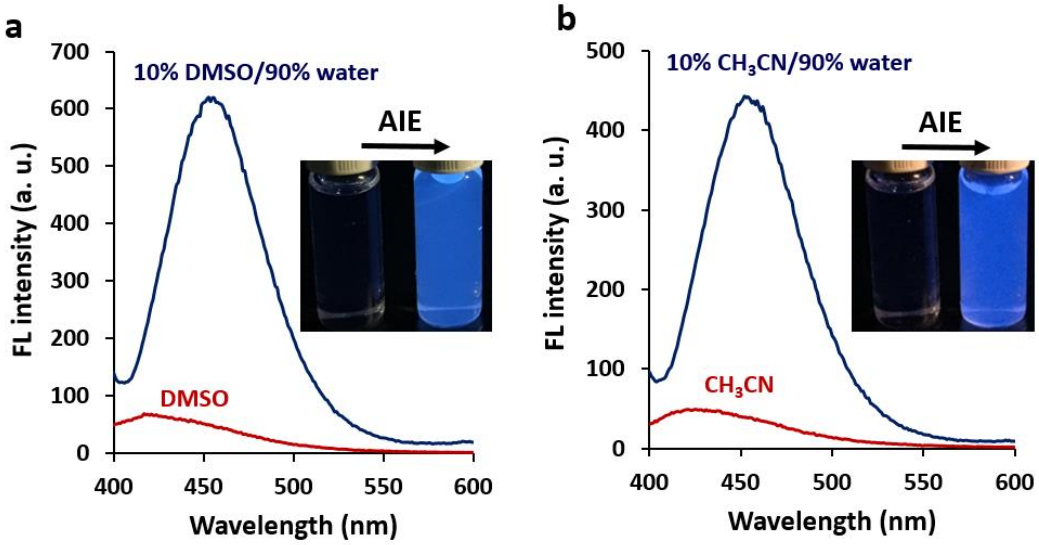

Figure S4.13 FL emission spectra for the solutions of MCsome FpC3BTh in (a) DMSO and DMSO/water and (b) in acetonitrile (CH_3CN) and CH_3CN/water solutions. (λ_{ex} = 350 nm).

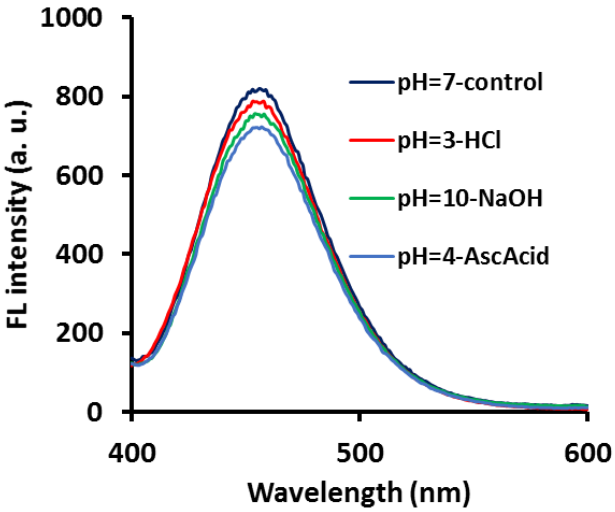

Figure S4.14 FL emission spectra for the aqueous colloids of MCsome FpC3BTh at different pH. (λ_{ex}= 350 nm).

Refractive index of FpC3BTh is measured using ellipsometry. A thin film of FpC3BTh was fabricated on a silicon waver using spin coating at a medium speed. Refractive index (*n*) profile was executed from the ellipsometric data revealed from J. A. Woollam Co. VASE® ellipsometer. Data were required, at angles of incidence of 55°, 60°, 65°, 70° and 75°, with spectral range from 1700 to 400 nm. The refractive index revealed from the ellipsometric experiments is ca. 1.71 (at λ = 633 nm).

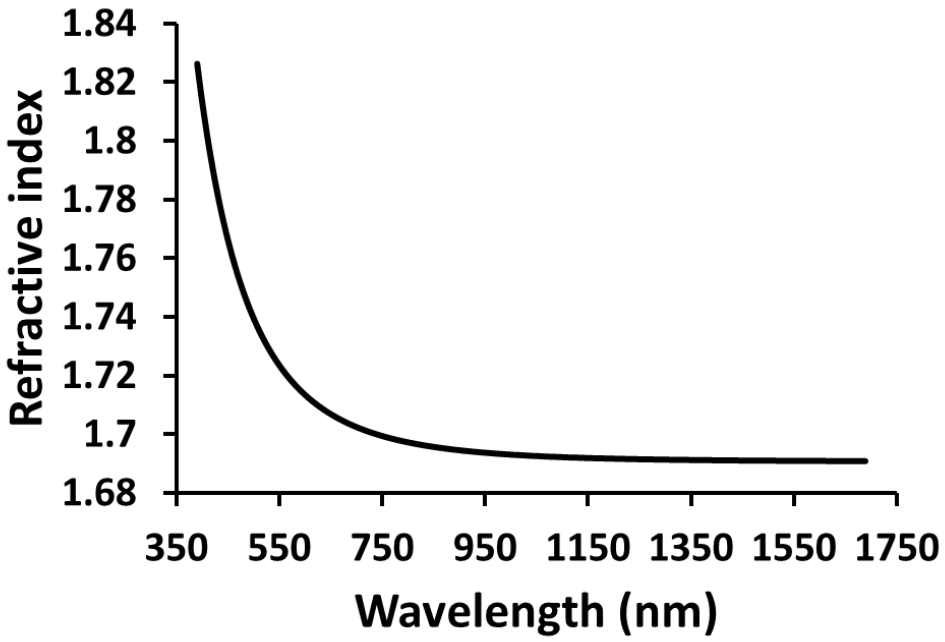

Figure S4.15 Refractive index of 1 executed from the ellipsometric experiment on a spin-coated thin film of FpC3BTh.

Supporting Information for Chapter 5

Fp- derivatives were prepared via MIR. Syntheses and characterizations were performed similar to that reported for FpC6 in the Experimental Section in Chapter 2.

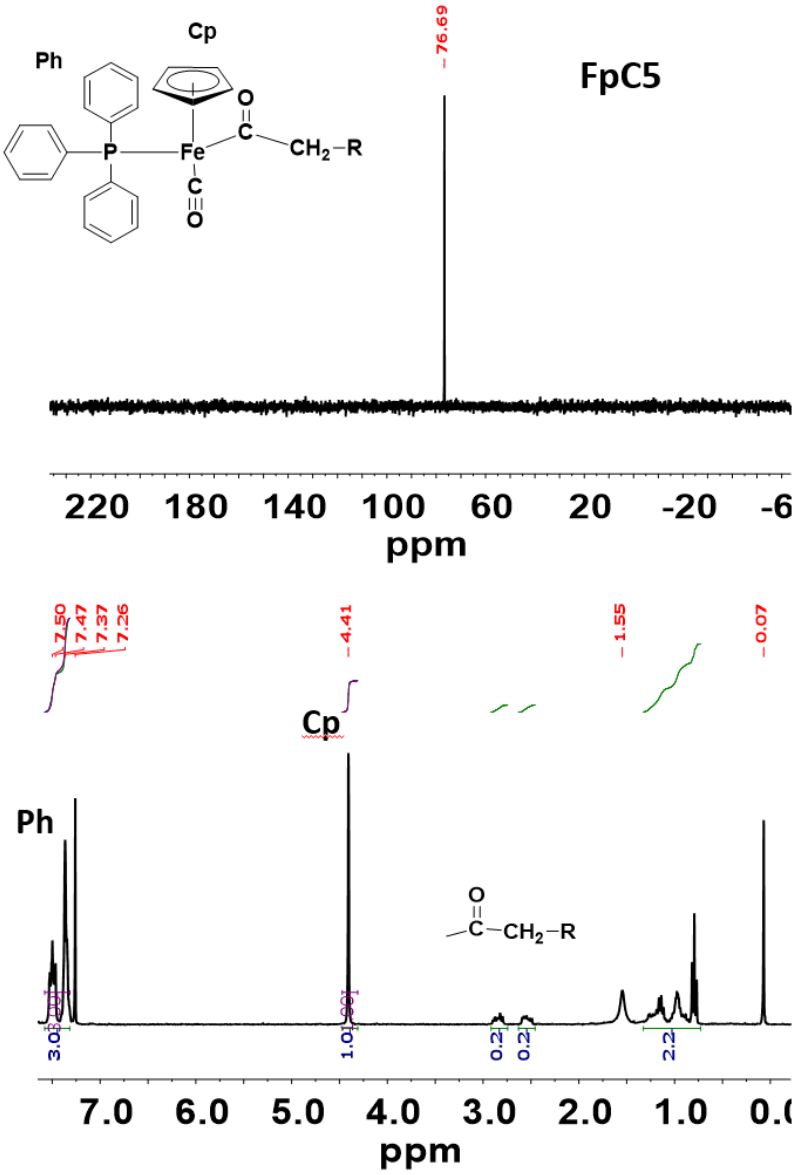

Figure S5.1 ^{31}P and ^{1}H NMR spectra ($CDCl_3$, 25 ^{o}C, 300 MHz) of FpC5

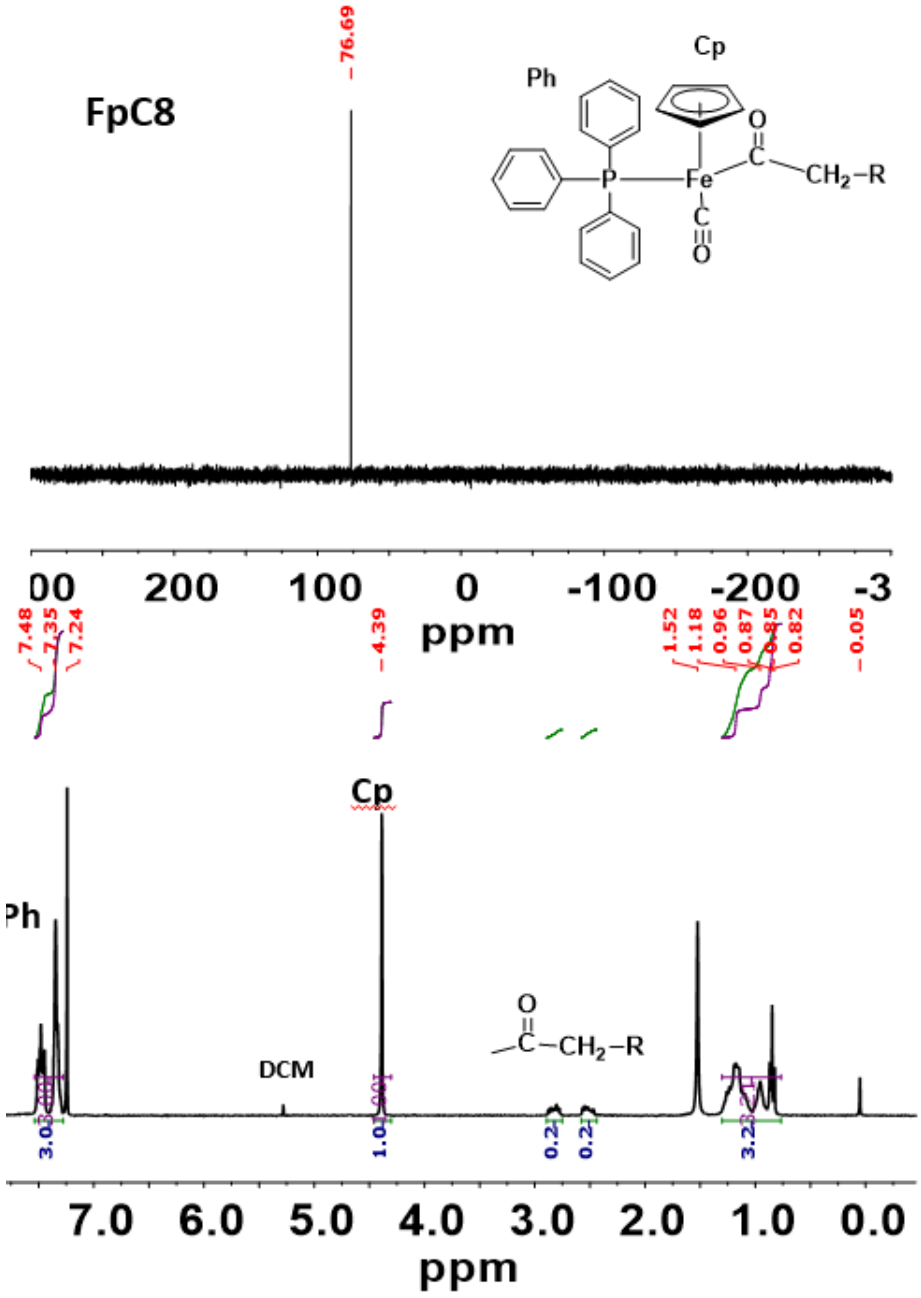

Figure S5.2 ^{31}P and ^{1}H NMR spectra ($CDCl_3$, 25 ^{o}C, 300 MHz) of FpC8

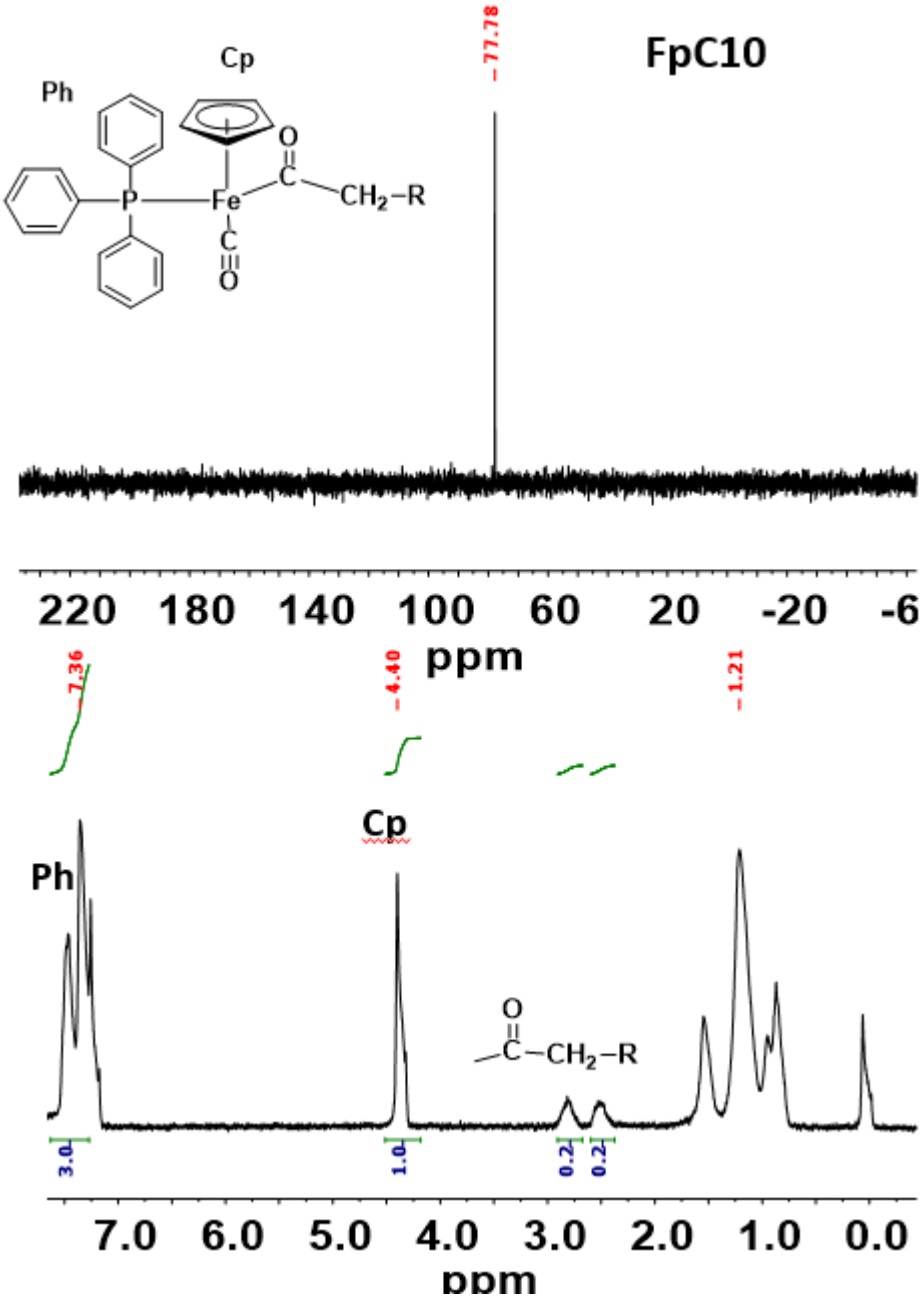

Figure S5.3 ^{31}P and ^{1}H NMR spectra ($CDCl_3$, 25 ^{o}C, 300 MHz) of FpC10

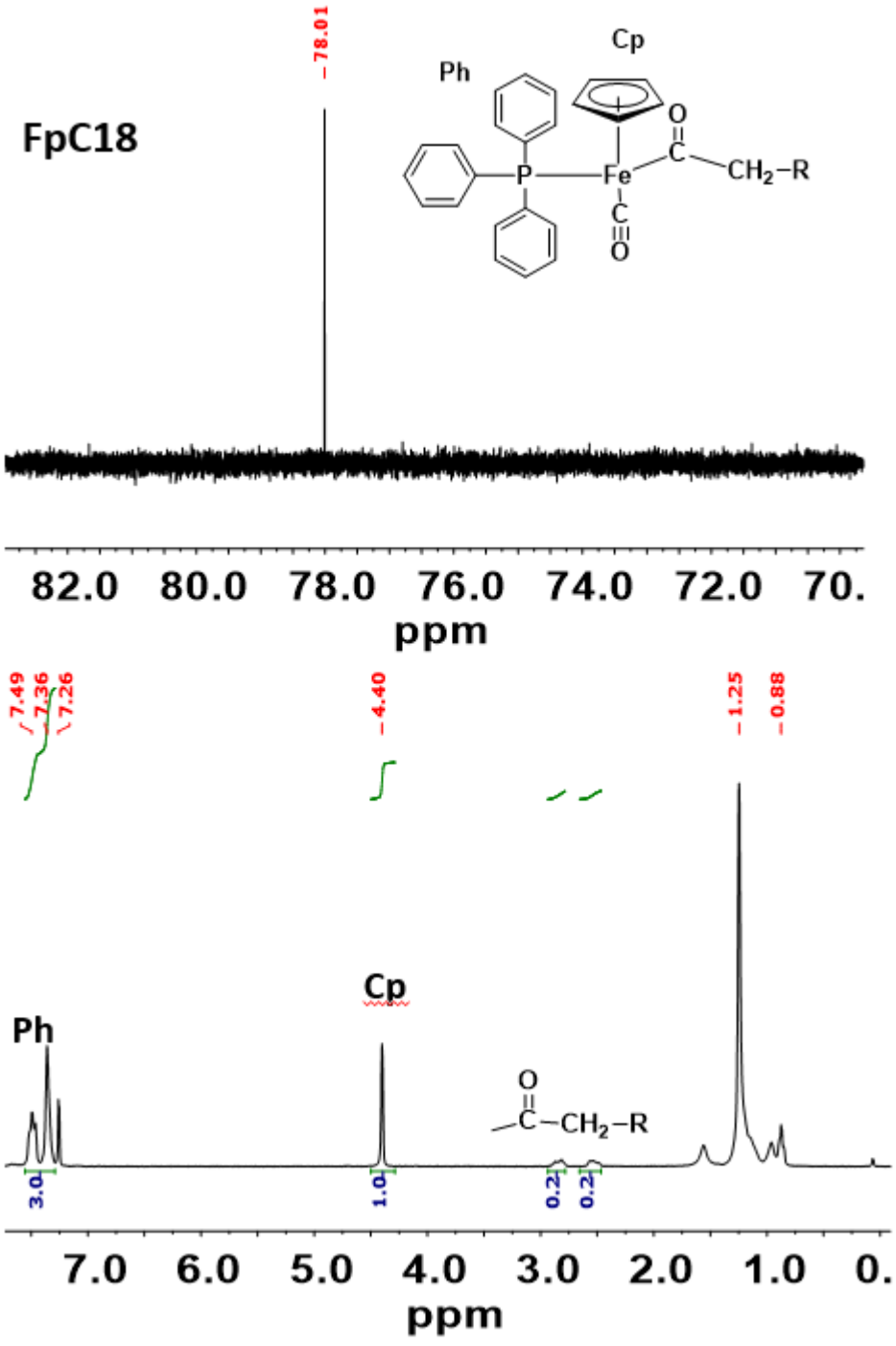

Figure S5.4 ^{31}P and ^{1}H NMR spectra ($CDCl_3$, 25 ^{o}C, 300 MHz) of FpC18

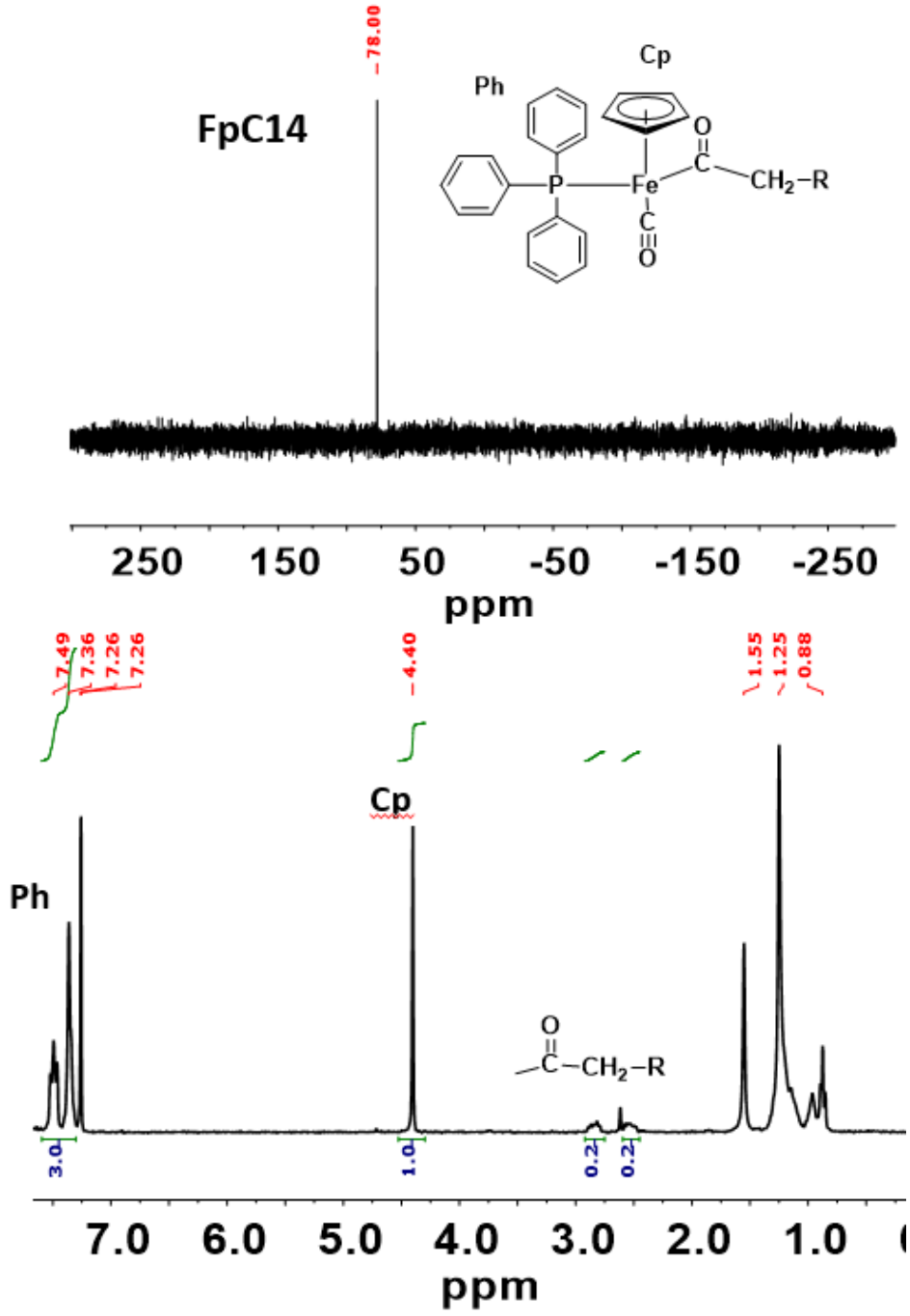

Figure S5.5 ^{31}P and ^{1}H NMR spectra ($CDCl_3$, 25 ^{o}C, 300 MHz) of FpC14

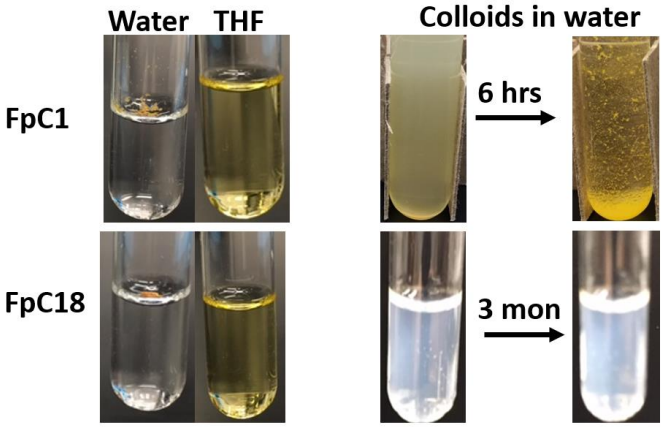

Figure S5.6 Photographs for FpC1 and FpC18 solutions. Left panel shows the solubility of FpC1 and FpC18 in water and THF. Right panel shows aqueous colloids of FpC1 and FpC18 over time.

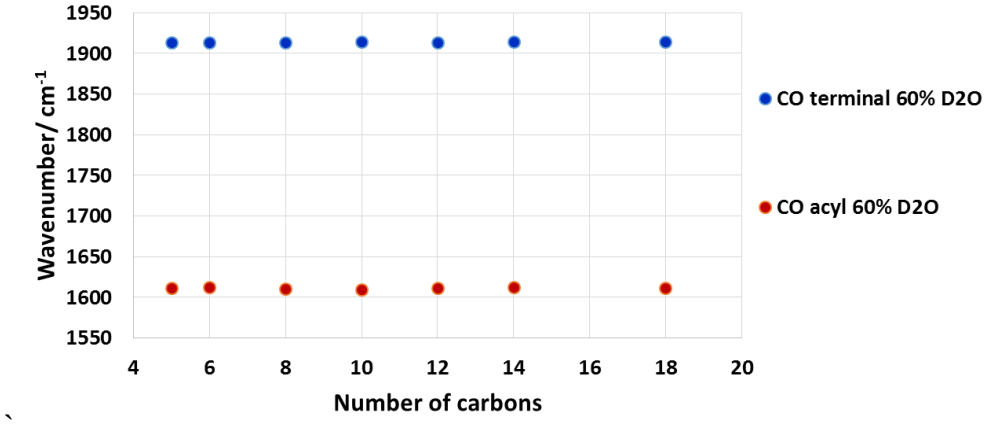

Figure S5.7 ATR-FTIR stretching frequencies (acyl and terminal CO groups) for the Fp-derivatives **5.2**–**5.7**, with different alkyl chain length self-assembled in 66 vol% D_2O in THF (2 M).

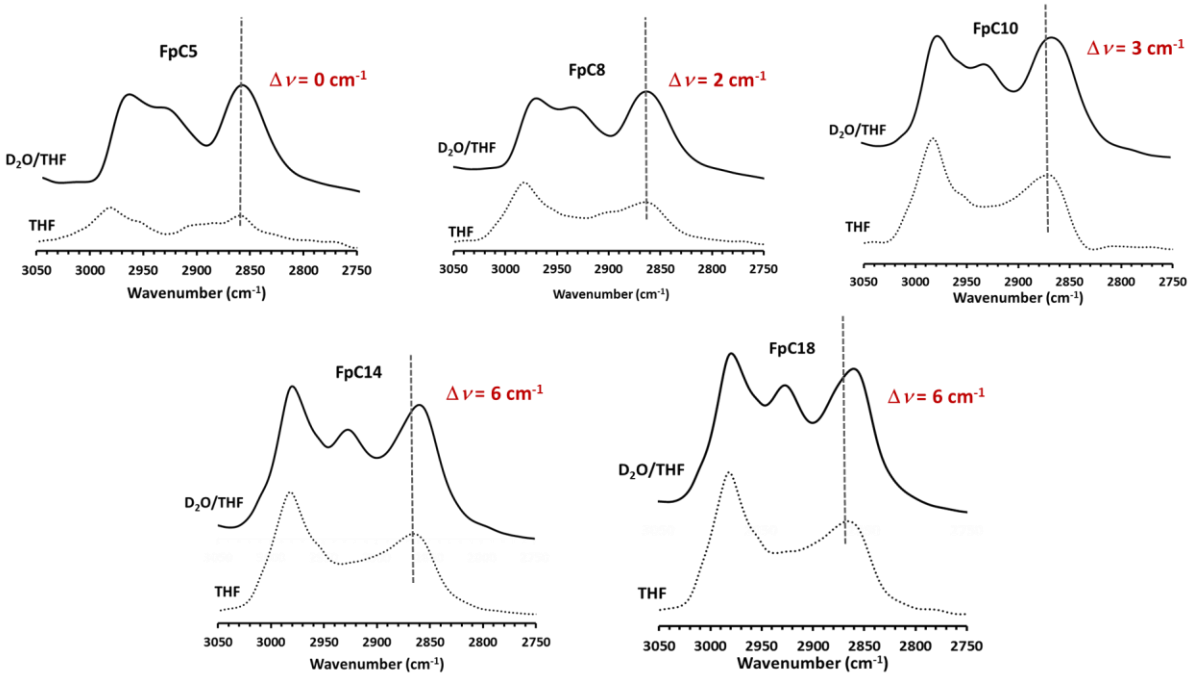

Figure S5.8 ATR-FTIR spectra (C-H stretching region) for FpCn in THF and 60 vol% D_2O in THF solutions.

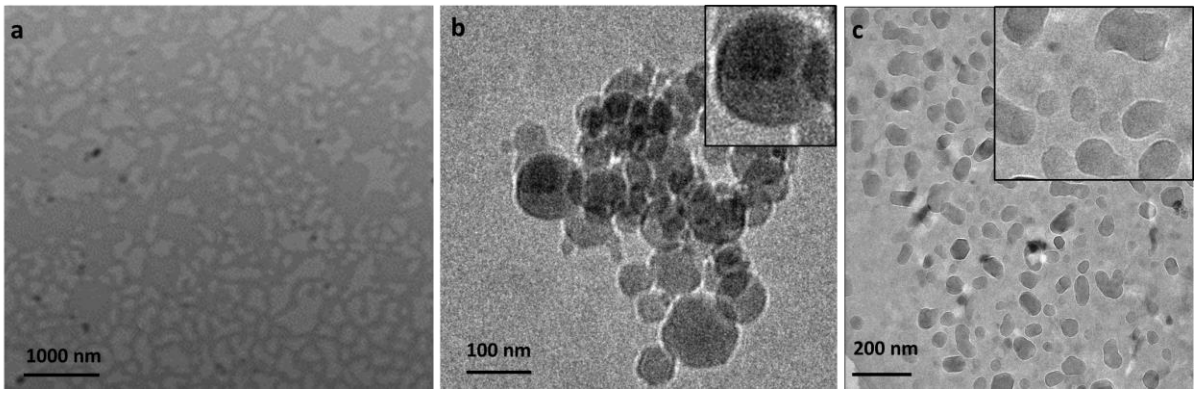

Figure S5.9 a) TEM image for FpC18 colloids. Cryo-TEM images for b) FpC10 and c) FpC18.

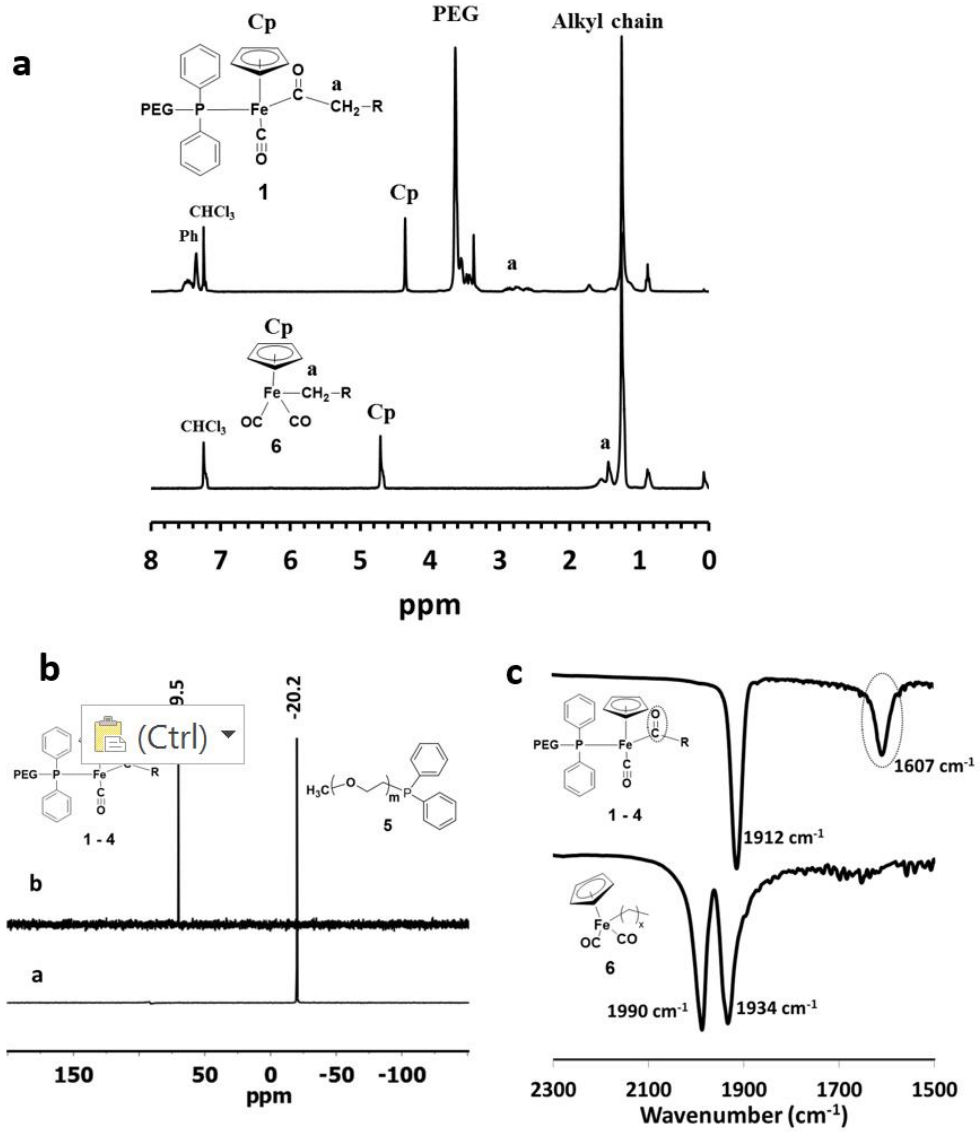

Figure S6.1 (**a**) Partial ^{1}H NMR for **6.1** and **6.6** and (**b**) ^{31}P NMR spectra for **6.5** and **6.1**($CDCl_3$, 25 ^{o}C, 300 MHz). (**c**) Partial FT-IR (KBr pellet) spectra of **6.6** and **6.1** before and after migration insertion reaction, respectively.

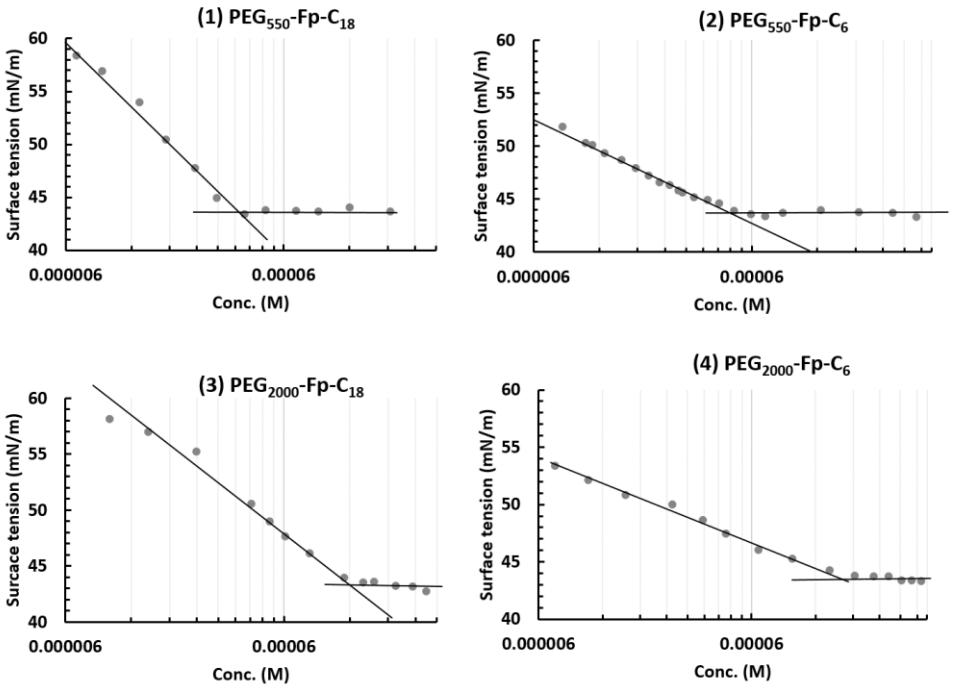

Figure S6.2 Surface tension as a function of solution concentrations for **6.1-6.4**.

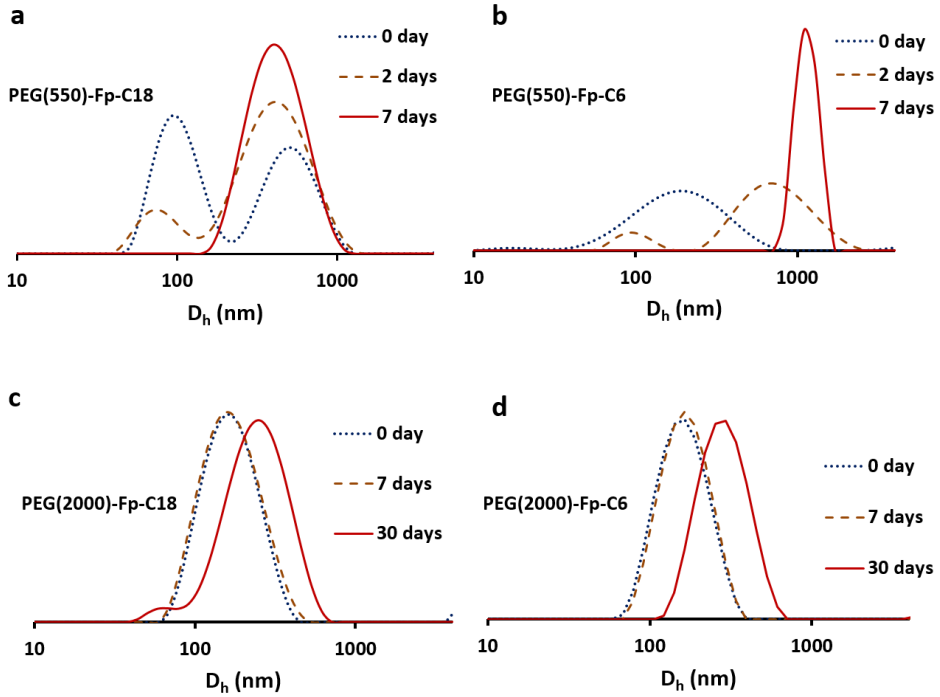

Figure S6.3 DLS results of the aqueous solutions of **6.1-6.4** over time.

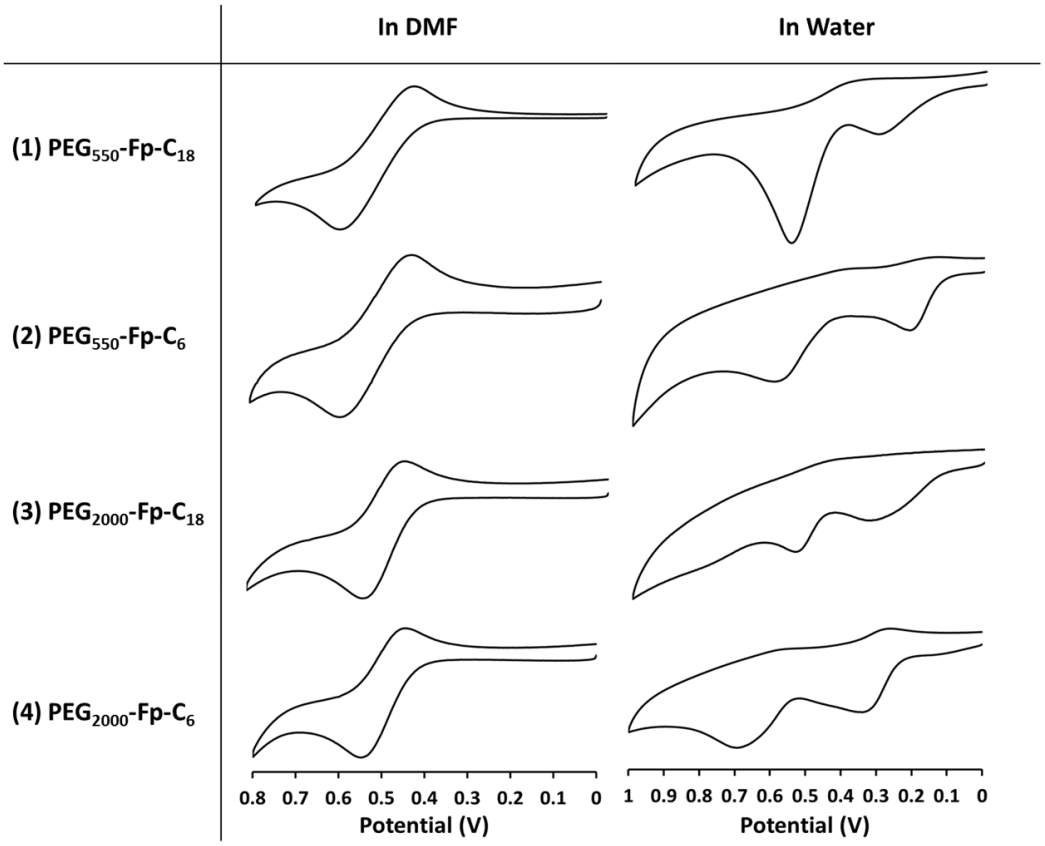

Figure S6.4 CV curves for **6.1**-**6.4** solutions in both DMF and water.

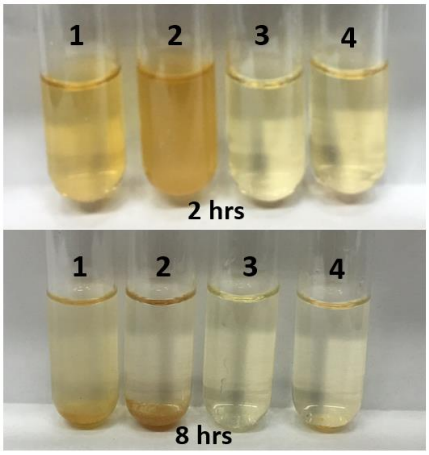

Figure S6.5 Photographs for the aqueous solutions of **6.1**-**6.4** heated at 50 ^{o}C.

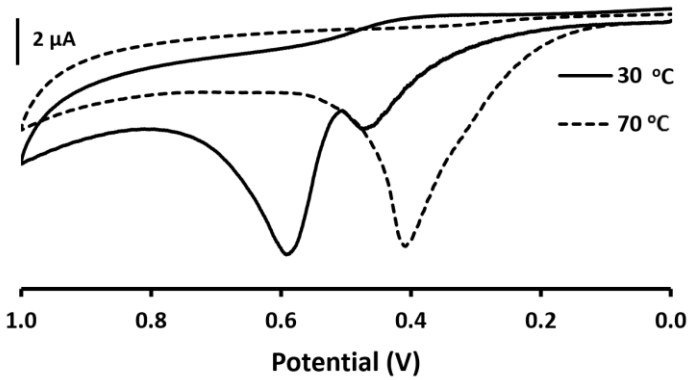

Figure S6.6 CV experiment results for aqueous solution of **6.1** (4 mg/mL) at 30 °C and 70 °C. (Scan rate 0.05 V/s)

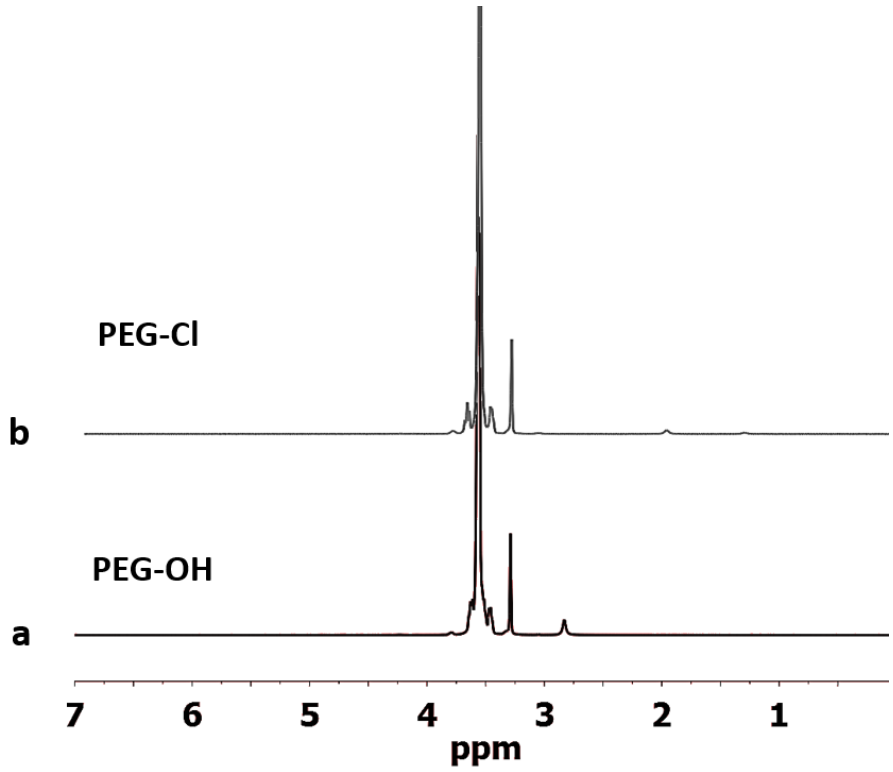

Figure S6.7 ^{1}H NMR spectra in $CDCl_3$ of (a) PEG-OH and (b) PEG-Cl. (Mn = 550)

^{1}H NMR spectra, for both PEG-OH and PEG-Cl, suggest successful conversion of the hydroxyl group into chlorine. Figure S6.7 shows the disappearance of OH proton peak at 2.8 ppm and evolving of a new triplet peaked at 3.7 ppm representing the methylene protons that close to chlorine atom.

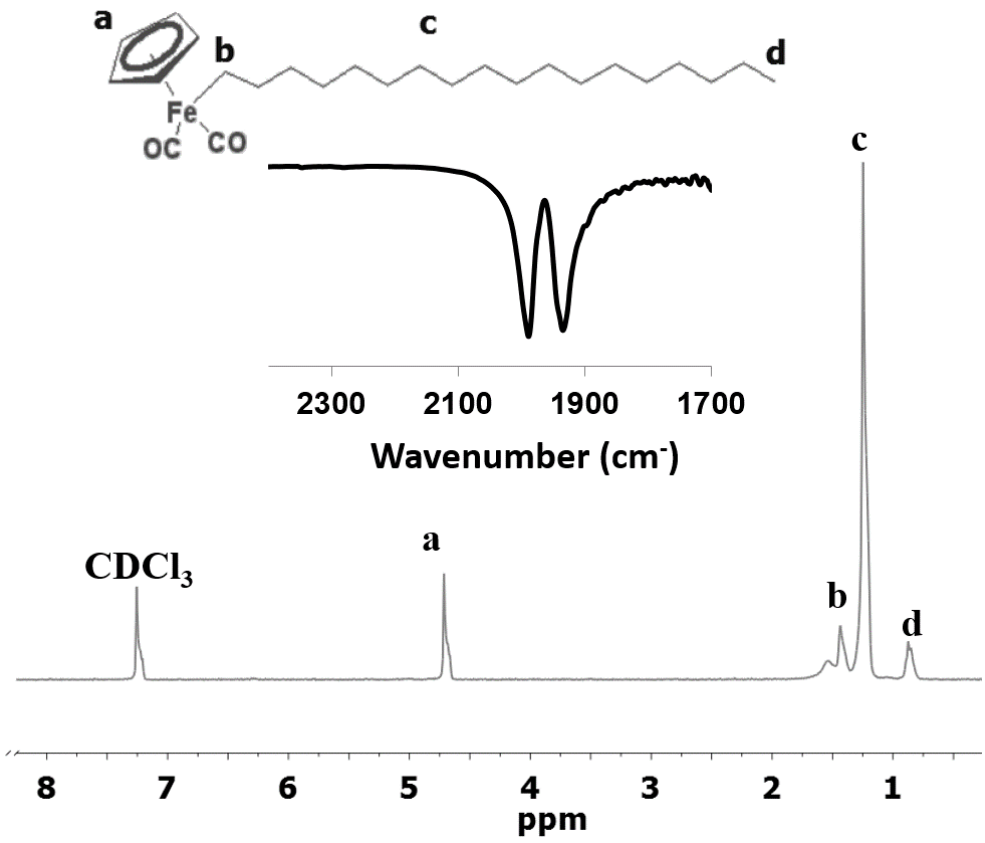

Figure S6.8 ^{1}H NMR, in $CDCl_3$, and FT-IR (KBr pallet) spectra of **6.6a** before MIR.

Table S6.1 CMC results and calculation of the area occupied per molecule (*A*) for **6.1**-**6.4**

	CMC (mg/mL)	CMC (mM)	Slope ($\delta \boldsymbol{\gamma} / \delta \ln(c)$)	Γ (mole/m^2) (-1/RT x (slope))	A=Area =1/Γ m^2/mol (m^2/molecule)
PEG_{2000}-Fp-C_{18} (**6.1**)	0.249	0.096	-7.757	3.137E-6	318783 (5.29E-19) = 52.9 A^{o2}
PEG_{550}-Fp-C_6 (**6.2**)	0.045	0.044	-4.473	1.809E-6	552828 (9.18E-19) = 91.8 A^{o2}
PEG_{550}-Fp-C_{18} (**6.3**)	0.041	0.036	-9.949	4.023E-6	248548 (4.13E-19) = 41.3 A^{o2}
PEG_{2000}-Fp-C_6 (**6.4**)	0.357	0.147	-3.11	1.25E-6	797529 (1.23E-18) = 132 A^{o2}